Interaction of multiphase fluids and solids: Theory, algorithms and applications

Jesus Bueno Alvarez
Supervisor: Héctor Gómez Díaz

A Thesis presented for the degree of
Doctor of Philosophy

Programa de Doutoramento en Enxeñaría Civil
Escola Técnica Superior de Enxeñeiros de Camiños, Canais e Portos
Departamento de Métodos Matemáticos e de Representación
Universidade da Coruña, Spain
March 2017

UNIVERSIDADE DA CORUÑA

Dedicated to my family
and especially, to my girlfriend:
Augusta Modestino.

Interaction of multiphase fluids and solids: Theory, algorithms and applications

Jesus Bueno Alvarez

Submitted for the degree of Doctor of Philosophy
March 2017

Abstract

The work presented in this thesis is devoted to the study and numerical simulation of Fluid-Structure Interaction (FSI) problems involving complex fluids. The nonlinear and time dependent nature of FSI problems makes the analytical solution very difficult or even impossible to obtain, requiring the use of experimental analysis and/or numerical simulations. This fact has prompted the development of a great variety of numerical models for the interaction of fluids and solid structures. However, most of the efforts have been focused on classical fluids governed by the Navier-Stokes equations, which cannot capture the physical mechanisms behind complex fluids. Here, we try to fill this gap by proposing several models for the interplay of solids and multi-phase or multi-component flows. The proposed models are then applied to particular problems that spark interest in fields, such as engineering, microfabrication and chemistry.

In this work, the behavior of the structure is described by the nonlinear equations of elastodynamics and treated as an hyperelastic solid. Two different constitutive theories are employed, a Neo-Hookean model with dilatational penalty and a Saint Venant-Kirchhoff model. The description of complex fluids is based on the diffuse-interface or phase-field method. In particular, two approaches are adopted. The first one is based on the Navier-Stokes-Korteweg equations, which describe compressible fluids that are composed by two phases of the same component that may undergo phase transformation, such as water vapor and liquid water. We use this model to study the influence of surface active agents in droplet coalescence and show that droplet motion may be driven by strain gradients -tensotaxis- of the underlying substrate. We also show several problems of phase-change-driven implosion, in which a thin structure collapses due to the condensation of a fluid. The second approach is based on the Cahn-Hilliard model, which we couple with the incompressible Navier-Stokes equations. We adopt an stabilization based on the residual-based variational multiscale formulation. This results in a model that describes two-component immiscible flows with surface tension. The potential of this model is illustrated by solving several elastocapillary problems in two and three dimensions including capillary origami, the static wetting of soft substrates and the deformation of micropillars.

As FSI technique, we adopt a moving mesh or boundary-fitted approach with matching discretization at the fluid-structure interface. This choice permits to strongly impose the kinematic compatibility conditions and results in more accurate solutions at the fluid-solid interface. In particular, we use the Lagrangian description to derive the semi-discrete form of the solid equations and the Arbitrary Lagrangian-Eulerian (ALE) description for the fluid domain. This means that the fluid mesh needs to be updated to accommodate the motion of the structure. For this purpose, we solve an additional linear elasticity problem subject to displacement boundary conditions coming from the motion of the solid.

For the spatial discretization of the solid and fluid domains, we adopt Isogeometric Analysis (IGA) based on Non-Uniform Rational B-Splines (NURBS), a generalization of the finite-element method that posseses higher-order global continuity and allows for a more precise geometric representation of complex objects. Regarding the time integration, we use a generalized-α scheme. The nonlinear system of equations is solved using a Newton-Raphson iteration procedure, which leads to a two-stage predictor-multicorrector algorithm. The resulting linear system is solved using a preconditioned GMRES method. A quasi-direct monolithic formulation is adopted for the solution of the FSI problem, that is, the fluid and solid equations are solved in a coupled fashion, while the mesh motion is solved separately using as input, data from the fluid-solid solve.

Resumen

El trabajo presentado en esta tesis está destinado al estudio y simulación numérica de problemas de interacción fluido-estructura (FSI de sus siglas en inglés) que involucran fluidos complejos. La naturaleza no lineal y dependiente del tiempo de los problemas FSI hace que su solución analítica sea muy difícil o incluso imposible de obtener, requiriendo el uso del análisis experimental y/o de simulaciones numéricas. Este hecho ha impulsado el desarrollo de una gran variedad de modelos numéricos para la interacción de fluidos y estructuras sólidas. Sin embargo, la mayoría de los esfuerzos se han centrado en fluidos clásicos gobernados por las ecuaciones de Navier-Stokes, las cuales no son capaces de capturar los mecanismos físicos detrás de los fluidos complejos. En este trabajo, intentamos rellenar ese hueco proponiendo varios modelos para la interacción de sólidos y fluidos multifase y multicomponente. Los modelos propuestos son aplicados a problemas particulares que desatan gran interés en campos como la ingeniería, la microfabricación y la química.

En este trabajo, el comportamiento de la estructura está descrito por las ecuaciones de la elastodinámica no lineal y es tratado como un sólido hiperelástico. Se emplean dos teorías constitutivas diferentes, un modelo Neo-Hookeano y un modelo Saint Venant. La descripción de los fluídos complejos está basada en el método de los campos de fase o método de interfaz difusa. En concreto, se adoptan dos técnicas diferentes. La primera se

basa en las ecuaciones de Navier-Stokes-Korteweg, las cuales describen fluidos compresibles que están compuestos por dos fases de un mismo componente como, por ejemplo, agua líquida y vapor de agua. Usamos este modelo para estudiar el papel de los tensoactivos en la coalescencia de gotas y mostrar que el movimiento de gotas puede desencadenarse por gradientes de deformación -tensotaxis- del substrato en el que se apoyan. Mostramos también varios ejemplos de implosión accionada por cambios de fase, en la cual una estructura delgada colapsa debido a la condensación de un fluido. La segunda técnica se basa en el modelo de Cahn-Hilliard, el cual acoplamos con las ecuaciones de Navier-Stokes incompresibles. En este modelo adoptamos una estabilización basada en la formulación variacional multiescala. Esto resulta en un modelo que describe flujos inmiscibles de dos componentes con tensión superficial. Ilustramos el potencial de este modelo resolviendo varios problemas de elastocapilaridad en dos y tres dimensiones incluyendo origamis por capilaridad, la deformación estática de substratos blandos con gotas o la deformación de micropilares.

Como técnica FSI, adoptamos un método de malla móvil con discretización compatible en la interfaz sólido-fluido. Esta elección permite imponer de forma fuerte las condiciones de compatibilidad cinemática y da lugar a resultados más precisos cerca de la interfaz sólido-fluido. En concreto, usamos una descripción Lagrangiana para derivar la forma semidiscreta de las ecuaciones del sólido y una descripción Arbitraria Lagrangiana-Euleriana (ALE) para el dominio del fluído. Esto significa que la malla del fluido tiene que ser actualizada para acomodar el movimiento de la estructura. Con este propósito resolvemos un problema adicional de elasticidad lineal en el que las condiciones de contorno son los desplazamientos procedentes del movimiento del sólido.

Para la discretización espacial tanto del dominio del sólido como del fluído, adoptamos Análisis Isogeométrico (IGA) basado en B-Splines racionales no uniformes (NURBS), una generalización del método de elementos finitos que posee continuidad global de alto orden y que permite una representación geométrica más precisa de objetos complejos. En lo que respecta a la integración temporal, usamos un esquema alfa generalizado. El sistema no lineal de ecuaciones se resuelve usando un método de Newton-Raphson iterativo, que lleva a un algoritmo de dos fases predictor-multicorrector. El sistema lineal resultante es resuelto mediante un método GMRES precondicionado. Se adopta además una formulación monolítica para la solución del problema FSI, esto es, las ecuaciones del fluido y del sólido se resuelven de manera acoplada mientras que el movimiento de la malla se resuelve separadamente, usando como input los datos del resolvedor sólido-fluido.

Resumo

O traballo presentado nesta tese está destinado ó estudo e simulación numérica de problemas de interacción fluído-estrutura (FSI nas súas siglas en inglés) que involucran fluídos complexos. A natureza non lineal e dependente do tempo deste tipo de problemas fai que a súa solución analítica sexa moi difícil ou mesmo imposible de conseguir, esixindo o uso de análises experimentais e / ou simulacións numéricas. Este feito levou ó desenvolvemento dunha gran variedade de modelos numéricos para a interacción de fluídos e estruturas sólidas. Con todo, a maioría dos esforzos concentráronse en fluídos clásicos gobernados polas ecuacións de Navier-Stokes, as cales non son capaces de capturar os mecanismos físicos detrás dos fluídos complexos. Nesta tese tratamos de encher este burato propoñendo modelos para a interacción de sólidos e líquidos multifase e multicompoñente. Os modelos propostos son aplicados a problemas específicos que espertan gran interese en campos como a enxeñería, a microfabricación e a química.

Neste traballo o comportamento da estrutura está descrito polas ecuacións da elastodinámica non lineal e é tratada como un sólido hiperelástico. Usamos dúas teorías constitutivas diferentes: un modelo Neo-Hookeano e un modelo Saint Venant. A descrición do fluído complexo baséase no método de campos de fase ou método de interfaz difusa. En concreto, adóptanse dúas técnicas diferentes. A primeira baséase nas ecuacións de Navier-Stokes-Korteweg, que describen fluídos compresibles que están compostos de dúas fases dun único compoñente, por exemplo, auga líquida e vapor de auga. Utilizamos este modelo para estudar o papel dos axentes tensoactivos na coalescencia de gotas e demostrar que o movemento de gotas pode ser desencadeado mediante gradientes de deformación do substrato no que se apoian -tensotaxe-. Tamén se mostran varios exemplos de implosión inducida por cambios de fase, no que unha estrutura fina colapsa pola condensación dun fluído. A segunda técnica está baseada no modelo de Cahn-Hilliard, o cal é acoplado coas ecuacións de Navier-Stokes. Neste modelo adoptamos unha estabilización baseada na formulación variacional multiscala. Isto resulta nun modelo que describe fluxos inmiscibles de dous compoñentes con tensión superficial. Ilustramos o potencial deste modelo resolvendo varios problemas de elastocapilaridade en dúas e tres dimensións, incluíndo origamis por capilaridade, a deformación estática de substratos brandos con gotas ou a deformación de micropilares.

Como técnica FSI, adoptamos un método de malla móbil con discretización compatible na interfaz sólido-líquido. Esta elección permite impoñer de xeito forte as condicións de compatibilidade cinemática e da lugar a resultados máis precisos preto da interfaz sólido-fluído. En concreto, usamos unha descrición Lagranxiana para derivar a forma semidiscreta das ecuacións do sólido e unha descrición Arbitraria Lagranxiana-Euleriana (ALE) para o dominio do fluído. Isto quere dicir que a malla do fluído ten que ser actualizada para acomodar o movemento da estrutura. Para iso, resolvemos un problema

adicional de elasticidade lineal no que as condicións de contorno son os desprazamentos procedentes do movemento do sólido.

Para a discretización espacial tanto do dominio do sólido coma do fluído adoptamos Análise Isoxeométrica (IGA) baseada en B-splines non uniformes (NURBS), unha xeneralización do método de elementos finitos que posúe continuidade global de alta orde e que permite unha representación máis precisa de obxectos complexos. No que respecta á integración temporal, usamos un esquema alfa xeneralizado. O sistema de ecuacións non lineais é resolto a través dun método de Newton-Raphson iterativo que da lugar a un algoritmo preditor-multicorrector. O sistema lineal resultante é tratado mediante un método GMRES precondicionado. Ademais, adoptamos unha formulación monolítica para o problema FSI, é dicir, as ecuacións do fluído e do sólido son resoltas de xeito acoplado mentres que o movemento da malla se resolve por separado, utilizando como input os datos do resolvedor sólido-fluído.

Acknowledgements

The PhD is often considered to be a lonely journey. However, that was not my case at all. It is true that it was long and it was hard but I have always been surrounded by extraordinary people, who provided never-ending support, immense knowledge and friendship during this process. This thesis is dedicated to all of them. I would like to express special thanks to the following individuals,

To my advisor Hector Gomez. I feel privileged to have undertaken my doctoral studies under your guidance. Thank you for everything: the weekly meetings, your patience and understanding, your motivation, and your enormous wisdom. I have learned so much from you.

To Professor Yuri Bazilevs. Thanks for acepting me in your team during my stays at UCSD. It gave me the opportunity to work and learn with an incredible group of people. Thanks also for your guidance and advices.

To my colleagues Guillermo Vilanova, Jiangping Xu, Hugo Casquero, Guillermo Lorenzo, Adrian Moure, Pablo Dominguez, and Carles Bona. Thank you for your friendship and the many hours we shared in the lab and in discussion of impossible things. I appreciate your valuable feedback, which have helped to give shape to the papers and the ideas presented in this thesis. I am also deeply grateful to Alba López for helping not only with administrative work, but also with wise advices. I greatly appreciate the privilege of being a member of such a wonderful group of people, both professionally and personally.

To my colleagues and friends at UCSD: Marco Pigazzini, Artem Korobenko, Jinhui Yan, Kazem Kamran, and specially to George Moutsanidis, who welcomed me with open arms and made me feel at home.

To my friends here and abroad. Special thanks to David, Eloy and Rodrigo, for your support and the immense amount of hours making silly jokes. Thanks also to Oytun and Ryan for hosting me at your place. You have become wonderful friends.

And finally, to my wonderfully supportive family and my beloved girlfriend, Augusta Modestino, without whom this journey would simply not have been possible: Thank you.

Contents

List of Figures

Chapter 1

Introduction

Fluid-Structure Interaction (FSI) encompasses a group of problems in which a deformable or movable solid interacts with an internal or surrounding fluid flow, that is, problems with an interdependence between a fluid and a solid structure. The nature of this kind of problems makes them ubiquitous in almost every branch of engineering and science. FSI problems are present in biomedical research [10, 12], aerospace and civil engineering [70, 138, 171], marine engineering [194, 199], and wind energy [11, 173] to name a few.

In the last decades, significant advances have been made in FSI research. However, a comprehensive study of FSI problems remains a challenge due to their nonlinear and time-dependent nature. In most cases, an analytical solution is very difficult or even impossible to obtain and experimental analysis and/or numerical simulations need to be employed. The same challenges appear in the interaction of complex fluids and solids. Complex fluids [81, 118] can be understood as a particular type of fluids in which different phases coexist, whether they are liquid, gaseous or solid phases. Prime examples are emulsions, foams, colloids, solutions of polymers, liquid crystals and, in general, any multiphase or multicomponent flow. Because of their unusual mechanical nature, the interaction of complex fluids and solids produces much richer physics than classical fluids, especially at small scales, giving rise to a great variety of problems. In this document, we focus on those problems involving multiphase and multicomponent flows; the term "complex fluids" will be used, in general, to refer to this particular type of fluids.

The development of accurate and efficient computational methods for the interaction of complex fluids and solids could potentially benefit a number of disciplines, such as mechanobiology, engineering or chemistry, among others:

- **Mechanobiology**. Cells can migrate in response to gradients in stiffness (durotaxis) and gradients in strain (tensotaxis) of the underlying substrate [123, 163]. The understanding of these mechanisms is still very limited but they seem to be controlled to a significant extent by mechanics, and it seems plausible that, at cellular scale, capillary forces play an important role. A theoretical model that allowed to study

(a) Railroad tank car before implosion (b) Railroad tank car after implosion

Figure 1.1: Implosive collapse of a railroad tank car. The implosion is triggered by reducing the internal pressure of the tank car. Figures obtained from [23]

durotaxis and/or tensotaxis would contribute to a better understanding of the process, and would allow to explore scenarios that are difficult to probe experimentally.

- **Engineering**. There is a enormous variety of engineering problems in which complex fluids play a prominent role. Among them, one of the most relevant problems is the implosive collapse of thin structures [110,144]. Structures containing a compressible fluid at a pressure below the external pressure have the potential to collapse inwards. For example, an air-filled structure may suffer an implosive collapse when it is immersed underwater due to the increase of the external pressure. In other situations, phase transformations may trigger the implosion of vapor-filled structures. Thermal variations may transform the vapor into liquid, reducing the internal pressure, which, in turn, may lead to a violent and rapid collapse of the structure, producing strong compressions and large deformations [111]. Strong implosions may also involve contact, plastic deformation, and fracture. See Fig. 1.1 for an example of implosive collapse of thin structures.

- **Chemistry**. From the perspective of the chemical community, there are innumerable problems in which complex fluids are present. A clear example is surface active agents or surfactants, that is, compounds that find energetically favorable to be located at the interfaces between fluids [71,133,149]. Surfactants are absorbed by the interface and they can significantly reduce the work required to generate it, altering completely the behavior of the system. For this reason, their use is overwhelming in the chemical industry (they can be found in detergents, cosmetics, dye, etc.) as well as in other fields, such as microelectronics [176], biotechnology [153,191], or medical research [73,146]. They also play an essential role in our organism, increasing the pulmonary compliance and preventing atelectasis [94,115], that is, the complete or the partial collapse of the lungs.

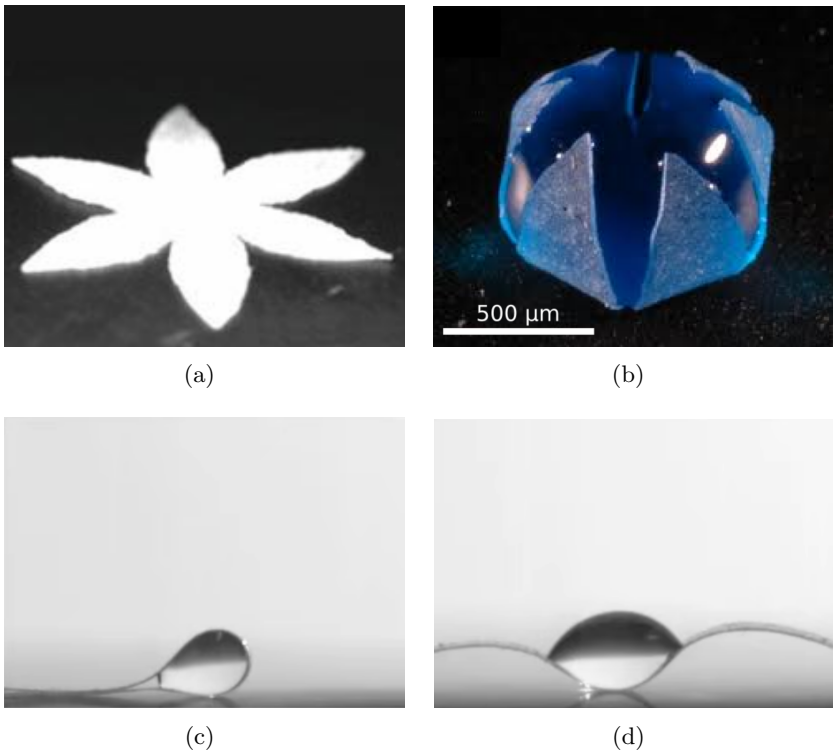

Figure 1.2: Ellastocapillary origami. The capillary forces at the liquid-vapor interface are able to deform slender structures at small scales. Upper figures present an example of the wrapping of a drop of water with a PDMS sheet. (a) The membrane (white color) is placed on a super-hydrophobic surface. (b) A drop of water is deposited on the PDMS and allowed to evaporate. During evaporation, the drop retracts and folds the membrane. In the bottom figures a liquid droplet impacts an elastic membrane triggering the wrapping of the droplet. (c) High impact velocities produce the complete encapsulation of the droplet. (d) Low velocities result in the partial wrapping of the droplet. Figs. (a) and (b) were obtained from [142]. Figs. (c) and (d) were retrieved from [145].

- **Microfabrication**. The growing interest for micro-devices has brought attention to the effects that surface tension of small droplets may have in soft or slender structures. As the dimensions of a a system are scaled down, capillary forces decrease slower than pressure and gravity forces and eventually become dominant, being able to deform elastic structures. This process is known as elastocapillarity [147, 160] (see Fig. 1.2 for an example of capillary forces acting on slender structures). Understanding the physical mechanisms underlying elastocapillary phenomena is essential for the design of new materials and devices at the micrometer and nanometer scale.

The computational models for FSI have traditionally focused on the interaction of solids with classical fluids governed by the Navier–Stokes equations of incompressible or compressible flows [14, 32, 91, 92, 124–126, 162, 170, 172, 174]. However, some FSI problems, such as those involving complex fluids, cannot be modeled using this paradigm because they fundamentally depend on physical mechanisms not captured by the Navier–Stokes

equations. As a consequence, the number of works that model the interaction of complex fluids and solids is very limited. A notable exception is [188].

In this thesis, we extend the state-of-the-art in interaction of complex fluids and solids by presenting the following developments:

- **A model based on the Navier-Stokes-Korteweg (NSK) equations for complex fluids with surfactants**. We present a new model for liquid-vapor flows with surface active agents that captures the dynamics of surfactants and accounts for phase transformations in the fluid. Our approach to phase transformation is based on the diffuse-interface or phase-field methods. In particular, our theory emanates from the isothermal Navier-Stokes-Korteweg equations, which describe single-component two-phase flow and naturally allow for spontaneous phase changes. We derive the model from a free energy functional by using a Coleman-Noll approach. The proposed theory has significant potential to study the influence of surfactants in vaporization and condensation processes. In order to tackle the numerical challenges posed by this model, such as the stiffness in space and time, the internal and boundary layers as well as the higher-order partial differential operators, we adopt as a computational technique Isogeometric Analysis (IGA) based on Non-Uniform Rational B-Splines (NURBS), which permits an accurate and efficient discretization. The viability of the theoretical framework and the effectiveness of the proposed algorithms are illustrated by solving several numerical problems in two and three dimensions. See [29] and Chapter 4 for more details.

- **An Arbitrary Lagrangian-Eulerian model for the interaction of complex fluids and solids based on the NSK equations and neo-Hookean solids**. Complex fluids produce much richer physics than classical fluids when they interact with solids, especially at small scales. We present a new mathematical model for FSI capable of capturing these physics for the case of single-component two-phase flow interacting with hyperelastic solids. In particular, the fluid is treated as a viscous and compressible fluid, governed by the Navier-Stokes-Korteweg equations, which allow the fluid to condensate and evaporate naturally due to temperature and/or pressure changes. The structure is treated as a nonlinear hyperelastic solid in the Lagrangian description and governed by the equations of nonlinear elastodynamics. The Arbitrary Lagrangian-Eulerian (ALE) description is utilized for the fluid subdomain. The motion of the fluid mesh is computed by solving the equations of elastostatics given the displacement data on the fluid-solid interface. A quasi-direct monolithic formulation is adopted for the solution of the FSI problem, that is, the fluid and solid equations are solved in a coupled fashion, while the mesh motion is solved separately using as input, data from the fluid-solid solve. A NURBS-based

isogeometric analysis methodology is employed for the spatial discretization of the fluid and the structural mechanics equations. We use the proposed model to simulate the implosive collapse of vapor-filled structures. We study different geometries in 2D and 3D, in which the implosion is triggered by thermal variations. See [27] and Chapter 5 for more details.

- **A model for the interaction of complex fluids and solids based on the NSK equations and a Saint-Venant structure**. The fluid model described in the previous point is coupled now with a Saint-Venant structure. The idea is to study, from a mechanical point of view, a particular problem known as tensotaxis, that is, the ability of cells to migrate in response to gradients in strain of the underlying substrate. The goal is to see if at small scales, capillary forces play an important role in this process, studying the particular case of droplets. Experimental studies of tensotaxis are particularly challenging because prestraining the substrate is often accompanied by an increase in the substrate stiffness as a result of nonlinear material response, thus producing a combination of tensotaxis and durotaxis. Replacing the neo-Hookean model used in the implosion problem with a Saint-Venant model allows us to consider geometric nonlinearities with a linear material response. As a consequence, the strains introduced in the substrate to trigger tensotaxis do not alter the stiffness of the solid, avoiding a situation with simultaneous tensotaxis and durotaxis. In summary, we propose a theoretical model that allows to isolate the effects of tensotaxis. We present numerical simulations in two and three dimensions, in which droplet motion and coalescence are triggered by applying localized forces in a soft substrate. See [26] and Chapter 6 for details.

- **A model based on Navier-Stokes-Cahn-Hilliard for the interaction of solids and incompressible complex fluids**. The FSI models presented in the previous points are able to describe the physics of single-component two-phase flows interacting with hyperelastic structures. However, there are a number of physical and engineering problems in which the fluid is not formed by two phases of the same component. It is the case, for example, of gas injection for oil recovering, fuel sprays in combustion processes, air-water flows, etc. For modeling this kind of problems, we propose a theory based on the Navier-Stokes-Cahn-Hilliard equations, which describe two-component immiscible flows with surface tension. The fluid is treated as a viscous and incompressible fluid in the Arbitrary Lagrangian-Eulerian description. The structure is treated as a nonlinear hyperelastic solid in the Lagrangian description and governed by the equations of nonlinear elastodynamics. The proposed model is used to predict the deformation caused by the capillary forces of a glycerol droplet deposited on a soft substrate. The results are then validated with experimental data.

The model is also used for the 2D and 3D simulation of other elastocapillary problems, such as capillary origami or the bending of flexible micro-pillars. The reader is referred to [28] and Chapter 7 for more details.

The rest of the thesis is organized as follows. Chapter 2 presents a quick overview of different computational methods for FSI problems, phase-field methods and isogeometric analysis. The research objectives of this thesis are stated in Chapter 3. Chapters 4, 5, 6 and 7 expand on the four contributions mentioned above. The idea of these Chapters is to describe concisely the goals of each contribution, provide both representative results and conclusions, and refer to the different papers attached as appendices for the details. In each of these Chapters the most significant contributions are highlighted at the end, as well as future research directions emerging from the work performed. Chapter 8 reports on collaborations in other research works not directly related with this thesis. Finally, in Chapter 9, some concluding remarks are commented.

Chapter 2

Background on computational modeling

2.1 Computational methods for FSI problems

Over the last decades, the modeling and simulation of fluid-structure interaction and other coupled problems has gained increasing attention among the computational mechanics community. FSI simulations are used for the design and analysis of heart valves [51,61,97], wind turbines [11, 96, 199], airplane wings [69, 108], for the study of aneurysms [12, 169], or for the modeling of spacecraft parachutes [167, 168] to name some applications. It is in these cases when a robust, accurate, geometrically flexible, and efficient computational method is essential. However, this is not always an easy challenge. Solving a FSI problem entails extra difficulties compared to a solid-only or a fluid-only problem.

In a single-field problem, there is only one set of differential equations in the problem domain, which may be fixed or not, and a set of boundary conditions. In FSI problems, the governing equations for the fluid and the solid must be satisfied simultaneously. The fluid and solid domain do not overlap and a set of coupling conditions – the compatibility of kinematics and tractions – must be satisfied all along the fluid-structure interface, which evolves in time. There are two main procedures or coupling techniques to solve theses equations: staggered and monolithic (see, for instance, [8]). In monolithic or strongly-coupled approaches, the fluid, solid and mesh equations are solved simultaneously in fully-coupled fashion. The main advantage is that the compatibility conditions are implicitly satisfied in the solution procedure and the solvers tend to be more robust. In contrast, in staggered or loosely-coupled techniques the fluid and structure equations are solved sequentially using explicitly the compatibility conditions for the exchange of information between both solvers. The main advantage of this approach is that existing and validated fluid and structural solvers may be used and, consequently, the code development time is reduced. On the other hand, convergence becomes difficult to achieve in FSI problems

where the structure is "light" and the fluid is "heavy" [15]. In the same way, convergence becomes an issue when an incompressible fluid is fully contained by a solid. With this in mind, one can clearly see that finding a unique computational FSI method capable of solving efficiently and accurately all kinds of fluid-structure interaction problems is a challenging and probably impossible task. For the moment, there exist different types of computational methods specially developed to deal with specific FSI problems. FSI methods can be classify into two main groups:

- **Interface tracking methods**. Also known as moving-mesh or boundary-fitted methods. When the structure moves, the shape of the fluid subdomain changes to adapt to the motion of the structure. As a consequence, the fluid-structure interface moves as well. In interface tracking methods – as it is the case of the Arbitrary Lagrangian-Eulerian and the space-time techniques – the mesh moves to follow that interface, that is, the mesh tracks the interface and is updated as the flow evolves. This way, we are able to control the mesh resolution near the interface and obtain accurate solutions as well as impose exactly the compatibility conditions. However, as the interface evolves, the quality of the mesh decreases, and it may reach a point where remeshing is needed, which can be time consuming. Moreover, the updating of the mesh requires solving a boundary-value problem in which the Dirichlet boundary conditions are the displacements of the solid at the interface. For a more detailed discussion on interface tracking methods the reader is referred to [8, 58, 179]. See Fig. 2.1 for an example of mesh discretization at the fluid-structure interface in ALE problems.

- **Interface capturing or nonmoving-mesh methods**. In this approach, the fluid mesh does not move to track the fluid-structure interface. The interface is captured by the mesh covering the region where the fluid-solid boundary is. As a consequence, the resolution near the interface will be limited by the resolution of the mesh in that region. This method enables a less accurate representation of the interface than the previous one although it is more flexible since it does not require mesh updating. This is the case of the immersed methods, in which a Lagrangian solid moves arbitrarily on top of a background fluid mesh in a non-conforming fashion. For a more detailed explanation of immersed methods the reader is remitted to [32, 130, 136, 200]. Fig. 2.1 presents an example of mesh discretization in immersed approaches.

2.2 Phase-field modeling

Phase transition phenomena has been traditionally modeled using sharp-interface models [5, 59, 117]. However, this approach presents several limitations. For many classes of

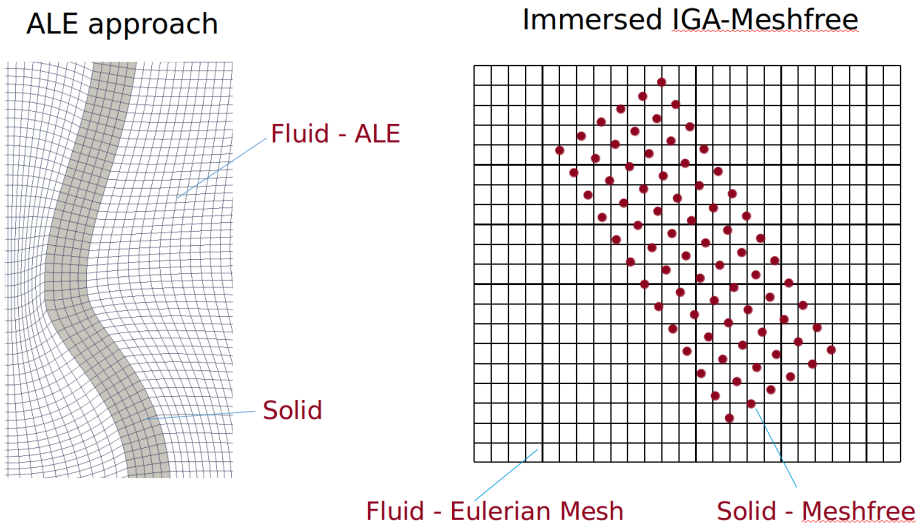

Figure 2.1: [Left] In ALE approaches, the fluid subdomain changes to adapt to the motion of the structure. The fluid mesh moves to follow the interface and thus, needs to be updated as the flow evolves. [Right] In immersed methods, the interface is captured by the mesh covering the region where the fluid-solid boundary is, which leads to less accurate representations of the interface.

problems, the appropriate sharp interface model is often not known [141]. Besides, their numerical simulation turns out to be extremely difficult. The most challenging aspect is the interaction between topologically complex interfaces that undergo merging and pinch-off during the course of a phase transformation. Note that one must solve simultaneously the partial differential equations that govern each phase dynamics and the boundary conditions that hold on a moving, and *a priori* unknown, interface, and this usually results in complex numerical treatment.

Another alternative to deal with moving interface problems are phase-field models [3, 39, 52, 67, 127, 129, 141]. The principal characteristic of this approach is the assumption that the interface actually represents a rapid but smooth transition of physical quantities between the bulk values – for this reason, phase-field models are also called diffuse-interface models. The idea of diffuse interfaces dates back to Poisson [140], Gibbs [82] and van der Waals [190]. However, it is in the last decades, when these models are gaining increasing interest in many fields, such as physics, material science and engineering. In particular, they have been applied with great success to solidification dynamics [31, 116, 135], foams [74], brittle fracture [21, 113], dendritic growth [106, 114], vesicle dynamics [17], microstructure evolution in solids [76], planet formation [187], infiltration of water into a porous medium [46, 85], coalescence of bubbles [88], cancer growth [75, 192, 197, 198], elasto-capillarity [188] or description of partial wetting [47, 134] to mention a few.

In phase-field models, the sharp description of the interface is replaced with a thin boundary layer by introducing an auxiliary field – the phase field or order parameter –

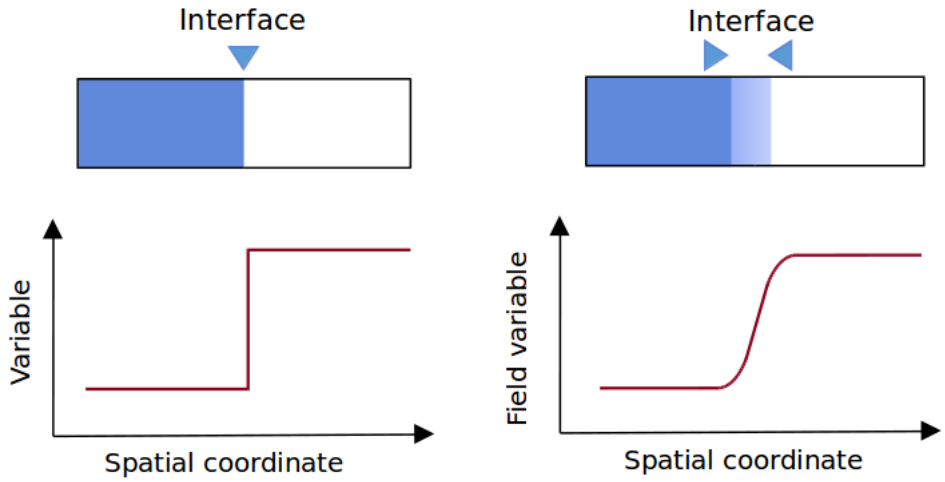

Figure 2.2: [Left] In sharp-interface models, the properties are discontinuous at the interface. [Right] In diffuse-interface or phase-field models the properties evolve continuously between the bulk values.

that varies smoothly on the entire computational domain and that acts as marker of the location of the different phases (see Fig. 2.2). This idea avoids some of the problems associated with sharp interface models. In particular, the numerics are notably simplified because the governing equations can now be solved on the entire computational domain, which is usually known and fixed. In general, instead of the boundary conditions at the interfaces, we have to solve a partial differential equation for the evolution of the order parameter.

Phase-field models also present important challenges that are currently being adressed (see [84, 87, 89, 122]) and that make difficult to use these approaches for quantitative modeling of experimentally relevant situations. For example, the presence of thin interfaces that must be captured by the computational mesh renders phase-field equations very stiff. The same way, the kinetics of the interface limits the numerical time steps that can be adopted in diffuse-interface theories, which makes difficult to model realistic time scales. Finally, from the computational point of view, another disadvantage is that the phase-field equation typically includes higher-order partial differential operators. This fact significantly limits the use of classical finite element methods since we need to employ basis functions of high global continuity, which can be very difficult or even impossible in 3D complicated geometries. In order to use FEM it is usually necessary to adopt a mixed formulation adding new degrees of freedom. The aforementioned difficulties can be tackled by using Isogeometric Analysis (IGA) for the spatial discretization of the problem (IGA will be the subject of Section 2.3), which permits generating basis functions with higher global continuity on non-trivial geometries.

Phase field models are connected to thermodynamics, in the sense that they can be

derived from free-energy functionals – written in terms of the phase field and other fields – using the classical theory of thermomechanics and Coleman-Noll approaches [41]. As an example, the classical Cahn-Hilliard equations as well as the Navier-Stokes-Korteweg equations can be derived using this framework. The former represents a theory for two-component immiscible fluids with surface tension. The latter is the most used theory for single component two-phase flow with phase transformations. Some diffuse-interface models can also be derived directly from sharp interface problems by simply smoothing them out to obtain its phase-field equivalent (see [90] for more details). The theory of matched asymptotic expansions [31, 72] can be used to verify the convergence of phase-field models to sharp-interface equations. For a more thorough discussion on phase-field methods the reader is referred to [3, 24, 39, 90, 157].

2.3 Isogeometric Analysis

Isogeometric Analysis based on Non-Uniform Rational B-Splines constitutes the main tool used for the spatial discretization of the models presented in this thesis. As such, it is interesting for the reader to have a basic knowledge of this computational technique. This is precisely the purpose of this section, where we briefly introduce the concept of NURBS and offer a quick overview of Isogeometric Analysis. For a more extensive discussion on IGA the reader is referred to [42].

IGA can be thought as a new computational technique that improves and generalizes the standard Finite Element Method (FEM). It was first proposed in [100] and further explained in [6,7,9,43,44]. IGA was developed with the purpose of simplifying the tedious communication process between design and analysis. One of the main time consuming steps in this process is the construction of analysis-suitable meshes from Computer Aided Design (CAD) geometries. Usually, an iterative process is required to create and mesh geometries that can be used as imput in Finite Element Analysis (FEA) codes. Moreover, this mesh is, in general, just an approximation of the geometry embedded in the CAD file and this may lead to important errors in the analysis process. The main reason of this bottleneck is the fact that CAD and FEA use different types of basis functions to represent geometries. Indeed, NURBS [137] are the most common basis functions employed in computer aided design whereas Lagrange polynomials [99] are the functions usually adopted in FEA codes. IGA tackles this problem by proposing a computational framework for analysis based on the functions employed in CAD systems.

Isogeometric analysis based on NURBS is convenient for free-form surface modeling. NURBS are capable of more precise geometric representation of complex objects than linear basis functions and, in particular, they can exactly represent many commonly engineered designs, like cylinders, spheres and tori. In addition, they exhibit important math-

ematical properties, such as derivative-continuity across element boundaries, higher-order accuracy, robustness, and the ability to be refined through knot insertion and degree elevation. Another important property of IGA that has been recently proven is that Galerkin solutions can be obtained with only one evaluation per degree of freedom using the concept of variational collocation [86].

One of the major limitations of NURBS is that they are not compatible with local refinement. This has lead to the development of other computational geometry technologies for IGA, such as, analysis-suitable T-splines (ASTS) [7,33,34], which allow to perform local h-refinement while maintaining all the important mathematical and geometrical properties of NURBS. Another option is subdivision surfaces [195]. Heretofore, Non-Uniform Rational B-Splines have been the functions most widely employed in IGA and they will also be used for our simulations. IGA has been previously used to solve phase-field and FSI problems with remarkable success [20, 52, 55, 84, 88, 89, 95].

2.3.1 B-splines

As its name suggests, Non-Uniform Rational B-Splines are obtained from B-splines (basis splines), which are piecewise polynomial curves constructed by taking linear combinations of B-spline basis functions. A necessary component for the construction of B-splines is the knot vector. A *knot vector* Ξ in one dimension is a set of non-decreasing coordinates in the parametric space, i.e., $\Xi = \{\xi_1, ..., \xi_{n_c+p+1}\}$, where $\xi_i \in \mathbb{R}$ is the ith knot, $i = 1, 2, ..., n_c + p + 1$, p is the polynomial order, and n_c is the number of basis functions that comprise the B-spline space. Knots divide the parametric space into knot spans or elements. However, they can be repeated, that is, more than one knot can be located at the same coordinate in the parametric space. This way, if the first and last knots of a knot vector are repeated $p + 1$ times, then the knot vector is said to be open. Otherwise, it is said to be a closed knot vector. If knots are equally-spaced in the parametric space, the knot vector is uniform. If they are unequally-spaced, the knot vector is non-uniform.

For a given knot vector, the B-spline basis functions are defined by the *Cox-de Boor recursion formula* (see, for instance, [45, 49]). Starting with piecewise constants ($p = 0$), i.e,

$$N_{i,0}(\xi) = \begin{cases} 1, & \text{if } \xi_i \leqslant \xi < \xi_{i+1}, \\ 0, & \text{otherwise} \end{cases}; \quad i = 1, \ldots, n_c \tag{2.3.1}$$

the basis functions of higher degrees (p = 1,2,3,...) are defined by

$$N_{i,p}(\xi) = \frac{\xi - \xi_i}{\xi_{i+p} - \xi_i} N_{i,p-1}(\xi) + \frac{\xi_{i+p+1} - \xi}{\xi_{i+p+1} - \xi_{i+1}} N_{i+1,p-1}(\xi); \quad i = 1, \ldots, n_c \tag{2.3.2}$$

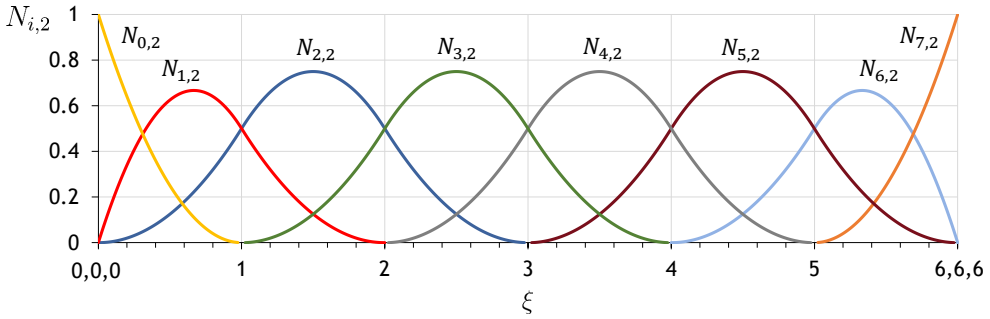

Figure 2.3: Quadratic basis functions formed from the open knot vector $\Xi = \{0, 0, 0, 1, 2, 3, 4, 5, 6, 6, 6\}$

In Fig. 2.3 we present an example of quadratic B-spline basis functions generated from the uniform open knot vector $\Xi = \{0, 0, 0, 1, 2, 3, 4, 5, 6, 6, 6\}$. Note that if internal knots are not repeated, the B-Spline basis functions are at least $\mathcal{C}^{p-1}$-continuous everywhere. More specifically, if a knot has multiplicity k, the basis is $\mathcal{C}^{p-k}$-continuous at that knot. This way, B-spline basis functions constructed using an open knot vector are interpolatory at the endpoints of the parametric interval, which facilitates the imposition of boundary conditions. For B-spline functions with polynomial order 0 and 1, we obtain standard piecewise constant and linear finite element functions, respectively. From the Cox-de Boor recursion formula, it can also be seen that B-Spline basis functions constitute a partition of unity, that is, $\sum_{i=1}^{n_c} N_{i,p}(\xi) = 1 \ \forall \xi$. Each basis $N_{i,p}$ is pointwise nonnegative over the entire domain, i.e., $N_{i,p}(\xi) \geqslant 0 \ \forall \xi$, and its support is compact. In particular, the support is always $p+1$ knot spans for B-spline functions of order p.

2.3.2 NURBS

Let d denote the space dimension. A NURBS entity in $\mathbb{R}^d$ can be obtained by a projective transformation of a B-spline object in $\mathbb{R}^{d+1}$. It is worth mentioning that all the conic sections can be exactly constructed by projective transformations of piecewise quadratic curves. Given the B-spline basis function $N_{i,p}(\xi)$, the one dimensional NURBS basis functions can be defined as

$$\mathcal{R}_i^p(\xi) = \frac{N_{i,p}(\xi)\, w_i}{\sum_{\hat{i}=1}^{n_c} N_{\hat{i},p}(\xi)\, w_{\hat{i}}}, \tag{2.3.3}$$

where w_i is a positive real weight. Analogously, for the 2D and 3D cases, the NURBS basis functions are given by

$$\mathcal{R}_{i,j}^{p,q}(\xi,\eta) = \frac{N_{i,p}(\xi)\, M_{j,q}(\eta)\, w_{i,j}}{\sum_{\hat{i}=1}^{n_c}\sum_{\hat{j}=1}^{m_c} N_{\hat{i},p}(\xi)\, M_{\hat{j},q}(\eta)\, w_{\hat{i},\hat{j}}}, \tag{2.3.4}$$

$$\mathcal{R}_{i,j,k}^{p,q,r}(\xi,\eta,\zeta) = \frac{N_{i,p}(\xi)\, M_{j,q}(\eta)\, L_{k,r}(\zeta)\, w_{i,j,k}}{\sum_{\hat{i}=1}^{n_c}\sum_{\hat{j}=1}^{m_c}\sum_{\hat{k}=1}^{l_c} N_{\hat{i},p}(\xi)\, M_{\hat{j},q}(\eta)\, L_{\hat{k},r}(\zeta)\, w_{\hat{i},\hat{j},\hat{k}}}. \tag{2.3.5}$$

In the expressions above, $\Xi = \{\xi_1, ..., \xi_{n_c+p+1}\}$, $\mathcal{H} = \{\eta_1, ..., \eta_{m_c+q+1}\}$ and $\mathcal{Z} = \{\zeta_1, ..., \zeta_{l_c+r+1}\}$ are the knot vectors; q and r denote the polynomial orders; m_c and l_c are the number of basis functions; and $w_{\hat{i},\hat{j}}$ and $w_{\hat{i},\hat{j},\hat{k}}$ are the weights. Note that the NURBS basis functions are no longer piecewise polynomials, but piecewise rationals. NURBS functions inherit most of the properties of B-splines. Their continuity, as well as their support is the same as for B-splines. They are pointwise nonnegative and they still constitute a partition of unity. Note also that if the weights are all equal, NURBS basis functions reduce to B-splines basis functions, i.e, $\mathcal{R}_i^p(\xi) = N_{i,p}(\xi)$.

NURBS curves are constructed by a linear combination of NURBS basis functions as

$$\boldsymbol{C}(\xi) = \sum_{i=1}^{n_c} \mathcal{R}_i^p(\xi)\, \boldsymbol{B}_i, \tag{2.3.6}$$

where $\{\boldsymbol{B}_i\}$, $i = 1, 2, ..., n_c$ are referred to as *control points*. These coefficients are points in space. The concept is similar to that of nodal coordinates in finite element analysis. The main difference is that in IGA the basis functions are, in general, non-interpolatory.

Analogously, a NURBS surface $\boldsymbol{S}(\xi,\eta)$ and a NURBS volume $\boldsymbol{V}(\xi,\eta,\zeta)$ may be defined as

$$\boldsymbol{S}(\xi,\eta) = \sum_{i=1}^{n_c}\sum_{j=1}^{m_c} \mathcal{R}_{i,j}^{p,q}(\xi,\eta)\, \boldsymbol{B}_{i,j}, \tag{2.3.7}$$

$$\boldsymbol{V}(\xi,\eta,\zeta) = \sum_{i=1}^{n_c}\sum_{j=1}^{m_c}\sum_{k=1}^{l_c} \mathcal{R}_{i,j,k}^{p,q,r}(\xi,\eta,\zeta)\, \boldsymbol{B}_{i,j,k}, \tag{2.3.8}$$

where $\{\boldsymbol{B}_{i,j}\}$ and $\{\boldsymbol{B}_{i,j,k}\}$ are the control points, $i = 1, 2, ..., n_c$, $j = 1, 2, ..., m_c$, $k = 1, 2, ..., l_c$.

2.3.3 Analysis framework

IGA is compatible with the two classical mesh refinement strategies, knot insertion (h-refinement) and order elevation (p-refinement). However, there is a third option, referred to as k-refinement (see, e.g., [100]), which allows to increase the order and the smoothness of the NURBS basis functions simultaneously.

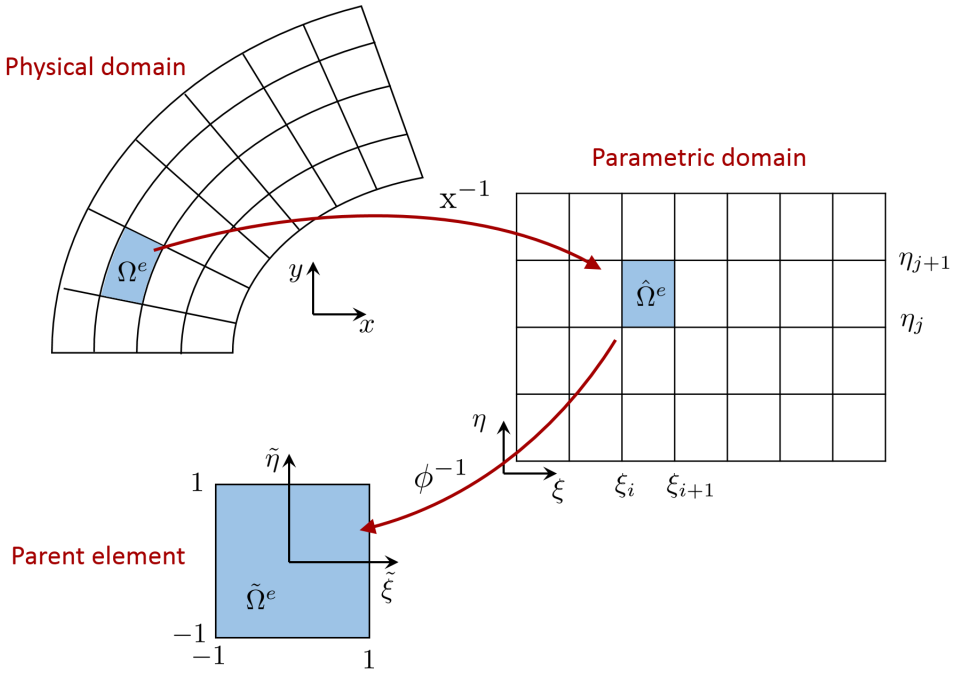

Figure 2.4: Integration is carried out through standard Gaussian quadrature on one element at a time. The geometrical mapping $\boldsymbol{x}$ is used to pull the physical element back to the parametric domain. The function $\boldsymbol{\phi}$ is then used to map the parametric element to the parent element.

In what follows, we will denote by $N(\boldsymbol{x})$ and $N(\boldsymbol{\xi})$ a generic NURBS basis function defined on the physical and parametric spaces, respectively (see Fig. 2.4). For simplicity, we omit the index of the basis functions that represents the polynomial degree. We also make use of a single-index notation, denoting by $A, B, C, ...$ the NURBS basis functions. Let n be the number of control points. With this in mind, the geometry mapping may be expressed as

$$\boldsymbol{x}(\boldsymbol{\xi}) = \sum_{A=1}^{n} \boldsymbol{x}_A N(\xi), \tag{2.3.9}$$

where $\boldsymbol{x}_A$'s are the control point coordinates.

As in finite elements, in Isogeometric Analysis the isoparametric concept is used, which means that the unknown variables are represented in terms of the same NURBS functions [see Eqs. (2.3.3)-(2.3.5)] that are used for defining the geometry. Thus, the IGA solution in the parametric domain may be expressed as

$$u(\boldsymbol{\xi}) = \sum_{A=1}^{n} u_A N(\boldsymbol{\xi}), \tag{2.3.10}$$

where u_A are the control variables or degrees of freedom. Analogously, in the physical

domain the isogeometric solution is defined by

$$u(\boldsymbol{x}) = \sum_{A=1}^{n} u_A N(\boldsymbol{x}), \tag{2.3.11}$$

where $N(\boldsymbol{x}) = N\left(\boldsymbol{\xi}^{-1}(\boldsymbol{x})\right)$. The properties of the function u follow directly from the basis. For example, the continuity across the boundary of an element is determined by the continuity of the basis across the corresponding knot span.

To perform integration in the examples presented in this thesis, we make use of the standard Gaussian quadrature rule (see Fig. 2.4). Other rules have been recently proposed for IGA (see, for instance, [102]), which could be used to improve the efficiency of the computational methods. Regarding the imposition of boundary conditions (BC), Neumann BC's are enforced weakly as in standard Finite Element Methods. Dirichlet boundary conditions can be imposed strongly by setting the appropiate values to the control variables of the boundary. Note that for open knot vectors, the basis functions are interpolatory at the endpoints. Nitsche-like methods can also be employed for a weak imposition of Dirichlet boundary conditions.

Chapter 3

Research objectives

The research objectives of this thesis can be summarized in the following points:

- Development of algorithms for the simulation of complex fluids and their interaction with solid structures. Numerical methods for FSI have traditionally focused on the interaction of solids with classical fluids governed by the Navier-Stokes equations [14, 125, 126, 165]. The coupling of solids and complex fluids remains practically unexplored, at least from the computational point of view, even when they give rise to much richer physics than classical fluids, especially at small scales. Our goal is to propose new numerical methods based on phase-field approaches [141] and capable of capturing the physical mechanisms behind complex fluids. The numerical challenges associated to phase-field models, such as, the stiffness in space and time and the higher-order partial differential operators, could be tackled by adopting a NURBS-based Isogeometric Analysis [42] for the spatial discretization. This approach should take advantage of the higher inter-element continuity of spline basis functions in order to enhance the accuracy and robustness with respect to the classical finite element method. The use of NURBS would also enable a more precise geometric representation of complex objects since they can exactly represent many commonly engineered designs, like cylinders, spheres and tori.

- Application of the proposed models. The idea is to illustrate the predictive ability of our models and the effectiveness of our computational methods by solving problems associated to different fields, such as engineering, mechanobiology, chemistry or microfabrication. In this sense, we study a number of physical problems, such as the influence of surfactants in single-component two-phase flows, the implosive collapse of vapor-filled structures, the role of capillary forces in droplet motion driven by tensotaxis, the spontaneous wrapping of droplets with elastic membranes or the bending of flexible micro-pillars due to elastocapillary forces.

- Implementation of the proposed algorithms. The optimization of FSI models, in-

cluding an efficient parallel implementation, is of high practical importance in order to solve realistic physical problems. For this reason, a key goal of this thesis is to perform a parallel implementation of the proposed models. This could be achieved, for example, in Fortran language by developing our own libraries and MPI parallel implementation. Another possibility is to build a C language code on top of PetIGA [48], which is a software framework that adds the NURBS discretization capabilities and integration of forms to PETSc [150]. This would result in a much more efficient and flexible code, which could easily use a great variety of solvers and preconditioners.

Chapter 4

A diffuse-interface model for liquid-vapor flows with surfactants

4.1 Introduction

Our first step into the realm of complex fluids will be the development of a diffuse-interface model for single-component two-phase flows that allows for phase transformations and captures the physics behind surfactant absorption phenomena.

Surface active agents, also known as surfactants, are compounds that find energetically favorable to be located at the interfaces of a system. The presence of these compounds at the boundary between phases may substantially modify its properties, for example, reducing the work required to generate the interface (the reader is referred to [71, 133, 149] for more details on surfactant properties). This ability to change the behavior of a system acting only on the interface, makes surfactants one of the most useful substances in the chemical industry [71, 139] as well as in other fields such as, biotechnology [153, 191], microelectronics [176], electronic printing [148] or medical research [73, 146]. In the literature, one can find a number of computational methods that describe surfactant absorption phenomena [2, 36, 60, 80, 104, 132, 178, 189]. However, most of these models only deal with soluble or insoluble surfactants in two-component inmiscible flows (see, for example, [68, 112, 120]). The influence of surfactants in single-component two-phase flows remains practically unexplored, at least from the computational point of view. For this reason, we firmly believe that a complex-fluid theory that allows for spontaneous vaporization and condensation and that captures the dynamics of surface active agents at the interfaces, may become a useful tool for further understanding the behavior of these compounds in phase-transition phenomena.

4.2 Derivation of the model

The model that we propose for this problem can be derived from a free energy functional by using the framework of thermomechanics and a Coleman-Noll approach [41]. Let us define the total energy of the system

$$\mathcal{E}(\rho, \boldsymbol{u}) = \int_{\Omega} \left(\Psi + \frac{1}{2}\rho \left|\boldsymbol{u}\right|^2 \right) \mathrm{d}\Omega, \tag{4.2.1}$$

where Ω is an open subset of $\mathbb{R}^3$ and $|\cdot|$ denotes the Euclidean norm of a vector; ρ is the fluid density and $\boldsymbol{u}$ represents the velocity vector. The free energy Ψ is assumed to belong to the constitutive class $\Psi = \widehat{\Psi}\left(\boldsymbol{L}, \rho, \nabla\rho, c\right)$, where c is the surfactant concentration and $\boldsymbol{L}$ is the symmetric part of the velocity gradient, that is, $\boldsymbol{L} = \left(\nabla\boldsymbol{u} + \nabla\boldsymbol{u}^T\right)/2$, In particular, for our problem, we consider the expression

$$\widehat{\Psi}(\rho, \nabla\rho, c) = \mathcal{W}\left(\rho\right) + \frac{\lambda\left(c\right)}{2}\left|\nabla\rho\right|^2 + \mathcal{U}\left(c\right), \tag{4.2.2}$$

where λ is a function of c that takes positive values and $\mathcal{U}\left(c\right)$ is the free energy associated to the surfactant. Here, we adopt $\mathcal{U}\left(c\right) = c^2\alpha/2$, where α is a positive constant. The second term in (4.2.2) represents the free energy that leads to capillary forces at gas-liquid interfaces. With the purpose of being able to predict phase transformations, we define $\mathcal{W}\left(\rho\right)$ as the Helmholtz free energy of a van der Waals fluid [56, 121].

Let us also define the classical balance laws for mass of fluid and surfactant, linear momentum and angular momentum, i.e.,

$$\dot{\rho} + \rho\nabla\cdot\boldsymbol{u} = 0, \tag{4.2.3}$$

$$\rho\dot{\boldsymbol{u}} = \nabla\cdot\boldsymbol{T} + \rho\boldsymbol{f}, \tag{4.2.4}$$

$$\boldsymbol{T} = \boldsymbol{T}^T, \tag{4.2.5}$$

$$\dot{c} + c\nabla\cdot\boldsymbol{u} = -\nabla\cdot\boldsymbol{j}, \tag{4.2.6}$$

where $\boldsymbol{T}$ is the Cauchy stress tensor, $\boldsymbol{f}$ represents body forces per unit mass and $\boldsymbol{j}$ describes the mass flux of surfactant; $\dot{\square}$ denotes the material time derivative of $\square$, i.e., the time derivative of $\square$ holding the material particle fixed.

The goal is to find a constitutive equation for $\boldsymbol{T}$ and $\boldsymbol{j}$ so that the energy of the system decreases with time for any arbitrary solution of the theory. This can be achieved, for example, with the following choices of $\boldsymbol{T}$ and $\boldsymbol{j}$ (see [29] for a detailed derivation of the

model),

$$\boldsymbol{T} = -p\boldsymbol{I} + \left[\frac{1}{2}\left(\lambda\left(c\right) - c\lambda'(c)\right)|\nabla\rho|^2 - \frac{\alpha}{2}c^2 + \rho\lambda'\left(c\right)\nabla c\cdot\nabla\rho + \lambda\left(c\right)\rho\Delta\rho\right]\boldsymbol{I}$$
$$- \lambda(c)\nabla\rho\otimes\nabla\rho + 2\bar{\mu}\boldsymbol{L} + \bar{\lambda}\nabla\cdot\boldsymbol{u}\boldsymbol{I}, \tag{4.2.7}$$
$$\boldsymbol{j} = -\kappa\nabla\left(\alpha c + \frac{\lambda'(c)}{2}|\nabla\rho|^2\right), \tag{4.2.8}$$

where $\boldsymbol{I}$ denotes the identity tensor; $\kappa > 0$; $\bar{\mu}$ and $\bar{\lambda}$ are viscosity coefficients, which must fulfill $\frac{2}{3}\bar{\mu} + \bar{\lambda} \geq 0$ and $\bar{\mu} \geq 0$; p denotes the thermodynamic pressure, that is, $p = \rho\mathcal{W}'\left(\rho\right) - \mathcal{W}\left(\rho\right)$.

4.3 Governing equations

The governing equations of the Navier-Stokes-Korteweg theory with surfactant can now be written in the Eulerian description as follows

$$\frac{\partial\rho}{\partial t} + \nabla\cdot\left(\rho\boldsymbol{u}\right) = 0, \tag{4.3.9}$$
$$\frac{\partial\left(\rho\boldsymbol{u}\right)}{\partial t} + \nabla\cdot\left(\rho\boldsymbol{u}\otimes\boldsymbol{u}\right) - \nabla\cdot\boldsymbol{T} - \rho\boldsymbol{f} = 0, \tag{4.3.10}$$
$$\frac{\partial c}{\partial t} + \nabla\cdot\left(c\boldsymbol{u}\right) + \nabla\cdot\boldsymbol{j} = 0, \tag{4.3.11}$$

where the surfactant mass flux and the stress tensor can be expressed as

$$\boldsymbol{j} = -\kappa\alpha\nabla c - \frac{\kappa}{2}\left(\lambda''(c)\nabla c\,|\nabla\rho|^2 + 2\lambda'(c)\nabla\nabla\rho^T\nabla\rho\right), \tag{4.3.12}$$
$$\boldsymbol{T} = \boldsymbol{\tau} - p\boldsymbol{I} + \boldsymbol{\varsigma} + \boldsymbol{\varsigma}_s. \tag{4.3.13}$$

Here, κ and α govern the relative strength of convection and diffusion processes, allowing to control the intensity with which the surfactant is drawn by liquid-vapor interfaces; $\boldsymbol{\varsigma}$ is the Korteweg tensor, $\boldsymbol{\varsigma}_s$ is the stress tensor associated to the surfactant and $\boldsymbol{\tau}$ corresponds to the viscous stress tensor of a Newtonian fluid (see, for example, [196]), i.e.,

$$\boldsymbol{\tau} = \bar{\mu}\left(\nabla\boldsymbol{u} + \nabla\boldsymbol{u}^T\right) + \bar{\lambda}\nabla\cdot\boldsymbol{u}\boldsymbol{I}, \tag{4.3.14}$$
$$\boldsymbol{\varsigma} = \lambda(c)\left(\rho\Delta\rho + \frac{1}{2}|\nabla\rho|^2\right)\boldsymbol{I} - \lambda(c)\nabla\rho\otimes\nabla\rho, \tag{4.3.15}$$
$$\boldsymbol{\varsigma}_s = \left(-\frac{\alpha}{2}c^2 - c\frac{\lambda'(c)}{2}|\nabla\rho|^2 + \rho\lambda'\left(c\right)\nabla c\cdot\nabla\rho\right)\boldsymbol{I}. \tag{4.3.16}$$

We assume that the Stokes hypothesis is satisfied, i.e., $\bar{\lambda} = -2\bar{\mu}/3$. Finally, as surface tension is approximately a linear function of $\sqrt{\lambda}$ and we want to model the capability of surfactants to lower surface tension, we assume that $\lambda(c) = \lambda_{min}g\left(c\right)$. Here, λ_{min} is a

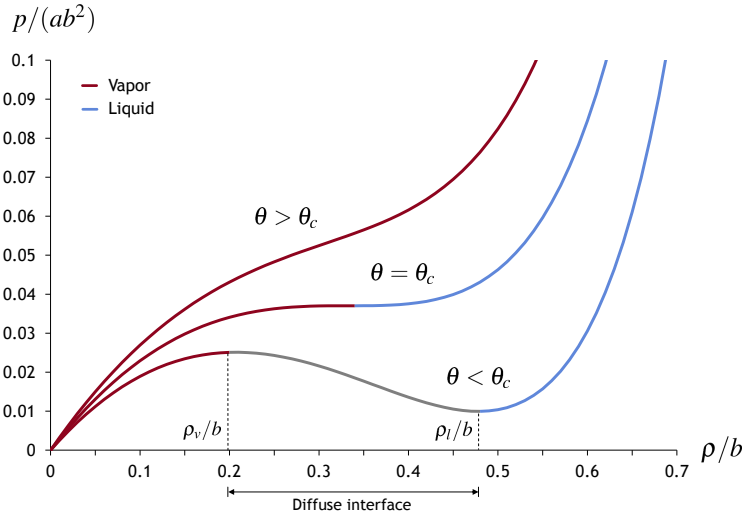

Figure 4.1: Non-dimensional plot of van der Waals pressure as a function of density for $\theta > \theta_c$, $\theta = \theta_c$ and $\theta < \theta_c$. Note that for values of temperature below the critical temperature ($\theta < \theta_c$), the pressure is a non-monotone function of density, which allows for spontaneous phase transformations.

positive constant that represents the minimum value allowed for the capillarity coefficient and $g(c) = 1 + \beta e^{-c^2}$ with $\beta > 0$.

The equation of state for the thermodynamic pressure is given by van der Waals equation, i.e.,

$$p = Rb\left(\frac{\rho\theta}{b-\rho}\right) - a\rho^2, \tag{4.3.17}$$

where a and b are positive constants, R is the specific gas constant and θ represents the temperature of the system. Fig. 4.1 shows a non-dimensional plot of van der Waals pressure with respect to density. Note that for values of θ above the critical temperature $\theta_c = 8ab/(27R)$, p is a monotonically increasing function of ρ, and the only phase that is stable is the vapor phase. However, for $\theta < \theta_c$ the pressure is no longer monotone, and we can differentiate three regions. The interval $\rho \in (0, \rho_v)$ corresponds to the vapor phase and the interval $\rho \in (\rho_l, b)$ corresponds to the liquid phase. Between these two regions, p decreases with respect to ρ (grey line in Fig. 4.1), allowing for the fluid to evaporate and condensate naturally due to pressure and/or temperature variations. The reader is referred to [56, 88, 121] for further details.

Boundary conditions

To define a well-posed boundary value problem we need to specify suitable boundary conditions. We assume solid wall boundary conditions, that is, $\boldsymbol{u} = \boldsymbol{u}_D$. Additionally, we set $\nabla\rho \cdot \boldsymbol{n} = |\nabla\rho|\cos(\varphi)$, where $\boldsymbol{n}$ denotes the unit outward normal to the boundary, and φ is the static contact angle between the liquid-vapor interface and the solid, measured

in the liquid phase. A similar idea can be adopted for the surfactant equation, that is, $\nabla c \cdot \boldsymbol{n} = |\nabla c| \cos(\varphi_s)$, where φ_s represents the angle between the surfactant gradient and the outward normal to the boundary. We must take into account that the boundary condition should be mass-preserving and that surfactants are naturally trapped by liquid-vapor interfaces. With this in mind, we relate φ_s with the contact angle φ using the expression $\cos(\varphi_s) = \cos(\varphi)h(\rho)$ where

$$h\left(\rho\right) = \tanh\left(\left(\frac{\rho_l^M + \rho_v^M}{2} - \rho\right) s\right). \tag{4.3.18}$$

Here, s is set to $s = 4/(\rho_l^M - \rho_v^M)$; the constants ρ_l^M and ρ_v^M denote the Maxwell states for the liquid and the vapor phases, respectively.

4.4 Numerical formulation

We employ a semi-discrete formulation based on Galerkin's method. In particular, for the spatial discretization of the problem, we make use of Isogeometric Analysis since it allows to generate the globally $\mathcal{C}^1$-continuous basis functions that are needed for the discretization of the third-order partial-differential operators of the momentum and the surfactant equations. The variational formulation of the problem can be found in [29]. We use the generalized-α method [40] as a time integration scheme. The nonlinear system of equations is solved using a Newton-Raphson iteration procedure, which leads to a two-stage predictor-multicorrector algorithm. The resulting linear system is solved using a preconditioned GMRES method [151].

4.5 Numerical examples

In order to obtain a non-dimensional form of our problem, we have rescaled the units of measurement of length, mass, time and temperature by L_0, bL_0^3, $L_0/\sqrt{ab}$ and θ_c, respectively, where $L_0 = 1$ denotes a length scale of the computational domain size. Using this non-dimensionalization, our problem is controlled by four dimensionless numbers, $Re = L_0 b\sqrt{ab}/\bar{\mu}$, $Ca = \sqrt{\lambda_{min}/a}/L_0$, $Ba = \alpha/(ab^2)$, and $Pe = L_0\sqrt{ab}/(\kappa\alpha)$, where Re is the Reynolds number, Ca denotes the capillary number, Ba is the non-dimensional form of α and Pe is the Peclet number. Ca and Re are chosen according to the methodology proposed in [88], which relates these parameters to the computational mesh.

4.5.1 Surface tension for the NSK model with surfactants

In the NSK model without surfactants, the surface tension σ_{LV} relates to the parameter λ through the expression $\sigma_{LV} \simeq K_0\sqrt{\lambda}$, where K_0 is a nonlinear function of θ (see, for

example, [56]). Our goal is to show that the non-dimensional form of this expression, i.e., $\gamma_{LV} \simeq k_0 Ca\sqrt{g(c)}$, holds for the NSK model with surfactants, where γ_{LV} is the non-dimensional surface tension and k_0 is a constant for a given temperature. With this purpose, we design a numerical experiment in which two vapor bubbles of different radius merge into a single vapor bubble. As initial condition, we impose a constant value of the surfactant concentration. We repeat this numerical simulation for different values of the initial surfactant concentration and for two different temperatures.

For each simulation we obtain the steady state and we measure the radius r of the resulting bubble and the pressure difference Δp between the liquid and the vapor phases. The product of this two values is an estimate of the suface tension according to Young-Laplace equation $\Delta p = \gamma_{LV}/r$. We plot (see Fig. 4.2) our estimate of suface tension with respect to $Ca\sqrt{g(c)}$. As it can be seen, the surface tension follows approximately a linear relation with the values of the capillarity function at the interface. This proves that the parameter k_0 remains constant in our model for a given temperature. We also plot our estimate of surface tension with respect to the surfactant concentration at the interface (see inset in Fig.4.2), which makes evident that surface tension decreases with surfactant concentration.

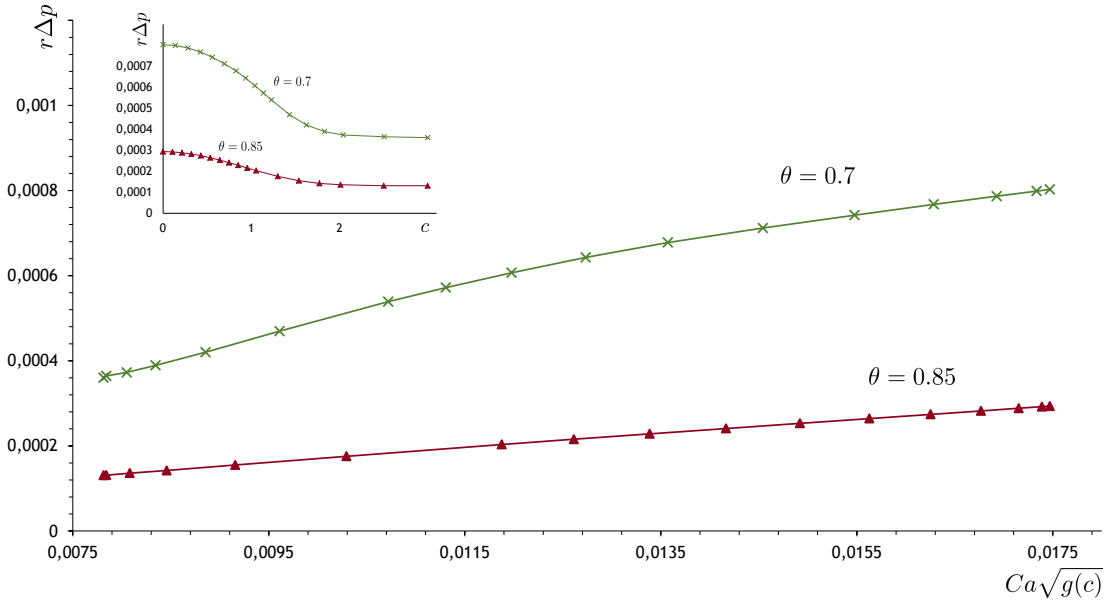

Figure 4.2: Non-dimensional plot of our estimate of surface tension $r\Delta p$ as a function of capillarity for two different temperatures. For the steady state, surface tension scales almost linearly with the values of the capillarity function at the interface. In the inset we also plot surface tension as a funcion of the surfactant concentration at the interface. Note that surface tension decreases with surfactant concentration.

4.5.2 Trapping of surfactant at the liquid-vapor interface

In order to show that our theory is capable of modeling that surfactants are trapped by interfaces as well as their ability to inhibit the coalescence of bubbles, we take a particular example for which the traditional NSK model (see left column in Fig. 4.3) predicts the merging of vapor bubbles. Then, we repeat exactly the same simulation with the theory presented herein (middle and right columns in Fig. 4.3) and we compare both results.

As it can be seen in the right column of Fig. 4.3, the surfactant is attracted by the regions with a higher density gradient, that is, the interfaces between the vapor and the liquid phases. In the simulation without surfactants (left column in 4.3), the bubbles that are closer are able to coalesce [Fig. 4.3(d)]. However, the presence of the surfactant inhibits the coalescence of these two bubbles in our model [Fig. 4.3(e)].

4.5.3 Attachment of a drop of water to a wall

The following example shows how the presence of the surfactant at the interface may modify the contact angle φ between a drop of water and a solid substrate. This angle can be approximated by the equilibrium contact angle predicted by Young's equation [50] for the case of rigid solid substrates, and by adopting the expression validated in Section 4.5.1 for the surface tension $\gamma_{LV} \simeq k_0 Ca\sqrt{g(c)}$, that is,

$$\cos(\varphi) \simeq \frac{\gamma_{SV} - \gamma_{SL}}{\gamma_{LV}} \simeq \frac{\varepsilon}{Ca\sqrt{g(c)}}, \tag{4.5.19}$$

where γ_{SV} and γ_{SL} are the surface tension at the solid-vapor interface and at the solid-liquid interface, respectively; $\varepsilon = (\gamma_{SV} - \gamma_{SL})/k_0$ is considered as a positive constant. The boundary conditions for the surfactant and the density variables become

$$\nabla\rho \cdot \boldsymbol{n} = |\nabla\rho| \, \frac{\varepsilon}{Ca\sqrt{g(c)}}, \tag{4.5.20}$$

$$\nabla c \cdot \boldsymbol{n} = |\nabla c| \, \frac{\varepsilon}{Ca\sqrt{g(c)}} h\left(\rho\right), \tag{4.5.21}$$

where $h(\rho)$ is given by (4.3.18).

In order to illustrate the effectiveness of this approach we carry out the following numerical simulation (see Fig. 4.4). A drop of liquid water [blue color in Fig. 4.4(a)] is initially located close to a solid boundary where we are imposing the aforementioned boundary conditions. The initial distribution for the surfactant [see Fig. 4.4(b)] consists of a drop of surfactant (green color) located near to the upper boundary. Note that we are neglecting gravity forces, so the water droplet is attracted by the lower boundary due to the capillary forces [see Fig. 4.4(e)]. The surfactant is rapidly attracted by the liquid-vapor interface, thus, modifying the contact angle. Different values of the initial surfactant

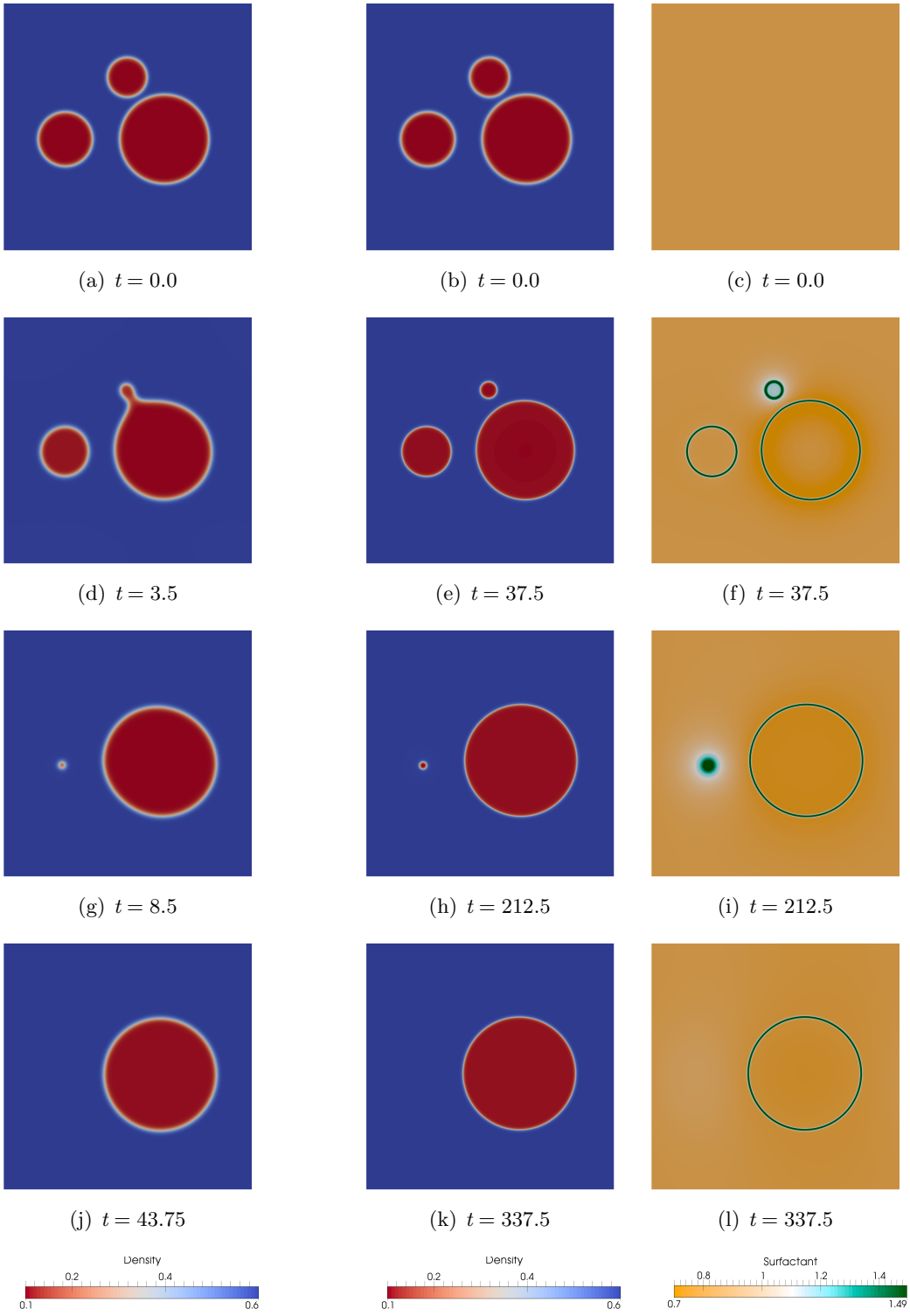

Figure 4.3: Simulation of three vapor bubbles using the NSK theory without surfactant (left column) and with surfactant (middle and right columns). The initial configuration consists of three vapor bubbles [red color in the density plots (a) and (b)] deposited on a liquid matrix (blue color). As initial condition we adopt an homogeneous distribution of the surfactant concentration. Comparing the density plots of both theories (left and middle columns) we can see that the NSK model with surfactant inhibits the coalescence of the small and big bubbles. The surfactant is attracted by the areas with higher density gradients, that is, the interfaces (green color in the surfactant plots).

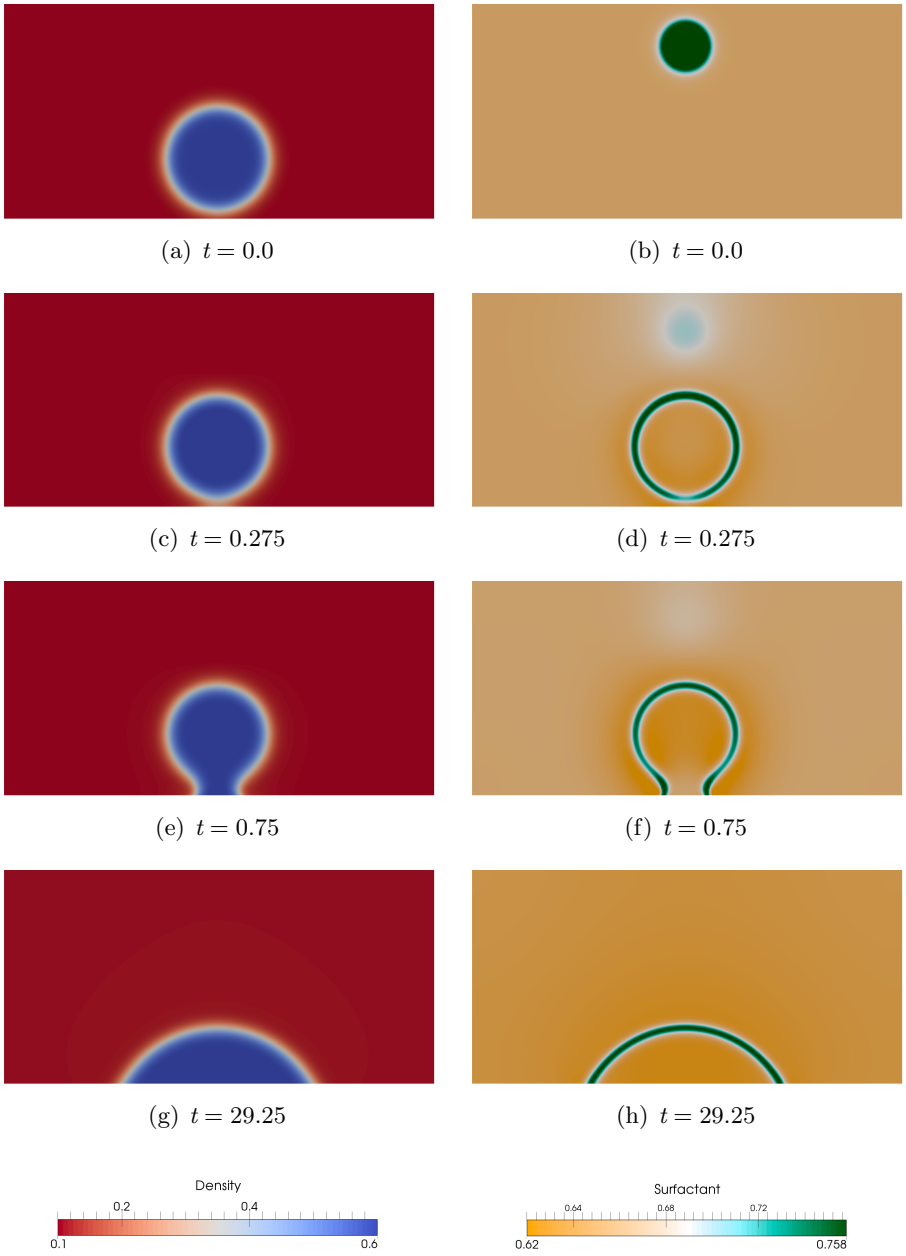

(a) $t = 0.0$ (b) $t = 0.0$

(c) $t = 0.275$ (d) $t = 0.275$

(e) $t = 0.75$ (f) $t = 0.75$

(g) $t = 29.25$ (h) $t = 29.25$

Figure 4.4: Evolution of density (left) and surfactant concentration (right) for the attachment of a drop of water to a wall. The computational domain is the rectangle $\Omega = (0, 1.0) \times (0, 0.5)$ and the computational mesh is uniform and composed of 256×128 $\mathcal{C}^1$-quadratic elements. Initially, a drop of liquid water (blue color in the density plot) is located close to the lower boundary where we are controlling the contact angle as a function of surfactant concentration. In the horizontal direction we adopt periodic boundary conditions. The surfactant is initially concentrated close to the upper boundary [Fig. 4.4(b)] though it is rapidly attracted by the liquid-vapor interface (green color in the surfactant plot). The water droplet is attracted by the lower boundary due to the capillary forces [see Fig.4.4(e)]. Note that we are neglecting gravity forces. We have adopted $Re = 512$, $Ca = 0.00390625$, $Ba = 0.04$, $Pe = 125$ and $\varepsilon = 0.003845215$.

concentration would lead to different static contact angles, which has great importance in practical applications as it allows to control the wettability of the solid surface using surfactants.

4.5.4 Coalescence of vapor bubbles in three dimensions

The last numerical example is the coalescence of two vapor bubbles in three dimensions (see Fig. 4.5). For the surfactant we adopt a constant initial condition. The results for the surfactant variable are plotted in Fig. 4.5, where we have made a cut of the cubic domain for visualization purposes. We plot an isocontour surface of the density (grey color) which represents the liquid-vapor interface. The results observed are consistent with the previous examples. The surfactant (green color) is trapped by the regions of higher density gradient, that is, the liquid-vapor interfaces (grey color).

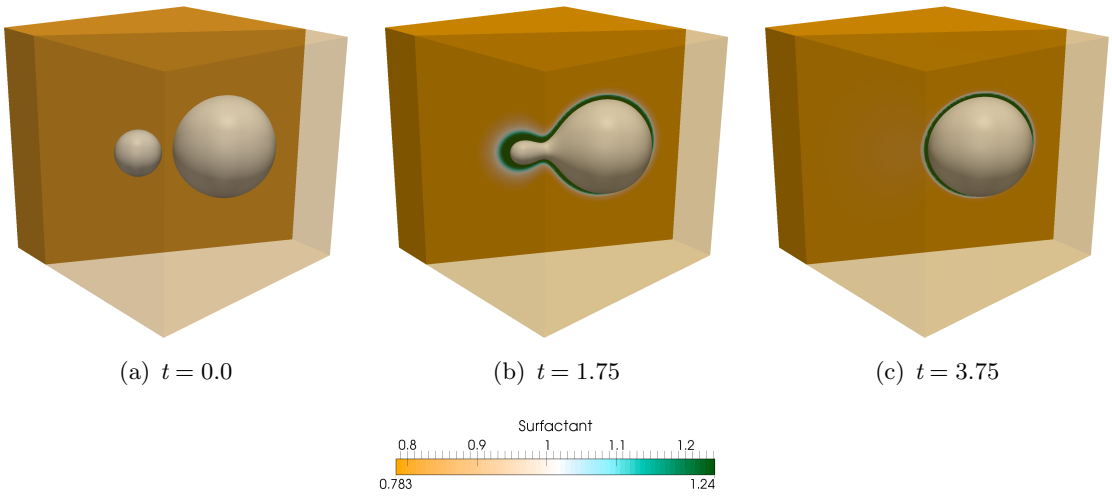

(a) $t = 0.0$ (b) $t = 1.75$ (c) $t = 3.75$

Figure 4.5: Evolution of surfactant concentration for the three dimensional coalescence of two vapor bubbles. The computational domain is the cube $\Omega = (0,1)^3$, which is composed of 128^3 $\mathcal{C}^1$-quadratic elements. We impose periodic boundary conditions in all directions. Initially, an homogeneous distribution of the surfactant concentration is adopted [Fig.4.5(a)], namely, $c_0 = 0.8$. We have made a clip of the geometry to facilitate the visualization of the results. We are plotting an isocontour surface of the density (grey color) which represents the liquid-vapor interface. The surfactant is trapped by the regions with higher density gradients, that is, the liquid-vapor interfaces. We have used the parameters $Re = 256$, $Ca = 0.0078125$, $Ba = 0.01$ and $Pe = 1000$.

4.6 Contributions and open lines for research

The most significant contributions of this work, which has been published as a research paper in [29], can be summarized in the following points:

- We have proposed a model for complex fluids with surfactants. The fluid is a single-component, two-phase flow that naturally undergoes phase-transformations between vapor and liquid states.
- The proposed model has been derived from a free-energy functional using a Coleman-Noll approach and the framework of thermodynamics.
- The theory successfully captures the dynamics of surface active agents at the interface. For example, the model predicts that surfactants are attracted by liquid-vapor interfaces as well as their ability to reduce surface tension, as observed in experiments.
- We have proposed a computational method based on Isogeometric Analysis that successfully tackles some of the computational challenges associated to phase-field methods, such as the presence of higher-order derivatives.

The main open ideas derived from this work are:

- Extending the proposed model to a thermally coupled theory.
- Studying in more detail the influence that surfactants have in phase transformations.
- Applying the model to real case scenarios.

Chapter 5

Interaction of complex fluids and solids: theory, algorithms and application to phase-change driven implosion

5.1 Introduction

Having already devised a computational model for single-component two-phase flows with surfactants, our next step will be to couple the complex fluid model governed by the NSK equations with a solid structure. In this sense, we need to choose a suitable Fluid-Structure Interaction technique for the problems that we want to solve. The idea is to conceive a model capable of reproducing the implosive collapse of vapor-filled structures and that serves as a basis for other future problems, such as tensotaxis or elastocapillarity. In all these cases, the accuracy at the fluid-solid boundary will be crucial, especially, in elastocapillary problems, as we need a rigorous control of the contact angle between the liquid-vapor interface and the solid surface as well as a precise fulfillment of the compatibility conditions. For this reason, a boundary-fitted approach or in particular an Arbitrary Lagrangian-Eulerian method, in which the fluid and the solid discretizations match at the interface, seems to be the most suitable choice. We are aware that very strong implosion problems can lead to significant distortions in the solid and the fluid mesh and, as a consequence, require remeshing procedures. We try to tackle this challenge by focusing on moderately strong implosions and by adopting the appropiate elastic coefficients for the moving mesh problem, preserving this way, the quality of the fluid mesh for as long as possible.

5.2 Governing equations

5.2.1 Kinematics

In the Arbitrary Lagrangian-Eulerian description the fluid suddomain moves to adapt to the solid boundary. However, this motion does not coincide with the motion of the fluid material particles, that is, the material particles are in relative motion with respect to the motion of a referencial domain. Let us denote by $\widehat{\boldsymbol{x}}$ the coordinates of that reference domain $\Omega_{\widehat{\boldsymbol{x}}}$, which is fixed in time. We define a function $\widehat{\boldsymbol{\phi}}$ that maps the reference domain $\Omega_{\widehat{\boldsymbol{x}}}$ into its spatial configuration at time t, Ω_t, that is, $\widehat{\boldsymbol{\phi}} : \Omega_{\widehat{\boldsymbol{x}}} \times]0, T[\to \Omega_t$, where $]0, T[$ is the time interval of interest. We denote by $\boldsymbol{x}$ the coordinates in the spatial configuration, i.e., $\Omega_t \ni \boldsymbol{x} = \widehat{\boldsymbol{\phi}}(\widehat{\boldsymbol{x}}, t)$. Using the mapping $\widehat{\boldsymbol{\phi}}$, we can define the displacement of a point in the referential domain $\widehat{\boldsymbol{u}}(\widehat{\boldsymbol{x}}, t) = \widehat{\boldsymbol{\phi}}(\widehat{\boldsymbol{x}}, t) - \widehat{\boldsymbol{x}}$, and its velocity $\widehat{\boldsymbol{v}} = \partial \widehat{\boldsymbol{u}} / \partial t$. Let us also define a material domain $\Omega_{\boldsymbol{X}}$ and the function $\boldsymbol{\phi} : \Omega_{\boldsymbol{X}} \times]0, T[\to \Omega_t$, which maps each material particle $\boldsymbol{X}$ into its spatial coordinate at time t, that is, $\boldsymbol{x} = \boldsymbol{\phi}(\boldsymbol{X}, t)$. From the function $\boldsymbol{\phi}$, we can define the particle displacement $\boldsymbol{u}(\boldsymbol{X}, t) = \boldsymbol{\phi}(\boldsymbol{X}, t) - \boldsymbol{X}$, its velocity $\boldsymbol{v} = \partial \boldsymbol{\phi} / \partial t = \partial \boldsymbol{u} / \partial t$, and the deformation gradient $\boldsymbol{F} = \partial \boldsymbol{\phi} / \partial \boldsymbol{X}$. In what follows, to avoid ambiguity in our notation we will use subscripts to clarify how derivatives are to be understood. We will adopt the subscript $\boldsymbol{X}$ (respectively, $\widehat{\boldsymbol{x}}$) to indicate that the derivative is taken by holding $\boldsymbol{X}$ (respectively, $\widehat{\boldsymbol{x}}$) fixed. When no subscript is specified, the derivative is assumed to be taken by holding $\boldsymbol{x}$ fixed.

5.2.2 Governing equations of fluid mechanics

In our model, the fluid behavior is governed by the Navier-Stokes-Korteweg equations, which account for mass, momentum and energy conservation. The NSK theory fits into classical thermodynamics and, as a consequence, it can be derived from a Helmholtz free-energy potential (see, for example, [90]). Its main particularity compared to the classical Navier-Stokes equations is that it allows for liquid-gas and gas-liquid phase transformations, which can happen spontaneously without precursors. In the ALE frame, the NSK equations are given by

$$\left.\frac{\partial \rho}{\partial t}\right|_{\widehat{x}} + (\boldsymbol{v} - \widehat{\boldsymbol{v}}) \cdot \nabla \rho + \rho \nabla \cdot \boldsymbol{v} = 0, \tag{5.2.1a}$$

$$\rho \left.\frac{\partial \boldsymbol{v}}{\partial t}\right|_{\widehat{x}} + \rho \, (\boldsymbol{v} - \widehat{\boldsymbol{v}}) \cdot \nabla \boldsymbol{v} - \nabla \cdot \boldsymbol{\sigma}^f - \rho \boldsymbol{f} = 0, \tag{5.2.1b}$$

$$\left.\frac{\partial \left(\rho s\right)}{\partial t}\right|_{\widehat{x}} + (\boldsymbol{v} - \widehat{\boldsymbol{v}}) \cdot \nabla \left(\rho s\right) + \rho s \nabla \cdot \boldsymbol{v} + \nabla \cdot \left(\frac{\boldsymbol{q}}{\theta}\right) = k \frac{1}{\theta^2} \left|\nabla \theta\right|^2 + \frac{1}{\theta} \boldsymbol{\tau} : \nabla \boldsymbol{v} + \frac{\rho r}{\theta} + \frac{\rho \boldsymbol{f} \cdot \boldsymbol{v}}{\theta}. \tag{5.2.1c}$$

In the expressions above, ρ is the density, $\boldsymbol{v}$ is the velocity vector, and $\otimes$ denotes the usual vector outer product; $\boldsymbol{f}$ represents body forces per unit mass, r is the heat supply per

unit mass and θ is the temperature; $\boldsymbol{q}$ denotes the heat flux, which will be defined by the isotropic Fourier law, that is, $\boldsymbol{q} = -k\nabla\theta$, where k is the thermal conductivity; $\boldsymbol{\sigma}^f$ is the fluid Cauchy stress tensor $\boldsymbol{\sigma}^f = \boldsymbol{\tau} - p\boldsymbol{I} + \boldsymbol{\varsigma}$, where p is the pressure, $\boldsymbol{\varsigma}$ denotes the so-called Korteweg tensor, which will give rise to capillary forces at liquid-vapor interfaces, and $\boldsymbol{\tau}$ is the viscous stress tensor of a Newtonian fluid, i.e.,

$$\boldsymbol{\varsigma} = \lambda\left(\rho\Delta\rho + \frac{1}{2}\left|\nabla\rho\right|^2\right)\boldsymbol{I} - \lambda\nabla\rho\otimes\nabla\rho. \tag{5.2.2a}$$

$$\boldsymbol{\tau} = \bar{\mu}\left(\nabla\boldsymbol{v} + \nabla^T\boldsymbol{v}\right) + \bar{\lambda}\nabla\cdot\boldsymbol{v}\boldsymbol{I}, \tag{5.2.2b}$$

Here, $\bar{\mu}$ and $\bar{\lambda}$ are the viscosity coefficients, which will be related through the Stokes hypothesis, that is, $\bar{\lambda} = -2\bar{\mu}/3$; $\lambda > 0$ is the capillarity coefficient, and $|\cdot|$ denotes the Euclidean norm of a vector. Finally, in (5.2.1), the state variables, that is, the thermodynamic pressure p and the entropy density s, are the ones corresponding to a van der Waals fluid [56, 121],

$$p = Rb\left(\frac{\rho\theta}{b-\rho}\right) - a\rho^2, \tag{5.2.3a}$$

$$s = -R\log\left(\frac{\rho}{b-\rho}\right) + c_{\boldsymbol{v}}\log\left(\frac{\theta}{\theta_c}\right) \tag{5.2.3b}$$

where R is the specific gas constant, and a and b are positive constants; $c_{\boldsymbol{v}}$ is the specific heat capacity and θ_c is the critical temperature $\theta_c = 8ab/(27R)$.

5.2.3 Governing equations of solid mechanics

The solid dynamics is described by the Lagrangian form of the momentum balance equation

$$\rho_0^s\left.\frac{\partial^2\boldsymbol{u}}{\partial t^2}\right|_X = \nabla_X\cdot\boldsymbol{P} + \rho_0^s\boldsymbol{f}^s, \tag{5.2.4}$$

where ρ_0^s is the mass density in the initial configuration, $\boldsymbol{f}^s$ represents body forces per unit mass, and $\boldsymbol{P}$ is the first Piola–Kirchhoff stress tensor, which needs to be defined from a constitutive theory. In our case, we adopt a hyperelastic model, namely, the generalized neo-Hookean model with dilatational penalty proposed in [152]. This material is described by the stored elastic energy density

$$W = \frac{\mu}{2}\left(J^{-2/d}\mathrm{tr}(\boldsymbol{C}) - d\right) + \frac{\kappa}{2}\left(\frac{1}{2}\left(J^2-1\right) - \ln J\right), \tag{5.2.5}$$

where d is the number of spatial dimensions, κ and μ are the material bulk and shear moduli; $\mathrm{tr}(\cdot)$ denotes the trace operator and and $J = \det(\boldsymbol{F})$, where $\boldsymbol{F}$ denotes the deformation gradient, i.e., $\boldsymbol{F} = \boldsymbol{I} + \nabla_X\boldsymbol{u}$. Here, $\boldsymbol{I}$ denotes the identity tensor. Finally, $\boldsymbol{C} = \boldsymbol{F}^T\boldsymbol{F}$ is the Cauchy–Green deformation tensor. The second Piola–Kirchhoff stress tensor can be com-

puted from W as $\boldsymbol{S} = \partial W/\partial \boldsymbol{E}$ while the first Piola–Kirchhoff stress tensor is obtained by $\boldsymbol{P} = \boldsymbol{F}\boldsymbol{S}$. The Cauchy stress tensor in the solid is given by $\boldsymbol{\sigma}^s = J^{-1}\boldsymbol{F}\boldsymbol{S}\boldsymbol{F}^T = J^{-1}\boldsymbol{P}\boldsymbol{F}^T$.

5.3 Numerical formulation

Let Ω_0 denote the initial configuration of the entire domain of the problem, that is, the fluid and solid domains combined. Ω_0 will be adopted as the reference configuration and also as material configuration. We may decompose Ω_0 as $\Omega_0 = \overline{\Omega_0^f \cup \Omega_0^s}$, with $\Omega_0^f \cap \Omega_0^s = \emptyset$, where s and f refer to the solid and the fluid domain, respectively. We may also decompose the spatial configuration of Ω_0 at time t, namely Ω_t, as $\Omega_t = \overline{\Omega_t^f \cup \Omega_t^s}$ with $\Omega_t^f \cap \Omega_t^s = \emptyset$. Let Γ_0 and Γ_t be the fluid-solid interface where the subscripts 0 and t denote the initial and the current configuration, respectively. We will denote by Γ_0^s and Γ_t^s (respectively, Γ_0^f and Γ_t^f) the boundary of the solid (respectively, the fluid) subdomain without the part of the fluid-structure interface.

Solid mechanics problem

Let us assume that the solid boundary Γ_0^s can be decomposed into Neumann and Dirichlet parts denoted by $(\Gamma_0^s)_N$ and $(\Gamma_0^s)_D$, respectively. We define a trial solution functional space $\mathcal{X}^s = \mathcal{X}^s(\Omega_0^s)$ whose members verify the Dirichlet boundary conditions of the problem, and a weighting function space $\mathcal{Y}^s = \mathcal{Y}^s(\Omega_0^s)$ which is identical to $\mathcal{X}^s$, but verifies homogeneous conditions on $(\Gamma_0^s)_D$. The variational formulation can be stated as follows: Find $\boldsymbol{u} \in \mathcal{X}^s$ such that $\forall \boldsymbol{w}^s \in \mathcal{Y}^s$,

$$B^s(\boldsymbol{w}^s, \boldsymbol{u}) = F^s(\boldsymbol{w}^s), \tag{5.3.6}$$

where

$$B^s(\boldsymbol{w}^s, \boldsymbol{u}) = \int_{\Omega_0^s} \left(\boldsymbol{w}^s \cdot \rho_0^s \left.\frac{\partial^2 \boldsymbol{u}}{\partial t^2}\right|_X + \nabla_X \boldsymbol{w}^s : \boldsymbol{P} \right) \mathrm{d}\Omega_0^s \tag{5.3.7}$$

and

$$F^s(\boldsymbol{w}^s) = \int_{\Omega_0^s} \boldsymbol{w}^s \cdot \rho_0^s \, \boldsymbol{f}^s \mathrm{d}\Omega_0^s + \int_{(\Gamma_0^s)_N} \boldsymbol{w}^s \cdot \widehat{\boldsymbol{h}} \, \mathrm{d}(\Gamma_0^s)_N. \tag{5.3.8}$$

Note that this variational formulation weakly enforces the Neumman boundary condition $\boldsymbol{P}\widehat{\boldsymbol{n}}^s = \widehat{\boldsymbol{h}}$ on $(\Gamma_0^s)_N$, where $\widehat{\boldsymbol{n}}^s$ is the unit outward normal to the solid boundary in the referential domain; $\widehat{\boldsymbol{h}}$ is a given traction, which for the case of a follower load p in the direction of the inner normal to the solid boundary is given by $\widehat{\boldsymbol{h}} = -\mathsf{p} J \boldsymbol{F}^{-T}\widehat{\boldsymbol{n}}^s$.

Fluid mechanics problem

For the fluid, let us assume solid-wall boundary conditions. Additionally, due to the third-order spatial derivative of the density in NSK equations, we enforce the boundary condition $\nabla\rho \cdot \boldsymbol{n}^f = -|\nabla\rho|\cos(\varphi)$ where $\boldsymbol{n}^f$ denotes the unit outward normal to the fluid

boundary, and φ is the contact angle between the liquid-vapor interface and the solid, measured in the vapor phase. The imposition of the aforementioned boundary condition can be simplified by introducing a new variable $\Upsilon = \Delta\rho$ in the momentum equation. Note that this step is not strictly necessary with isogeometric analysis since IGA allows to use the globally $\mathcal{C}^1$-continuous basis functions that are required to approximate the NSK equations in primal form (see [88]). Let us introduce the trial solution space $\mathcal{X}^f = \mathcal{X}^f(\Omega_t^f)$ whose members satisfy all Dirichlet boundary conditions. The weighting functions space $\mathcal{Y}^f = \mathcal{Y}^f(\Omega_t^f)$ is identical to $\mathcal{X}^f$, but all restrictions on the Dirichlet boundary are homogeneous. The variational formulation is stated as follows: Find $\boldsymbol{U} = \{\rho, \boldsymbol{v}, \Upsilon, \theta\} \in \mathcal{X}^f$ such that $\forall \boldsymbol{W} = \{w^1, \boldsymbol{w}^2, w^3, w^4\} \in \mathcal{Y}^f$,

$$B^f(\boldsymbol{W}, \boldsymbol{U}; \widehat{\boldsymbol{v}}) = 0, \tag{5.3.9}$$

where

$$\begin{aligned}
B^f(\boldsymbol{W}, \boldsymbol{U}; \widehat{\boldsymbol{v}}) = &\int_{\Omega_t^f} w^1 \left(\left.\frac{\partial \rho}{\partial t}\right|_{\widehat{x}} + (\boldsymbol{v} - \widehat{\boldsymbol{v}}) \cdot \nabla \rho + \rho \nabla \cdot \boldsymbol{v} \right) \mathrm{d}\Omega_t^f \\
&+ \int_{\Omega_t^f} \boldsymbol{w}^2 \cdot \left(\rho \left.\frac{\partial \boldsymbol{v}}{\partial t}\right|_{\widehat{x}} + \rho \left(\boldsymbol{v} - \widehat{\boldsymbol{v}}\right) \cdot \nabla \boldsymbol{v} - \rho \boldsymbol{f} \right) \mathrm{d}\Omega_t^f + \int_{\Omega_t^f} \nabla \boldsymbol{w}^2 : (\boldsymbol{\tau} - p\boldsymbol{I}) \, \mathrm{d}\Omega_t^f \\
&+ \int_{\Omega_t^f} \nabla \cdot \boldsymbol{w}^2 \lambda \left(\rho \Upsilon + \frac{1}{2} |\nabla \rho|^2 \right) \mathrm{d}\Omega_t^f - \int_{\Omega_t^f} \nabla \boldsymbol{w}^2 : \lambda \nabla \rho \otimes \nabla \rho \mathrm{d}\Omega_t^f \\
&+ \int_{\Omega_t^f} w^3 \Upsilon \mathrm{d}\Omega_t^f + \int_{\Omega_t^f} \nabla w^3 \cdot \nabla \rho \mathrm{d}\Omega_t^f + \int_{\Gamma_t^f \cup \Gamma_t} w^3 |\nabla \rho| \cos(\varphi) \mathrm{d}(\Gamma_t^f \cup \Gamma_t) \\
&+ \int_{\Omega_t^f} w^4 \left(\left.\frac{\partial \left(\rho s\right)}{\partial t}\right|_{\widehat{x}} + (\boldsymbol{v} - \widehat{\boldsymbol{v}}) \cdot \nabla \left(\rho s\right) \right) \mathrm{d}\Omega_t^f - \int_{\Omega_t^f} w^4 \left(\frac{\rho r}{\theta} + \frac{\rho \boldsymbol{f} \cdot \boldsymbol{v}}{\theta} \right) \mathrm{d}\Omega_t^f \\
&+ \int_{\Omega_t^f} w^4 \left(\rho s \nabla \cdot \boldsymbol{v} - \frac{1}{\theta} \boldsymbol{\tau} : \nabla \boldsymbol{v} - k \frac{1}{\theta^2} |\nabla \theta|^2 \right) \mathrm{d}\Omega_t^f - \int_{\Omega_t^f} \nabla w^4 \cdot \frac{\boldsymbol{q}}{\theta} \mathrm{d}\Omega_t^f .
\end{aligned} \tag{5.3.10}$$

Note that if Dirichlet boundary conditions are not set on the entire boundary for velocity or temperature, then the variational formulation weakly imposes the conjugate stress-free condition or vanishing heat flux at the wall.

Fluid domain motion

The goal of this problem is to produce a smooth evolution of the fluid domain given the displacement data on the fluid–solid interface. This motion will be associated to the mapping $\widehat{\boldsymbol{\phi}}$, and will be understood as a succession of fictitious linear elastic boundary-value problems [107, 156, 180, 182–184]. Let us define the displacement of the reference domain at time t as $\widehat{\boldsymbol{u}}_t(\widehat{\boldsymbol{x}}) = \widehat{\boldsymbol{u}}(\widehat{\boldsymbol{x}}, t) = \widehat{\boldsymbol{\phi}}_t(\widehat{\boldsymbol{x}}) - \widehat{\boldsymbol{x}}$. To determine $\widehat{\boldsymbol{\phi}}_t$, and thus, the motion of the fluid domain, we use the identity $\widehat{\boldsymbol{\phi}}_t(\widehat{\boldsymbol{x}}) = \widehat{\boldsymbol{\phi}}_{\tilde{t}}(\widehat{\boldsymbol{x}}) + (\widehat{\boldsymbol{u}}_t - \widehat{\boldsymbol{u}}_{\tilde{t}})(\widehat{\boldsymbol{x}})$, where $\widehat{\boldsymbol{u}}_t - \widehat{\boldsymbol{u}}_{\tilde{t}}$ is

obtained from a linear elastic boundary–value problem. Here, $\tilde{t} < t$ is a time instant close to t. In general, in our problems $\tilde{t}$ is the final configuration of the previous time step.

Let us define $\boldsymbol{u}^m$ as $\boldsymbol{u}^m = \widehat{\boldsymbol{u}}_t - \widehat{\boldsymbol{u}}_{\tilde{t}}$. $\boldsymbol{u}^m$ is obtained by solving fictitious linear–elastic boundary value problems, subject to the Dirichlet boundary conditions $\boldsymbol{u}^m = \boldsymbol{u}_t \circ \boldsymbol{\phi}_t^{-1} - \boldsymbol{u}_{\tilde{t}} \circ \boldsymbol{\phi}_{\tilde{t}}^{-1}$ on $\Gamma_{\tilde{t}}$, where $\boldsymbol{u}_t$ and $\boldsymbol{u}_{\tilde{t}}$ are the particle displacement at times t and $\tilde{t}$, respectively. These Dirichlet boundary conditions are strongly built into the trial solution space $\mathcal{V}^m = \mathcal{V}^m(\Omega_{\tilde{t}}^f)$. The corresponding weighting function space, satisfying homogeneous conditions on the boundary, is denoted by $\mathcal{W}^m = \mathcal{W}^m(\Omega_{\tilde{t}}^f)$. The variational formulation can be stated as follows: Find $\boldsymbol{u}^m \in \mathcal{V}^m$ such that $\forall \boldsymbol{w}^m \in \mathcal{W}^m$,

$$B^m(\boldsymbol{w}^m, \boldsymbol{u}^m) = 0, \tag{5.3.11}$$

where

$$B^m(\boldsymbol{w}^m, \boldsymbol{u}^m) = \int_{\Omega_{\tilde{t}}^f} \nabla_{\tilde{x}}^{sym} \boldsymbol{w}^m : 2\mu^m \nabla_{\tilde{x}}^{sym} \boldsymbol{u}^m \mathrm{d}\Omega_{\tilde{t}}^f + \int_{\Omega_{\tilde{t}}^f} \nabla_{\tilde{x}} \cdot \boldsymbol{w}^m \lambda^m \nabla_{\tilde{x}} \cdot \boldsymbol{u}^m \mathrm{d}\Omega_{\tilde{t}}^f, \tag{5.3.12}$$

while μ^m and λ^m are the Lamé parameters of the fictitious elastic model characterizing the motion of the fluid domain; $\nabla_{\tilde{x}}$ is the gradient operator on $\Omega_{\tilde{t}}$ and $\nabla_{\tilde{x}}^{sym}$ is its symmetric part.

Coupled FSI problem

Now we have all the ingredients to define the coupled fluid-structure interaction problem. The variational formulation of the problem is stated as follows: Find $\boldsymbol{U} = \{\rho, \boldsymbol{v}, \Upsilon, \theta\} \in \mathcal{X}^f$, $\boldsymbol{u} \in \mathcal{X}^s$ and $\boldsymbol{u}^m \in \mathcal{V}^m$ such that $\forall \boldsymbol{W} = \{w^1, \boldsymbol{w}^2, w^3, w^4\} \in \mathcal{Y}^f$, $\forall \boldsymbol{w}^s \in \mathcal{Y}^s$ and $\forall \boldsymbol{w}^m \in \mathcal{W}^m$,

$$B^f(\boldsymbol{W}, \boldsymbol{U}; \widehat{\boldsymbol{v}}) + B^s(\boldsymbol{w}^s, \boldsymbol{u}) + B^m(\boldsymbol{w}^m, \boldsymbol{u}^m) = F^s(\boldsymbol{w}^s), \tag{5.3.13}$$

with the following fluid-solid interface conditions:

$$\boldsymbol{v} = \frac{\partial \boldsymbol{u}}{\partial t} \circ \widehat{\boldsymbol{\phi}}^{-1} \quad \text{on} \quad \Gamma_t, \tag{5.3.14}$$

$$\boldsymbol{w}^2 = \boldsymbol{w}^s \circ \widehat{\boldsymbol{\phi}}^{-1} \quad \text{on} \quad \Gamma_t. \tag{5.3.15}$$

Note that Eq. (5.3.14) ensures strong kinematical compatibility at the fluid-structure interface. Eq. (5.3.15) leads to a weak enforcement of traction compatibility at the interface, which in the spatial configuration may be expressed as $\boldsymbol{\sigma}^f \boldsymbol{n}^f + \boldsymbol{\sigma}^s \boldsymbol{n}^s = 0$ on Γ_t, where $\boldsymbol{n}^s$ is the unit outward normal to the solid in the spatial configuration.

For the spatial discretization of the coupled problem we make use of NURBS-based isogeometric analysis. We use the generalized-α method as a time integration scheme. The nonlinear system of equations is solved using a Newton-Raphson iteration procedure,

which leads to a two-stage predictor-multicorrector algorithm. The resulting linear system is solved using a preconditioned GMRES method. To solve the FSI equations, we adopt a quasi-direct solution strategy (see [184–186] for the definition of terminology and methods), where the fluid and solid equations are solved in a coupled fashion, while the mesh motion equations are solved separately, using the data from the fluid–solid solve as input.

5.4 Numerical examples

The FSI problem was solved in a non-dimensional form. We rescaled the units of measurement of length, mass, time and temperature by L_0, bL_0^3, $L_0/\sqrt{ab}$ and θ_c, respectively, where $L_0 = 1$ denotes a length scale of the computational domain size. Using this non-dimensionalization, our FSI problem can be defined using six dimensionless numbers, $Re = L_0 b\sqrt{ab}/\bar{\mu}$, $Ca = \sqrt{\lambda/a}/L_0$, $Pr = L_0 ab^2\sqrt{ab}/(\theta_c k)$, $c = 8c_v/(27R)$, $\widehat{\mu} = \mu/(\rho_0^s ab)$, and $\widehat{\kappa} = \kappa/(\rho_0^s ab)$.

5.4.1 2D example

The first numerical example of phase-change-driven implosion is the collapse of a vapor-filled ring. The external radius of the ring is $L_0 = 1$, and the thickness of the solid is $L_0/40$. The system is initially in thermal and mechanical equilibrium, as we impose in the external surface a follower load of identical value than the initial vapor pressure. We trigger the implosion by suddenly reducing the temperature at the fluid–solid interface using the temperature boundary condition. The temperature reduction makes the vapor condensate, reducing the internal pressure and increasing the density.

Fig. 5.1 shows the time evolution of the density (left) and temperature (right) in the fluid subdomain. Initially, all the fluid subdomain is in gaseous state [red color in Fig. 5.1(a)]. The thin grey color that encloses the fluid represents the structure. The initial value of the fluid density is the one corresponding to the Maxwell state at $\theta_0 = 0.85$. On the fluid-structure interface we apply a temperature boundary condition given by $\theta_D = 0.5 < \theta_0$. As a consequence, the temperature of the gas close to the structure is reduced and the gas turns into liquid (blue) [Fig. 5.1(c)]. The pressure decreases inside and the structure is deformed due to the external pressure [Fig. 5.1(c)]. The process continues so that all the gas is transformed into liquid and the structure is completely collapsed.

5.4.2 3D example

The second numerical example is the collapse of a three-dimensional box of side $2L_0$ and thickness $L_0/40$ [see Fig. 5.2(a)]. The parameters and initial conditions are the same as in the 2D case, but the collapse is stronger because the structure is geometrically softer.

Fig. 5.2 shows the evolution of the density (left) and temperature (right). It is observed that the temperature boundary condition triggers the transformation of vapor into liquid creating a blue area in the density plot which represents liquid water.

5.5 Contributions and open lines for research

The most significant contributions of this work, which has been published as a research paper in [27], can be summarized in the following points:

- We have proposed a computational model for the interaction of complex fluids and solid structures. The fluid is a single-component, two-phase flow that naturally undergoes phase-transformations between vapor and liquid states.
- To the best of our knowledge, the proposed theory is the first model that captures all the relevant physics behind phase-change driven implosion.
- Isogeometric analysis based on NURBS is adopted for the spatial discretization of both the solid and the fluid subdomains, which allows for a exact representation of many commonly engineered designs, like cylinders, spheres and tori. It also allows to tackle some of the computational challenges posed by phase-field methods.

The main open ideas derived from this work are:

- Validating our model with experimental data.
- Solving other problems that involve the interaction of complex fluids and solids, such as capillary origami or droplet motion driven by stiffness gradients of the underlying substrate.

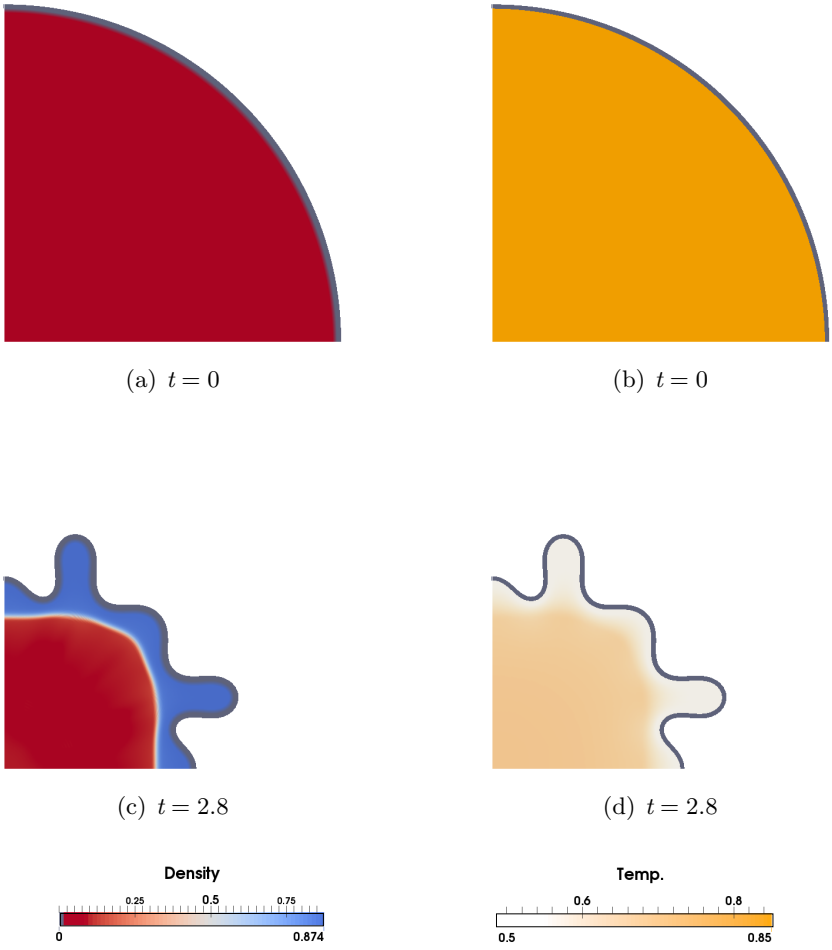

(a) $t = 0$ (b) $t = 0$

(c) $t = 2.8$ (d) $t = 2.8$

Figure 5.1: Evolution of density (left) and temperature (right) in a 2D phase-change-driven implosion problem. Initially, water-vapor (red color in the density plot) is filling up a hollow structure (a) and a low temperature $\theta_D = 0.5$ is applied at the fluid-structure interface. The vapor close to the boundaries increases its density and turns into liquid [blue in the density plot, (c)]. The pressure inside is reduced and the structure deforms due to the external load. We have used the parameters $Re = 256$, $Ca = 0.0078125$, $Pr = 0.013$, $c = 0.73$, $\widehat{\mu} = 1.0$, $\widehat{\kappa} = 1.0$.

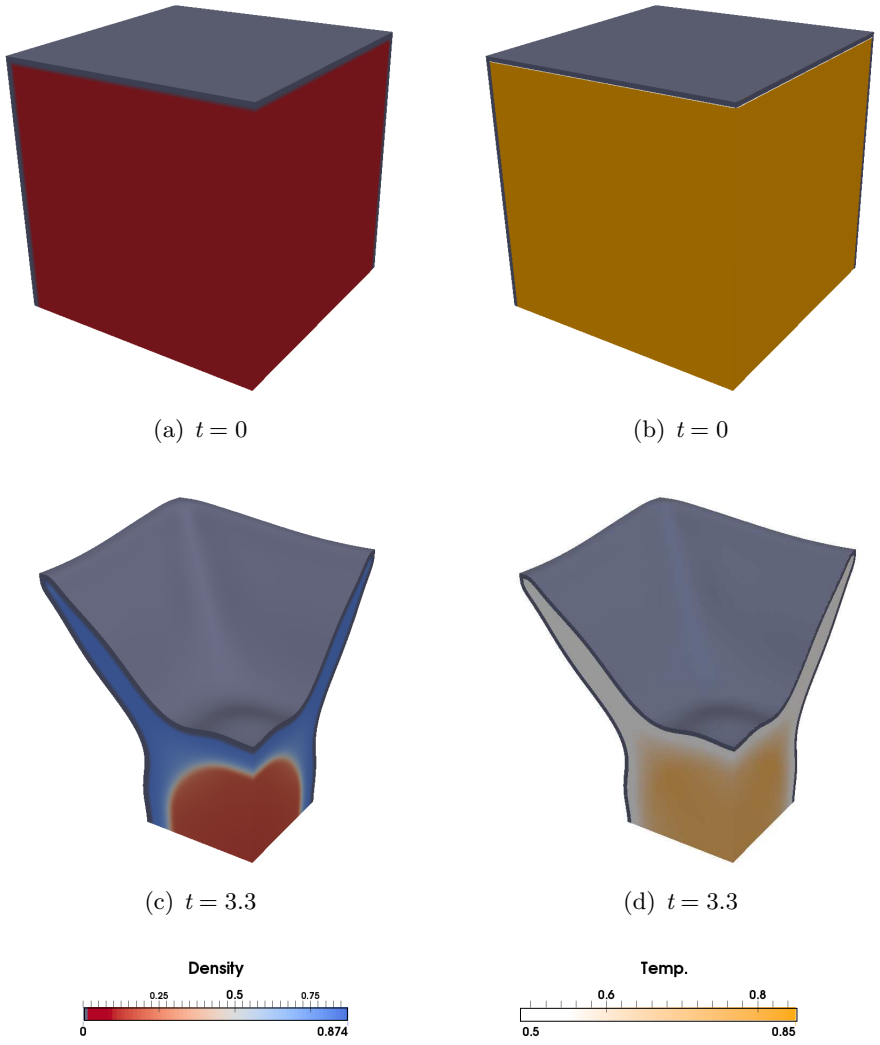

(a) $t = 0$ (b) $t = 0$

(c) $t = 3.3$ (d) $t = 3.3$

Figure 5.2: Evolution of density (left) and temperature (right) in a 3D phase-change-driven implosion problem. Initially, water-vapor (red color in the density plot) is filling up a hollow structure (a) and a low temperature $\theta_D = 0.5$ is applied at the fluid-structure interface. The vapor close to the boundaries increases its density and turns into liquid (blue color in the density plot) [(c) and (e)]. The pressure inside is reduced and the structure deforms due to the external load. We have used the parameters $Re = 256$, $Ca = 0.0078125$, $Pr = 0.013$, $c = 0.73$, $\widehat{\mu} = 1.0$, $\widehat{\kappa} = 1.0$.

Chapter 6

Interaction of complex fluids and solids. Application to tensotaxis

6.1 Introduction

One of the fields that could benefit the most from a FSI model with complex fluids is mechanobiology. Some of the mechanisms that control cell motion, such as durotaxis [123, 163] or tensotaxis [123], are still not completely understood, to the point that it is still not clear if cells perform an active role in these processes. For example, Style et al. [161] showed recently that droplets could undergo durotaxis, that is, motion due to gradients in the stiffness of the underlying substrate. This discovery has revived the debate about the relevance of mechanics in cell migration. It seems plausible that at cellular scale capillary forces play an important role. In this sense, a theoretical model that allows studying durotaxis and/or tensotaxis would contribute to a better understanding of the process and would allow to explore scenarios that are difficult to probe experimentally.

Here, we focus on the case of tensotaxis, that is, motion along strain gradients. Several mechanistic models have been proposed [19,131] in the literature for this process. However, the understanding of tensotaxis is still very limited. The main reason is that controlled experimental studies of this mechanism are particularly challenging because prestraining the substrate is often accompanied by an increase in the substrate stiffness as a result of nonlinear material response [119], thus producing a combination of tensotaxis and durotaxis. We develop a model that allows to isolate the effects of tensotaxis and we carry out several numerical experiments, which show that liquid droplets on soft substrates move toward areas of higher compressive strains, the same behavior observed in cell migration.

6.2 Droplet motion

The static configuration that droplets adopt on rigid substrates can be explained by Young–Drupré equation, that is, the following balance of forces at the contact line,

$$\gamma_{SL} + \gamma_{LV}\cos(\alpha) = \gamma_{SV}. \tag{6.2.1}$$

Here, α is the contact angle, and γ_{LV}, γ_{SV} and γ_{SL} denote the surface tension at the liquid-vapor, solid-vapor and solid-liquid interface, respectively (see Fig. 6.1). If there is a imbalance of these forces, for example, if the actual contact angle of the droplet is different from its equilibrium contact angle, the contact line will move trying to recover equilibrium.

Young–Dupré theory is valid only for ideal solid surfaces, where the solid is flat and infinitely rigid. It assumes no deformation of the substrate due to capillary forces or the Laplace pressure [see Fig. 6.1(A)]. The immediate consequence is that Young–Drupré equation is violated when the surface tension of the droplet is sufficiently strong as to deform the substrate. This may happen for slender structures [18, 62, 63] but also when the droplet is small or when it is deposited on a very soft substrate [158, 159]. In such cases, where small droplets wet soft substrates, the interfacial forces pull up the contact line and the Laplace pressure dimples the substrate under the drop. As a consequence, the apparent contact angle [angle formed by the liquid–vapor interface and the undeformed surface of the substrate (φ in Fig. 6.1)] will be smaller than the angle predicted by Young–Dupré equation.

We hypothesize that, for a non–zero Poisson's ratio and in absence of gravity, forces applied on the plane of the substrate may cause a strain gradient, which in turn, has an impact on the apparent contact angle, causing an imbalance of forces and triggering droplet motion towards the compressed part of the solid. To verify our hypothesis, we develop a fluid–structure interaction model that couples a Saint Venant–Kirchhoff solid with a complex fluid. Our choice of a Saint Venant–Kirchhoff model for the solid allows us to consider geometric nonlinearities with a linear material response. As a consequence, the strains introduced in the substrate to trigger tensotaxis do not alter the stiffness of the solid, avoiding a situation with simultaneous tensotaxis and durotaxis. The fluid is governed by the Navier–Stokes–Korteweg (NSK) equations, a phase-field theory that allows for the stable coexistence of a liquid and a gaseous phase. Using this computational approach, we try to mimic the cell locomotion experiments reported in [123]. A microneedle is inserted into the substrate and exerts a force either toward the droplet or away from the droplet [see Fig. 6.1(C)].

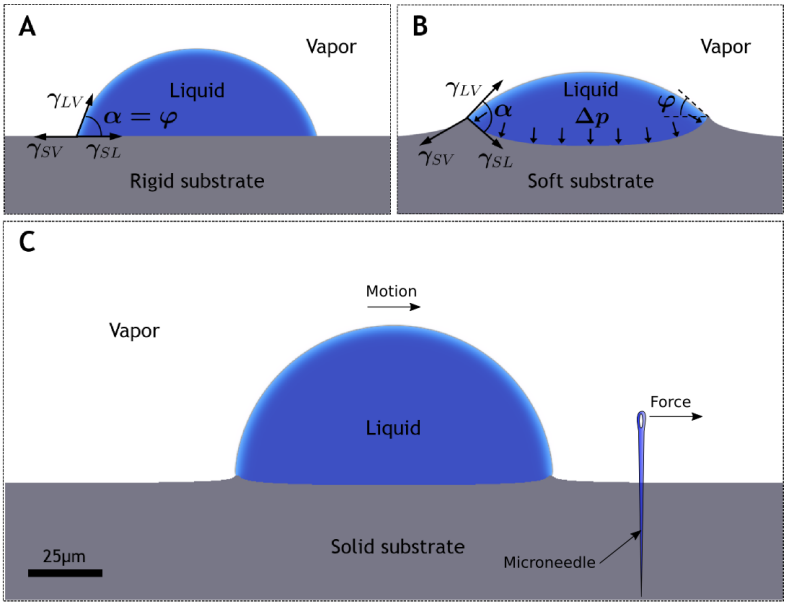

Figure 6.1: Droplet motion driven by tensotaxis. (A) Liquid droplet (blue) deposited on a rigid substrate (gray). The surface tensions at the contact line γ_{LV}, γ_{SV} and γ_{SL} are represented with arrows. (B) Liquid droplet on a soft substrate. The solid is deformed under the combined action of the surface tensions and the internal Laplace pressure Δp. The plot shows that the static contact angle α and the apparent contact angle φ are different when the solid is deformable. (C) Tensotaxis can be triggered by inserting a microneedle in the substrate and moving it toward the droplet or away from the droplet.

6.3 Governing equations

Solid mechanics equations

The solid dynamics is described by the Lagrangian form of the momentum balance equation

$$\rho_0^s \left.\frac{\partial^2 \boldsymbol{u}}{\partial t^2}\right|_{\boldsymbol{X}} = \nabla_{\boldsymbol{X}} \cdot \boldsymbol{P} + \rho_0^s \boldsymbol{f}^s, \tag{6.3.2}$$

where $\nabla_{\boldsymbol{X}}$ is the gradient with respect to the material coordinates $\boldsymbol{X}$ and $|_{\boldsymbol{X}}$ indicates that the time derivative is taken by holding $\boldsymbol{X}$ fixed; $\boldsymbol{u}$ is the solid displacement and ρ_0^s is the mass density in the initial configuration; $\boldsymbol{f}^s$ represents body forces per unit mass, and $\boldsymbol{P}$ is the first Piola–Kirchhoff stress tensor. The Saint Venant–Kirchhoff model is described by the stored elastic energy density [15, 128]

$$W = \frac{\lambda^s}{2} (\mathrm{tr}(\boldsymbol{E}))^2 + \mu^s \,\mathrm{tr}(\boldsymbol{E}^2), \tag{6.3.3}$$

Here, $\mathrm{tr}(\cdot)$ denotes the trace operator whereas λ^s and μ^s are the first and second Lamé parameters, which can be written as a function of the Young modulus E^s and the Poisson ratio ν: $\lambda^s = \nu E^s/((1+\nu)(1-2\nu))$ and $\mu^s = E^s/(2(1+\nu))$. The Green–Lagrange strain tensor is defined by $\boldsymbol{E} = (\boldsymbol{C} - \boldsymbol{I})/2$, where $\boldsymbol{I}$ denotes the identity tensor and $\boldsymbol{C} = \boldsymbol{F}^T\boldsymbol{F}$

is the Cauchy–Green deformation tensor. Here, $\boldsymbol{F}$ denotes the deformation gradient, i.e., $\boldsymbol{F} = \boldsymbol{I} + \nabla_X \boldsymbol{u}$. The second Piola–Kirchhoff stress tensor can be computed from W as $\boldsymbol{S} = \partial W/\partial \boldsymbol{E}$ while the first Piola–Kirchhoff stress tensor is obtained by $\boldsymbol{P} = \boldsymbol{F}\boldsymbol{S}$. The Cauchy stress tensor in the solid is given by $\boldsymbol{\sigma}^s = J^{-1}\boldsymbol{F}\boldsymbol{S}\boldsymbol{F}^T = J^{-1}\boldsymbol{P}\boldsymbol{F}^T$, where $J = \det(\boldsymbol{F})$.

Fluid mechanics equations

We use the isothermal form of the Navier–Stokes–Korteweg (NSK) equations to describe the fluid dynamics. The NSK equations account for mass and momentum conservation. They describe single-component two-phase flow and naturally allow for phase transformations, which can happen spontaneously due to pressure and/or temperature variations. The NSK theory is a diffuse-interface model where the fluid density itself is the phase-field that identifies the liquid and vapor phases. The reader is referred to Chapter 4 and [56, 88, 122] for a more detailed discussion on NSK. In the Arbitrary Lagrangian-Eulerian description, the isothermal NSK equations are given by

$$\left.\frac{\partial \rho}{\partial t}\right|_{\widehat{\boldsymbol{x}}} + (\boldsymbol{v} - \widehat{\boldsymbol{v}}) \cdot \nabla \rho + \rho \nabla \cdot \boldsymbol{v} = 0, \tag{6.3.4a}$$

$$\rho \left.\frac{\partial \boldsymbol{v}}{\partial t}\right|_{\widehat{\boldsymbol{x}}} + \rho\,(\boldsymbol{v} - \widehat{\boldsymbol{v}}) \cdot \nabla \boldsymbol{v} - \nabla \cdot \boldsymbol{\sigma}^f = 0, \tag{6.3.4b}$$

where $\widehat{\boldsymbol{v}}$ is the fluid domain velocity and $\widehat{\boldsymbol{x}}$ is a coordinate in the reference domain; ρ denotes the density and $\boldsymbol{v}$ is the velocity vector. $\boldsymbol{\sigma}^f$ is the Cauchy stress tensor for the fluid, which is defined as $\boldsymbol{\sigma}^f = \boldsymbol{\tau} - p\boldsymbol{I} + \boldsymbol{\varsigma}$. Here $\boldsymbol{\tau}$ is the viscous stress tensor of a Newtonian fluid, $\boldsymbol{\varsigma}$ is the Korteweg tensor and p denotes the thermodynamic pressure, which will be defined by van der Waals equation (see Chapter 4 for a detailed definition).

Since the NSK system includes a third-order spatial derivative of the fluid density in the linear momentum balance equation, the classical solid-wall boundary conditions are insufficient to render a well-posed boundary value problem. Therefore, we additionally impose the boundary condition $\nabla \rho \cdot \boldsymbol{n}^f = |\nabla \rho| \cos\alpha$, where $\boldsymbol{n}^f$ denotes the unit outward normal to the fluid boundary, and α is the contact angle (see Fig. 6.1). Note that this boundary condition allows to control the contact angle α at the fluid–structure interface, but the apparent contact angle φ will still be free to change as a result of the substrate deformation.

Computational method

Our computational approach is similar to those presented in [8, 27]. We solve the coupled system composed by Eqs. (6.3.2) and (6.3.4) subject to the kinematic compatibility ($\boldsymbol{v} = \partial \boldsymbol{u}/\partial t$) and traction balance constraints ($\boldsymbol{\sigma}^f \boldsymbol{n}^f - \boldsymbol{\sigma}^s \boldsymbol{n}^f = 0$). Equations (6.3.2) and (6.3.4)

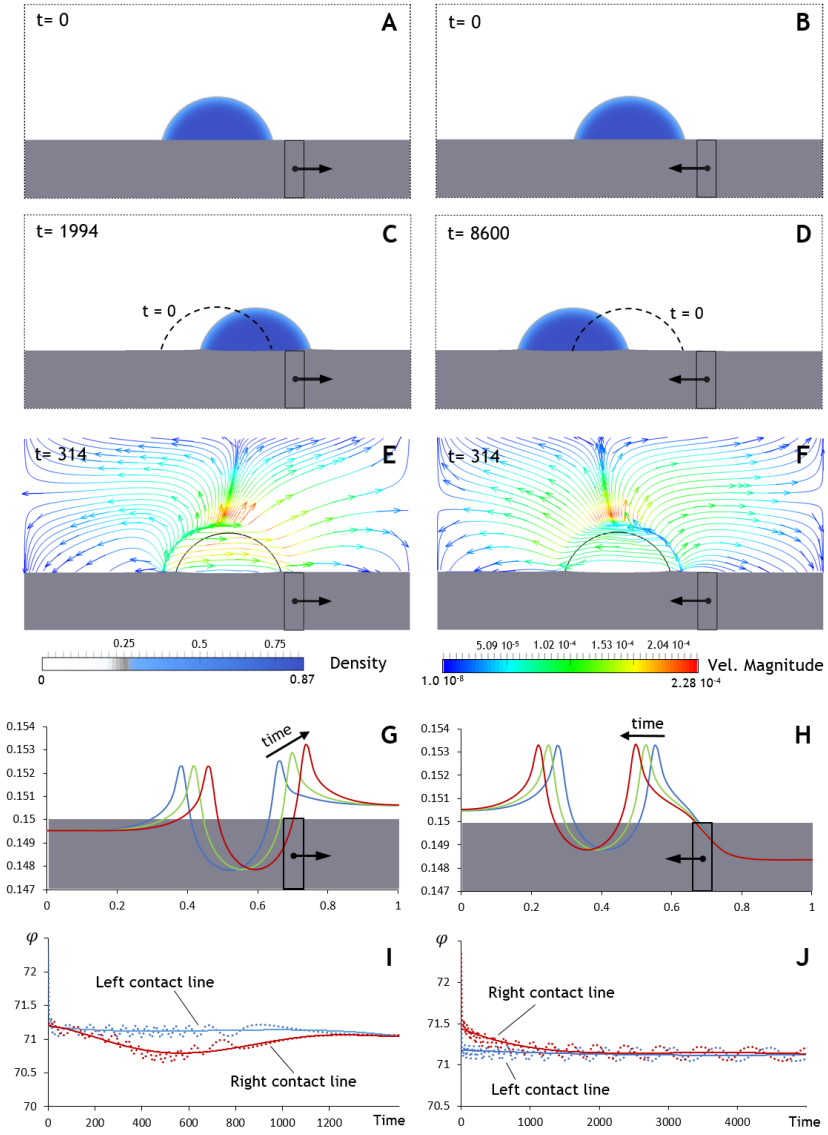

Figure 6.2: Mechanism of tensotaxis. Left panels refer to the case in which the applied force pulls the droplet. Right panels refer to case in which the applied force pushes the droplet. (A) and (B) Initial configuration of a droplet on a deformable substrate. We apply a force per unit mass that points away from the droplet (A) and toward the droplet (B) in the marked rectangular region. (C) and (D) The droplet moves in the direction of the applied force. The dashed black line represents the position of the droplet at the initial time. (E) and (F) Streamlines of the fluid velocity colored with the velocity magnitude. The droplet is represented by a black, solid line. (G) and (H) Vertical displacements at the fluid–solid interface for different times. (I) and (J) Time evolution of the apparent contact angles at the left (blue dashed line) and right (red dashed line) contact lines of the droplet. Trend lines are ploted using a blue and red solid lines, respectively. The difference in apparent contact angles between the two contact lines is responsible for the motion of the droplet. The computational domain is the rectangle $\Omega = [0, 1.0] \times [0, 0.5]$, which is discretized with a uniform mesh of 128×64 $\mathcal{C}^1$-quadratic elements. The static contact angle is $\alpha = 75°$. We have used the parameters $\nu = 0.45$, $\widehat{\mu} = 1/256$, $\widehat{\gamma} = 1/64$, $\widehat{E} = 0.7554$, and $\widehat{\theta} = 0.39$. The magnitude of the force applied on the substrate is $\left|\widehat{\boldsymbol{f}}^s\right| = 0.16215$.

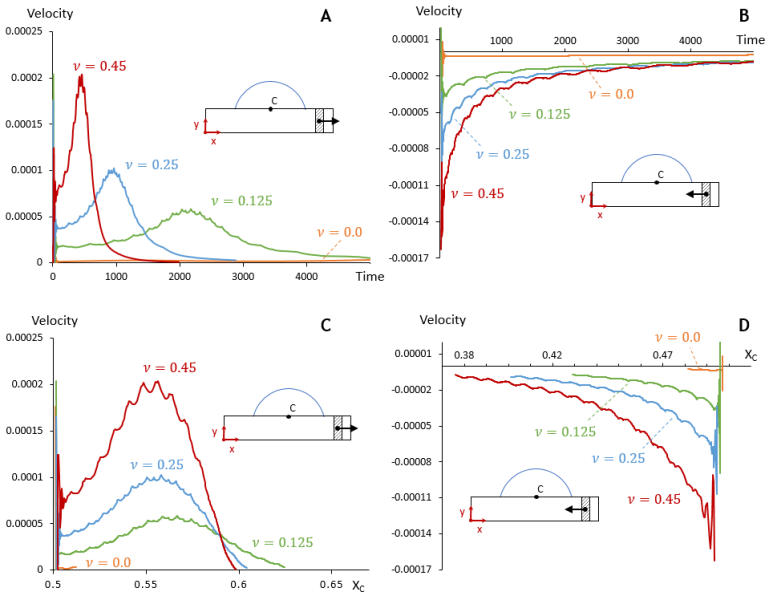

Figure 6.3: Pulling and pushing the droplet. Left panels refer to the case in which the applied force pulls the droplet. Right panels refer to case in which the applied force pushes the droplet. (A) and (B) Droplet velocity with respect to time for different Poisson's ratios ν. When pulling, the droplet initially accelerates and then decelerates as it passes through the localized applied force. When pushing, the velocity decreases monotonically. (C) and (D) Droplet velocity with respect to the position of the droplet center X_c. In all cases the velocity is reduced as the Poisson ratio drops, and for $\nu = 0$ the applied force induces no droplet motion.

can be written in variational form and discretized in space using Isogeometric Analysis. We use the generalized–α method [40] as a time integration scheme. The nonlinear system of equations is solved using a Newton–Raphson iteration procedure, which leads to a two-stage predictor–multicorrector algorithm. The resulting linear system is solved using a preconditioned GMRES method.

6.4 Results

The FSI problem was solved in a non-dimensional form by rescaling length, time, mass and temperature by L_0, $L_0/\sqrt{ab}$, bL_0^3 and θ_c, respectively, where $L_0 = 1$ is a length scale of the computational domain and $\theta_c = 8ab/(27R)$ is the critical temperature. Using this non–dimensionalization, the problem is characterized by six dimensionless numbers, the Poisson ratio ν, the dimensionless Young Modulus $\widehat{E} = (E^s/\rho_0^s ab)$, a dimensionless body force $\widehat{\boldsymbol{f}}^s = \boldsymbol{f}^s/(ab/L_0)$, a non-dimensional form of the surface tension $\widehat{\gamma} = (\sqrt{\lambda/a})/(L_0)$, a dimensionless viscosity $\widehat{\mu} = \bar{\mu}(L_0 b\sqrt{ab})$ and a non-dimensional temperature $\widehat{\theta} = \theta/\theta_c$.

The first numerical example that we performed tries to mimic the experiments conducted for cells [Fig. 6.1(C)]. The effect of the needle is modeled as a horizontal force per unit mass applied on a localized area [Figs. 6.2(A)–(B)]. Our simulations show that the

droplet moves in the direction of the force [Figs. 6.2(C)–(D)], in agreement with the behavior observed in cells [123]. The applied load produces vertical displacements in the solid, as it would be expected in a material with a nonzero Poisson ratio [Figs. 6.2(G)–(H)]. This results in the rotation of the contact lines, that is, the solid deformation produces different apparent contact angles at the two contact lines, leading to an imbalance of horizontal forces [Figs. 6.2(I)–(J)].

From the velocity plots in Fig. 6.3 we can see the different behavior depending on the direction of the applied force. Pulling induces increasing velocities of the droplet as the contact line approaches the region of the applied force, but ultimately traps the droplet in the loaded area [Figs. 6.3(A) and (C)]. In contrast, pushing repels the droplet monotonically, albeit with a time-decreasing velocity [Figs. 6.3(B) and (D)]. In all cases, the droplet velocity is smaller as the Poisson ratio decreases – indeed, the droplet remains immobile if the Poisson ratio is zero.

We also carried out 3D simulations of tensotaxis. In the left column of Fig. 6.4, we present the 3D analogue of the needle experiment in Fig. 6.1(C). In the right column, we show a system with two droplets of different size, each "pushed" toward the other by the action of a localized force [Fig. 6.4(D)]. As the droplets approach each other, they eventually coalesce [Fig. 6.4(E)] and quickly readjust into a single droplet, trapped by the two applied forces of opposite sign [Fig. 6.4(F)]. Note that the presence of multiple droplets increases the complexity of the problem, as we must consider their mechanical interactions through the deformable substrate, as well as through the fluid domain.

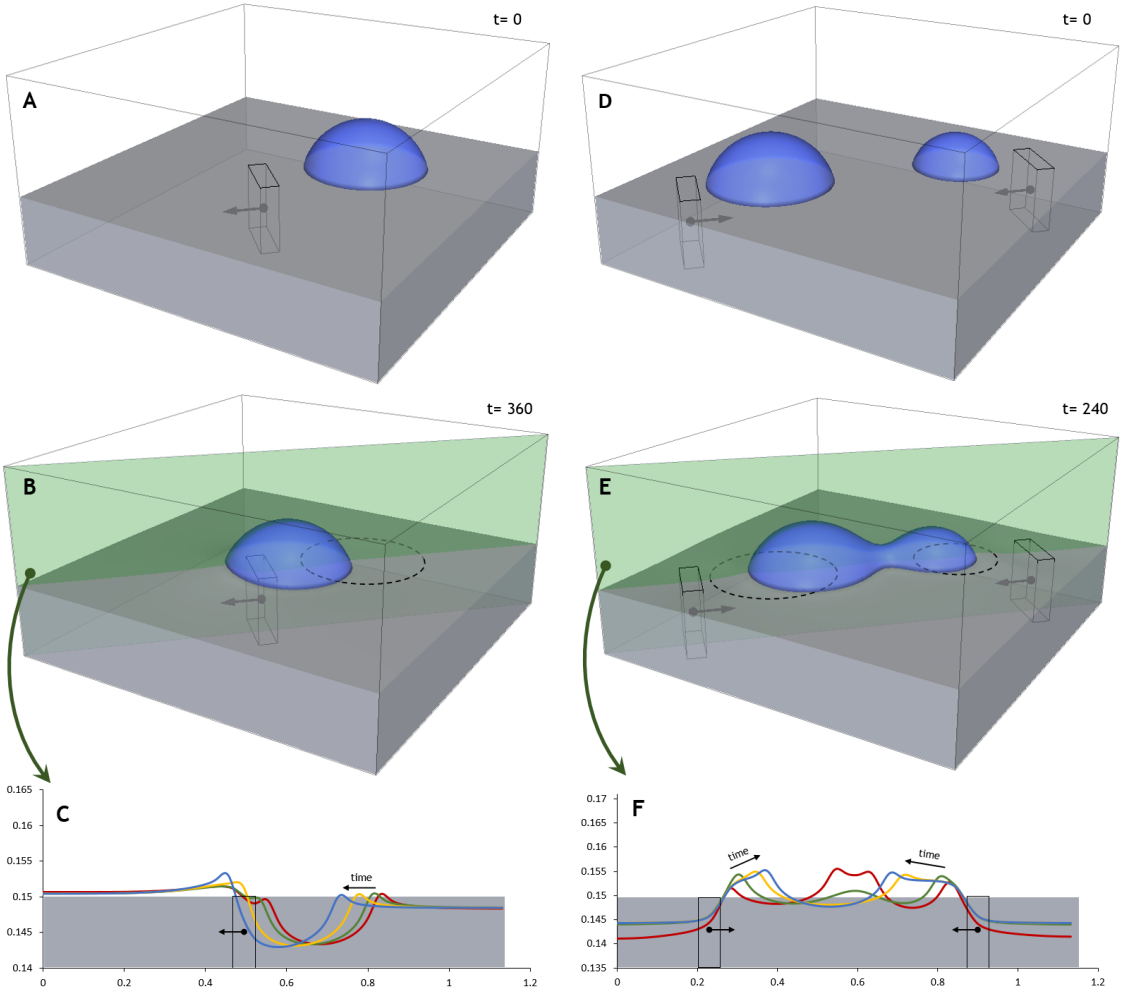

Figure 6.4: Three-dimensional droplet motion triggered by tensotaxis. (Left column) 3D analogue of the needle experiment in Fig. 6.1(C). (Right column) Droplet coalescence induced by tensotaxis. (A) A liquid droplet is deposited on a deformable substrate. A horizontal force is applied at the center of the substrate. (B) The droplet moves in the direction of the applied force. (D) Two forces of the same magnitude are applied on the substrate, pushing the droplets towards the center of the domain. (E) When the droplets are sufficiently close, capillary forces promote coalescence of the two droplets. The black, dashed line indicates the initial position of the droplet. (C) and (F) Vertical displacement of the solid–liquid interface at the diagonal plane [green color in panels (B) and (E)] at different times. In both experiments the computational domain $\Omega = [0, 0.8] \times [0, 0.8] \times [0, 0.4]$ is discretized with $80 \times 80 \times 40$ $\mathcal{C}^1$-quadratic elements. We have adopted $\nu = 0.45$, $\widehat{\mu} = 1/200$, $\widehat{\gamma} = 1/50$, $\widehat{E} = 0.7554$, $\widehat{\theta} = 0.39$, and $\alpha = 75°$. The load that triggers droplet motion is a body force per unit mass of value $\left|\widehat{\boldsymbol{f}}^s\right| = 1.376$ and $\left|\widehat{\boldsymbol{f}}^s\right| = 2.7519$ for the left and right columns, respectively.

6.5 Contributions and open lines for research

The most significant contributions of this work, which has been published as a research paper in [26], can be summarized in the following points:

- We have proposed a nonlinear coupled model of fluid–structure interaction to elucidate the physics of droplet tensotaxis. Adopting a Saint Venant–Kirchhoff model for the solid allows us to consider geometric nonlinearities with a linear material response and thus, avoid a situation with simultaneous tensotaxis and durotaxis.
- We have shown that simple liquid droplets on soft substrates undergo tensotaxis, with a similar behavior than the one observed in cells.
- Our numerical experiments illustrate the ability of the phase-field methodology to simulate complex scenarios of tensotaxis in 3D that involve droplet motion, coalescence and trapping. We have also revealed the key role of Poisson's ratio in tensotaxis.

The main open ideas derived from this work are:

- Validating our model with experimental data.
- In future research, it would be interesting to study in more detail how the presence of other droplets in the surrounding substrate may alter droplet motion driven by tensotaxis.

Chapter 7

Interaction of two-component immiscible fluids and hyperelastic structures.

7.1 Introduction

The FSI models proposed so far describe the physics of single-component two-phase flows interacting with hyperelastic structures. However, there are a number of physical and engineering problems in which the fluid is not formed by phases of the same component. It is the case, for example, of gas injection for oil recovering, fuel sprays in combustion processes, air-water flows, etc. For modeling this kind of problems, we propose a computational model that couples nonlinear hyperelastic solids with two–component immiscible fluids described by the Navier–Stokes–Cahn–Hilliard equations.

We use this theory to simulate different elastocapillary phenomena [147, 160], that is, how capillary forces at fluid–fluid interfaces deform solids. Elastocapillarity, can be observed, for example, when water interacts with hair and other flexible fibers, which tend to assemble into bundles [18,62,63]. Another example can be found in our organism, where capillary forces may cause atelectasis [115], that is, the complete or partial collapse of the pulmonary alveoli. However, it is in micro and nanotechnologies, where the effect of elastocapillary forces is sparking greatest interest. Understanding elastocapillarity is essential for the design of new materials and devices at small scales. Capillary forces can damage microelectromechanical structures [143, 175] and carbon nanotube carpets [38], but, under control, they can be used as a fabrication technique to deform straight pillars and build complex and robust 3D geometries at the micrometer and nanometer scales [54, 177]. A numerical method capable of capturing the physics behind elastocapillary phenomena could become a useful tool for a better design of microfabricated products.

7.2 Governing equations

In our model, the behavior of the structure will be governed by the momentum balance equation, which has been previously presented in Section 5.2 (see also [28]). On the other hand, the dynamics of the fluid system is governed by the Navier–Stokes–Cahn–Hilliard equations, which describe the motion of two immiscible and incompressible fluids with matched density and viscosity. The ALE form of the NSCH equations can be written as follows,

$$\nabla \cdot \boldsymbol{v} = 0, \tag{7.2.1a}$$

$$\rho \left(\left. \frac{\partial \boldsymbol{v}}{\partial t} \right|_{\widehat{x}} + (\boldsymbol{v} - \widehat{\boldsymbol{v}}) \cdot \nabla \boldsymbol{v} \right) - \nabla \cdot \boldsymbol{\sigma}^f - \rho \boldsymbol{f} = 0, \tag{7.2.1b}$$

$$\left. \frac{\partial \varphi}{\partial t} \right|_{\widehat{x}} + (\boldsymbol{v} - \widehat{\boldsymbol{v}}) \cdot \nabla \varphi - \nabla \cdot \left(M_\varphi \gamma_f \nabla \left(\frac{1}{\epsilon} W'_\varphi - \epsilon \Delta \varphi \right) \right) = 0, \tag{7.2.1c}$$

where $\widehat{\boldsymbol{v}}$ is the velocity of the fluid domain [8], ρ is the fluid density that we consider to be constant, $\boldsymbol{f}$ represents body forces per unit mass and $\varphi \in [-1, 1]$ is the phase–field variable. W_φ is a double–well potential, which we define as $W_\varphi = \left(\varphi^2 - 1\right)^2 / 4$. The constant γ_f denotes the surface tension and ϵ is the interface thickness. M_φ represents the mobility, which is assumed to be constant for the examples presented herein. The fluid Cauchy stress tensor $\boldsymbol{\sigma}^f$ is given by $\boldsymbol{\sigma}^f = \boldsymbol{\tau} - p\boldsymbol{I} - \gamma_f \epsilon \nabla\varphi \otimes \nabla\varphi$, where $\otimes$ denotes the usual vector outer product, p represents the mechanical pressure and $\boldsymbol{\tau}$ is the viscous stress tensor. For incompressible Newtonian fluids, $\boldsymbol{\tau}$ is defined as $\boldsymbol{\tau} = \bar{\mu} \left(\nabla \boldsymbol{v} + \nabla^T \boldsymbol{v} \right)$, where $\bar{\mu}$ is the viscosity coefficient, which is assumed to be constant.

In the fluid mechanics problem we focus on solid–wall boundary conditions, by setting the velocity to a given value. Additionally, and with the purpose of attaining well–posedness in the NSCH system, we enforce the following boundary conditions on the phase–field variable,

$$\nabla\varphi \cdot \boldsymbol{n}^f = |\nabla\varphi| \cos(\theta_c) \qquad \text{on} \quad \Gamma_t, \tag{7.2.2a}$$

$$\nabla\varphi \cdot \boldsymbol{n}^f = 0 \qquad \text{on} \quad \Gamma_t^f, \tag{7.2.2b}$$

and

$$M_\varphi \gamma_f \nabla \left(\frac{1}{\epsilon} W'_\varphi - \epsilon \Delta \varphi \right) \cdot \boldsymbol{n}^f = 0 \quad \text{on} \quad \Gamma_t^f \cup \Gamma_t, \tag{7.2.3}$$

where $\boldsymbol{n}^f$ is the unit outward normal to the fluid boundary and θ_c denotes the contact angle between the fluid–fluid interface and the solid, measured in the phase of value $\varphi = 1$. The imposition of boundary condition (7.2.2) can be notably simplified by introducing in our problem a new variable $\Upsilon = \Delta\varphi$. This implies that the phase–field equation (7.2.1c)

is split into two lower–order equations, allowing to use the classical finite element method for the spatial discretization of the problem.

7.3 Numerical formulation

7.3.1 Semidiscrete formulation

We use NURBS–based isogeometric analysis for the spatial discretization of our problem. Additionally, in order to stabilize the NSCH equations, we will make use of the VMS method and split the weighting and the trial solution spaces corresponding to the pressure and the velocity field into a coarse and a fine scale subspaces. Let H^1 be the Sobolev space of square–integrable functions with square–integrable first derivatives. We will denote by $\mathcal{X}_h^\varphi$ and $\mathcal{X}_h^\Upsilon$ a finite-dimensional aproximation of the trial solution spaces for Υ and φ, respectively. $\mathcal{X}_h^\varphi$ and $\mathcal{X}_h^\Upsilon$ will be subsets of $H^1(\Omega_t^f)$. Let also $\mathcal{Y}_h^\varphi$ and $\mathcal{Y}_h^\Upsilon$ be the corresponding finite–dimensional weigthing function spaces. $\mathcal{Y}_h^\varphi$ and $\mathcal{Y}_h^\Upsilon$ will be identical to $\mathcal{X}_h^\varphi$ and $\mathcal{X}_h^\Upsilon$, respectively. Analogously, let us define a finite–dimensional trial solution space for the coarse scales of $\boldsymbol{v}$ and p, which we will denote by $\mathcal{X}_h^v$ and $\mathcal{X}_h^p$, respectively. $\mathcal{X}_h^v$ will be a subset of $H^1(\Omega_t^f)$ whose members satisfy all Dirichlet boundary conditions. The weighting function space for p, $\mathcal{Y}_h^p$ will be indentical to $\mathcal{X}_h^p$. Let $\mathcal{X}_h^s$ and $\mathcal{V}_h^m$ be a finite-dimensional aproximation of the trial solution spaces for $\boldsymbol{u}$ and $\boldsymbol{u}^m$. $\mathcal{X}_h^s$ and $\mathcal{V}_h^m$ are subsets of $H^1(\Omega_0^s)$ and $H^1(\Omega_{\tilde{t}}^f)$, respectively, whose members satisfy all Dirichlet boundary conditions; see Section 5.3 and [28] for the definition of $\tilde{t}$. Finally, we denote by $\mathcal{Y}_h^s$ and $\mathcal{W}_h^m$ the corresponding finite–dimensional weigthing function spaces, which will be identical to $\mathcal{X}_h^s$ and $\mathcal{V}_h^m$, except that all restrictions on the Dirichlet boundary are homogeneous.

With the previous considerations, we can approximate our FSI problem by the following variational formulation over the finite element spaces: Find $p_h \in \mathcal{X}_h^p$, $\boldsymbol{v}_h \in \mathcal{X}_h^v$, $\varphi_h \in \mathcal{X}_h^\varphi$, $\Upsilon_h \in \mathcal{X}_h^\Upsilon$, $\boldsymbol{u}_h \in \mathcal{X}_h^s$ and $\boldsymbol{u}_h^m \in \mathcal{V}_h^m$ such that $\forall w_h^1 \in \mathcal{Y}_h^p$, $\boldsymbol{w}_h^2 \in \mathcal{Y}_h^v$, $w_h^3 \in \mathcal{Y}_h^\varphi$, $w_h^4 \in \mathcal{Y}_h^\Upsilon$, $\boldsymbol{w}_h^s \in \mathcal{Y}^s{}_h$ and $\boldsymbol{w}_h^m \in \mathcal{W}_h^m$,

$$\begin{aligned} &B_{MS}^f(w_h^1, \boldsymbol{w}_h^2, w_h^3, w_h^4, p_h, \boldsymbol{v}_h, \varphi_h, \Upsilon_h; \widehat{\boldsymbol{v}_h}) + B^s(\boldsymbol{w}_h^s, \boldsymbol{u}_h) \\ &+ B^m(\boldsymbol{w}_h^m, \boldsymbol{u}_h^m) = F^f(\boldsymbol{w}_h^2) + F^s(\boldsymbol{w}_h^s), \end{aligned} \tag{7.3.4}$$

where B^s and F^s consitute the weak form of the solid equations and have been defined in Section 5.3. B^m denotes the weak form of the mesh motion problem (see Section 5.3).

Finally, B^f_{MS} stands for the stabilized weak form of the fluid problem, i.e.,

$$
\begin{aligned}
&B^f_{MS}(w^1_h, \boldsymbol{w}^2_h, w^3_h, w^4_h, p_h, \boldsymbol{v}_h, \varphi_h, \Upsilon_h; \widehat{\boldsymbol{v}_h}) = \int_{\Omega^f_t} w^1_h \nabla\cdot\boldsymbol{v}_h \mathrm{d}\Omega^f_t \\
&+ \int_{\Omega^f_t} \boldsymbol{w}^2_h \cdot \rho \left(\left.\frac{\partial \boldsymbol{v}_h}{\partial t}\right|_{\widehat{x}} + (\boldsymbol{v}_h - \widehat{\boldsymbol{v}}_h)\cdot\nabla\boldsymbol{v}_h \right) \mathrm{d}\Omega^f_t + \int_{\Omega^f_t} \nabla \boldsymbol{w}^2_h : \boldsymbol{\sigma}^f_h \mathrm{d}\Omega^f_t \\
&+ \int_{\Omega^f_t} w^3_h \left(\left.\frac{\partial \varphi_h}{\partial t}\right|_{\widehat{x}} + (\boldsymbol{v}_h - \widehat{\boldsymbol{v}}_h)\cdot\nabla\varphi_h \right) \mathrm{d}\Omega^f_t + \int_{\Omega^f_t} \nabla w^3_h \cdot M_\varphi \gamma_f \nabla \left(\frac{1}{\epsilon} W'_\varphi - \epsilon \Upsilon_h \right) \mathrm{d}\Omega^f_t \\
&+ \int_{\Omega^f_t} w^4_h \Upsilon_h \mathrm{d}\Omega^f_t + \int_{\Omega^f_t} \nabla w^4_h \cdot \nabla\varphi_h \mathrm{d}\Omega^f_t - \int_{\Gamma_t} w^4_h |\nabla\varphi_h| \cos(\theta_c) \mathrm{d}\Gamma_t \\
&+ \sum_{e=1}^{n_{el}} \int_{\Omega^{f,e}_t} \tau_{SUPS} \left((\boldsymbol{v}_h - \widehat{\boldsymbol{v}}_h)\cdot\nabla\boldsymbol{w}^2_h + \frac{\nabla w^1_h}{\rho} \right) \cdot \boldsymbol{r}_M \mathrm{d}\Omega^f_t \\
&+ \sum_{e=1}^{n_{el}} \int_{\Omega^{f,e}_t} \nu_{LSIC} \rho \nabla\cdot\boldsymbol{w}^2_h r_C \mathrm{d}\Omega^f_t - \sum_{e=1}^{n_{el}} \int_{\Omega^{f,e}_t} \tau_{SUPS} \boldsymbol{w}^2_h \cdot (\boldsymbol{r}_M \cdot \nabla\boldsymbol{v}_h) \, \mathrm{d}\Omega^f_t \\
&- \sum_{e=1}^{n_{el}} \int_{\Omega^{f,e}_t} \frac{\nabla \boldsymbol{w}^2_h}{\rho} : (\tau_{SUPS}\boldsymbol{r}_M \otimes \tau_{SUPS}\boldsymbol{r}_M) \, \mathrm{d}\Omega^f_t - \sum_{e=1}^{n_{el}} \int_{\Omega^{f,e}_t} \frac{\tau_{SUPS}}{\rho} w^3_h \boldsymbol{r}_M \cdot \nabla\varphi_h \mathrm{d}\Omega^f_t
\end{aligned}
\tag{7.3.5}
$$

and

$$
F^f(\boldsymbol{w}^2_h) = \int_{\Omega^f_t} \boldsymbol{w}^2_h \cdot \rho\, \boldsymbol{f} \mathrm{d}\Omega^f_t. \tag{7.3.6}
$$

Here, n_{el} is the total number of elements on the fluid mesh and $\Omega^{f,e}_t$ the region of the physical space occupied by element e at time t. In Eq. (7.3.5), $\boldsymbol{r}_M$ and r_C are given by

$$
\boldsymbol{r}_M = \rho \left(\left.\frac{\partial \boldsymbol{v}_h}{\partial t}\right|_{\widehat{x}} + (\boldsymbol{v}_h - \widehat{\boldsymbol{v}}_h)\cdot\nabla\boldsymbol{v}_h \right) - \nabla\cdot\boldsymbol{\sigma}^f_h - \rho\boldsymbol{f}, \tag{7.3.7a}
$$

$$
r_C = \nabla\cdot\boldsymbol{v}_h, \tag{7.3.7b}
$$

where $\boldsymbol{\sigma}^f_h = \bar{\mu}\left(\nabla\boldsymbol{v}_h + \nabla^T\boldsymbol{v}_h\right) - p_h\boldsymbol{I} - \gamma_f\epsilon\nabla\varphi_h\otimes\nabla\varphi_h$. For the stabilization parameters τ_{SUPS} and ν_{LSIC} we use the expressions

$$
\tau_{SUPS} = \left(\frac{4}{\Delta t^2} + (\boldsymbol{v}_h - \widehat{\boldsymbol{v}}_h)\cdot\boldsymbol{G}\,(\boldsymbol{v}_h - \widehat{\boldsymbol{v}}_h) + C_I \nu^2 \boldsymbol{G} : \boldsymbol{G} \right)^{-1/2}, \tag{7.3.8a}
$$

$$
\nu_{LSIC} = \left(\mathrm{tr}(\boldsymbol{G})\, \tau_{SUPS} \right)^{-1}, \tag{7.3.8b}
$$

where Δt is, in a time-discrete context, the time step; $C_I = 1/12$ is a positive constant; ν is the kinematic viscosity; and $\boldsymbol{G}$ denotes the element metric tensor [15].

In order to enforce the compatibility conditions at the fluid-structure interface and taking into account that we work with matching discretizations, we define a unique set of both trial an test functions for the velocity at the fluid–structure interface. This leads to strong (pointwise) satisfaction of the kinematics condition and weak satisfaction of the

traction compatibility condition. The reader is referred to [28] for more details on the numerical formulation of the FSI problem.

7.3.2 Time discretization and numerical implementation

For the time integration of the FSI problem, we adopt the generalized-α method, which was originally proposed by Chung and Hulbert [40] for the equations of structural dynamics. Subsequently, this technique was extended to the equations of fluid mechanics [105] and successfully applied to fluid-structure interaction problems (see, for instance, [8, 27, 32]). The nonlinear system of equations is solved using a Newton–Raphson iteration procedure.

7.4 Numerical examples

7.4.1 Coalescence of droplets

The NSCH model without solid is used to simulate the 2D coalescence of two water droplets (see Fig. 7.1 for a sucession of isocontour plots of the interface along the coalescence process). During the merger of droplets, a meniscus is formed at the confluence region. Experimental [1] and theoretical results [64] have shown that the radius of the meniscus $r(t)$ (defined as indicated in the bottom-right inset of Fig. 7.2) scales with the square root of time t, i.e., $r(t) \propto \sqrt{t}$, for $r \gtrsim 0.03R$, where R is the droplet radius. Fig. 7.2 shows the time evolution of r obtained from the simulation (red squares) and the function $g(t) = \chi\sqrt{t}$ (blue solid line), where χ is a constant of value $\chi = 22.9$. Note that the initial time in Fig. 7.2, that is, $t = 0.0$, does not refer to the initial time of the simulation, but the instant when the interfaces of both droplets come into contact. The diagram illustrates a good agreement between both functions, showing that our model reproduces the initial dynamics of merging droplets.

7.4.2 Static wetting on soft substrates

The static equilibrium shape of a small liquid droplet on a flat and rigid substrate is well understood. The droplet's shape is a spherical cap which contacts the solid with an equilibrium contact angle $\theta_E = \arccos[(\gamma_{SG} - \gamma_{SL})/\gamma_f]$ given by the Young-Dupré equation [50]. In the contact angle equation, γ_{SG} and γ_{SL} are the surface tension at the solid-gas and at the solid-liquid interface, respectively. When the solid is sufficiently compliant or the droplet sufficiently small for the elastocapillary length scale $l_{ec} = \gamma_f/E$ to be comparable to the droplet radius, Young–Dupré's equation breaks down. The excess Laplace pressure in the interior of the droplet creates a dimple in the wet area and capillary forces produce a ridge at the contact line. To show that our FSI model can successfully predict this phenomenon, we reproduce one of the experiments reported in [158]. In

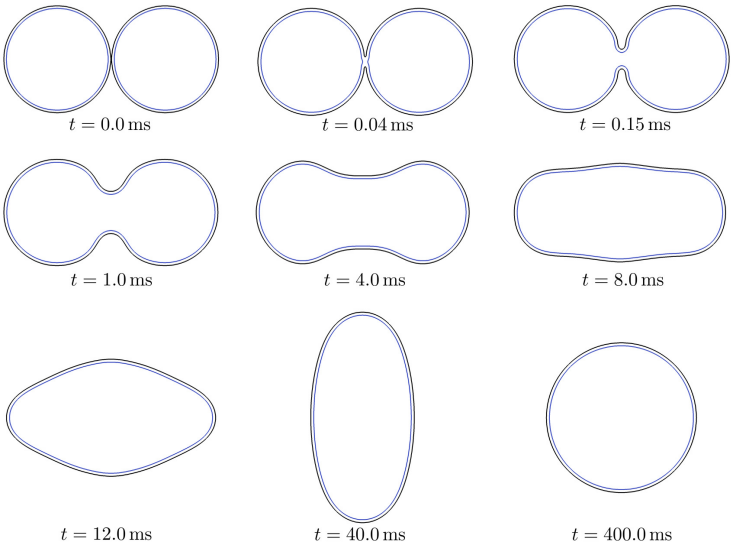

Figure 7.1: Time evolution of the interface shown by isocontour lines of φ. We plot $\varphi = 0.7$ (blue) and $\varphi = -0.7$ (black). The computational domain (not shown) is $\Omega = (0, 1.5L) \times (0, L)$, where $L = 1.0\,\mathrm{cm}$. The mesh is composed of 256×384 $\mathcal{C}^1$-quadratic elements. We imposed periodic boundary conditions in both directions. The initial configuration consisted of two water droplets of radius $R = 0.2\,\mathrm{cm}$ centered at $(0.543L\,, 0.5L)$ and $(0.957L, 0.5L)$, respectively. The physical parameters correspond to water at 20°C, i.e., $\gamma_f = 72.86\,m\mathrm{N/m}$, $\mu = 1.0\,m\mathrm{Pa\,s}$ and $\rho = 1.0\,\mathrm{g/cm^3}$. The thickness of the interface and the mobility were set to $\epsilon = 3.9\,10^{-3}\,\mathrm{cm}$, and $M_\varphi = 10^{-3}\,\mathrm{cm^3 s/g}$, respectively.

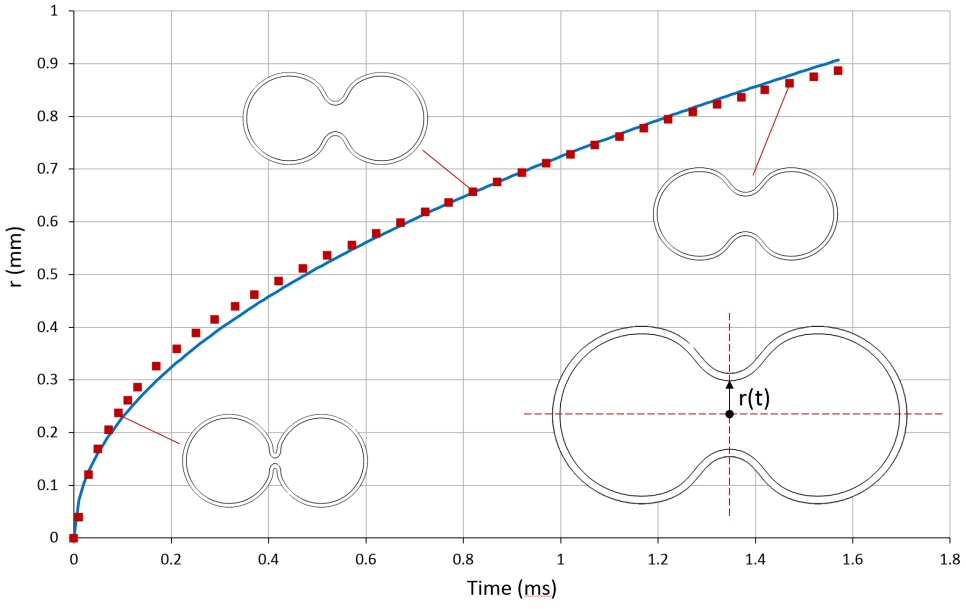

Figure 7.2: Time evolution of the meniscus radius r obtained from the computation (red points) and trend line given by $g(t) = \chi\sqrt{t}$ with $\chi = 22.9$ (blue line). The initial time on the horizontal axis refers to the instant when the interfaces of both droplets come into contact.

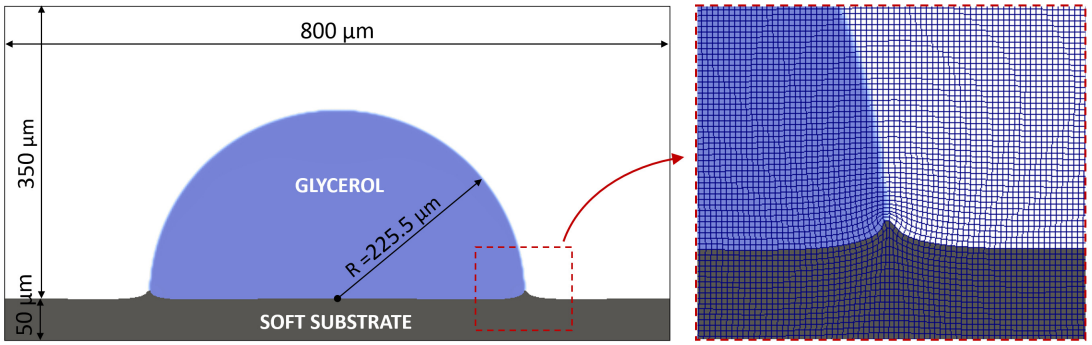

(a) Stationary configuration of the fluid–solid system

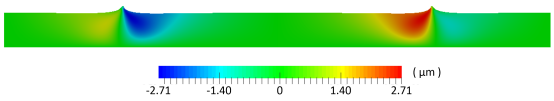

(b) Solid displacements in horizontal direction

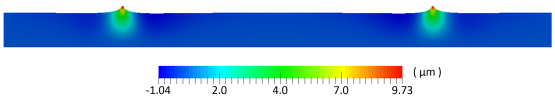

(c) Solid displacements in vertical direction

Figure 7.3: Glycerol droplet deposited on a soft substrate. (a) Stationary configuration (left) and detail of the contact line region after deformation (right). (b), (c) solid displacements in the horizontal and vertical directions, respectively. We use a uniform mesh of 400×200 quadratic elements. On the left, right and lower boundaries of the computational domain, we impose zero velocity in the normal direction. On the upper boundary, zero velocity is imposed in both directions. We adopted the values of surface tension reported in [158], i.e., $\gamma_f = 46.0\, m\mathrm{N/m}$, $\gamma_{SA} = 31\, m\mathrm{N/m}$ and $\gamma_{SL} = 36\, m\mathrm{N/m}$. For the viscosity and density parameters, we use values for glycerol: $\mu = 1412.0\, m\mathrm{Pa\,s}$ and $\rho = 1.26\, p\mathrm{g}/\mu\mathrm{m}^3$. We took $\epsilon = 2.0\, \mu\mathrm{m}$ and $M_\varphi = 0.1\, \mu\mathrm{m}^3\mu\mathrm{s}/p\mathrm{g}$. The parameters for the solid correspond to a silicone gel with $E = 3.0\, k\mathrm{Pa}$, $\nu^s = 0.499$ and $\rho^s = 12.6\, p\mathrm{g}/\mu\mathrm{m}^3$.

particular, a glycerol droplet of radius $R = 225.5\, \mu\mathrm{m}$ is deposited on a soft substrate with Young's modulus $E = 3.0\, k\mathrm{Pa}$. The droplet deforms the substrate as shown on the left–hand side of Fig. 7.3(a). The contact angle θ_c in the boundary condition (7.2.2) is given by $\theta_E = \arccos[(\gamma_{SG} - \gamma_{SL})/\gamma_f]$, but the solid deformation produces an apparent contact angle (measured with respect to a horizontal line) that is smaller than θ_E. The right–hand side of Fig. 7.3(a) portraits a detailed view of the contact line neighborhood and also shows the mesh in the current configuration. Figs. 7.3(b) and 7.3(c) show, respectively, the substrate's displacements in the horizontal and vertical directions, when equilibrium is reached. To perform a more quantitative analysis, we measured the displacement of the fluid–solid interface close to the contact line and we compared our results with the experimental data reported in [158]; see Fig. 7.4. The experimental results are available only for the stationary configuration (blue dots).

7.4.3 Capillary origami

We use our theory to simulate the spontaneous wrapping of glycerol droplets with elastic membranes. We place a semicircular droplet of radius $R = 146.0\, \mu\mathrm{m}$ on an elastic mem-

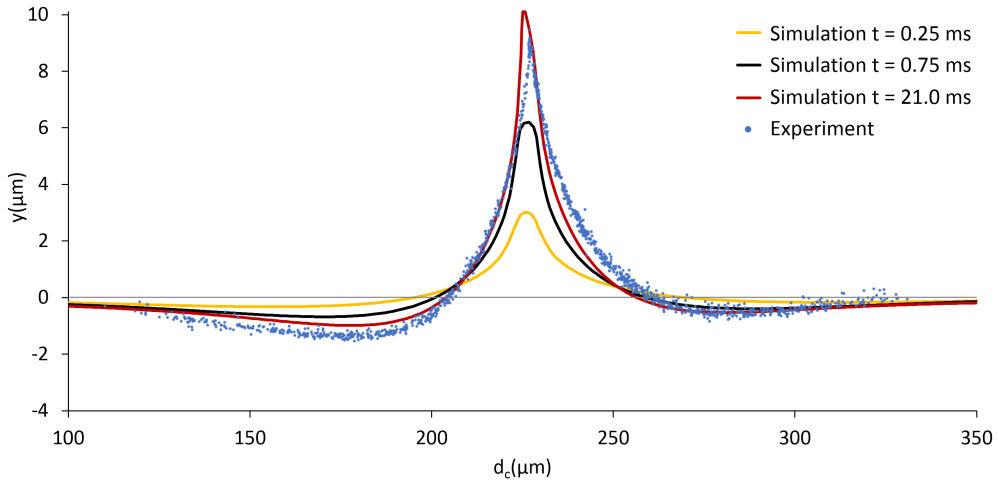

Figure 7.4: Vertical displacements of the fluid–solid interface. d_c in the horizontal axis represents the distance to the center of the droplet. The blue circles are the experimental measurements reported in [158], which represent a stationary configuration. The computational results are reported at $t = 0.25\,ms$ (yellow), $t = 0.75\,ms$ (purple) and $t = 21.0\,ms$ (red), when the solution is considered to be stationary. The horizontal line $y = 0$ corresponds to the fluid–solid interface before deformation.

brane [see Fig. 7.5(a) for the setup of the problem] and we impose different contact angles θ_c along the fluid–structure interface. In particular, we analyze three cases, $\theta_c = 60°$, $\theta_c = 90°$ and $\theta_c = 120°$. Figs. 7.5(b), 7.5(c) and 7.5(d) show three different moments of droplet wrapping for $\theta_c = 90°$. In Fig. 7.7 we plot two configurations computed for $\theta_c = 60°$ and $\theta_c = 90°$. The capillary forces are able to deform the thin structure, which gradually wraps the droplet. The configurations adopted by the system differ considerably depending on the contact angle at the fluid–solid interface [see Figs. 7.5(d), 7.7(a) and 7.7(b)]. The results also suggest that droplet encapsulation occurs faster for more wetting fluids. This observation can be used to have better control in the process of self-assembly of micro- and nano-structures. Fig. 7.6 shows the solid mesh in the current configuration and the streamlines at time $t = 0.045\,s$. The fluid–fluid interface is drawn as a black solid line. The flow inside the droplet is predominantly vertical. Outside the droplet, the membrane's motion produces well-defined vortices.

7.4.4 Wetting of elastic micropillars

Wetting of fibrous media has been widely studied due to its importance in natural and engineered systems. However, most of the research focuses on rigid fibers. At small scales, capillary forces outweigh bulk forces and deform fibers significantly, which produces a coupled problem combining elasticity and wetting [63]. Here, we use our FSI model to study quantitatively the deformation of micropillars produced by a fluid–fluid interface. Fig. 7.8(a) shows the setup of our problem. We place a small amount of liquid (blue) between

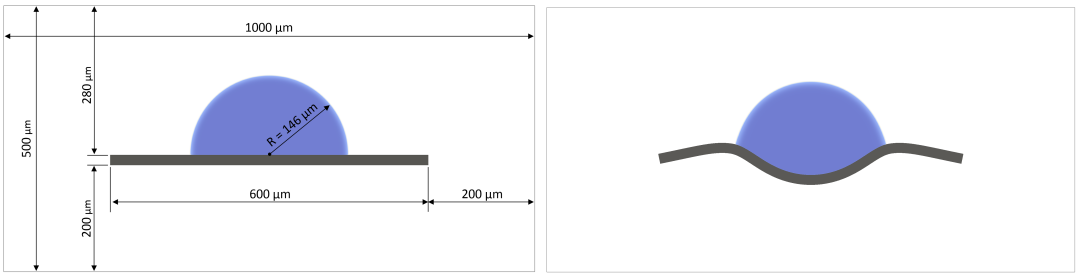

(a) $\theta_c = 90°, t = 0.0\,\mathrm{s}$ (b) $\theta_c = 90°, t = 0.014\,\mathrm{s}$

(c) $\theta_c = 90°, t = 0.075\,\mathrm{s}$ (d) $\theta_c = 90°, t = 0.138\,\mathrm{s}$

Figure 7.5: Capillary origami. (a) Initial condition. A semicircular droplet (blue) is deposited on an elastic membrane (grey). (b), (c) and (d) Current configuration at $t = 0.014\,\mathrm{s}$, $t = 0.075\,\mathrm{s}$ and $t = 0.138\,\mathrm{s}$, respectively. We use a uniform mesh of 200×100 quadratic elements. We impose zero velocity in normal direction on all boundaries. The parameters employed in this computation for the fluid correspond to a glycerol droplet, in particular, $\mu = 1412.0\,m\mathrm{Pa\,s}$, $\gamma_f = 46.0\,m\mathrm{N/m}$, and $\rho = 1.26\,\mathrm{pg}/\mu\mathrm{m}^3$. We take $\epsilon = 5.0\,\mu\mathrm{m}$ and $M_\varphi = 0.1\,\mu\mathrm{m}^3\mu\mathrm{s}/\mathrm{pg}$. For the elastic membrane we adopt $E = 30.0\,k\mathrm{Pa}$, $\nu^s = 0.45$, and $\rho^s = 12.6\,\mathrm{pg}/\mu\mathrm{m}^3$.

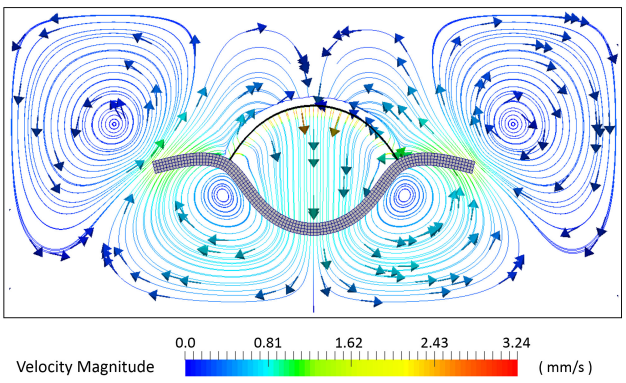

Figure 7.6: Solid mesh and streamlines of the fluid velocity at time $t = 0.045\,\mathrm{s}$ for the capillary origami of Fig. 7.5. The arrows show the direction of the velocity field. The streamlines and the arrows are colored with the velocity magnitude. The interface of the droplet is represented by a black, solid line.

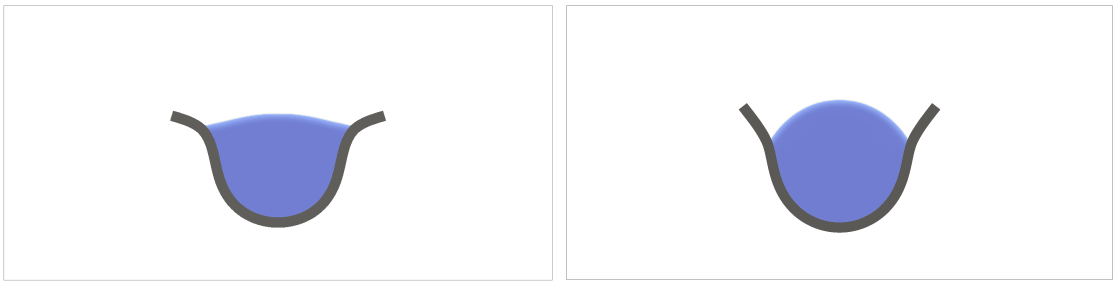

(a) $\theta_c = 60°, t = 0.065\,\mathrm{s}$ (b) $\theta_c = 120°, t = 0.302\,\mathrm{s}$

Figure 7.7: Capillary origami for two different contact angles. (a) Wetting droplet at time $t = 0.065\,\mathrm{s}$. (b) Non–wetting droplet at time $t = 0.302\,\mathrm{s}$.

the two micropillars (grey) and let capillary forces deform the fibers. The micropillars are clamped at the bottom by preventing the displacements in horizontal and vertical directions. Fig. 7.8(b) shows how surface tension deforms the fibers bringing them close to each other, which, in turn, produces the rise of the liquid.

We observe that, in addition to the obvious parameters controlling the dynamics (the geometry and the mechanical properties of the fibers as well as the physical properties of the fluid) the volume of liquid placed between the micropillars plays a key role. We quantified the volume using the height of the liquid column as shown in Fig. 7.8; see the plots on the left-hand side. The left, middle and right columns correspond, respectively, to $h = 200.0\,\mu$m, $h = 300.0\,\mu$m and $h = 400.0\,\mu$m. It may be observed that for a given geometrical configuration of the fibers, larger volumes of liquid produce larger deformations. In addition, the dynamics of the process seems to be faster for larger volumes of liquid.

7.4.5 Three dimensional wrapping of a liquid droplet

Here, we study the three dimensional wrapping of a liquid droplet with an elastic membrane. Fig. 7.9(a) shows the initial configuration of the problem, which consists of a droplet of radius $R = 146.0\,\mu$m (blue) deposited on an membrane of thickness $20.0\,\mu$m (grey) that covers an entire horizontal plane of the computational domain. The elastic membrame is clampled to the lateral boundaries, where we have prevented the displacements in normal and vertical directions. We carry out this simulation assuming that the droplet is a wetting liquid that forms a contact angle of $\theta_c = 60°$ with the solid membrane. The left panels in Fig. 7.9 show an upper view of the problem. The right panels are vertically flipped, so that we can easily observe the membrane's deformation. The surface tension at the interface folds the solid, resulting in the partial wrapping of the droplet [see Fig. 7.9(b)]. The initial square shape of the elastic membrane leads to a non–axisymmetric deformation of the structure and triggers the formation of wrinkles [Fig. 7.9(c)]. Different values of surface tension and solid stiffness should result in different patterns of the

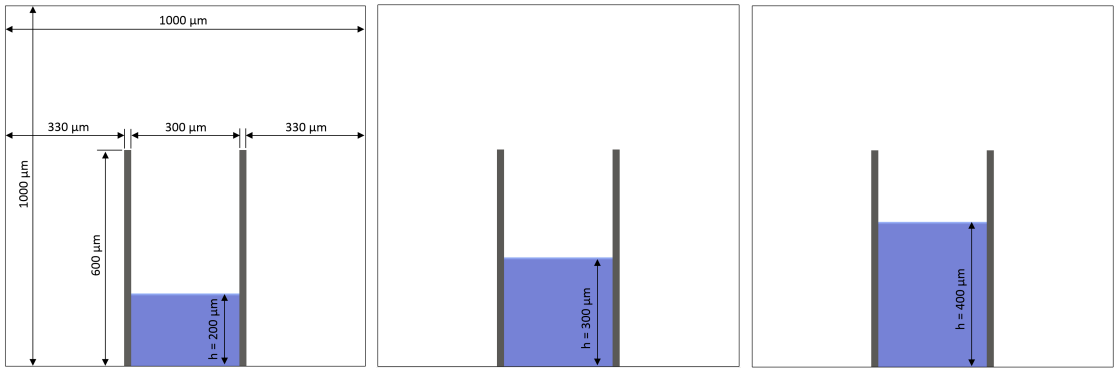

(a) $t = 0.0\,\mathrm{s}$ (b) $t = 0.0\,\mathrm{s}$ (c) $t = 0.0\,\mathrm{s}$

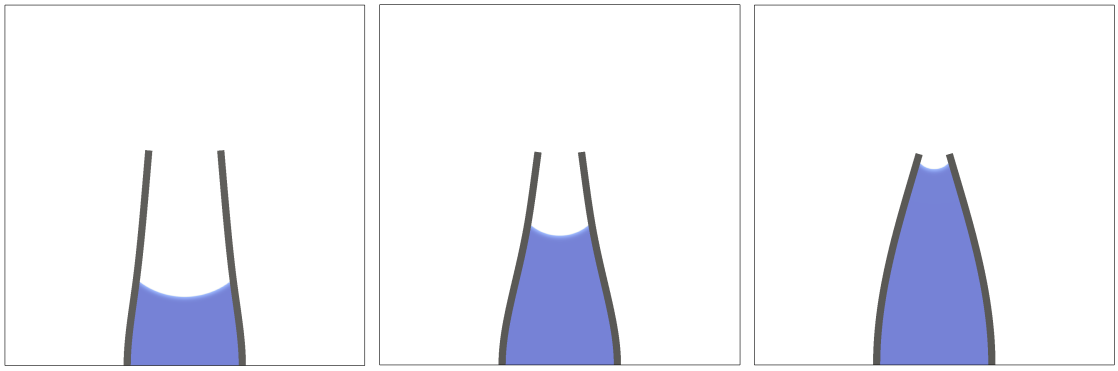

(d) $t = 0.3225\,\mathrm{s}$ (e) $t = 0.2975\,\mathrm{s}$ (f) $t = 0.15075\,\mathrm{s}$

Figure 7.8: Wetting of elastic micropillars. The left, middle and right columns correspond, respectively, to $h = 200.0\,\mu\mathrm{m}$, $h = 300.0\,\mu\mathrm{m}$ and $h = 400.0\,\mu\mathrm{m}$. We impose zero velocity in normal direction on all the boundaries, except on the upper one, where we only enforce a stress–free condition. We use a wetting liquid with contact angle $\theta_c = 60°$. The parameters are $\mu = 1412.0\,m\mathrm{Pa\,s}$, $\gamma_f = 46.0\,m\mathrm{N/m}$, $\epsilon = 2.5\,\mu\mathrm{m}$, $\rho = 1.26\,p\mathrm{g}/\mu\mathrm{m}^3$, $M_\varphi = 0.1\,\mu\mathrm{m}^3\mu\mathrm{s}/p\mathrm{g}$, $E = 320.0\,k\mathrm{Pa}$, $\nu^s = 0.45$ and $\rho^s = 12.6\,p\mathrm{g}/\mu\mathrm{m}^3$.

wrinkling instability [37, 98].

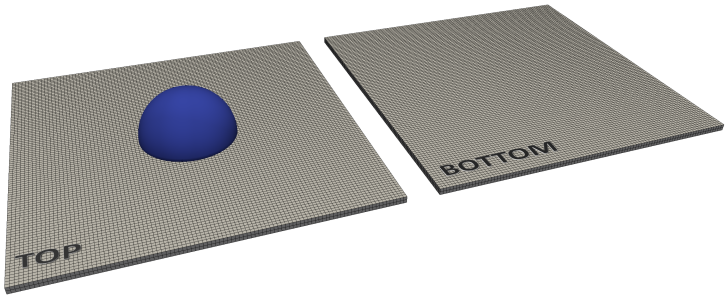

(a) $t = 0.0\,\mathrm{s}$

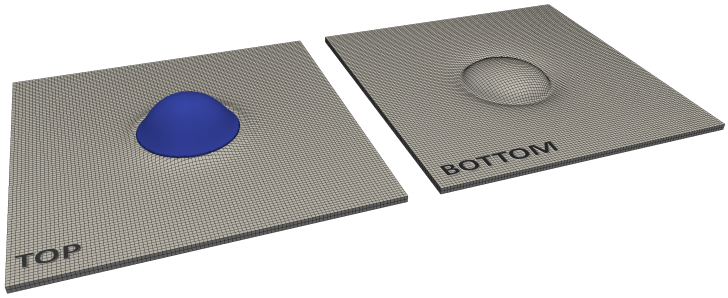

(b) $t = 0.00625\,\mathrm{s}$

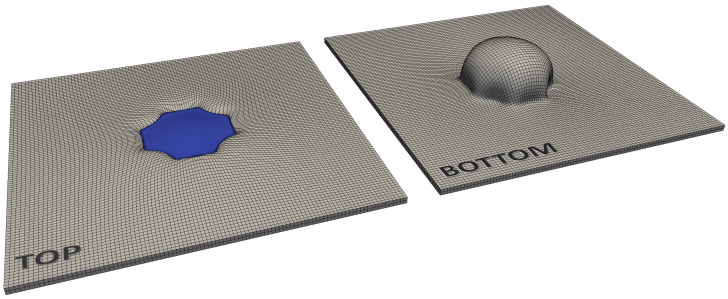

(c) $t = 0.125\,\mathrm{s}$

Figure 7.9: Top view (left panels) and bottom view (right panels) of the three dimensional wrapping of a liquid droplet. (a) A hemispherical droplet is deposited on an elastic membrane that is clamped to the lateral boundaries of the computational domain. (b) Capillary forces fold the membrane and lead to the partial wrapping of the liquid droplet. (c) A wrinkling instability is developed on the structure, triggered by the non–axisymmetric shape of the membrane. Note that we are only representing the solid domain and one of the fluid phases. The computational domain (not shown) is $\Omega = (0, L)\times(0, L)\times(0, 0.5L)$, where $L = 1$ mm. We used a uniform mesh with $100\times100\times50$ quadratic elements. We impose zero velocity in normal direction on all the boundaries as well as zero vertical velocity on the lateral boundaries. The parameters correspond to a glycerol droplet: $\mu = 1412.0\,m\mathrm{Pa\,s}$, $\gamma_f = 46.0\,m\mathrm{N/m}$, $\rho = 1.26\,pg/\mu\mathrm{m}^3$. We take $\epsilon = 10.0\,\mu\mathrm{m}$ and $M_\varphi = 0.1\,\mu\mathrm{m}^3, \mu\mathrm{s}/pg$. For the membrane we employ $E = 0.6\,k\mathrm{Pa}$, $\nu^s = 0.45$, and $\rho^s = 12.6\,pg/\mu\mathrm{m}^3$.

7.5 Contributions and open lines for research

The most significant contributions of this work, which has been published as a research paper in [28], can be summarized in the following points:

- We have proposed a computational method for three–dimensional, dynamic simulation of elastocapillarity, in which the fluid is a two-component, immiscible flow with surface tension.
- We have shown the viability of our theoretical framework and numerical algorithm by solving several examples of elastocapillary phenomena in two and three dimensions such as, capillary origami, the static wetting of soft substrates and the deformation of micropillars.
- The model was validated by comparing the numerical results with experimental data from the literature.

The main open ideas derived from this work are:

- In future research, it would be interesting to study capillary origamis with a model that accounts for evaporation of the droplet.
- The proposed framework could also be extended to model capillary fracture [22]. This can be accomplished by coupling the current model with a fracture theory.
- Using divergence-conforming B-splines for the NSCH equations with solid would allow to solve the FSI problem without stabilization.

Chapter 8

Collaboration in other works

8.1 Air-blast fluid-structure interaction

During my doctoral studies, I had the opportunity to start a close and valuable collaboration with the group of Professor Yuri Bazilevs, at University of California, San Diego. The purpose of this joint effort is to develop a new model for air-blast fluid-structure interaction phenomena and, so far, has resulted in the publication of the research paper [13]. This kind of FSI problems poses important computational challenges as they require an accurate and robust numerical formulation for the fluid in order to capture air flow in the regime of high Reynolds and Mach numbers. Also, the solid should be able to undergo large inelastic deformations as well as disintegration into fragments, which typically occurs during explosions. The latter will be the reason why we propose a immersed methodology (see, for instance, [32, 35, 109, 200]) for our FSI problem, instead of a moving-mesh technique, such as the Arbitrary Lagrangian-Eulerian [57, 58, 101] or the Space-Time [15, 16, 164, 166] approaches. The advantage of moving-mesh methods over immersed technologies emanates from their higher accuracy near the fluid-structure interfaces. However, in this problem, where big topological changes are expected, an ALE approach would translate into highly distorted meshes. Remeshing procedures would be required, increasing the computational cost and introducing inaccuracies. For this reason, we adopt an immersed approach where the solid can move freely on top of a background mesh.

In our method, the compressible Navier-Stokes equations are coupled with a large-deformation inelastic solid. The fluid equations are written in terms of the pressure primitive variables which are compatible with the solid degrees of freedom. A Streamline-Upwind/Petrov-Galerkin method or SUPG [25] is adopted for enhancing the stability of the fluid problem. Additionally, in order to capture properly the discontinuities of the flow, such as shocks, we use a residual- and solution gradient-based discontinuity capturing operator [181]. The balance equations for both, the solid structure and the fluid, are

written in the weak form on the current configuration, and the compatibility conditions are imposed at a fully continuous level. We employ two different discretizations for the FSI problem. The foreground solid is discretized using a Reproducing-Kernel Particle Method (RKPM), which is a Meshfree technique that can handle with relative simplicity fragmentation scenarios. The foreground discretization moves with the solid material particles, and allows to track the solid current position, and carry out numerical quadratures for the solid terms in the coupled FSI problem. An Eulerian discretization based on Isogeometric Analysis is adopted for the background. Both fluid and structural quantities, are solved on the background grid, that is, the NURBS basis functions from the background will be used to approximate the unknowns of the coupled problem and for the exchange of information between the fluid and the structure. The FSI problem is integrated in time using an explicit generalized-α method. Our methodology results in *a priori* monolithic formulation, which guarantees the compatibility of tractions at the fluid-structure interface.

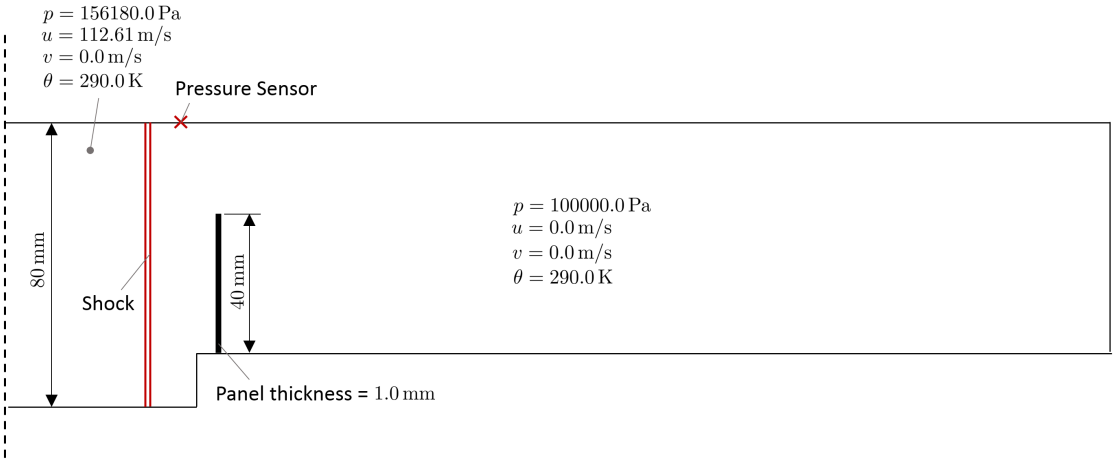

Figure 8.1: Shock wave impacting an elastic panel. Problem setup.

The proposed model was initially used to test the accuracy of our standalone compressible-flow and solid mechanics formulations. In particular, a shock tube, a Sedov blast, and a Taylor bar impact problems were solved. The model was also used to reproduce different FSI problems, such as a detonation with multiple objects or a flexible panel subjected to a shock load. In the latter, a thin steel panel is impacted by a planar shock wave in air; see Fig. 8.1 for the setup of the problem. Inflow boundary conditions are applied on the left side and rigid-wall boundary conditions are applied elsewhere. In this example the panel material is assumed to be elastic. The background mesh is composed of 480×64 elements, while the panel foreground mesh makes use of 10×500 Lagrangian particles. The problem has been previously investigated both experimentally and numerically in [53, 83]. Fig. 8.2 shows the pressure field and panel displaced configuration at different time instants. After the initial impact of the shock wave the panel begins to oscillate. Fig. 8.3(a) shows a comparison of the computed and measured panel-tip displacement time histories. The

two quantities are in good agreement, both in terms of the oscillation magnitude and frequency, suggesting that the background mesh is sufficiently fine to provide the appropriate level of the panel through-thickness resolution. Fig. 8.3(b) compares the computed and measured pressure time histories at the pressure-sensor position. Very good agreement is obtained in this case as well, suggesting that the complex dynamics of shocked flow is well captured in the simulation.

(a) $t = 70.0\,\mu$s

(b) $t = 570.0\,\mu$s

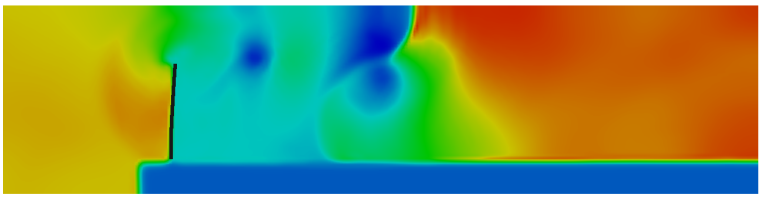

(c) $t = 1245.0\,\mu$s

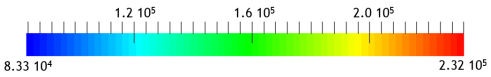

Figure 8.2: Shock wave impacting an elastic panel. Pressure field and deflected panel at different time instants.

8.2 The modified phase-field crystal equation

Another collaboration was initiated with Professor Peter Galenko, which resulted in the publication of the research paper [30]. The goal was to solve the modified phase field crystal equations in three dimensions and study the evolution of crystal structures to their steady equilibrium state for various atomic densities and temperatures.

Phase field crystal (PFC) theories were initially extended from the traditional diffuse interface models in order to account for phenomena naturally embedded on atomic length

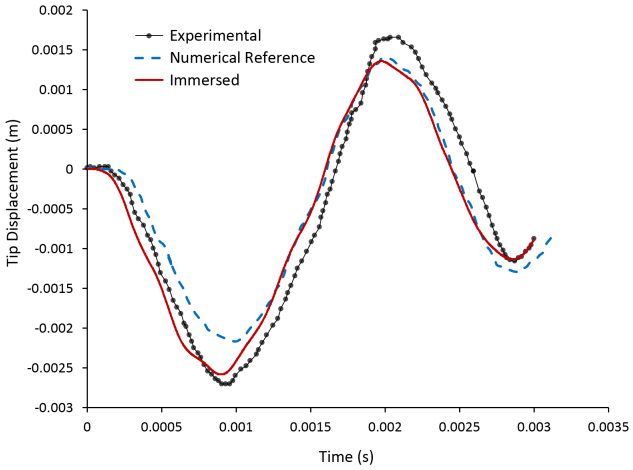

(a)

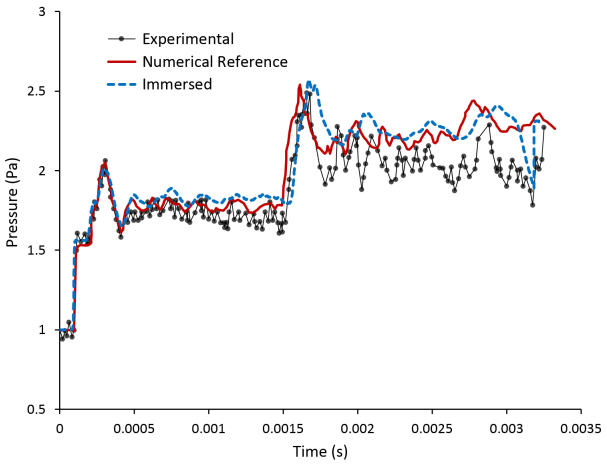

(b)

Figure 8.3: Shock wave impacting an elastic panel. Time history of (a) Panel tip displacement; (b) Pressure at the sensor location. Computational results from [53] are also shown for comparison.

and diffusive time scales [65, 66]. Originally, PFC models were formulated in a parabolic form allowing for the description of pure dissipative dynamics. Subsequently, the modified PFC equation was introduced, which includes an inertial term and thus, allows to capture both fast and slow phenomena in phase transformations [4, 77–79, 154, 155, 193]. Important progress has been made in the two dimensional modified PFC equation for the last years (see, for instance, [4, 79, 193]). However, physically reasonable and practically important results were absent for the case of the three spatial dimensions. Additionally, the transition from two dimensional to three dimensional crystal lattice leads to a higher variety of patterns. This motivated us to compute for the first time numerical results in three dimensional structures predicted by the modified PFC equation. To do so, a NURBS-based Isogeometric Analysis method was used, which allowed for a straightforward resolution of the sixth-order equation. The results obtained have shown to be consistent with the

structure diagram predicted using a one-mode approximation of the analytical solution of the PFC equation (see Fig. 8.4).

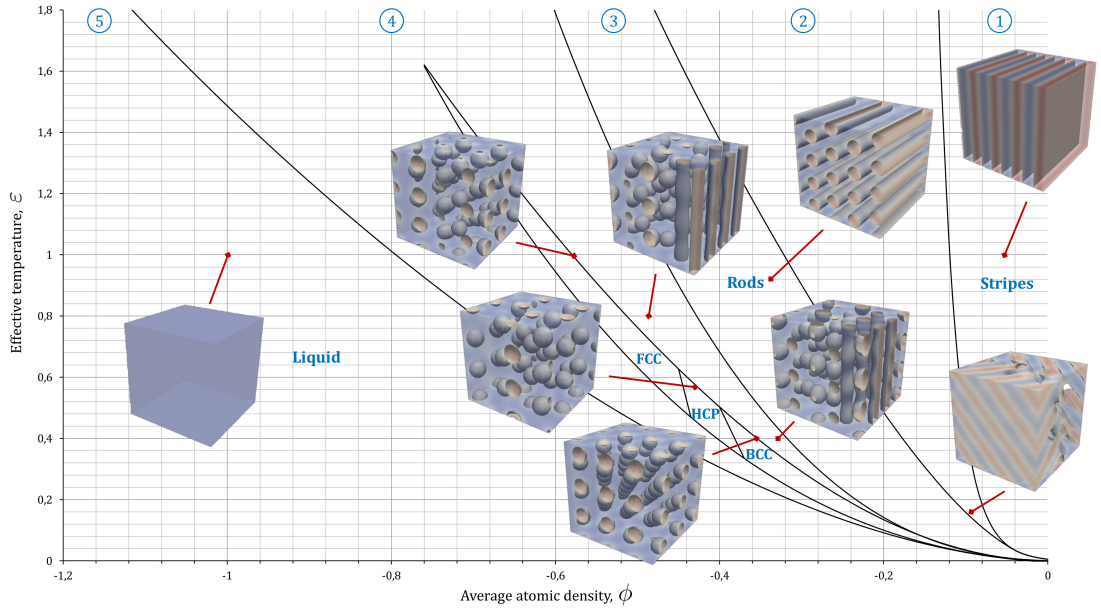

Figure 8.4: Computed structures in comparison with the regions of the diagram of Jaatinen and Ala-Nissila [103]. Regions of existing structures are: (1) Stripes; (2) Stripes and Rods; (3) Rods; (4) mixed structures with the existence of pure body centered cubic (BCC), pure hexagonal close packed (HCP), and pure face centered cubic (FCC) crystalline patterns; (5) homogeneous phase (liquid).

Chapter 9

Conclusions

This Chapter outlines the main contributions of this thesis. The major goal of this work is the development of computational models for the interaction of complex fluids and solids. In this sense, we have proposed two different fluid-structure interaction models with the following features:

- Two distinct diffuse-interface approaches with surface tension have been adopted for the description of the fluid. The first one is based on the Navier-Stokes-Korteweg equations [88], allowing for the modeling of compressible fluids that are composed by two phases of the same component, e.g., water vapor and liquid water. This model naturally allows for phase transformations on the fluid. The second approach is based on the Cahn-Hilliard model [84], which is coupled with the incompressible Navier-Stokes equations. The result is a model that describes two-component immiscible flows with surface tension. In both approaches, we assume Newtonian fluids.

- The NSK model requires no stabilization. However, for the NSCH model we propose a residual-based variational multiscale (RBVMS) formulation [15].

- The structure is governed in all cases by the nonlinear equations of elastodynamics and treated as an hyperelastic solid. Two different models have been employed, a Neo-Hookean model with dilatational penalty and a Saint Venant-Kirchhoff model (see, for instance, [128]). Nevertheless, other material models for the solid could be easily implemented in the algorithms proposed in this thesis.

- An Arbitrary Lagrangian-Eulerian approach [57, 58, 101] is employed for the fluid-structure interaction models proposed here. ALE is a moving mesh or boundary-fitted technique in which the fluid and the solid discretizations match at the interface. This allows for accurate solutions close to the interface and the exact fulfillment of the compatibility conditions. However, as the interface evolves, the fluid mesh needs

to be updated. This is accomplished by solving a boundary-value problem in which the Dirichlet boundary conditions are the displacements of the solid at the interface.

- IGA based on NURBS [42] is used for the spatial discretization of both solid and fluid subdomains. IGA can be thought of as a generalization of the finite-element method. It exhibits important mathematical properties, such as higher-order accuracy, robustness, the ability to be refined through knot insertion and degree elevation, and higher-order global continuity. The latter is particularly useful for the problem class of interest, as phase-field approaches include higher order operators in primal form, that otherwise should be treated adopting a mixed formulation. Furthermore, IGA based on NURBS allows for more precise geometric representation of complex objects than FEA and, in particular, it can exactly represent many commonly engineered designs, like cylinders, spheres and tori.

- A quasi-direct monolithic formulation is adopted for the solution of the FSI problem, that is, the fluid and solid equations are solved in a coupled fashion, while the mesh motion is solved separately using as input, data from the fluid-solid solve. Adopting a monolithic approach imposes implicitly the compatibility of tractions at the interface. Regarding the time integration, we use a generalized-α scheme [40]. The nonlinear system of equations is solved using a Newton-Raphson iteration procedure, which leads to a two-stage predictor-multicorrector algorithm. The resulting linear system is solved using a preconditioned GMRES method [151].

- The FSI codes employed in this thesis were initially implemented in Fortran language and using our own libraries and parallel implementation. A C language code was subsequently developed on top of PetIGA [48], which adds the NURBS discretization capabilities and integration of forms to PETSc [150]. This has resulted in a much more efficient and flexible code, which can easily use a great variety of solvers and preconditioners.

The aforementioned models have been applied to a large variety of problems involving complex fluids. Among them, we outline the following applications:

- Surfactants or surface active agents. Surfactants are compounds that are attracted by the interfaces of a system. They have the ability to reduce the work required to generate the interface, that is, the surface tension associated to that interface. This particularity makes surfactants one of the most useful substances in the chemical industry. In the literature, several models have been proposed to describe surfactant absorption phenomena in two-component immiscible flows. The influence of surfactants in fluids composed of two phases of the same component remains practically unexplored, at least from the computational point of view. Here we have proposed a

complex-fluid theory that allows for spontaneous vaporization and condensation and that captures the dynamics of surface active agents at interfaces. We firmly believe that our theory may become a useful tool for further understanding the behavior of these compounds in phase-transition phenomena.

- Phase-change driven implosion. The implosive collapse of vapor-filled structures is studied with a thermally-coupled FSI theory based on the Navier-Stokes-Korteweg equations. In particular, we focus on the collapse inwards of thin structures, in which a thermal variation transforms the internal vapor into liquid, reducing the pressure inside and triggering the implosion of the solid.

- Tensotaxis. We use our FSI model based on the NSK equations to simulate droplet motion driven by strain gradients in the underlying substrate. This process, known as tensotaxis, had been previously observed for cells. Here, we show that simple liquid droplets can also undergo tensotaxis, suggesting that mechanics may play an important role in this process. Our model seems to be a promising tool for further understanding the role of capillary forces in this mechanism.

- Coalescence of droplets. The NSCH model for immiscible flows – without solid – is used for modeling the coalescence of two liquid-water droplets. We compare the radius of the meniscus formed during this process with the behavior observed in experiments and suggested in theoretical models. The purpose is to validate our model as there is no widely accepted numerical benchmark among the computational mechanics community.

- Elastocapillarity. At small scales, surface tension may become dominant and deform slender and/or soft structures, giving rise to a wide range of interesting FSI problems. We use the proposed FSI theory for immiscible flows to study some of these problems. The first one is the deformation of soft substrates under the action of the capillary forces of liquid droplets. We use this problem to validate our model. A glycerol droplet is deposited on a substrate. We measure the vertical displacements in the substrate and we compare them with experimental data. In the second example we simulate elastocapillary origami, that is, the wrapping of thin membranes around liquid droplets. Finally, we study the bending of micropillars under the action of capillary forces. We place a liquid drop between two initially parallel elastic micropillars and analyze the deformation for different volumes of the liquid.

The work presented in this thesis opened the door to several lines of research that should be addressed in the future. Among them, we highlight the following

- The complex fluid theory proposed for the modeling of surface active agents in single-component two-phase flows should be extended to a thermally-coupled theory.

This would allow to study much more complicated scenarios where surfactants alter temperature-driven phase transformations. It would also be interesting to calibrate and validate the model using experimental data.

- Phase-change-driven implosions can lead to a violent and rapid collapse of the structure with strong compressions and large deformations. With the adopted FSI technique, that is, the Arbitrary Lagrangian-Eulerian method, this would result in significant distortions in the solid and the fluid mesh, and remeshing procedures would be necessary. We have tackled this problem by focusing on moderately strong implosions. However, it would be interesting to simulate strong implosions, either using the finite element method and remeshing when needed, or adopting a different FSI technique, e.g., an immersed approach. Another future goal should be the implementation of a model capable of simulating solid contact, plastic deformation and fracture.

- We have used the FSI model based on the NSK equations to show that droplets may undergo tensotaxis. However, other cell motion mechanisms have also been observed for droplets. It is the case of durotaxis or motion due to stiffness gradients in the underlying substrate. Our model seems to be a suitable tool to study this mechanism and explore scenarios that are difficult to reproduce experimentally.

- The FSI model based on the NSCH equations was stabilized adopting a residual-based variational multiscale formulation. In the future, we aim to use divergence-conforming B-spline spaces to obtain a discrete pointwise divergence-free velocity field and thus, avoid the use of any kind of stabilization. It could also be interesting to extend our framework to model capillary fracture. This can be accomplished by coupling the current model with a fracture theory.

Chapter 10

Extended summary in Spanish

10.1 Introducción

El término interacción fluido-estructura (FSI en sus siglas en inglés) engloba un grupo de problemas en los que un sólido móvil o deformable interactúa con un fluido interior o exterior a este, es decir, problemas en los que existe una interdependencia entre un fluido y una estructura sólida. La naturaleza de este tipo de problemas los hace omnipresentes en casi todas las ramas de la medicina, la ingeniería y la ciencia. Los problemas FSI están presentes en la investigación biomédica [10, 12], en la ingeniería civil y aeroespacial [70, 138, 171], en la ingeniería marítima [194, 199] y en la energía eólica [11, 173] por citar tan solo algunas aplicaciones.

En las últimas décadas se han hecho avances importantes en la investigación de esta clase de problemas. Sin embargo, el estudio extensivo de problemas de interacción fluido-estructura sigue siendo un desafío debido a su naturaleza no lineal y dependiente del tempo. En la mayoría de los casos es muy difícil o incluso imposible obtener una solución analítica y es necesario recurrir a análisis experimentales y/o simulaciones numéricas. Los mismos desafíos aparecen en el estudio de la interacción de fluidos complejos y sólidos. Los fluidos complejos [81] pueden entenderse como un tipo especial de fluidos formados por mezclas binarias en las que coexisten diferentes fases, ya sean estas líquidas, gaseosas o sólidas. Los ejemplos más conocidos son los polímeros, emulsiones, geles, espumas, cristales líquidos y, en general, cualquier fluido multifase o multicomponente. El desarrollo de métodos computacionales eficientes y precisos para la interacción de fluidos complejos y sólidos puede potencialmente beneficiar disciplinas como la mecanobioloxía, la ingeniería o la química:

- **Mecanobiología**. Las células pueden migrar en respuesta a gradientes de rigidez (durotaxis) y/o gradientes de deformación (tensotaxis) del substrato en el que se apoyan [123, 163]. La comprensión de estos mecanismos es aún muy limitada pero parecen estar controlados hasta cierto punto por la mecánica y parece plausible que,

a una escala celular, las fuerzas de capilaridad jueguen un papel importante. Un modelo teórico que permita estudiar la durotaxis y/o la tensotaxis contribuiría a un mejor entendimiento de estos procesos y permitiría explorar escenarios que son difíciles de probar experimentalmente.

- **Ingeniería**. Hay una gran variedad de problemas ingenieriles en los que los fluidos complejos juegan un papel importante. Entre ellos, uno de los más relevantes es el colapso implosivo de estructuras delgadas [110, 144]. Aquellas estructuras que contienen un fluido compresible a una presión inferior a la presión externa tienen el potencial de colapsar hacia el interior. Por ejemplo, una estructura llena de aire puede sufrir un colapso implosivo cuando es sumergida bajo agua debido al incremento de la presión externa. En otras situaciones, los cambios de fase pueden ser los responsables de la implosión de estructuras llenas de vapor. Las variaciones térmicas pueden transformar el vapor en líquido reduciendo la presión interna, lo cual, a su vez, puede llevar al colapso violento y rápido de la estructura produciendo fuertes compresiones y grandes deformaciones. Las implosiones violentas pueden también dar lugar al contacto entre sólidos, a deformaciones plásticas y a fracturas.

- **Química**. Desde la perspectiva de la comunidad química hay innumerables problemas en los que los fluidos complejos están presentes. Un ejemplo claro es el de los tensoactivos o surfactantes, es decir, compuestos que encuentran favorable desde un punto de vista energético estar situados en las interfaces del sistema [71, 133, 149]. Los surfactantes son atrapados por las interfaces, reduciendo el trabajo necesario para generar esas interfaces y alterando completamente el comportamiento del sistema. Por esta misma razón su uso es omnipresente en la industria química - pueden encontrarse en detergentes, cosméticos, tintes, etc. - así como en otros campos, tales como la microelectrónica [176], la biotecnología [153, 191] o la investigación médica [73, 146]. También juegan un papel primordial en nuestro organismo, incrementando la distensibilidad pulmonar y previniendo la atelectasis [94, 115], esto es, el colapso completo o parcial de los pulmones.

- **Microfabricación**. El creciente interés por los microdispositivos está atrayendo una gran atención sobre los efectos que la tensión superficial de las gotas puede tener en estructuras blandas o esbeltas. A medida que se reduce la escala de un sistema, las fuerzas capilares disminuyen más lentamente que las fuerzas de presión y gravitacionales y eventualmente llegan a ser dominantes, siendo capaces de deformar estructuras elásticas. Este fenómeno es conocido como elastocapilaridad [147, 160]. Entender los mecanismos físicos detrás de los fenómenos de elastocapilaridad es esencial para el diseño de nuevos materiales y dispositivos a micro y nanoescala.

Tradicionalmente, los métodos numéricos para problemas FSI se centraron en la interacción

de sólidos y fluidos clásicos gobernados por las ecuaciones de Navier-Stokes para flujos compresibles o incompresibles (véase, por ejemplo, [14, 124–126, 162, 165, 167, 170–172, 174]). No obstante, hay muchos problemas de FSI, como por ejemplo, aquellos que involucran fluidos complejos, que no pueden ser modelados usando estas teorías pues dependen fundamentalmente de mecanismos físicos no capturados por las ecuaciones de Navier-Stokes por sí solas. En esta tesis extendemos el estado del arte en la interacción de fluidos complejos y sólidos mediante las siguientes contribuciones:

- **Un modelo basado en las ecuaciones de Navier-Stokes-Korteweg (NSK) para fluidos complejos con tensoactivos**. Presentamos un nuevo modelo para flujos líquido-vapor con tensoactivos que captura la dinámica de los surfactantes y permite la transformación de fases en el fluido. Nuestro enfoque para la transformación de fases está basada en los modelos de interfaz difusa o campo de fases. En concreto, nuestra teoría emana de las ecuaciones de Navier-Stokes-Korteweg isotermas, las cuales describen flujos de un solo componente y dos fases y permiten de forma natural el cambio de fases. Derivamos nuestro modelo a partir de un funcional de energía usando una técnica Coleman-Noll. La teoría propuesta tiene un gran potencial para estudiar la influencia de los tensoactivos en procesos de evaporación y condensación. Para hacer frente a los desafíos numéricos impuestos por este modelo, tales como la rigidez en el espacio y en el tempo, las capas internas y de contorno, así como los operadores en derivadas parciales de alto orden, adoptamos como técnica computacional el Análisis Isogeométrico (IGA en sus siglas en inglés) basado en Non-Uniform Rational B-Splines (NURBS), lo cual permite una discretización eficiente y precisa. La viabilidad del marco teórico y la efectividad de los algoritmos propuestos es ilustrada resolviendo varios ejemplos numéricos en dos y tres dimensiones. Véase [29] y el Capítulo 4 para más detalles.

- **Un modelo Arbitrario Lagrangiano-Euleriano para la interacción de fluidos complejos y sólidos basado en las ecuaciones NSK y en sólidos Neo-Hookeanos**. Cuando interactúan con sólidos, los fluidos complejos dan lugar a una física mucho más rica que los fluidos clásicos, especialmente a pequeñas escalas. En esta tesis presentamos un nuevo modelo matemático para FSI capaz de capturar esta física para el caso de fluidos de dos fases y un solo componente interactuando con sólidos hiperelásticos. En concreto, el fluido es tratado como un fluido viscoso y compresible, gobernado por las ecuaciones de Navier-Stokes-Korteweg, lo cual permite que el fluido se condense o evapore de forma natural debido a cambios de presión y/o temperatura. La estructura es tratada como un sólido Lagrangiano gobernado por las ecuaciones de las elastodinámica no lineal. La descripción Arbitraria Lagrangiana-Euleriana es utilizada para el subdominio del fluido. El movimiento

de la malla del fluido es computado resolviendo las ecuaciones de la elastostática dados los datos de desplazamiento en la interfaz sólido-fluido. Para la resolución del problema acoplado adoptamos una formulación monolítica quasi-directa, es decir, las ecuaciones del sólido y el fluido son resueltas de una forma acoplada mientras que el movimiento de la malla es calculado separadamente usando como input datos del resolvedor sólido-fluido. Para la discretización espacial de las ecuaciones del fluido y de la estructura empleamos Análisis Isogeométrico basado en NURBS. El modelo propuesto es usado para simular el colapso implosivo de estructuras llenas de vapor. Estudiamos diferentes geometrías en dos y tres dimensiones, en las cuales la implosión es desencadenada por variaciones térmicas. Véase [27] y el Capítulo 5 para más detalles.

- **Un modelo para la interacción de fluidos complejos y sólidos basado en las ecuaciones NSK y en estructuras Saint Venant**. El modelo para el fluido descrito en el punto anterior es acoplado ahora con una estructura Saint Venant. La idea es estudiar desde un punto de vista mecánico un problema concreto conocido como tensotaxis, es decir, la habilidad que tienen las células para migrar en respuesta a gradientes de deformación del substrato en el que se apoyan. El objetivo es ver si a pequeñas escalas las fuerzas de capilaridad juegan un papel importante en este proceso, estudiando para ello el caso particular de las gotas. Los estudios experimentales de tensotaxis son especialmente desafiantes pues predeformar el substrato da lugar habitualmente a un incremento en la rigidez del mismo como resultado de la respuesta no lineal del material y produciendo de esta forma una combinación de tensotaxis y durotaxis. Reemplazar el modelo neo-Hokeano usado en el problema de la implosión con un modelo Saint-Venant nos permite considerar nolinearidades geométricas manteniendo una respuesta lineal del material. Como consecuencia, las deformaciones introducidas en el substrato para desencadenar la tensotaxis no alteran la rigidez del sólido, evitando una situación de tensotaxis y durotaxis simultáneas. En resumen, proponemos un modelo teórico que permite aislar los efectos de la tensotaxis. Presentamos además varias simulaciones numéricas en dos y tres dimensiones en las que el movimiento y la coalescencia de gotas son accionados aplicando fuerzas localizadas en un substrato blando. Véase [26] y el Capítulo 6 para más detalles.

- **Un modelo basado en las ecuaciones de Navier-Stokes-Cahn-Hilliard para la interacción de sólidos y fluidos complejos incompresibles**. Los modelos FSI presentados en los puntos anteriores son capaces de describir la física detrás de fluidos de dos fases y un solo componente interactuando con estructuras hiperelásticas. Sin embargo, hay un gran número de problemas físicos e ingenieriles

donde el fluido no está formado por fases de un mismo componente. Es el caso, por ejemplo, de la inyección de gases para la extracción de petróleo, espráis de combustible en procesos de combustión, flujos de aire y agua, etc. Para modelar este tipo de problemas, proponemos una teoría basada en las ecuaciones de Navier-Stokes-Cahn-Hilliard, las cuales permiten describir fluidos inmiscibles de dos componentes con tensión superficial. El fluido es tratado como un fluido viscoso e incompresible en una descripción Arbitraria Lagrangiana-Euleriana. La estructura es tratada como un sólido hiperelástico y Lagrangiano gobernado por las ecuaciones de la elastodinámica no lineal. El modelo propuesto es usado para predecir la deformación causada por las fuerzas de capilaridad de gotas de glicerina en substratos blandos. Los resultados obtenidos son posteriormente validados con datos experimentales. El modelo es usado también para la simulación bidimensional y tridimensional de otros fenómenos de elastocapilaridad tales como origamis por capilaridad o el colapso de micropilares flexibles. Véase [28] y el Capítulo 7 para más detalles.

10.2 Objetivos

Los objetivos de la investigación llevada a cabo en esta tesis pueden resumirse en los siguientes puntos:

- Desarrollo de modelos numéricos para la simulación de fluidos complejos y su interacción con estructuras sólidas. Tradicionalmente, los métodos numéricos para FSI se han enfocado en la interacción de sólidos y fluidos clásicos gobernados por las ecuaciones de Navier-Stokes. El acoplamento entre sólidos y fluidos complejos permanece prácticamente inexplorado, al menos desde el punto de vista computacional, a pesar que este suele dar lugar a una física mucho más rica que los fluidos clásicos, especialmente a pequeña escala. Nuestro objetivo es el de proponer nuevos modelos numéricos basados en el método de campos de fases y capaces de capturar los mecanismos físicos detrás de los fluidos complejos. Los desafíos numéricos asociados a los modelos de campos de fase, tales como la rigidez en espacio y en el tempo y la inclusión de operadores en derivadas parciales de alto orden, son afrontados mediante la utilización de la técnica de Análisis Isogeométrico basada en NURBS para la discretización espacial. Este método debería aprovechar la continuidad de alto orden entre elementos de las funciones de base para mejorar la precisión y la robustez con respecto al método clásico de elementos finitos. El uso de NURBS permite además una representación geométrica de obyectos complejos más precisa ya que estas pueden representar de forma exacta muchos diseños comúnmente empleados en ingeniería tales como cilindros, esferas o toroides.

- Aplicación de los modelos propuestos. La idea es ilustrar la habilidad predictiva de

nuestros modelos y la efectividad de nuestros métodos computacionales mediante la resolución de problemas asociados a una gran variedad de campos, tales como la ingeniería, la mecanobiología, la química y la microfabricación. En este sentido, estudiamos un gran número de problemas físicos como la influencia de los tensoactivos en flujos de dos fases y un solo componente, el colapso implosivo de estructuras llenas de vapor, el papel de las fuerzas de capilaridad en el movimiento de gotas causado por tensotaxis, el envolvimiento espontáneo de gotas con membranas elásticas o el colapso de micropilares flexibles debido a fuerzas de elastocapilaridad.

- Implementación de los algoritmos propuestos. La optimización de los modelos FSI, incluyendo una eficiente implementación en paralelo es de transcendental importancia a la hora de resolver problemas físicos realistas. Por este motivo un objetivo primordial es llevar a cabo a implementación en paralelo de los modelos propuestos.

10.3 Contribuciones de la tesis

Esta sección resalta las principales contribuciones e ideas de la investigación llevada a cabo en esta tesis. El objetivo principal de este trabajo es el desarrollo de modelos computacionales para la interacción de fluidos complejos y sólidos. En este sentido, hemos propuesto dos modelos de interacción fluido-estructura diferentes con las siguientes características:

- Dos enfoques de interfaz difusa diferentes fueron adoptados para la descripción del fluido. El primero está basado en las ecuaciones de Navier-Stokes-Korteweg [88], permitiendo el modelado de fluidos compresibles que están compuestos por dos fases de un mismo componente como, por ejemplo, vapor de agua y agua líquida. Este modelo permite además de forma natural la transformación de fases en el fluido. El segundo enfoque está basado en el modelo de Cahn-Hilliard [84], el cual es acoplado con las ecuaciones de Navier-Stokes incompresibles. El resultado es un modelo que describe flujos de dos componentes inmiscibles con tensión superficial. En ambos casos asumimos fluidos newtonianos.

- El modelo NSK no requiere ningún tipo de estabilización. Sin embargo, para el modelo NSCH adoptamos una formulación multiescala variacional y basada en el residuo [15].

- La estructura está gobernada en todos los casos por las ecuaciones de la elastodinámica no lineal y tratada como un sólido hiperelástico. Utilizamos dos modelos diferentes, un modelo Neo-Hookeano y un modelo de Saint Venant (ver, por ejemplo, [128]). En cualquier caso, otros modelos materiales para el sólido podrían ser fácilmente implementados en los algoritmos propuestos en esta tesis.

- Adoptamos un enfoque Arbitrario Lagrangiano-Euleriano [57, 58, 101] para los modelos de interacción fluido-estructura propuestos en esta tesis. ALE es una técnica de malla móvil en la que las discretizaciones del sólido y del fluido coinciden a lo largo de la interfaz. Esto permite soluciones precisas cerca de la interfaz y la satisfacción exacta de las condiciones de compatibilidad. Sin embargo, a medida que la interfaz evoluciona, la malla del fluido necesita ser actualizada. Esto se consigue mediante la resolución de un problema de contorno en el que las condiciones Dirichlet son los desplazamientos del sólido a lo largo de la interfaz.

- El método de Análisis Isogeométrico basado en NURBS [42] es usado para la discretización espacial tanto del sólido como del fluido. IGA pude entenderse como una generalización del método de elementos finitos que posee importantes propiedades matemáticas, tales como precisión de alto orden, robustez, refinamiento mediante inserción de nodos y elevación de orden y continuidad global de alto orden. Esta última propiedad es especialmente útil a la hora de tratar nuestros problemas FSI pues las técnicas de campos de fase incluyen operadores de alto orden en su forma primaria que, de otra forma, deberían ser tratados adoptando una formulación mixta. Además, IGA basado en NURBS permite una representación más exacta de objetos complejos que el método FEM y, en concreto, puede representar de forma exacta cilindros, esferas, y toroides.

- Se adopta una formulación monolítica quasi-directa para la solución de los problemas FSI, esto es, las ecuaciones del fluido y del sólido son resueltas de una forma acoplada, mientras que el movimiento de la malla se resuelve de forma separada usando como input datos procedentes de la resolución del sólido y del fluido. Adoptar un enfoque monolítico impone implícitamente la compatibilidad de tracciones en la interfaz. En lo relativo a la integración en el tiempo usamos un esquema α generalizado [40]. El sistema de ecuaciones no lineal es resuelto usando un procedimiento Newton-Raphson iterativo, el cual da lugar a un algoritmo predictor-multicorrector de dos fases. El sistema lineal resultante es resuelto usando un método GMRES precondicionado [151].

- El código FSI empleado en esta tesis fue inicialmente desarrollado en lenguaje Fortran y usando nuestras propias librerías e implementación en paralelo. Posteriormente, se desarrolló un código en lenguaje C usando como base PetIGA [48], el cual añade la capacidad de discretización de las NURBS y la integración de formas a PETSc [150]. Esto resultó en un código mucho más flexible y eficiente, el cual puede emplear una gran variedad de resolvedores y precondicionadores.

Los modelos antes mencionados fueron aplicados a una gran variedad de problemas que involucran fluidos complejos. Entre ellos cabe destacar las siguientes aplicaciones:

- Tensoactivos o surfactantes. Los surfactantes son compuestos que son atraídos por las interfaces presentes en un sistema. Tienen la habilidad de reducir el trabajo requerido para generar la interfaz, esto es, reducir la tensión superficial asociada a dicha interfaz. Esta particularidad hace de los surfactantes una de las substancias más usadas en la industria química. En la literatura se pueden encontrar varios modelos que describen fenómenos de absorción de surfactantes en flujos inmiscibles de dos componentes. La influencia de surfactantes en fluidos de dos fases y un solo componente permanece prácticamente inexplorada, al menos desde un punto de vista computacional. En esta tesis hemos propuesto una teoría de fluidos complejos que permite la espontánea vaporización y condensación del fluido y que captura la dinámica de los tensoactivos. Creemos firmemente que nuestra teoría puede llegar a ser una herramienta útil para la comprensión del comportamiento de estas substancias en fenómenos de transición de fase.

- Implosión debida a cambios de fase. El colapso implosivo de estructuras llenas de vapor es estudiado con una teoría de FSI térmicamente acoplada y basada en las ecuaciones de Navier-Stokes-Korteweg. En concreto, nos centramos en el colapso hacia el interior de estructuras delgadas en las que una variación térmica transforma el vapor presente en el interior en líquido, reduciendo así la presión interna y provocando la implosión del sólido.

- Tensotaxis. Usamos nuestro modelo FSI basado en las ecuaciones NSK para simular el movimiento de gotas debido a gradientes de deformación del substrato en el que se apoyan. Este proceso, conocido como tensotaxis, fue previamente observado en células. Aquí, nosotros mostramos que simples gotas líquidas pueden también experimentar tensotaxis, sugiriendo que la mecánica puede jugar un papel importante en este proceso. Nuestro modelo parece ser una herramienta prometedora para un mayor entendimiento del papel que juegan las fuerzas de capilaridad en este mecanismo.

- Coalescencia de gotas. El modelo NSCH para flujos inmiscibles es usado para el modelado de la coalescencia de dos gotas de agua. Comparamos el radio del menisco formado durante este proceso con el comportamiento observado en experimentos y sugerido en modelos teóricos. El propósito es validar nuestro modelo ya que no existen estándares de referencia ampliamente aceptados para esta teoría.

- Elastocapilaridad. A pequeñas escalas, la tensión superficial puede llegar a ser dominante y deformar estructuras esbeltas y/o blandas, dando lugar a una gran variedad de problemas FSI muy interesantes. En este trabajo usamos la teoría FSI de fluidos inmiscibles para estudiar algunos de estos problemas. El primero consiste en

la deformación de substratos blandos debido a las fuerzas de capilaridad en gotas líquidas. Usamos este problema para validar nuestro modelo. Una gota de glicerina es depositada en un substrato. Medimos los desplazamientos verticales causados en el substrato y los comparamos con datos experimentales. En el segundo ejemplo, simulamos origamis por elastocapilaridad, esto es, el envolvimiento de membranas delgadas entorno a gotas líquidas. Finalmente, estudiamos la flexión de micropilares bajo la acción de fuerzas capilares, para lo cual, colocamos una gota líquida entre dos micropilares elásticos inicialmente paralelos.

10.4 Futuras líneas de trabajo

El trabajo presentado en esta tesis ha abierto la puerta a varias líneas de investigación que deberían ser tratadas en el futuro. Entre ellas, destacamos las siguientes:

- La teoría de fluidos complejos propuesta para el modelado de tensoactivos en flujos de un componente y dos fases debería ser extendida a una teoría térmicamente acoplada. Esto permitiría el estudio de escenarios mucho más complejos donde los surfactantes alteren transformaciones de fase inducidas por cambios de temperatura. Sería además interesante calibrar y validar el modelo usando datos experimentales.

- Las implosiones inducidas por cambios de fase pueden llevar al colapso violento y rápido de la estructura, produciendo grandes compresiones y deformaciones. Con la técnica FSI adoptada, es decir, el método Arbitrario Lagranxiano-Euleriano, esto resultaría en distorsiones significativas en el sólido y en la malla del fluido, y sería necesario realizar procesos de remallado. Nosotros intentamos hacer frente a este desafío centrándonos en implosiones moderadamente fuertes. Sin embargo, sería interesante simular implosiones fuertes, ya sea usando el método de elementos finitos y remallando cuando es necesario o adoptando una técnica FSI diferente, por ejemplo, una técnica inmersa. Otro objetivo futuro debería ser la implementación de un modelo capaz de simular el contacto entre sólidos, deformación plástica y fractura.

- Usamos el modelo FSI basado en las ecuaciones de NSK para mostrar que las gotas también pueden experimentar tensotaxis. Sin embargo, otros mecanismos de movimiento celular han sido observados en gotas. Es el caso de la durotaxis o movimiento debido a gradientes de rigidez del substrato. Nuestro modelo parece ser una herramienta adecuada para analizar este mecanismo y sugerir escenarios que son difíciles de estudiar experimentalmente.

- El modelo FSI basado en las ecuaciones de NSCH fue estabilizado adoptando una formulación variacional multiescala. En el futuro, tenemos como objetivo usar espacios B-Spline divergentes y conformantes para obtener campos de velocidades discretos

de divergencia nula en cada punto, evitando así la necesidad de cualquier tipo de estabilización. Sería también interesante acoplar nuestro modelo con una teoría de fractura y ser así capaces de simular fractura capilar.

Chapter 11

Extended summary in Galician

11.1 Introdución

O termo interacción fluído-estrutura (FSI nas súas siglas en inglés) engloba un grupo de problemas nos que un sólido móbil ou deformable interacta cun fluído interior ou exterior a este, é dicir, problemas nos que existe unha interdependencia entre un fluído e unha estrutura sólida. A natureza deste tipo de problemas fainos omnipresentes en case todas as ramas da medicina, da enxeñaría e da ciencia. Os problemas FSI están presentes na investigación biomédica [10,12], na enxeñaría civil e aeroespacial [70,138,171], na enxeñaría marítima [194, 199] e na enerxía eólica [11, 173] por nomear tan só algunhas aplicacións.

Nas últimas décadas fixéronse avances importantes na investigación desta clase de problemas. Sen embargo, o estudo extensivo de problemas interacción fluído-estrutura segue sendo un desafío debido á súa natureza non lineal e dependente do tempo. Na maioría dos casos, é moi difícil ou incluso imposible obter unha solución analítica e é necesario recorrer a análises experimentais e/ou simulacións numéricas. Os mesmos desafíos aparecen no estudo da interacción de fluídos complexos e sólidos. Os fluídos complexos [81] poden entenderse como un tipo especial de fluídos formados por mesturas binarias nas que coexisten diferentes fases, xa sexan estas líquidas, gasosas ou sólidas. Os exemplos máis coñecidos son os polímeros, emulsións, xeles, espumas, cristais líquidos e, en xeral, calquera fluído multifase ou multicompoñente. O desenvolvemento de métodos computacionais eficientes e precisos para a interacción de fluídos complexos e sólidos pode potencialmente beneficiar disciplinas como a mecanobioloxía, a enxeñaría ou a química:

- **Mecanobioloxía**. As células poden migrar en resposta a gradientes de rixidez (durotaxe) e/ou gradientes de deformación (tensotaxe) do substrato no que se apoian [123, 163]. A comprensión destes mecanismos é aínda moi limitada pero semellan estar controlados ata certo punto pola mecánica e parece plausible que a unha escala celular as forzas de capilaridade xoguen un papel importante. Un modelo teórico que permita estudar a durotaxe e/ou a tensotaxe contribuiría a un mellor entende-

mento destes procesos, e permitiría explorar escenarios que son difíciles de probar experimentalmente.

- **Enxeñaría**. Hai unha gran variedade de problemas enxeñerís nos que os fluídos complexos xogan un papel importante. Entre eles, un dos máis relevantes é o colapso implosivo de estruturas delgadas. Aquelas estruturas que conteñen un fluído compresible a unha presión inferior á presión externa teñen o potencial de colapsar cara ó interior. Por exemplo, unha estrutura chea de aire pode sufrir un colapso implosivo cando é somerxida baixo a auga debido ó incremento da presión externa. Noutras situacións, os cambios de fase poden ser os responsables da implosión de estruturas cheas de vapor. As variacións térmicas poden transformar o vapor en líquido reducindo a presión interna, o cal, á súa vez, pode levar ó colapso violento e rápido da estrutura, producindo compresións fortes e grandes deformacións. As implosión violentas poden tamén dar lugar ó contacto entre sólidos, deformacións plásticas e fracturas.

- **Química**. Dende a perspectiva da comunidade química, hai innumerables problemas nos que os fluídos complexos están presentes. Un exemplo claro é o dos tensioactivos ou surfactantes, é dicir, compostos que encontran favorable, dende un punto de vista enerxético, estar situados nas interfaces do sistema [71,133,149]. Os surfactantes son atrapados polas interfaces, reducindo o traballo necesario para xerar esas interfaces e alterando completamente o comportamento do sistema. Por esta mesma razón, o seu uso é omnipresente na industria química - poden atoparse en deterxentes, cosméticos, tintes, etc. - así coma noutros campos tales como a microelectrónica [176], a biotecnoloxía [153,191] ou a investigación médica [73,146]. Tamén xogan un papel primordial no noso organismo, incrementando a distensibilidade pulmonar e previndo a atelectase [94,115], isto é, o colapso completo ou parcial dos pulmóns.

- **Microfabricación**. O crecente interese polos microdispositivos está a atraer unha gran atención sobre os efectos que a tensión superficial das gotas pode ter en estruturas brandas ou esveltas. A medida que se reducen as escalas dun sistema, as forzas capilares diminúen máis lentamente que as forzas de presión e gravitacionais, e eventualmente chegan a ser dominantes, sendo capaces de deformar estruturas elásticas. Este fenómeno é coñecido como elastocapilaridade [147, 160]. Entender os mecanismos físicos detrás dos fenómenos de elastocapilaridade é esencial para o deseño de novos materiais e dispositivos a micro e nanoescala.

Tradicionalmente, os métodos numéricos para problemas FSI enfocáronse na interacción de sólidos e fluídos clásicos gobernados polas ecuacións de Navier-Stokes para fluxos compresibles ou incompresibles (véxase, por exemplo, [14,93,124–126,162,165,167,170–172,174]). Non obstante, hai moitos problemas de FSI, como, por exemplo, aqueles que involucran

fluídos complexos, que non poden ser modelados usando estas teorías pois dependen fundamentalmente de mecanismos físicos non capturados polas ecuacións de Navier-Stokes por si soas. Nesta tese estendemos o estado da arte na interacción de fluídos complexos e sólidos mediante as seguintes contribucións:

- **Un modelo baseado nas ecuacións de Navier-Stokes-Korteweg (NSK) para fluídos complexos con tensioactivos**. Presentamos un novo modelo para fluxos liquido-vapor con tensioactivos que captura a dinámica dos surfactantes e permite a transformación de fases no fluído. O noso enfoque para a transformación de fases está baseada nos modelos de interface difusa ou campo de fases. En concreto, a nosa teoría emana das ecuacións de Navier-Stokes-Korteweg isotermas, as cales describen fluxos dun só compoñente e dúas fases e permiten de xeito natural o cambio de fases. Derivamos o noso modelo a partir dun funcional de enerxía usando unha técnica Coleman-Noll. A teoría proposta ten un gran potencial para estudar a influencia dos tensioactivos en procesos de evaporación e condensación. Para facer fronte ós desafíos numéricos impostos por este modelo, tales como a rixidez no espazo e no tempo, as capas internas e de contorno así como os operadores en derivadas parciais de alto orde, adoptamos como técnica computacional Análise Isoxeométrico (IGA nas súas siglas en inglés) baseado en Non-Uniform Rational B-Splines (NURBS), o cal permite unha discretización eficiente e precisa. A viabilidade do marco teórico e a efectividade dos algoritmos propostos é ilustrada resolvendo varios exemplos numéricos en dúas e tres dimensións. Véxase [29] e o Capítulo 4 para máis detalles.

- **Un modelo Arbitrario Lagranxiano-Euleriano para a interacción de fluídos complexos e sólidos baseado nas ecuacións NSK e en sólidos Neo-Hookeanos**. Cando interactúan con sólidos, os fluídos complexos dan lugar a unha física moito máis rica que os fluídos clásicos, especialmente a pequenas escalas. Nesta tese presentamos un novo modelo matemático para FSI capaz de capturar esta física para o caso de fluídos de dúas fases e un só compoñente interactuando con sólidos hiperelásticos. En concreto, o fluído é tratado como un fluído viscoso e compresible, gobernado polas ecuacións de Navier-Stokes-Korteweg, o cal permite que o fluído condense ou evapore de xeito natural debido a cambios de presión e/ou temperatura. A estrutura é tratada como un sólido Lagranxiano gobernado polas ecuacións da elastodinámica non lineal. A descrición Arbitraria Lagranxiana-Euleriana é utilizada para o subdominio do fluído. O movemento da malla do fluído é computada resolvendo as ecuacións da elastostática dados os datos de desprazamento na interface sólido-fluído. Para a resolución do problema acoplado adoptamos unha formulación monolítica case directa, é dicir, as ecuacións do sólido e o fluído son resoltas dun xeito acoplado, mentres que o movemento da malla é calculado separadamente us-

ando como input datos do resolvedor sólido-fluído. Para a discretización espacial das ecuacións do fluído e da estrutura empregamos Análise Isoxeométrico baseado en NURBS. O modelo proposto é usado para simular o colapso implosivo de estruturas cheas de vapor. Estudamos diferentes xeometrías en dúas e tres dimensións, nas cales a implosión é iniciada por variacións térmicas. Véxase [27] e o Capítulo 5 para máis detalles.

- **Un modelo para a interacción de fluídos complexos e sólidos baseado nas ecuacións NSK e nunha estrutura Saint Venant**. O modelo para o fluído descrito no punto anterior é acoplado agora cunha estrutura Saint Venant. A idea é estudar dende un punto de vista mecánico, un problema concreto coñecido como tensotaxe, é dicir, a habilidade que teñen as células para migrar en resposta a gradientes de deformación do substrato no que se apoian. O obxectivo é ver se a pequenas escalas as forzas de capilaridade xogan un papel importante neste proceso, estudando para elo o caso particular das gotas. Os estudos experimentais de tensotaxe son especialmente desafiantes pois predeformar o substrato da lugar habitualmente a un incremento na rixidez do mesmo como resultado da resposta non lineal do material e producindo deste xeito unha combinación de tensotaxe e durotaxe. Reemprazar o modelo neo-Hokeano usado no problema da implosión cun modelo Saint-Venant permítenos considerar nonlinearidades xeométricas mantendo unha resposta lineal do material. Como consecuencia, as deformacións introducidas no substrato para desencadear a tensotaxe non alteran a rixidez do sólido, evitando unha situación de tensotaxe e durotaxe simultáneas. En resumo, estamos a propoñer un modelo teórico que permite aillar os efectos da tensotaxe. Presentamos ademais, varias simulacións numéricas en dúas e tres dimensións nas que o movemento e a coalescencia de gotas é accionado aplicando forzas localizadas nun substrato brando. Véxase [26] e o Capítulo 6 para máis detalles.

- **Un modelo baseado nas ecuación de Navier-Stokes-Cahn-Hilliard para a interacción de sólido e fluídos complexos incompresibles**. Os modelos FSI presentados nos puntos anteriores son capaces de describir a física detrás de fluídos de dúas fases e un só compoñente interactuando con estruturas hiperelásticas. Sen embargo, hai un gran número de problemas físicos e enxeñerís onde o fluído non esta formado por fases dun mesmo compoñente. é o caso, por exemplo, da inxección de gases para a extracción de petróleo, esprais de combustible en procesos de combustión, fluxos de aire e auga, etc. Para modelar este tipo de problemas, propoñemos unha teoría baseada nas ecuacións de Navier-Stokes-Cahn-Hilliard, as cales permiten describir fluídos inmiscibles de dous compoñentes con tensión superficial. O fluído é tratado como un fluído viscoso e incompresible nunha descrición Ar-

bitraria Lagranxiana-Euleriana. A estrutura é tratada como un sólido hiperelástico e lagranxiano gobernado polas ecuacións de elastodinámica non lineal. O modelo proposto é usado para predicir a deformación causada polas forzas de capilaridade de gotas de glicerina en substratos brandos. Os resultados obtidos son posteriormente validados con datos experimentais. O modelo é usado tamén para a simulación bidimensional e tridimensional doutros procesos de elastocapilaridade tales como os origamis por capilaridade e o colapso de micropilares flexibles. Véxase [28] e o Capítulo 7 para máis detalles.

11.2 Obxectivos

Os obxectivos da investigación levada a cabo nesta tese poden resumirse nos seguintes puntos:

- Desenvolvemento de modelos numéricos para a simulación de fluídos complexos e a súa interacción con estruturas sólidas. Tradicionalmente, os métodos numéricos para FSI enfocáronse na interacción de sólidos con fluídos clásicos gobernados polas ecuacións de Navier-Stokes. O acoplamento entre sólidos e fluídos complexos permanece practicamente inexplorado, cando menos, dende o punto de vista computacional a pesar que este adoita dar lugar a unha física moito máis rica que os fluídos clásicos, especialmente a pequena escala. O noso obxectivo é o de propoñer novos modelos numéricos baseados en métodos de campos de fases e capaces de capturar os mecanismos físicos detrás dos fluídos complexos. Os desafíos numéricos asociados ós modelos de campos de fase, tales como, a rixidez no espazo e no tempo e a inclusión de operadores en derivadas parciais de alto orde, son afrontados mediante a utilización da técnica de Análise Isoxeométrico baseada en NURBS para a discretización espacial. Este método debería aproveitar a continuidade de alto orde entre elementos das función de base splines para mellorar a precisión e a robustez con respecto ó método clásico de elementos finitos. O uso de NURBS permite ademais una representación xeométrica de obxectos complexos máis precisa xa que estas poden representar de xeito exacto moitos deseños comunmente empregados en enxeñaría tales como cilindros, esferas ou toroides.

- Aplicación dos modelos propostos. A idea é ilustrar a habilidade predictiva dos noso modelos e a efectividade dos nosos métodos computacionais mediante a resolución de problemas asociados a unha gran variedade de campos, tales como, a enxeñaría, a mecanobioloxía, a química e a microfabricación. Neste sentido, estudamos un gran número de problemas físicos como a influencia dos tensioactivos en fluxos de dúas fases e un só compoñente, o colapso implosivo de estruturas cheas de vapor, o papel

das forzas de capilaridade no movemento de gotas causado por tensotaxe, o envolvemento espontáneo de gotas con membranas elásticas ou o colapso de micropilares flexibles debido a forzas de elastocapilaridade.

- Implementación dos algoritmos propostos. A optimización dos modelos FSI, incluíndo unha eficiente implementación en paralelo, é de importancia transcendental á hora de resolver problemas físicos realistas. Por este motivo, un obxectivo primordial é levar a cabo a implementación en paralelo dos modelos propostos.

11.3 Contribucións da tese

Esta sección subliña as principais contribucións e ideas de investigación desta tese. O obxectivo principal deste traballo é o desenvolvemento de modelos computacionais para a interacción de fluídos complexos e sólidos. Neste sentido, propuxemos dous modelos de interacción fluído-estrutura diferentes coas seguintes características:

- Dous enfoques de interface difusa diferentes foron adoptados para a descrición do fluído. O primeiro está baseado nas ecuacións de Navier-Stokes-Korteweg [88], permitindo o modelado de fluídos compresibles que están compostos por dúas fases dun mesmo compoñente como, por exemplo, vapor de auga e auga líquida. Este modelo permite ademais a transformación de fases no fluído de xeito natural. O segundo enfoque está baseado no modelo de Cahn-Hilliard [84], o cal é acoplado coas ecuacións de Navier-Stokes incompresibles. O resultado é un modelo que describe fluxos de dúas compoñentes inmiscibles con tensión superficial. En ambos casos asumimos fluídos newtonianos.

- O modelo NSK non require ningún tipo de estabilización. Sen embargo, para o modelo NSCH, adoptamos unha formulación multiescala variacional e baseada no residuo [15].

- A estrutura está gobernada en todos os casos polas ecuacións non lineais da elastodinámica, e tratada como un sólido hiperelástico. Empréganse dous modelos diferentes, un modelo Neo-Hookeano e un modelo de Saint Venant (ver, por exemplo, [128]). De calquera xeito, outros modelos materiais para o sólido poderían ser facilmente implementados nos algoritmos propostos nesta tese.

- Emprégase un enfoque Arbitrario Lagranxiano-Euleriano [57,58,101] para os modelos de interacción fluído-estrutura propostos. ALE é unha técnica de malla móbil na que as discretizacións do sólido e do fluído coinciden ó longo da interface. Isto permite solucións precisas preto da interface e a exacta satisfacción das condicións de compatibilidade. Sen embargo, a medida que a interface evoluciona, a malla do

fluído necesita ser actualizada. Isto conséguese mediante a resolución dun problema de contorno no que as condicións Dirichlet son os desprazamentos do sólido ó longo da interface.

- O método de Análise Isoxeométrico baseado en NURBS [42] é usado para a discretización espacial tanto do sólido como do fluído. IGA pode entenderse como unha xeneralización do método de elementos finitos que posúe importantes propiedades matemáticas como precisión de alto orde, robustez, a habilidade de ser refinados mediante a inserción de nodos e a elevación da orde, e continuidade global de alto orde. Esta última propiedade é especialmente útil á hora de tratar os nosos problemas, pois as técnicas de campos de fase inclúen operadores de alto orde na forma primaria que, doutro xeito, deberían ser tratados adoptando unha formulación mixta. Ademais, IGA baseado en NURBS permite unha representación máis exacta de obxectos complexos que o método FEM e, en concreto, pode representar de xeito exacto cilindros, esferas, e toroides.

- Adóptase una formulación monolítica quasi-directa para a solución dos problemas FSI, isto é, as ecuacións do fluído e do sólido son resoltas dun xeito acoplado, mentres que o movemento da malla é resolto separadamente usando como input datos procedentes da resolución do sólido e o fluído. Adoptar un enfoque monolítico impón implicitamente a compatibilidade de traccións na interface. No relativo á integración no tempo usamos un esquema α xeneralizado [40]. O sistema non lineal de ecuacións é resolto usando un procedemento Newton-Raphson iterativo, o cal da lugar a un algoritmo predictor-multicorrector de dúas fases. O sistema lineal resultante é resolto usando un método GMRES precondicionado [151].

- O código FSI empregado nesta tese foi inicialmente implementado en código Fortran e usando as nosas propias librerías e implementación en paralelo. Posteriormente, desenvolveuse un código en linguaxe C usando como base PetIGA [48], o cal engade a capacidade de discretización das NURBS e a integración de formas a PETSc [150]. Isto resultou nun código moito máis flexible e eficiente, o cal pode empregar unha gran variedade de resolvedores e precondicionadores.

O modelos antes mencionados foron aplicados a unha grande variedade de problemas que involucran fluídos complexos. Entre eles, cabe destacar as seguintes aplicacións

- Tensioactivos ou surfactantes. Os surfactantes son compostos que son atraídos polas interfaces presentes nun sistema. Teñen a habilidade de reducir o traballo requirido para xerar a interface, isto é, reducir a tensión superficial asociada a dita interface. Esta particularidade fai dos surfactantes unha das substancias máis usadas na industria química. Na literatura, varios modelos foron propostos para describir os

fenómenos de absorción dos surfactantes en fluxos inmiscibles de dous compoñentes. A influencia de surfactantes en fluídos de dúas fases e un só compoñente permanece practicamente inexplorada, cando menos, dende o punto de vista computacional. Nesta tese, nos propuxemos unha teoría de fluídos complexos que permite a espontánea vaporización e condensación e que captura a dinámica dos tensioactivos presentes nas interfaces. Creemos firmemente que a nosa teoría pode chegar a ser unha ferramenta útil para a comprensión do comportamento destes compostos en fenómenos de transición de fase.

- Implosión debida a cambios de fase. O colapso implosivo de estruturas cheas de vapor é estudiado cunha teoría de FSI termicamente acoplada e baseada nas ecuacións de Navier-Stokes-Korteweg. En concreto, centrámonos no colapso cara ó interior de estruturas delgadas, nas cales unha variación térmica transforma o vapor presente no interior en líquido, reducindo así a presión interna e provocando a implosión do sólido.

- Tensotaxe. Usamos o noso modelo FSI baseado nas ecuacións NSK para simular o movemento de gotas debido a gradientes de deformación do substrato no que se apoian. Este proceso, coñecido como tensotaxe, foi previamente observado en células. Aquí, nós mostramos que simples gotas líquidas poden tamén experimentar tensotaxe, suxerindo que a mecánica pode xogar un papel importante neste proceso. O noso modelo semella ser unha ferramenta prometedora para un maior entendemento do papel que xogan as forzas de capilaridade neste mecanismo.

- Coalescencia de gotas. O modelo NSCH para fluxos inmiscibles é usado para o modelado da coalescencia de dúas gotas de auga. Comparamos o radio do menisco formado durante este proceso co comportamento observado en experimentos e suxerido en modelos teóricos. O propósito é validar o noso modelo, xa que non existen estándares de referencia amplamente aceptados para esta teoría.

- Elastocapilaridade. A pequenas escalas, a tensión superficial pode chegar a ser dominante e deformar estruturas esveltas e/ou brandas, dando lugar a unha gran variedade de problemas FSI moi interesantes. Nós usamos a teoría FSI de fluídos inmiscibles para estudar algúns destes problemas. O primeiro é a deformación de substratos brandos debido ás forzas de capilaridade de gotas líquidas. Usamos este problema para validar o noso modelo. Unha gota de glicerina é depositada nun substrato. Medimos os desprazamentos verticais causados no substrato e comparámolos con datos experimentais. No segundo exemplo, simulamos origami por elastocapilaridade, isto é, o envolvemento de membranas delgadas entorno a gotas líquidas. Finalmente, estudamos a flexión de micropilares baixo a acción de forzas capilares,

para o cal, colocamos unha gota líquida entre dous micropilares elásticos inicialmente paralelos

11.4 Futuras liñas de traballo

O traballo presentado nesta tese abriu as portas a varias liñas de investigación que deberían ser tratadas no futuro. Entre elas, destacamos as seguintes:

- A teoría de fluídos complexos proposta para o modelado de tensioactivos en fluxos dun compoñente e dúas fases debería ser estendida a unha teoría termicamente acoplada. Isto permitiría o estudo de escenarios moito máis complexos onde os surfactantes alteren transformacións de fase inducidas por cambios de temperatura. Sería ademais interesante calibrar e validar o modelo usando datos experimentais.

- As implosións inducidas por cambios de fase poden levar ó colapso violento e rápido da estrutura, producindo grandes compresións e deformacións. Coa técnica FSI adoptada, é dicir, o método Arbitrario Lagranxiano-Euleriano, isto resultaría en distorsións significativas no sólido e na malla do fluído, e sería necesario realizar procesos de remallado. Nós intentamos facer fronte a este desafío centrándonos en implosións moderadamente fortes. Sen embargo, sería interesante simular implosións fortes, xa sexa usando o método de elementos finitos e remallando cando é necesario ou adoptando unha técnica FSI diferente, por exemplo, unha técnica inmersa. Outro obxectivo futuro debería ser a implementación de un modelo capaz de simular o contacto entre sólidos, deformación plástica e fractura.

- Usamos o modelo FSI baseado nas ecuacións de NSK para mostrar que as gotas tamén poden experimentar tensotaxe. Sen embargo, outros mecanismos de movemento celular teñen sido observados en gotas. é o caso da durotaxe ou movemento debido a gradientes de rixidez do substrato. O noso modelo semella ser unha ferramenta adecuada para analizar este mecanismo e suxerir escenarios que son difíciles de estudar experimentalmente.

- O modelo FSI baseado nas ecuacións de NSCH foi estabilizado adoptando unha formulación variacional multiescala baseada no residuo. No futuro, temos como obxectivo usar espazos B-Spline diverxentes e conformantes para obter campos de velocidades discretos de diverxencia nula en cada punto, evitando así a necesidade de calquera tipo de estabilización. Sería tamén interesante acoplar o noso modelo cunha teoría de fractura e ser así capaz de simular fractura capilar.

Bibliography

[1] D. G. A. L. Aarts, H. N. W. Lekkerkerker, H. Guo, G. H. Wegdam, and D. Bonn. Hydrodynamics of droplet coalescence. *Physical Review Letters*, 95:164503, 2005.

[2] S. Aland and A. Voigt. Simulation of common features and differences of surfactant-based and solid-stabilized emulsions. *Colloids and Surfaces A: Physicochemical and Engineering Aspects*, 413:298–302, 2012.

[3] D. M. Anderson, G. B. McFadden, and A. A. Wheeler. Diffuse-interface methods in fluid mechanics. *Annual Review of Fluid Mechanics*, 30:139–165, 1998.

[4] A. Baskaran, Z. Hu, J. S. Lowengrub, C. Wang, S. M. Wise, and P. Zhou. Energy stable and efficient finite-difference nonlinear multigrid schemes for the modified phase field crystal equation. *Journal of Computational Physics*, 250:270–292, 2013.

[5] G. K. Batchelor. *An introduction to fluid dynamics*. Cambridge University Press, 2000.

[6] Y. Bazilevs, L. Beirão Da Veiga, J.A. Cottrell, T.J.R. Hughes, and G. Sangalli. Isogeometric Analysis: Approximation, stability and error estimates for h-refined meshes. *Mathematical Models and Methods in Applied Sciences*, 16(07):1031–1090, 2006.

[7] Y. Bazilevs, V.M. Calo, J.A. Cottrell, J.A. Evans, T.J.R. Hughes, S. Lipton, M.A. Scott, and T.W. Sederberg. Isogeometric Analysis using T-splines. *Computer Methods in Applied Mechanics and Engineering*, 199(58):229 – 263, 2010.

[8] Y. Bazilevs, V.M. Calo, T.J.R. Hughes, and Y. Zhang. Isogeometric Fluid-Structure Interaction: Theory, algorithms, and computations. *Computational Mechanics*, 43(1):3–37, 2008.

[9] Y. Bazilevs, V.M. Calo, Y. Zhang, and T.J.R. Hughes. Isogeometric Fluid-Structure Interaction analysis with applications to arterial blood flow. *Computational Mechanics*, 38(4-5):310–322, 2006.

[10] Y. Bazilevs, M.-C. Hsu, D.J. Benson, S. Sankaran, and A.L. Marsden. Computational Fluid-Structure Interaction: Methods and application to a total cavopulmonary connection. *Computational Mechanics*, 45(1):77–89, 2009.

[11] Y. Bazilevs, M.-C. Hsu, J. Kiendl, R. Wüchner, and K.-U. Bletzinger. 3D simulation of wind turbine rotors at full scale. part II: Fluid–structure interaction modeling with composite blades. *International Journal for Numerical Methods in Fluids*, 65(1-3):236–253, 2011.

[12] Y. Bazilevs, M.-C. Hsu, Y. Zhang, W. Wang, T. Kvamsdal, S. Hentschel, and J.G. Isaksen. Computational vascular Fluid-Structure Interaction: Methodology and application to cerebral aneurysms. *Biomechanics and Modeling in Mechanobiology*, 9(4):481–498, 2010.

[13] Y. Bazilevs, G. Moutsanidis, J. Bueno, K. Kamran, D. Kamensky, M.C. Hillman, H. Gomez, and J.S. Chen. A New Formulation for Air-Blast Fluid-Structure Interaction Using an Immersed Approach: Part II – Coupling of IGA and Meshfree Discretizations. *Computational Mechanics*, pages 1–16, 2017.

[14] Y. Bazilevs, K. Takizawa, and T. E. Tezduyar. Challenges and directions in computational fluid-structure interaction. *Mathematical Models and Methods in Applied Sciences*, 23:215–221, 2013.

[15] Y. Bazilevs, K. Takizawa, and T.E. Tezduyar. *Computational Fluid-Structure Interaction. Methods and Applications*. Wiley, 2013.

[16] Y. Bazilevs, K. Takizawa, T.E. Tezduyar, M.-C. Hsu, N. Kostov, and S. McIntyre. Aerodynamic and FSI Analysis of Wind Turbines with the ALE-VMS and ST-VMS Methods. *Archives of Computational Methods in Engineering*, 21(4):359–398, 2014.

[17] T. Biben, K. Kassner, and C. Misbah. Phase-field approach to three-dimensional vesicle dynamics. *Physical Review E*, 72:041921, Oct 2005.

[18] J. Bico, B. Roman, L. Moulin, and A. Boudaoud. Adhesion: elastocapillary coalescence in wet hair. *Nature*, 432(7018):690–690, 2004.

[19] I. B. Bischofs and U. S. Schwarz. Cell organization in soft media due to active mechanosensing. *Proceedings of the National Academy of Sciences*, 100(16):9274–9279, 2003.

[20] M.J. Borden, T.J.R. Hughes, C.M. Landis, and C.V. Verhoosel. A higher-order phase-field model for brittle fracture: Formulation and analysis within the isogeometric analysis framework. *Computer Methods in Applied Mechanics and Engineering*, 273:100 – 118, 2014.

[21] M.J. Borden, C.V. Verhoosel, M.A. Scott, T.J.R. Hughes, and C.M. Landis. A phase-field description of dynamic brittle fracture. *Computer Methods in Applied Mechanics and Engineering*, 217220(0):77 – 95, 2012.

[22] J. B. Bostwick and K. E. Daniels. Capillary fracture of soft gels. *Physical Review E*, 88(4):042410, 2013.

[23] T. Brattain. Railroad tank car vacuum implosion, 2008. Retrieved from `https://www.youtube.com/watch?v=Zz95_VvTxZM`.

[24] A.J. Bray. Theory of phase ordering kinetics. *Physica A: Statistical Mechanics and its Applications*, 194(14):41 – 52, 1993.

[25] A. N. Brooks and T.J.R. Hughes. Streamline upwind/petrov-galerkin formulations for convection dominated flows with particular emphasis on the incompressible navier-stokes equations. *Computer Methods in Applied Mechanics and Engineering*, 32(1-3):199–259, 1982.

[26] J. Bueno, Y. Bazilevs, R. Juanes, and H. Gomez. Droplet motion driven by tensotaxis. *Extreme Mechanics Letters*, 13:10 – 16, 2017.

[27] J. Bueno, C. Bona-Casas, Y. Bazilevs, and H. Gomez. Interaction of complex fluids and solids: Theory, algorithms and application to phase-change-driven implosion. *Computational Mechanics*, 55(6):1105–1118, 2015.

[28] J. Bueno, H. Casquero, Y. Bazilevs, and H. Gomez. Three-dimensional dynamic simulation of elastocapillarity. Accepted for publication. DOI: 10.1007/s11012-017-0667-4, 2017.

[29] J. Bueno and H. Gomez. Liquid-vapor transformations with surfactants. phase-field model and isogeometric analysis. *Journal of Computational Physics*, 321:797 – 818, 2016.

[30] J. Bueno, I. Starodumov, H. Gomez, P. Galenko, and D. Alexandrov. Three dimensional structures predicted by the modified phase field crystal equation. *Computational Materials Science*, 111:310 – 312, 2016.

[31] G. Caginalp. Stefan and hele-shaw type models as asymptotic limits of the phase-field equations. *Physical Review A*, 39:5887–5896, Jun 1989.

[32] H. Casquero, C. Bona-Casas, and H. Gomez. A NURBS-based immersed methodology for fluid-structure interaction. *Computer Methods in Applied Mechanics and Engineering*, 284:943–970, 2015.

[33] H. Casquero, L. Lei, J. Zhang, A. Reali, and H. Gomez. Isogeometric collocation using analysis-suitable T-splines of arbitrary degree. *Computer Methods in Applied Mechanics and Engineering*, 301:164 – 186, 2016.

[34] H. Casquero, L. Lei, Y. Zhang, A. Reali, J. Kiendl, and H. Gomez. Arbitrary-degree T-splines for isogeometric analysis of fully nonlinear Kirchhoff-Love shells. *Computer-Aided Design*, 82:140–153, 2017.

[35] H. Casquero, L. Liu, C. Bona-Casas, Y. Zhang, and H. Gomez. A hybrid variational-collocation immersed method for fluid-structure interaction using unstructured T-splines. *International Journal for Numerical Methods in Engineering*, 105(11):855–880, 2016.

[36] H.D. Ceniceros. The effects of surfactants on the formation and evolution of capillary waves. *Physics of Fluids*, 15(1):245–256, 2003.

[37] E. Cerda and L. Mahadevan. Geometry and physics of wrinkling. *Physical Review Letters*, 90(7):074302, 2003.

[38] N. Chakrapani, B. Wei, A. Carrillo, P. M. Ajayan, and R. S. Kane. Capillarity-driven assembly of two-dimensional cellular carbon nanotube foams. *Proceedings of the National Academy of Sciences*, 101(12):4009–4012, 2004.

[39] L.Q. Chen. Phase-field models for microstructure evolution. *Annual Review of Materials Research*, 32(1):113–140, 2002.

[40] J. Chung and G.M. Hulbert. A time integration algorithm for structural dynamics with improved numerical dissipation: The generalized-α method. *Journal of Applied Mechanics*, 60:371–375, 1993.

[41] B. D. Coleman and W. Noll. The thermodynamics of elastic materials with heat conduction and viscosity. *Archive for Rational Mechanics and Analysis*, 13(1):167–178, 1963.

[42] J.A. Cottrell, T.J.R. Hughes, and Y. Bazilevs. *Isogeometric Analysis: Toward Integration of CAD and FEA*. Wiley, 2009.

[43] J.A. Cottrell, T.J.R. Hughes, and A. Reali. Studies of refinement and continuity in Isogeometric structural analysis. *Computer Methods in Applied Mechanics and Engineering*, 196(4144):4160 – 4183, 2007.

[44] J.A. Cottrell, A. Reali, Y. Bazilevs, and T.J.R. Hughes. Isogeometric Analysis of structural vibrations. *Computer Methods in Applied Mechanics and Engineering*, 195(4143):5257 – 5296, 2006.

[45] M. G. Cox. The numerical evaluation of B-splines. *IMA Journal of Applied Mathematics*, 10(2):134–149, 1972.

[46] L. Cueto-Felgueroso and R. Juanes. Nonlocal interface dynamics and pattern formation in gravity-driven unsaturated flow through porous media. *Physical Review Letters*, 101:244504, 2008.

[47] L. Cueto-Felgueroso and R. Juanes. Macroscopic phase-field modeling of partial wetting: bubbles in a capillary tube. *Physical Review Letters*, 108:144502, 2012.

[48] L. Dalcin, N. Collier, P. Vignal, A.M.A. Crtes, and V.M. Calo. Petiga: A framework for high-performance isogeometric analysis. *Computer Methods in Applied Mechanics and Engineering*, 308:151 – 181, 2016.

[49] C. de Boor. On calculating with B-splines. *Journal of Approximation Theory*, 6(1):50 – 62, 1972.

[50] P. G. de Gennes. Wetting: statics and dynamics. *Review of Modern Physics*, 57:827–863, 1985.

[51] J. De Hart, G.W.M. Peters, P.J.G. Schreurs, and F.P.T. Baaijens. A three-dimensional computational analysis of fluid–structure interaction in the aortic valve. *Journal of Biomechanics*, 36(1):103–112, 2003.

[52] L. Dedè, M.J. Borden, and T.J.R. Hughes. Isogeometric analysis for topology optimization with a phase field model. *Archives of Computational Methods in Engineering*, 19(3):427–465, 2012.

[53] R. Deiterding and S. Wood. Parallel adaptive fluid–structure interaction simulation of explosions impacting on building structures. *Computers and Fluids*, 88:719–729, 2013.

[54] M. DeVolder and A. J. Hart. Engineering hierarchical nanostructures by elastocapillary self-assembly. *Angewandte Chemie International Edition*, 52(9):2412–2425, 2013.

[55] R. Dhote, H. Gomez, R. Melnik, and J. Zu. Isogeometric analysis of coupled thermomechanical phase-field models for shape memory alloys using distributed computing. *Procedia Computer Science*, 18:1068 – 1076, 2013. 2013 International Conference on Computational Science.

[56] D. Diehl. *Higher Order Schemes for Simulation of Compressible Liquid-Vapor Flow with Phase Change*. PhD thesis, Albert-Ludwigs-Universitt Freiburg, 2007.

[57] J. Donea and A. Huerta. *Finite Element Methods for Flow Problems*. Wiley, 2003.

[58] J. Donea, A. Huerta, J.-Ph. Ponthot, and A. Rodrguez-Ferran. *Encyclopedia of Computational Mechanics. Arbitrary Lagrangian-Eulerian Methods.*, volume 1, chapter 14. John Wiley & Sons, Ltd, 2004.

[59] P. G. Drazin and W. H. Reid. *Hydrodynamic stability.* Cambridge University Press, 2004.

[60] M. A. Drumright-Clarke and Y. Renardy. The effect of insoluble surfactant at dilute concentration on drop breakup under shear with inertia. *Physics of Fluids*, 16(1):14–21, 2004.

[61] K. Dumont, J. Vierendeels, R. Kaminsky, G. Van Nooten, P. Verdonck, and D. Bluestein. Comparison of the hemodynamic and thrombogenic performance of two bileaflet mechanical heart valves using a cfd/fsi model. *Journal of Biomechanical Engineering*, 129(4):558–565, 2007.

[62] C. Duprat, A. D. Bick, P. B. Warren, and H. A. Stone. Evaporation of drops on two parallel fibers: Influence of the liquid morphology and fiber elasticity. *Langmuir*, 29(25):7857–7863, 2013. PMID: 23705986.

[63] C. Duprat, S. Protiere, A. Y. Beebe, and H. A. Stone. Wetting of flexible fibre arrays. *Nature*, 482(7386):510–513, 2012.

[64] J. Eggers, J. R. Lister, and H. A. Stone. Coalescence of liquid drops. *Journal of Fluid Mechanics*, 401:293–310, 1999.

[65] K. R. Elder and M. Grant. Modeling elastic and plastic deformations in nonequilibrium processing using phase field crystals. *Physical Review E*, 70(5):051605, 2004.

[66] K. R. Elder, N. Provatas, J. Berry, P. Stefanovic, and M. Grant. Phase-field crystal modeling and classical density functional theory of freezing. *Physical Review B*, 75(6):064107, 2007.

[67] H. Emmerich. *The Diffuse Interface Approach in Materials Science: Thermodynamic Concepts and Applications of Phase-Field Models.* Springer Publishing Company, Incorporated, 2011.

[68] S. Engblom, M. Do-Quang, G. Amberg, and A.K. Tornberg. On diffuse interface modeling and simulation of surfactants in two-phase fluid flow. *Communications in Computational Physics*, 14:879–915, 2013.

[69] C. Farhat, M. Lesoinne, and P. Le Tallec. Load and motion transfer algorithms for fluid/structure interaction problems with non-matching discrete interfaces: Momentum and energy conservation, optimal discretization and application to aeroelas-

ticity. *Computer Methods in Applied Mechanics and Engineering*, 157(1-2):95–114, 1998.

[70] C. Farhat, K. G. Van der Zee, and P. Geuzaine. Provably second-order time-accurate loosely-coupled solution algorithms for transient nonlinear computational aeroelasticity. *Computer Methods in Applied Mechanics and Engineering*, 195(17):1973–2001, 2006.

[71] R.J. Farn. *Chemistry and Technology of Surfactants.* Wiley, 2008.

[72] P. C. Fife. *Dynamics of internal layers and diffusive interfaces.* SIAM, 1988.

[73] A.T. Florence and J.M.N. Gillan. Biological implications of the use of surfactants in medicines: and the biphasic effects of surfactants in biological systems. *Pesticide Science*, 6(4):429–439, 1975.

[74] I. Fonseca, M. Morini, and V. Slastikov. Surfactants in foam stability: A phase-field model. *Archive for Rational Mechanics and Analysis*, 183(3):411–456, 2007.

[75] H.B. Frieboes, B.J.S. Lowengrub, S. Wise, B.X. Zheng, B.P. Macklin, E.L. Bearer, and V. Cristini A. Computer simulation of glioma growth and morphology. Neuroimage 37. *NeuroImage*, pages 59–70, 2007.

[76] E. Fried and M.E. Gurtin. Dynamic solid-solid transitions with phase characterized by an order parameter. *Physica D: Nonlinear Phenomena*, 72(4):287 – 308, 1994.

[77] P. K Galenko, D. A. Danilov, and V. G. Lebedev. Phase-field-crystal and Swift-Hohenberg equations with fast dynamics. *Physical Review E*, 79(5):051110, 2009.

[78] P. K. Galenko and K. R. Elder. Marginal stability analysis of the phase field crystal model in one spatial dimension. *Physical Review B*, 83(6):064113, 2011.

[79] P.K. Galenko, H. Gomez, N.V. Kropotin, and K.R. Elder. Unconditionally stable method and numerical solution of the hyperbolic phase-field crystal equation. *Physical Review E*, 88(1):013310, 2013.

[80] H. Garcke, K.F. Lam, and B. Stinner. Diffuse interface modelling of soluble surfactants in two-phase flow. *Communications in Mathematical Sciences*, 12:1475–1522, 2014.

[81] W.M. Gelbart and A. Ben-Shaul. The new science of complex fluids. *The Journal of Physical Chemistry*, 100(31):13169–13189, 1996.

[82] J.W. Gibbs. *On the Equilibrium of Heterogeneous Substances.* 1876.

[83] J. Giordano, G. Jourdan, Y. Burtschell, M. Medale, D.E. Zeitoun, and L. Houas. Shock wave impacts on deforming panel, an application of fluid-structure interaction. *Shock Waves*, 14(1-2):103–110, 2005.

[84] H. Gomez, V.M. Calo, Y. Bazilevs, and T.J.R. Hughes. Isogeometric Analysis of the Cahn-Hilliard phase-field model. *Computer Methods in Applied Mechanics and Engineering*, 197:43334352, 2008.

[85] H. Gomez, L. Cueto-Felgueroso, and R. Juanes. Three-dimensional simulation of unstable gravity-driven infiltration of water into a porous medium. *Journal of Computational Physics*, 238:217–239, 2013.

[86] H. Gomez and L. De Lorenzis. The variational collocation method. *Computer Methods in Applied Mechanics and Engineering*, 309:152–181, 2016.

[87] H. Gomez and T.J.R. Hughes. Provably unconditionally stable, second-order time-accurate, mixed variational methods for phase-field models. *Journal of Computational Physics*, 230(13):5310–5327, 2011.

[88] H. Gomez, T.J.R. Hughes, X. Nogueira, and V.M. Calo. Isogeometric Analysis of the isothermal Navier-Stokes-Korteweg equations. *Computer Methods in Applied Mechanics and Engineering*, 199(25-28):1828–1840, 2010.

[89] H. Gomez, A. Reali, and G. Sangalli. Accurate, efficient, and (iso) geometrically flexible collocation methods for phase-field models. *Journal of Computational Physics*, 262:153–171, 2014.

[90] H. Gomez and K. van der Zee. *Encyclopedia of Computational Mechanics. Computational phase-field modeling.* John Wiley & Sons, Ltd, 2017.

[91] E. Hachem, S. Feghali, R. Codina, and T. Coupez. Anisotropic adaptive meshing and monolithic variational multiscale method for fluid–structure interaction. *Computers and Structures*, 122:88–100, 2013.

[92] E. Hachem, S. Feghali, R. Codina, and T. Coupez. Immersed stress method for fluid–structure interaction using anisotropic mesh adaptation. *International Journal for Numerical Methods in Engineering*, 94(9):805–825, 2013.

[93] E. Hachem, S. Feghali, T. Coupez, and R. Codina. A three-field stabilized finite element method for fluid-structure interaction: elastic solid and rigid body limit. *International Journal for Numerical Methods in Engineering*, 104(7):566–584, 2015.

[94] H.L. Halliday. Surfactants: past, present and future. *Journal of Perinatology*, 28:S47–S56, 2008.

[95] L. Heltai, J. Kiendl, A. DeSimone, and A. Reali. A natural framework for isogeometric fluid–structure interaction based on BEM–shell coupling. *Computer Methods in Applied Mechanics and Engineering*, 2016.

[96] M.-C. Hsu and Y. Bazilevs. Fluid-Structure Interaction modeling of wind turbines: Simulating the full machine. *Computational Mechanics*, 50(6):821–833, 2012.

[97] M.-C. Hsu, D. Kamensky, Y. Bazilevs, M. S. Sacks, and T.J.R. Hughes. Fluid–structure interaction analysis of bioprosthetic heart valves: significance of arterial wall deformation. *Computational mechanics*, 54(4):1055–1071, 2014.

[98] J. Huang, M. Juszkiewicz, W. H. de Jeu, E. Cerda, T. Emrick, N. Menon, and T. P. Russell. Capillary wrinkling of floating thin polymer films. *Science*, 317(5838):650–653, 2007.

[99] T.J.R. Hughes. *The Finite Element Method: linear static and dynamic finite element analysis*. Dover Civil and Mechanical Engineering Series. Dover Publications, 2000.

[100] T.J.R. Hughes, J.A. Cottrell, and Y. Bazilevs. Isogeometric Analysis: CAD, Finite Elements, NURBS, exact geometry and mesh refinement. *Computer Methods in Applied Mechanics and Engineering*, 194(39-41):4135 – 4195, 2005.

[101] T.J.R. Hughes, W.K. Liu, and T.K. Zimmermann. Lagrangian-Eulerian Finite Element formulation for incompressible viscous flows. *Computer Methods in Applied Mechanics and Engineering*, 29(3):329 – 349, 1981.

[102] T.J.R. Hughes, A. Reali, and G. Sangalli. Efficient quadrature for nurbs-based isogeometric analysis. *Computer Methods in Applied Mechanics and Engineering*, 199(5):301–313, 2010.

[103] A Jaatinen and T Ala-Nissila. Extended phase diagram of the three-dimensional phase field crystal model. *Journal of Physics: Condensed Matter*, 22(20):205402, 2010.

[104] A.J. James and J. Lowengrub. A surfactant-conserving volume-of-fluid method for interfacial flows with insoluble surfactant. *Journal of Computational Physics*, 201(2):685–722, 2004.

[105] K.E. Jansen, C.H. Whiting, and G.M. Hulbert. A generalized-α method for integrating the filtered Navier-Stokes equations with a stabilized Finite Element Method. *Computer Methods in Applied Mechanics and Engineering*, 190(34):305 – 319, 2000.

[106] J.H. Jeong, N. Goldenfeld, and J.A. Dantzig. Phase field model for three-dimensional dendritic growth with fluid flow. *Physical Review E*, 64:041602, 2001.

[107] A.A. Johnson and T.E. Tezduyar. Mesh update strategies in parallel finite element computations of flow problems with moving boundaries and interfaces. *Computer Methods in Applied Mechanics and Engineering*, 119:73–94, 1994.

[108] R. Kamakoti and W. Shyy. Fluid–structure interaction for aeroelastic applications. *Progress in Aerospace Sciences*, 40(8):535–558, 2004.

[109] D. Kamensky, M.-C. Hsu, D. Schillinger, J. A. Evans, A. Aggarwal, Y. Bazilevs, M. S. Sacks, and T.J.R. Hughes. An immersogeometric variational framework for fluid-structure interaction: Application to bioprosthetic heart valves. *Computer Methods in Applied Mechanics and Engineering*, 284:1005–1053, 2015.

[110] K. Kamran, R. Rossi, E. Oñate, and S.R. Idelshon. A compressible lagrangian framework for modeling the fluid–structure interaction in the underwater implosion of an aluminum cylinder. *Mathematical Models and Methods in Applied Sciences*, 23(02):339–367, 2013.

[111] K. Kamran, R. Rossi, E. Oñate, and S.R. Idelsohn. A compressible lagrangian framework for the simulation of the underwater implosion of large air bubbles. *Computer Methods in Applied Mechanics and Engineering*, 255:210–225, 2013.

[112] S. Khatri and A.-K. Tornberg. An embedded boundary method for soluble surfactants with interface tracking for two-phase flows. *Journal of Computational Physics*, 256:768 – 790, 2014.

[113] J. Kiendl, M. Ambati, L. De Lorenzis, H. Gomez, and A. Reali. Phase-field description of brittle fracture in plates and shells. *Computer Methods in Applied Mechanics and Engineering*, 312:374–394, 2016.

[114] Y.T. Kim, N. Provatas, N.D. Goldenfeld, and J.A. Dantzig. Universal dynamics of phase-field models for dendritic growth. *Physical Review E*, 59:2546, 1999.

[115] R.J. King. Pulmonary surfactant. *Journal of Applied Physiology*, 53(1):1–8, 1982.

[116] R. Kobayashi. A numerical approach to three-dimensional dendritic solidification. *Experimental Mathematics*, 3(1):59–81, 1994.

[117] H. Lamb. *Hydrodynamics*. Courier Corporation, 1945.

[118] R.G. Larson. *The Structure and Rheology of Complex Fluids*. Topics in Chemical Engineering. OUP USA, 1999.

[119] S.-L. Lin, J.-C. Yang, K.-N. Ho, C.-H. Wang, C.-W. Yeh, and H.-M. Huang. Effects of compressive residual stress on the morphologic changes of fibroblasts. *Medical & Biological Engineering & Computing*, 47(12):1273–1279, 2009.

[120] H. Liu and Y. Zhang. Phase-field modeling droplet dynamics with soluble surfactants. *Journal of Computational Physics*, 229(24):9166 – 9187, 2010.

[121] J. Liu. *Thermodynamically consistent modeling and simulation of multiphase flows*. PhD thesis, The University of Texas at Austin, 2014.

[122] J. Liu, H. Gomez, J.A. Evans, T.J.R. Hughes, and C.M. Landis. Functional entropy variables: A new methodology for deriving thermodynamically consistent algorithms for complex fluids, with particular reference to the isothermal Navier-Stokes-Korteweg equations. *Journal of Computational Physics*, 248:47–86, 2013.

[123] C.-M. Lo, H.-B. Wang, M. Dembo, and Y.-L. Wang. Cell movement is guided by the rigidity of the substrate. *Biophysical Journal*, 79(1):144–152, 2000.

[124] C.C. Long, M. Esmaily-Moghadam, A.L. Marsden, and Y. Bazilevs. Computation of residence time in the simulation of pulsatile ventricular assist devices. *Computational Mechanics*, 54:911–919, 2014.

[125] C.C. Long, A.L. Marsden, and Y. Bazilevs. Fluid–structure interaction simulation of pulsatile ventricular assist devices. *Computational Mechanics*, 52:971–981, 2013.

[126] C.C. Long, A.L. Marsden, and Y. Bazilevs. Shape optimization of pulsatile ventricular assist devices using FSI to minimize thrombotic risk. *Computational Mechanics*, 54:921–932, 2014.

[127] J. S. Lowengrub, A. Rätz, and A. Voigt. Phase-field modeling of the dynamics of multicomponent vesicles: Spinodal decomposition, coarsening, budding, and fission. *Physical Review E*, 79(3):031926, 2009.

[128] J. E. Marsden and T. J. R. Hughes. *Mathematical Foundations of Elasticity*. Prentice-Hall, Englewood Cliffs, NJ, 1983. Reprinted with corrections, Dover, New York, 1994.

[129] C Miehe, F Welschinger, and M Hofacker. Thermodynamically consistent phase-field models of fracture: Variational principles and multi-field fe implementations. *International Journal for Numerical Methods in Engineering*, 83(10):1273–1311, 2010.

[130] R. Mittal and G. Iaccarino. Immersed boundary methods. *Annual Review of Fluid Mechanics*, 37:239–261, 2005.

[131] P. Moreo, J. M. García-Aznar, and M. Doblaré. Modeling mechanosensing and its effect on the migration and proliferation of adherent cells. *Acta Biomaterialia*, 4(3):613–621, 2008.

[132] M. Muradoglu and G. Tryggvason. A front-tracking method for computation of interfacial flows with soluble surfactants. *Journal of Computational Physics*, 227(4):2238–2262, 2008.

[133] D. Myers. *An Overview of Surfactant Science and Technology.* John Wiley & Sons, Inc., 2005.

[134] A. Pahlavan, L. Cueto-Felgueroso, and R. Juanes. Thin films in partial wetting: internal selection of contact-line dynamics. *Physical Review Letters*, 115:034502, 2015.

[135] O. Penrose and P.C. Fife. Thermodynamically consistent models of phase-field type for the kinetic of phase transitions. *Physica D: Nonlinear Phenomena*, 43(1):44 – 62, 1990.

[136] C. S. Peskin. The immersed boundary method. *Acta Numerica*, 11:479–517, 2002.

[137] L. Piegl and W. Tiller. *The NURBS book.* Springer Science & Business Media, 2012.

[138] S. Piperno, C. Farhat, and B. Larrouturou. Partitioned procedures for the transient solution of coupled aroelastic problems part i: Model problem, theory and two-dimensional application. *Computer Methods in Applied Mechanics and Engineering*, 124(1-2):79–112, 1995.

[139] N. V. Plechkova and K. R. Seddon. Applications of ionic liquids in the chemical industry. *Chemical Society Reviews*, 37(1):123–150, 2008.

[140] S.D. Poisson. *Nouvelle théorie de l'action capillaire.* Bachelier père et fils, 1831.

[141] N. Provatas and K. Elder. *Phase-Field Methods in Materials Science and Engineering.* Wiley-VCH Verlag GmbH & Co. KGaA, 2010.

[142] C. Py, P. Reverdy, L. Doppler, J. Bico, B. Roman, and C. N. Baroud. Capillary origami: Spontaneous wrapping of a droplet with an elastic sheet. *Physical Review Letters*, 98:156103, Apr 2007.

[143] O. Raccurt, F. Tardif, F. A. d'Avitaya, and T. Vareine. Influence of liquid surface tension on stiction of soi mems. *Journal of Micromechanics and Microengineering*, 14(7):1083, 2004.

[144] A.S.D. Rallu. *A Multiphase Fluid-Structure Computational Framework for Underwater Implosion Problems.* PhD thesis, Standford University, 2009.

[145] M. Rivetti. Elastocapillary wrapping driven by drop impact, 2011. Retrieved from `https://www.youtube.com/watch?v=-FewxlkYOME`.

[146] L. Rodrigues, I.M. Banat, J. Teixeira, and R. Oliveira. Biosurfactants: potential applications in medicine. *Journal of Antimicrobial Chemotherapy*, 57(4):609–618, 2006.

[147] B. Roman and J. Bico. Elasto-capillarity: deforming an elastic structure with a liquid droplet. *Journal of Physics: Condensed Matter*, 22(49):493101, 2010.

[148] M.J. Rosen. *Surfactants in Emerging Technology.* Surfactant Science. Taylor & Francis, 1987.

[149] M.J. Rosen. *Characteristic Features of Surfactants*, pages 1–33. John Wiley & Sons, Inc., 2004.

[150] S. Balay et al. PETSc users manual. Technical Report ANL-95/11 - Revision 3.6, Argonne National Laboratory, 2015.

[151] Y. Saad and M.H. Schultz. GMRES: A generalized minimal residual algorithm for solving nonsymmetric linear systems. *SIAM Journal on Scientific and Statistical Computing*, 7(3):856–869, July 1986.

[152] J.C. Simo and T.J.R. Hughes. *Computational Inelasticity.* Springer-Verlag, New Yoirk, 1998.

[153] A. Singh, J.D. Van Hamme, and O.P. Ward. Surfactants in microbiology and biotechnology: Part 2. Application aspects. *Biotechnology Advances*, 25(1):99 – 121, 2007.

[154] P. Stefanovic, M. Haataja, and N. Provatas. Phase-field crystals with elastic interactions. *Physical Review Letters*, 96(22):225504, 2006.

[155] P. Stefanovic, M. Haataja, and N. Provatas. Phase field crystal study of deformation and plasticity in nanocrystalline materials. *Physical Review E*, 80(4):046107, 2009.

[156] K. Stein, T. Tezduyar, and R. Benney. Mesh moving techniques for fluid–structure interactions with large displacements. *Journal of Applied Mechanics*, 70:58–63, 2003.

[157] I. Steinbach. Phase-field models in materials science. *Modelling and Simulation in Materials Science and Engineering*, 17(7):073001, 2009.

[158] R. W. Style, R. Boltyanskiy, Y. Che, J. S. Wettlaufer, L. A. Wilen, and E. R. Dufresne. Universal deformation of soft substrates near a contact line and the direct measurement of solid surface stresses. *Physical Review Letters*, 110:066103, Feb 2013.

[159] R. W. Style and E. R. Dufresne. Static wetting on deformable substrates, from liquids to soft solids. *Soft Matter*, 8(27):7177–7184, 2012.

[160] R. W. Style, A. Jagota, C.-Y. Hui, and E. R. Dufresne. Elastocapillarity: Surface tension and the mechanics of soft solids. *Annual Review of Condensed Matter Physics*, 8(0), 2016.

[161] R.W. Style, Y. Che, S.J. Park, B.M. Weon, J.H. Je, C. Hyland, G.K. German, M.P. Power, L.A. Wilen, J.S. Wettlaufer, et al. Patterning droplets with durotaxis. *Proceedings of the National Academy of Sciences*, 110(31):12541–12544, 2013.

[162] H. Suito, K. Takizawa, V.Q.H. Huynh, D. Sze, and T. Ueda. FSI analysis of the blood flow and geometrical characteristics in the thoracic aorta. *Computational Mechanics*, 54:1035–1045, 2014.

[163] R. Sunyer, V. Conte, J. Escribano, A. Elosegui-Artola, A. Labernadie, L. Valon, D. Navajas, J. M. García-Aznar, J. J. Muñoz, P. Roca-Cusachs, and X. Trepat. Collective cell durotaxis emerges from long-range intercellular force transmission. *Science*, 353(6304):1157–1161, 2016.

[164] K. Takizawa. Computational engineering analysis with the new-generation space–time methods. *Computational Mechanics*, 54:193–211, 2014.

[165] K. Takizawa, Y. Bazilevs, T.E. Tezduyar, M.-C. Hsu, O. Oiseth, K.M. Mathisen, N. Kostov, and S. McIntyre. Engineering Analysis and Design with ALE-VMS and Space-Time Methods. *Archives of Computational Methods in Engineering*, 21(4):481–508, 2014.

[166] K. Takizawa, Y. Bazilevs, T.E. Tezduyar, C.C. Long, A.L. Marsden, and K. Schjodt. ST and ALE-VMS methods for patient-specific cardiovascular fluid mechanics modeling. *Mathematical Models and Methods in Applied Sciences*, 24:2437–2486, 2014.

[167] K. Takizawa, D. Montes, M. Fritze, S. McIntyre, J. Boben, and T.E. Tezduyar. Methods for FSI modeling of spacecraft parachute dynamics and cover separation. *Mathematical Models and Methods in Applied Sciences*, 23:307–338, 2013.

[168] K. Takizawa, C. Moorman, S. Wright, T. Spielman, and T. E. Tezduyar. Fluid–structure interaction modeling and performance analysis of the orion spacecraft parachutes. *International Journal for Numerical Methods in Fluids*, 65(1-3):271–285, 2011.

[169] K. Takizawa, K. Schjodt, A. Puntel, N. Kostov, and T. E. Tezduyar. Patient-specific computational analysis of the influence of a stent on the unsteady flow in cerebral aneurysms. *Computational Mechanics*, 51:1061–1073, 2013.

[170] K. Takizawa, H. Takagi, T. E. Tezduyar, and R. Torii. Estimation of element-based zero-stress state for arterial FSI computations. *Computational Mechanics*, 54:895–910, 2014.

[171] K. Takizawa, T. E. Tezduyar, R. Kolesar, C. Boswell, T. Kanai, and K. Montel. Multiscale methods for gore curvature calculations from FSI modeling of spacecraft parachutes. *Computational Mechanics*, 54(6):1461–1476, 2014.

[172] K. Takizawa, T.E. Tezduyar, J. Boben, N. Kostov, C. Boswell, and A. Buscher. Fluid-structure interaction modeling of clusters of spacecraft parachutes with modified geometric porosity. *Computational Mechanics*, 52(6):1351–1364, 2013.

[173] K. Takizawa, T.E. Tezduyar, S. McIntyre, N. Kostov, R. Kolesar, and C. Habluetzel. Space-time VMS computation of wind-turbine rotor and tower aerodynamics. *Computational Mechanics*, 53(1):1–15, 2014.

[174] K. Takizawa, R. Torii, H. Takagi, T.E. Tezduyar, and X.Y. Xu. Coronary arterial dynamics computation with medical-image-based time-dependent anatomical models and element-based zero-stress state estimates. *Computational Mechanics*, 54:1047–1053, 2014.

[175] T. Tanaka, M. Morigami, and N. Atoda. Mechanism of resist pattern collapse during development process. *Japanese Journal of Applied Physics*, 32(12S):6059, 1993.

[176] Q.Y. Tang, Y.C. Chan, N.B. Wong, and R. Cheung. Surfactant-assisted processing of polyimide/multiwall carbon nanotube nanocomposites for microelectronics applications. *Polymer International*, 59(9):1240–1245, 2010.

[177] S. H. Tawfick, J. Bico, and S. Barcelo. Three-dimensional lithography by elastocapillary engineering of filamentary materials. *MRS Bulletin*, 41(02):108–114, 2016.

[178] C.H. Teng, I.L. Chern, and M.C. Lai. Simulating binary fluid-surfactant dynamics by a phase field model. *Discrete and Continuous Dynamical Systems - Series B*, 17(4):1289–1307, 2012.

[179] T. E. Tezduyar, S. Sathe, J. Pausewang, M. Schwaab, J. Christopher, and J. Crabtree. Interface projection techniques for fluid–structure interaction modeling with moving-mesh methods. *Computational Mechanics*, 43(1):39–49, 2008.

[180] T.E. Tezduyar. Finite element methods for flow problems with moving boundaries and interfaces. *Archives of Computational Methods in Engineering*, 8:83–130, 2001.

[181] T.E. Tezduyar. *Finite Element Methods for Fluid Dynamics with Moving Boundaries and Interfaces*. John Wiley & Sons, Ltd, 2004.

[182] T.E. Tezduyar, S. Aliabadi, M. Behr, A. Johnson, and S. Mittal. Parallel finite-element computation of 3D flows. *Computer*, 26(10):27–36, 1993.

[183] T.E. Tezduyar, M. Behr, S. Mittal, and A.A. Johnson. Computation of unsteady incompressible flows with the finite element methods–space–time formulations, iterative strategies and massively parallel implementations. In *New Methods in Transient Analysis*, PVP-Vol.246/AMD-Vol.143, pages 7–24, New York, 1992. ASME.

[184] T.E. Tezduyar and S. Sathe. Modeling of fluid–structure interactions with the space–time finite elements: Solution techniques. *International Journal for Numerical Methods in Fluids*, 54:855–900, 2007.

[185] T.E. Tezduyar, S. Sathe, R. Keedy, and K. Stein. Space–time finite element techniques for computation of fluid–structure interactions. *Computer Methods in Applied Mechanics and Engineering*, 195(17-18):2002–2027, 2006.

[186] T.E. Tezduyar, S. Sathe, and K. Stein. Solution techniques for the fully-discretized equations in computation of fluid–structure interactions with the space–time formulations. *Computer Methods in Applied Mechanics and Engineering*, 195:5743–5753, 2006.

[187] S. Tremaine. On the origin of irregular structure in saturn's rings. *The Astronomical Journal*, 125(2):894, 2003.

[188] E.H. van Brummelen, H. S. Roudbari, and G.J. van Zwieten. Elasto-capillarity simulations based on the Navier-Stokes-Cahn-Hilliard equations. *ArXiv 1510.02441v1*, pages 1– 8, 2015.

[189] R.G.M. van der Sman and S. van der Graaf. Diffuse interface model of surfactant adsorption onto flat and droplet interfaces. *Rheologica Acta*, 46(1):3–11, 2006.

[190] J.D. van der Waals. The thermodynamic theory of capillarity under the hypothesis of a continuous variation of density. *Journal of Statistical Physics*, 20(2):200–244, 1893.

[191] J.D. Van Hamme, A. Singh, and O.P Ward. Surfactants in microbiology and biotechnology: Part 1. Physiological aspects. *Biotechnology Advances*, 24:604–620, 2006.

[192] G. Vilanova, I. Colominas, and H. Gomez. Capillary networks in tumor angiogenesis: From discrete endothelial cells to phase-field averaged descriptions via isogeometric analysis. *International Journal for Numerical Methods in Biomedical Engineering*, 29(10):1015–1037, 2013.

[193] C. Wang and S. M. Wise. An energy stable and convergent finite-difference scheme for the modified phase field crystal equation. *SIAM Journal on Numerical Analysis*, 49(3):945–969, 2011.

[194] C. Wang, M.C.H. Wu, F. Xu, M.-C. Hsu, and Y. Bazilevs. Modeling of a hydraulic arresting gear using fluid–structure interaction and isogeometric analysis. *Computers and Fluids*, 142:3–14, 2017.

[195] J. Warren and H. Weimer. *Subdivision Methods for Geometric Design: A Constructive Approach*. Morgan Kaufmann Publishers Inc., San Francisco, CA, USA, 1st edition, 2001.

[196] F.M. White. *Fluid Mechanics*. McGraw-Hill international editions. McGraw-Hill, 2003.

[197] X. Wu, G. J. van Zwieten, and K. G. van der Zee. Stabilized second-order convex splitting schemes for Cahn-Hilliard models with application to diffuse-interface tumor-growth models. *International Journal for Numerical Methods in Biomedical Engineering*, 30(2):180–203, 2014.

[198] J. Xu, G. Vilanova, and H. Gomez. A mathematical model coupling tumor growth and angiogenesis. *PloS one*, 11(2):e0149422, 2016.

[199] J Yan, A Korobenko, X Deng, and Y Bazilevs. Computational free-surface fluid–structure interaction with application to floating offshore wind turbines. *Computers and Fluids*, 141:155–174, 2016.

[200] L. Zhang, A. Gerstenberger, X. Wang, and W. K. Liu. Immersed finite element method. *Computer Methods in Applied Mechanics and Engineering*, 193(21):2051–2067, 2004.

Appendices

A Paper #1: "Liquid-vapor transformations with surfactants. Phase-field model and Isogeometric Analysis"

Journal of Computational Physics 321 (2016) 797–818

Contents lists available at ScienceDirect

Journal of Computational Physics

www.elsevier.com/locate/jcp

Liquid-vapor transformations with surfactants. Phase-field model and Isogeometric Analysis

Jesus Bueno *, Hector Gomez

Departamento de Métodos Matemáticos e de Representación, Universidade da Coruña, Campus de Elviña, 15192, A Coruña, Spain

ARTICLE INFO

Article history:
Received 22 January 2016
Received in revised form 24 May 2016
Accepted 6 June 2016
Available online 9 June 2016

Keywords:
Surfactants
Surface tension
Navier–Stokes–Korteweg (NSK)
Complex fluids
Phase-field model
Isogeometric Analysis (IGA)

ABSTRACT

Surfactants are compounds that find energetically favorable to be located at the boundaries between fluids. They are able to modify the properties of those interfaces, for example, reducing surface tension. Here, we propose a new model for liquid–vapor flows with surfactants which captures the dynamics of the surfactant and accounts for phase transformations in the fluid. The aforementioned model is derived from a free energy functional by using a Coleman–Noll approach. The proposed theory emanates from the isothermal Navier–Stokes–Korteweg equations, which describe single-component two-phase flow and naturally allow for phase transformations. We believe that our model has significant potential to study the influence of surfactants in vaporization and condensation processes. From a numerical point of view, the proposed model poses significant challenges to existing discretization methods, including stiffness in space and time, internal and boundary layers as well as higher-order partial differential operators. To overcome these challenges we propose algorithms based on Isogeometric Analysis, which permit an accurate and efficient discretization. Finally, we illustrate the viability of the theoretical framework and the effectiveness of our algorithms by solving several numerical problems in two and three dimensions.

1. Introduction

Surfactants are very useful products in the chemical industry. They can be found in detergents, cosmetics, or the dye of our clothes. However, the chemical industry is not the only beneficiary of these extraordinary compounds. In recent decades, surfactants have also been used in other fields such as biotechnology [1,2], electronic printing [3], microelectronics [4] or medical research [5,6]. They also play an essential role in our organism, increasing the pulmonary compliance and preventing atelectasis [7,8], that is, the complete or the partial collapse of the lungs.

The word surfactant is an abbreviation of *surface active agent* and is used to name different types of compounds that find energetically favorable to be located at the interfaces of a system. The consequence is that surfactants are absorbed by the interface, that is, they get trapped at the boundary between different phases. Even if they are usually very thin, interfaces play a crucial role in the system dynamics. The composition in the interfacial region can differ dramatically from that of the bulk phases. Indeed, across interfaces there are rapid property changes that lead to an excess of free energy, related to the amount of work required to create the interface. The presence of surfactants at the interface can significantly reduce the

* Corresponding author.
E-mail address: jesus.bueno@udc.es (J. Bueno).

http://dx.doi.org/10.1016/j.jcp.2016.06.008
0021-9991/

work required to generate interfaces, altering completely the behavior of the system [9–13]. For a more detailed discussion on surfactant properties the reader is referred to [14–16].

In the literature, one can find a number of computational methods that describe surfactant absorption phenomena. For this purpose, different techniques have been employed, such as phase-field models [17–21], front tracking methods [19,22] or volume of fluid schemes [23,24]. However, most of these models only deal with soluble or insoluble surfactants in two-component inmiscible flows (see, for example, [25–27]). The influence of surfactants in single-component two-phase flows remains practically unexplored, at least from the computational point of view. For this reason, we present our initial steps toward a computational model for surfactants that tries to capture the behavior and the effects of surface active agents at the interfaces of single component flows. The proposed model is based on a complex-fluid theory that allows for spontaneous vaporization and condensation, so it may have a significant potential to study the influence of surfactants in phase-transition phenomena.

1.1. Fluid dynamics with phase changes

There exist two different approaches to deal with phase transformations: sharp-interface and diffuse interface models. The former usually results in mathematical models that require complex numerical treatment: one must solve simultaneously the partial differential equations that govern each phase's dynamics as well as the boundary conditions that hold on a moving, and *a priori* unknown, interface [28]. An alternative to the previous approach is the diffuse-interface method in which sharp interfaces are replaced by thin transition regions. The idea is to define an order parameter, also called phase-field, that varies smoothly on the entire computational domain and acts as marker of the location of the different phases. This notably simplifies the numerics because the governing equations can be solved on the entire domain, which is usually known and fixed. In general, instead of the boundary conditions at the interfaces, we have to solve a partial differential equation for the evolution of the order parameter. From the computational point of view, the main disadvantage is that this equation typically includes higher-order partial-differential operators, and it produces thin layers that evolve dynamically over the computational domain. However, most of these computational challenges are being addressed [29–32], and in recent decades phase-field models have been successfully applied to a large number of fields such as solidification dynamics [33–35], foams [36], fracture dynamics [37], dendritic growth [38,39], vesicle dynamics [40], microstructure evolution in solids [41], planet formation [42], infiltration of water into a porous medium [43,44], coalescence of bubbles [45], cancer growth [46–48], elasto-capillarity [49] or fluid–structure interaction [50]. For recent reviews of phase-field methods the reader is referred to [51–55].

To develop our theory of liquid–vapor flows with surfactants, we use as a starting point the Navier–Stokes–Korteweg (NSK) equations, which are a phase-field theory for single-component two-phase flows [45]. The model allows for the fluid to evaporate and condensate naturally due to pressure and/or temperature variations. An interesting feature of the model is that the fluid density acts directly as the phase-field identifying the liquid and vapor phases. The NSK system is the result of several works, including the contributions of Gibbs [56], Korteweg [57], van der Waals [58] and Dunn and Serrin [59]. Although the current form of the system has been known for several years, computational methods for the NSK equations are still in their infancy. Some noteworthy publications are, for example, [32,45,60–63].

Including surfactants in the theory makes the computational treatment even more difficult. Since surfactants tend to be located primarily on the interfaces, a common approach is to model surfactant dynamics as a partial-differential equation that is posed on the lower-dimensional manifold defined by the interface. Our goal is to adhere to the phase-field philosophy also to model the surfactant dynamics and define a global field which naturally localizes to the interface. This leads to a much simpler computational treatment.

1.2. Computational challenges

One of the main challenges when dealing with phase-field approaches or in particular with the Navier–Stokes–Korteweg equations, is that these models include a length scale that represents the thickness of the interfaces, which must be extremely small in order for the model to be realistic. This interface length scale must be captured by the computational mesh, which makes the NSK theory more difficult to treat numerically than classical Navier–Stokes equations. Additionally, our model involves third-order partial-differential spatial operators both in the NSK system and in the equation that describes the behavior of the surfactant. This fact significantly limits the use of finite element methods since we need to employ basis functions with $\mathcal{C}^1$ global continuity, which is very difficult or even impossible in 3D complicated geometries.

The aforementioned difficulties are tackled by using Isogeometric Analysis (IGA) for the spatial discretization of the problem. IGA is a new computational technique that improves and generalizes the standard finite element method. It was first proposed in [64] and further developed in [65–69]. The main objective of IGA is to bridge the gap between Computer Aided Design (CAD) and Finite Element Analysis by developing a computational framework based on the functions employed in CAD systems. There are a number of computational geometry technologies that may be used in Isogeometric Analysis. Heretofore, Non-Uniform Rational B-Splines (NURBS) have been the functions most widely employed in IGA, and they will also be used for our simulations. However, there are other options such as T-Splines (see, for example, [66,70,71]) or subdivision surfaces [72]. Isogeometric analysis based on NURBS presents a series of attributes that can be exploited in problems involving higher-order partial-differential operators. Among them, it is worth highlighting the following: higher-order accuracy, robustness, and especially, higher-order global continuity of the basis functions. IGA has been previously

used to solve phase-field problems with remarkable success [29,31,45,50,73–76]. Another important property of IGA that has been recently proven is that Galerkin solutions can be obtained with only one evaluation per degree of freedom using the concept of variational collocation [77].

1.3. Structure and content of the paper

The rest of the paper is organized as follows. Section 2 gives a quick overview of Isogeometric Analysis based on NURBS. In Section 3, we derive our model from a free energy functional by using a Coleman–Noll approach [78]. In Section 4, we describe the governing equations of the model at the continuous level. Then, we present the weak form of the problem as well as the discretization process. We employ a semi-discrete formulation based on Galerkin's method and we integrate in time using a generalized-α scheme [79]. Section 5 displays several numerical examples in 2D and 3D. The first example aims at finding the relation between the surface tension at liquid–vapor interfaces and the parameters of the proposed model. It also shows that our theory succeeds in reproducing the way in which surfactants lower surface tension. The second simulation demonstrates that surfactants are naturally trapped at interfaces in accordance with the expected physical behavior of a surface active agent. We also use this example to show that our model is able to reproduce how surfactants may inhibit the coalescence of bubbles. For this particular case, we plot the evolution of the free energy with respect to time, and we confirm that it decreases monotonically as it was imposed in the derivation of the theory. Subsequently, we present a numerical example in which a drop of water is attracted by a solid-like boundary due to the capillarity forces associated to the liquid–vapor interfaces. The contact angle between those interfaces and the boundary will be altered because of the surfactant concentration. Additionally, a three-dimensional numerical simulation is presented. Finally, in Section 6, some concluding remarks are commented.

2. A brief overview of NURBS-based Isogeometric Analysis

The current implementation of our IGA model is based on Non-Uniform Rational B-Splines (NURBS). The goal of this section is to introduce NURBS briefly and to present a quick overview of Isogeometric Analysis. For a more extensive discussion on IGA the reader is referred to [80].

B-splines are piecewise polynomial curves constructed by taking linear combinations of B-spline basis functions. The coefficients of these basis are points in space, which are referred to as *control points*. The concept is similar to that of nodal coordinates in finite element analysis. The only difference is that in IGA the basis functions are, in general, non-interpolatory. A *knot vector* Ξ in one dimension is a set of non-decreasing coordinates in the parametric space, i.e., $\Xi = \{\xi_1, ..., \xi_{n_c+p+1}\}$, where $\xi_i \in \mathbb{R}$ is the ith knot, $i = 1, 2, ..., n_c + p + 1$, p is the polynomial order, and n_c is the number of basis functions that comprise the B-spline space. Knots divide the parametric space into knot spans or elements.

For a given knot vector, the B-spline basis functions are defined by the *Cox–de Boor recursion formula* (see [81,82]). This way, starting with piecewise constants ($p = 0$), i.e,

$$N_{i,0}(\xi) = \begin{cases} 1, & \text{if } \xi_i \leqslant \xi < \xi_{i+1}, \\ 0, & \text{otherwise} \end{cases}; \quad i = 1, \ldots, n_c \tag{1}$$

the basis functions of higher degrees are defined by

$$N_{i,p}(\xi) = \frac{\xi - \xi_i}{\xi_{i+p} - \xi_i} N_{i,p-1}(\xi) + \frac{\xi_{i+p+1} - \xi}{\xi_{i+p+1} - \xi_{i+1}} N_{i+1,p-1}(\xi); \quad i = 1, \ldots, n_c \tag{2}$$

Note that for B-spline functions with polynomial order 0 and 1, we obtain standard piecewise constant and linear finite element functions, respectively. From the Cox–de Boor recursion formula, it can be seen that B-Spline basis functions constitute a partition of unity, that is, $\sum_{i=1}^{n_c} N_{i,p}(\xi) = 1 \ \forall \xi$. Moreover, each basis $N_{i,p}$ is pointwise nonnegative over the entire domain, i.e., $N_{i,p}(\xi) \geqslant 0 \ \forall \xi$, and its support is compact. For B-spline functions of order p the support is always $p + 1$ knot spans. It is also important to note that if internal knots are not repeated, the B-Spline basis functions are at least $\mathcal{C}^{p-1}$-continuous everywhere. More specifically, if a knot has multiplicity k, the basis is $\mathcal{C}^{p-k}$-continuous at that knot. In Fig. 1 we present an example of quadratic B-spline basis functions generated from the uniform open knot vector $\Xi = \{0, 0, 0, 1, 2, 3, 4, 5, 6, 6, 6\}$.

NURBS are built from B-splines. In particular, a NURBS entity in $\mathbb{R}^d$ can be obtained by a projective transformation of a B-spline object in $\mathbb{R}^{d+1}$. Given the B-spline basis function $N_{i,p}(\xi)$, the one dimensional NURBS basis can be defined as

$$\mathcal{R}_i^p(\xi) = \frac{N_{i,p}(\xi)\, w_i}{\sum_{\hat{i}=1}^{n_c} N_{\hat{i},p}(\xi)\, w_{\hat{i}}}, \tag{3}$$

where w_i is a positive real weight. For the two and three dimensional cases, the NURBS basis functions are given by

$$\mathcal{R}_{i,j}^{p,q}(\xi, \eta) = \frac{N_{i,p}(\xi)\, M_{j,q}(\eta)\, w_{i,j}}{\sum_{\hat{i}=1}^{n_c} \sum_{\hat{j}=1}^{m_c} N_{\hat{i},p}(\xi)\, M_{\hat{j},q}(\eta)\, w_{\hat{i},\hat{j}}}, \tag{4}$$

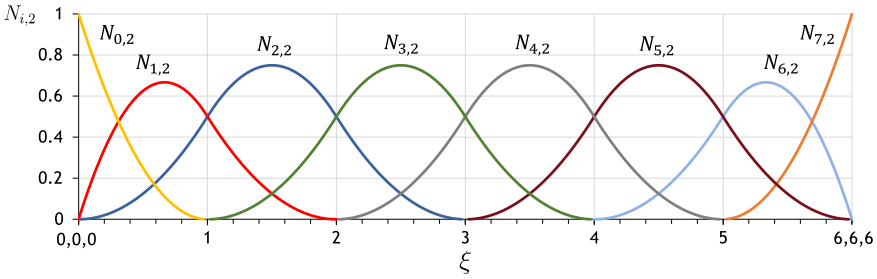

Fig. 1. Quadratic basis functions formed from the open knot vector $\Xi = \{0, 0, 0, 1, 2, 3, 4, 5, 6, 6, 6\}$.

$$\mathcal{R}^{p,q,r}_{i,j,k}(\xi,\eta,\zeta) = \frac{N_{i,p}(\xi)\, M_{j,q}(\eta)\, L_{k,r}(\zeta)\, w_{i,j,k}}{\sum_{\hat{i}=1}^{n_c}\sum_{\hat{j}=1}^{m_c}\sum_{\hat{k}=1}^{l_c} N_{\hat{i},p}(\xi)\, M_{\hat{j},q}(\eta)\, L_{\hat{k},r}(\zeta)\, w_{\hat{i},\hat{j},\hat{k}}}. \tag{5}$$

In the expressions above, $\Xi = \{\xi_1, ..., \xi_{n_c+p+1}\}$, $\mathcal{H} = \{\eta_1, ..., \eta_{m_c+q+1}\}$ and $\mathcal{Z} = \{\zeta_1, ..., \zeta_{l_c+r+1}\}$ are the knot vectors; p, q and r denote the polynomial orders, and $w_{\hat{i},\hat{j}}$ and $w_{\hat{i},\hat{j},\hat{k}}$ are the weights. Note that the NURBS basis functions are no longer piecewise polynomials, but piecewise rationals. They can exactly represent all conic sections. NURBS functions inherit most of the properties of B-splines. They are pointwise nonnegative and they still constitute a partition of unity. Their continuity, as well as their support is the same as for B-splines. Note also that if the weights are all equal, as it is the case for the computations presented herein, then NURBS basis functions reduce to B-splines basis functions, i.e, $\mathcal{R}^p_i(\xi) = N_{i,p}(\xi)$.

Given a mesh of control points, $\{\boldsymbol{B}_i\}$, $i = 1, 2, ..., n_c$, polynomial order p and knot vector $\Xi = \{\xi_1, ..., \xi_{n_c+p+1}\}$ a NURBS curve may be defined as

$$\boldsymbol{C}(\xi) = \sum_{i=1}^{n_c} \mathcal{R}^p_i(\xi)\, \boldsymbol{B}_i. \tag{6}$$

Analogously, a NURBS surface $\boldsymbol{S}(\xi,\eta)$ and a NURBS volume $\boldsymbol{V}(\xi,\eta,\zeta)$ may be defined as

$$\boldsymbol{S}(\xi,\eta) = \sum_{i=1}^{n_c}\sum_{j=1}^{m_c} \mathcal{R}^{p,q}_{i,j}(\xi,\eta)\, \boldsymbol{B}_{i,j}, \tag{7}$$

$$\boldsymbol{V}(\xi,\eta,\zeta) = \sum_{i=1}^{n_c}\sum_{j=1}^{m_c}\sum_{k=1}^{l_c} \mathcal{R}^{p,q,r}_{i,j,k}(\xi,\eta,\zeta)\, \boldsymbol{B}_{i,j,k}, \tag{8}$$

where $\{\boldsymbol{B}_{i,j}\}$ and $\{\boldsymbol{B}_{i,j,k}\}$ are the control points, $i = 1, 2, ..., n_c$, $j = 1, 2, ..., m_c$, $k = 1, 2, ..., l_c$.

IGA is compatible with the two classical mesh refinement strategies, knot insertion (h-refinement) and order elevation (p-refinement). However, there is a third option, referred to as k-refinement (see, e.g., [64]), which allows to increase the order and the smoothness of the NURBS basis functions simultaneously. As in finite elements, in Isogeometric Analysis the isoparametric concept is used, which means that the unknown variables are represented in terms of the same NURBS functions [see Eqs. (3)–(5)] that are used for defining the geometry.

Remark. In what follows, for simplicity, we will omit the index of the basis functions that represents the polynomial degree. This information will be inferred from the context.

3. Mathematical model

In this section, we show how our model can be derived from a free energy functional. By using a Coleman–Noll procedure [78] we will find sufficient conditions that must be satisfied to enforce the dissipation inequality for any arbitrary solution of the theory. We will also show that our model fulfills those conditions. For simplicity, we will focus on the isothermal case, but similar arguments may be used to derive a thermally-coupled theory (see, e.g., [63]).

3.1. Energy functional

Let us define the total energy of the system

$$\mathcal{E}(\rho,\boldsymbol{u}) = \int_\Omega \left(\Psi + \frac{1}{2}\rho\,|\boldsymbol{u}|^2\right) \mathrm{d}\Omega, \tag{9}$$

where Ω is an open subset of $\mathbb{R}^3$ and $|\cdot|$ denotes the Euclidean norm of a vector; ρ is the fluid density and $\boldsymbol{u}$ represents the velocity vector. The free energy Ψ is assumed to belong to the following constitutive class

$$\Psi = \widehat{\Psi}\left(\boldsymbol{L}, \rho, \nabla\rho, c\right). \tag{10}$$

In the above expression, c is the surfactant concentration and $\boldsymbol{L}$ is the symmetric part of the velocity gradient, that is,

$$\boldsymbol{L} = \frac{1}{2}\left(\nabla\boldsymbol{u} + \nabla\boldsymbol{u}^T\right), \tag{11}$$

where $\square^T$ denotes the transpose of $\square$.

3.2. Derivation of the model

Our starting point will be the classical balance laws for mass of fluid and surfactant [see Eqs. (12) and (15), respectively], linear momentum [Eq. (13)] and angular momentum [Eq. (14)]. These equations may be written as,

$$\dot{\rho} + \rho\nabla\cdot\boldsymbol{u} = 0, \tag{12}$$

$$\rho\dot{\boldsymbol{u}} = \nabla\cdot\boldsymbol{T} + \rho\boldsymbol{f}, \tag{13}$$

$$\boldsymbol{T} = \boldsymbol{T}^T, \tag{14}$$

$$\dot{c} + c\nabla\cdot\boldsymbol{u} = -\nabla\cdot\boldsymbol{j}, \tag{15}$$

where $\boldsymbol{T}$ is the Cauchy stress tensor, $\boldsymbol{f}$ represents body forces per unit mass and $\boldsymbol{j}$ describes the mass flux of surfactant; $\dot{\square}$ denotes the material time derivative of $\square$ and may also be expressed as $\partial\square/\partial t + \boldsymbol{u}\cdot\nabla\square$. The quantity $\dot{\square}$ may also be understood as the time derivative of $\square$ holding the material particle fixed.

Our goal is to find a constitutive equation for $\boldsymbol{T}$ and $\boldsymbol{j}$ so that the energy of the system decreases with time for any arbitrary solution of the theory. In order to do so, we will use the framework of thermomechanics and the Coleman–Noll approach. We will assume that $\boldsymbol{T}$ belongs to the constitutive class

$$\boldsymbol{T} = \widehat{\boldsymbol{T}}\left(\boldsymbol{L}, \rho, \nabla\rho, c, \mu\right), \tag{16}$$

where μ is the chemical potential and is defined as

$$\mu = \frac{\delta}{\delta\rho}\left(\int_\Omega \Psi \mathrm{d}\Omega\right) = \frac{\partial\widehat{\Psi}}{\partial\rho} - \nabla\cdot\left(\frac{\partial\widehat{\Psi}}{\partial\nabla\rho}\right), \tag{17}$$

with $\dfrac{\delta}{\delta\rho}$ denoting the variational derivative with respect to density. Let us also define the following energy dissipation law

$$\mathcal{R} = \frac{\mathrm{d}}{\mathrm{d}t}\left\{\int_{\mathcal{P}_t}\left(\Psi + \frac{1}{2}\rho\left|\boldsymbol{u}\right|^2\right)\mathrm{d}\mathcal{P}_t\right\} = \mathcal{W}\left(\mathcal{P}_t\right) - \mathcal{D}\left(\mathcal{P}_t\right) + \Phi\left(\partial\mathcal{P}_t\right) \qquad \text{with} \qquad \mathcal{D}\left(\mathcal{P}_t\right) \geq 0. \tag{18}$$

Here, $\mathcal{P}_t$ is an arbitrary set of material particles and $\partial\mathcal{P}_t$ denotes its boundary. $\mathcal{W}\left(\mathcal{P}_t\right)$ is the work associated to the external forces, $\Phi\left(\partial\mathcal{P}_t\right)$ represents the energy supplies coming through $\partial\mathcal{P}_t$ and $\mathcal{D}\left(\mathcal{P}_t\right)$ is the dissipation, which must be non-negative for all conceivable processes. Using the Reynolds transport theorem (see, for example, [83]), it follows that

$$\frac{\mathrm{d}}{\mathrm{d}t}\left\{\int_{\mathcal{P}_t}\Psi\mathrm{d}\mathcal{P}_t\right\} = \int_{\mathcal{P}_t}\left(\dot{\Psi} + \Psi\nabla\cdot\boldsymbol{u}\right)\mathrm{d}\mathcal{P}_t, \tag{19}$$

$$\begin{aligned}\frac{\mathrm{d}}{\mathrm{d}t}\left\{\int_{\mathcal{P}_t}\frac{1}{2}\rho\left|\boldsymbol{u}\right|^2\mathrm{d}\mathcal{P}_t\right\} &= \int_{\mathcal{P}_t}\left[\left(\frac{1}{2}\rho\left|\boldsymbol{u}\right|^2\right)^{\cdot} + \frac{1}{2}\rho\left|\boldsymbol{u}\right|^2\nabla\cdot\boldsymbol{u}\right]\mathrm{d}\mathcal{P}_t = \int_{\mathcal{P}_t}\left(\frac{1}{2}\dot{\rho}\left|\boldsymbol{u}\right|^2 + \rho\boldsymbol{u}\cdot\dot{\boldsymbol{u}} + \frac{1}{2}\rho\left|\boldsymbol{u}\right|^2\nabla\cdot\boldsymbol{u}\right)\mathrm{d}\mathcal{P}_t \\ &= \int_{\mathcal{P}_t}\rho\boldsymbol{u}\cdot\dot{\boldsymbol{u}}\mathrm{d}\mathcal{P}_t.\end{aligned} \tag{20}$$

Note that in (20) we have used the mass conservation equation (12). Taking into account the constitutive class of Ψ given by Eq. (10), and relations (19) and (20), the dissipation law can be written

$$\mathcal{R} = \frac{\mathrm{d}}{\mathrm{d}t}\left\{\int_{\mathcal{P}_t}\left(\Psi + \frac{1}{2}\rho\,|\boldsymbol{u}|^2\right)\mathrm{d}\mathcal{P}_t\right\} = \int_{\mathcal{P}_t}\left(\frac{\partial\widehat{\Psi}}{\partial\boldsymbol{L}} : \dot{\boldsymbol{L}} + \frac{\partial\widehat{\Psi}}{\partial\rho}\dot{\rho} + \frac{\partial\widehat{\Psi}}{\partial\nabla\rho}\cdot(\nabla\rho)^{\cdot} + \frac{\partial\widehat{\Psi}}{\partial c}\dot{c} + \Psi\nabla\cdot\boldsymbol{u} + \rho\boldsymbol{u}\cdot\dot{\boldsymbol{u}}\right)\mathrm{d}\mathcal{P}_t, \tag{21}$$

where the symbol : denotes the usual double-dot product. At this point, we introduce the classical relation

$$(\nabla\rho)^{\cdot} = \nabla\dot{\rho} - \nabla\boldsymbol{u}\nabla\rho. \tag{22}$$

In component notation, the vector $\nabla\boldsymbol{u}\nabla\rho$ would be understood as the product of a square matrix ($\nabla\boldsymbol{u}$) with a column vector ($\nabla\rho$), that is, $[\nabla\boldsymbol{u}\nabla\rho]_i = \frac{\partial u_i}{\partial x_j}\frac{\partial\rho}{\partial x_j}$. Using Eqs. (13), (15) and (22), $\mathcal{R}$ results in the following expression

$$\mathcal{R} = \int_{\mathcal{P}_t}\left(\frac{\partial\widehat{\Psi}}{\partial\boldsymbol{L}} : \dot{\boldsymbol{L}} + \frac{\partial\widehat{\Psi}}{\partial\rho}\dot{\rho} + \frac{\partial\widehat{\Psi}}{\partial\nabla\rho}\cdot\nabla\dot{\rho} - \frac{\partial\widehat{\Psi}}{\partial\nabla\rho}\cdot\nabla\boldsymbol{u}\nabla\rho - \frac{\partial\widehat{\Psi}}{\partial c}\nabla\cdot\boldsymbol{j} - \frac{\partial\widehat{\Psi}}{\partial c}c\nabla\cdot\boldsymbol{u} + \Psi\nabla\cdot\boldsymbol{u} + \boldsymbol{u}\cdot(\nabla\cdot\boldsymbol{T} + \rho\boldsymbol{f})\right)\mathrm{d}\mathcal{P}_t. \tag{23}$$

Integrating by parts the terms with $\nabla\dot{\rho}$, $\nabla\cdot\boldsymbol{j}$ and $\nabla\cdot\boldsymbol{T}$, we obtain

$$\begin{aligned}\mathcal{R} = &\int_{\mathcal{P}_t}\left(\frac{\partial\widehat{\Psi}}{\partial\boldsymbol{L}} : \dot{\boldsymbol{L}} + \frac{\partial\widehat{\Psi}}{\partial\rho}\dot{\rho} - \nabla\cdot\left(\frac{\partial\widehat{\Psi}}{\partial\nabla\rho}\right)\dot{\rho} - \frac{\partial\widehat{\Psi}}{\partial\nabla\rho}\cdot\nabla\boldsymbol{u}\nabla\rho + \nabla\left(\frac{\partial\widehat{\Psi}}{\partial c}\right)\cdot\boldsymbol{j}\right.\\ &\left. - \frac{\partial\widehat{\Psi}}{\partial c}c\nabla\cdot\boldsymbol{u} + \Psi\nabla\cdot\boldsymbol{u} - \boldsymbol{T} : \nabla\boldsymbol{u} + \rho\boldsymbol{u}\cdot\boldsymbol{f}\right)\mathrm{d}\mathcal{P}_t\\ &+ \int_{\partial\mathcal{P}_t}\left(\dot{\rho}\frac{\partial\widehat{\Psi}}{\partial\nabla\rho}\cdot\boldsymbol{n} - \frac{\partial\widehat{\Psi}}{\partial c}\boldsymbol{j}\cdot\boldsymbol{n} + \boldsymbol{u}\cdot\boldsymbol{T}\boldsymbol{n}\right)\mathrm{d}(\partial\mathcal{P}_t).\end{aligned} \tag{24}$$

Let us now use that

$$\frac{\partial\widehat{\Psi}}{\partial\nabla\rho}\cdot\nabla\boldsymbol{u}\nabla\rho = \frac{\partial\widehat{\Psi}}{\partial\nabla\rho}\otimes\nabla\rho : \nabla\boldsymbol{u}, \tag{25}$$

$$\nabla\cdot\boldsymbol{u} = \boldsymbol{I} : \nabla\boldsymbol{u}, \tag{26}$$

where $\boldsymbol{I}$ represents the identity tensor and $\otimes$ denotes the usual vector outer product. With these identities in mind and using the mass balance equation (12), it can be shown that $\mathcal{R}$ takes on the form

$$\begin{aligned}\mathcal{R} = &\int_{\mathcal{P}_t}\left(\frac{\partial\widehat{\Psi}}{\partial\boldsymbol{L}} : \dot{\boldsymbol{L}} - \frac{\partial\widehat{\Psi}}{\partial\rho}\rho\boldsymbol{I} : \nabla\boldsymbol{u} + \nabla\cdot\left(\frac{\partial\widehat{\Psi}}{\partial\nabla\rho}\right)\rho\boldsymbol{I} : \nabla\boldsymbol{u} - \frac{\partial\widehat{\Psi}}{\partial\nabla\rho}\otimes\nabla\rho : \nabla\boldsymbol{u} + \nabla\left(\frac{\partial\widehat{\Psi}}{\partial c}\right)\cdot\boldsymbol{j}\right)\mathrm{d}\mathcal{P}_t\\ &+ \int_{\mathcal{P}_t}\left(-\frac{\partial\widehat{\Psi}}{\partial c}c\boldsymbol{I} : \nabla\boldsymbol{u} + \Psi\boldsymbol{I} : \nabla\boldsymbol{u} - \boldsymbol{T} : \nabla\boldsymbol{u} + \rho\boldsymbol{u}\cdot\boldsymbol{f}\right)\mathrm{d}\mathcal{P}_t + \int_{\partial\mathcal{P}_t}\left(\dot{\rho}\frac{\partial\widehat{\Psi}}{\partial\nabla\rho}\cdot\boldsymbol{n} - \frac{\partial\widehat{\Psi}}{\partial c}\boldsymbol{j}\cdot\boldsymbol{n} + \boldsymbol{u}\cdot\boldsymbol{T}\boldsymbol{n}\right)\mathrm{d}(\partial\mathcal{P}_t)\\ = &\int_{\mathcal{P}_t}\left(\frac{\partial\widehat{\Psi}}{\partial\boldsymbol{L}} : \dot{\boldsymbol{L}} + \left[\left(-\frac{\partial\widehat{\Psi}}{\partial\rho}\rho + \nabla\cdot\left(\frac{\partial\widehat{\Psi}}{\partial\nabla\rho}\right)\rho - \frac{\partial\widehat{\Psi}}{\partial c}c + \Psi\right)\boldsymbol{I} - \boldsymbol{T} - \frac{\partial\widehat{\Psi}}{\partial\nabla\rho}\otimes\nabla\rho\right] : \nabla\boldsymbol{u}\right.\\ &\left. + \nabla\left(\frac{\partial\widehat{\Psi}}{\partial c}\right)\cdot\boldsymbol{j} + \rho\boldsymbol{u}\cdot\boldsymbol{f}\right)\mathrm{d}\mathcal{P}_t\\ &+ \int_{\partial\mathcal{P}_t}\left(\dot{\rho}\frac{\partial\widehat{\Psi}}{\partial\nabla\rho}\cdot\boldsymbol{n} - \frac{\partial\widehat{\Psi}}{\partial c}\boldsymbol{j}\cdot\boldsymbol{n} + \boldsymbol{u}\cdot\boldsymbol{T}\boldsymbol{n}\right)\mathrm{d}(\partial\mathcal{P}_t)\end{aligned} \tag{27}$$

Examining the previous expression and comparing it with the energy dissipation law defined in Eq. (18), we can identify the working $\mathcal{W}(\mathcal{P}_t)$, the dissipation $\mathcal{D}(\mathcal{P}_t)$ and the energy supplies across the boundaries $\Phi(\partial\mathcal{P}_t)$ as

$$\Phi(\partial\mathcal{P}_t) = \int_{\partial\mathcal{P}_t}\left(\dot{\rho}\frac{\partial\widehat{\Psi}}{\partial\nabla\rho}\cdot\boldsymbol{n} - \frac{\partial\widehat{\Psi}}{\partial c}\boldsymbol{j}\cdot\boldsymbol{n} + \boldsymbol{u}\cdot\boldsymbol{T}\boldsymbol{n}\right)\mathrm{d}(\partial\mathcal{P}_t), \tag{28}$$

$$\mathcal{D}(\mathcal{P}_t) = \int_{\mathcal{P}_t}\left(-\frac{\partial\widehat{\Psi}}{\partial\boldsymbol{L}} : \dot{\boldsymbol{L}} + \left[\left(\mu\rho - \Psi + \frac{\partial\widehat{\Psi}}{\partial c}c\right)\boldsymbol{I} + \boldsymbol{T} + \frac{\partial\widehat{\Psi}}{\partial\nabla\rho}\otimes\nabla\rho\right] : \nabla\boldsymbol{u} - \nabla\left(\frac{\partial\widehat{\Psi}}{\partial c}\right)\cdot\boldsymbol{j}\right)\mathrm{d}\mathcal{P}_t, \tag{29}$$

$$\mathcal{W}(\mathcal{P}_t) = \int_{\mathcal{P}_t}\rho\boldsymbol{u}\cdot\boldsymbol{f}\,\mathrm{d}\mathcal{P}_t. \tag{30}$$

Note that in Eq. (29) we have used the definition of μ given in (17). At this point we just need to find constitutive equations for $\boldsymbol{T}$ and $\boldsymbol{j}$ such that $\mathcal{E}$ decreases with time for any arbitrary solution of the theory. This can be guaranteed by imposing $\mathcal{D}(\mathcal{P}_t) \geq 0$ for all conceivable processes. In order to do so, we will analyze all the terms in expression (29). For the first term, we will take into account that the constitutive class of Ψ [see Eq. (10)] does not allow the dependence of Ψ on $\dot{\boldsymbol{L}}$. Therefore, the only way to ensure that this term is pointwisely positive or zero is by taking

$$\frac{\partial \widehat{\Psi}}{\partial \boldsymbol{L}} = 0. \tag{31}$$

Focusing now on the last term of Eq. (29), the constitutive choice

$$\boldsymbol{j} = -\kappa \nabla \left(\frac{\partial \widehat{\Psi}}{\partial c} \right) \qquad \text{with} \qquad \kappa > 0, \tag{32}$$

guarantees that this term will be pointwise non-negative. Considering this, we enforce the inequality

$$\left[\left(\mu\rho - \Psi + c\frac{\partial \widehat{\Psi}}{\partial c} \right) \boldsymbol{I} + \boldsymbol{T} + \frac{\partial \widehat{\Psi}}{\partial \nabla \rho} \otimes \nabla \rho \right] : \nabla \boldsymbol{u} \geq 0. \tag{33}$$

Note that Eqs. (31)–(33) are sufficient conditions to guarantee $\mathcal{D}(\mathcal{P}_t) \geq 0$. To obtain a constitutive equation for $\boldsymbol{T}$ that verifies Eq. (33) we assume, without loss of generality, the following splitting of the velocity gradient

$$\nabla \boldsymbol{u} = \boldsymbol{L} + \boldsymbol{W} = \boldsymbol{L}^d + \boldsymbol{L}^h + \boldsymbol{W}, \tag{34}$$

where $\boldsymbol{W}$ is the skew-symmetric part of the velocity gradient

$$\boldsymbol{W} = \frac{1}{2}\left(\nabla \boldsymbol{u} - \nabla \boldsymbol{u}^T \right), \tag{35}$$

and $\boldsymbol{L}^h$ and $\boldsymbol{L}^d$ are the dilatational and the deviatoric parts of $\boldsymbol{L}$, that is,

$$\boldsymbol{L}^h = \frac{1}{3}\nabla \cdot \boldsymbol{u}\boldsymbol{I}, \tag{36}$$

$$\boldsymbol{L}^d = \boldsymbol{L} - \frac{1}{3}\nabla \cdot \boldsymbol{u}\boldsymbol{I}. \tag{37}$$

It is easily seen that both $\boldsymbol{L}^d$ and $\boldsymbol{L}^h$ are symmetric tensors and that $\boldsymbol{L}^d$ is traceless, i.e., $\mathrm{tr}(\boldsymbol{L}^d) = 0$. Using now Eqs. (34), (35) and (14), it is straightforward to obtain the following identities

$$\boldsymbol{T} : \nabla \boldsymbol{u} = \boldsymbol{T} : (\boldsymbol{L} + \boldsymbol{W}) = \boldsymbol{T} : \boldsymbol{L}, \tag{38}$$

$$\boldsymbol{I} : \nabla \boldsymbol{u} = \boldsymbol{I} : (\boldsymbol{L} + \boldsymbol{W}) = \boldsymbol{I} : \boldsymbol{L}. \tag{39}$$

Additionally, frame invariance arguments may be used (see, e.g., [84]) to show that $\dfrac{\partial \widehat{\Psi}}{\partial \nabla \rho} \otimes \nabla \rho$ is a symmetric tensor. Therefore,

$$\frac{\partial \widehat{\Psi}}{\partial \nabla \rho} \otimes \nabla \rho : \nabla \boldsymbol{u} = \frac{\partial \widehat{\Psi}}{\partial \nabla \rho} \otimes \nabla \rho : \boldsymbol{L}. \tag{40}$$

Taking into account Eqs. (38), (39) and (40), we can rewrite the inequality (33) as

$$\left[\left(\mu\rho - \Psi + c\frac{\partial \widehat{\Psi}}{\partial c} \right) \boldsymbol{I} + \boldsymbol{T} + \frac{\partial \widehat{\Psi}}{\partial \nabla \rho} \otimes \nabla \rho \right] : \boldsymbol{L} \geq 0. \tag{41}$$

The goal now is to choose the term in brackets in (41) in such a way that its double contraction with $\boldsymbol{L}$ is non-negative. We will prove that this can be achieved taking

$$\left[\mu\rho - \Psi + c\frac{\partial \widehat{\Psi}}{\partial c} \right] \boldsymbol{I} + \boldsymbol{T} + \frac{\partial \widehat{\Psi}}{\partial \nabla \rho} \otimes \nabla \rho = 2\bar{\mu}\boldsymbol{L} + \bar{\lambda}\nabla \cdot \boldsymbol{u}\boldsymbol{I}, \tag{42}$$

where $\bar{\mu}$ and $\bar{\lambda}$ are viscosity coefficients that must fulfill a series of conditions that will be shown later. Using Eqs. (36), (37) and basic properties of the double dot product, we obtain

$$\begin{aligned}
\left(2\bar{\mu}\boldsymbol{L} + \bar{\lambda}\nabla \cdot \boldsymbol{u}\boldsymbol{I}\right) : \boldsymbol{L} &= 2\bar{\mu}\boldsymbol{L} : \boldsymbol{L} + \bar{\lambda}\nabla \cdot \boldsymbol{u}\,(\boldsymbol{I} : \boldsymbol{L}) \\
&= 2\bar{\mu}\boldsymbol{L}^d : \boldsymbol{L}^d + 4\bar{\mu}\boldsymbol{L}^d : \boldsymbol{L}^h + 2\bar{\mu}\boldsymbol{L}^h : \boldsymbol{L}^h + \bar{\lambda}\nabla \cdot \boldsymbol{u}\,\mathrm{tr}\,(\boldsymbol{L}) \\
&= 2\bar{\mu}\,\mathrm{tr}\left((\boldsymbol{L}^d)^2\right) + \frac{4}{3}\bar{\mu}\nabla \cdot \boldsymbol{u}\,\mathrm{tr}(\boldsymbol{L}^d) + \frac{2}{9}\bar{\mu}\,(\nabla \cdot \boldsymbol{u})^2\,\mathrm{tr}\,(\boldsymbol{I}) + \bar{\lambda}\,(\nabla \cdot \boldsymbol{u})^2 \\
&= 2\bar{\mu}\,\mathrm{tr}\left((\boldsymbol{L}^d)^2\right) + \left(\frac{2}{3}\bar{\mu} + \bar{\lambda}\right)(\nabla \cdot \boldsymbol{u})^2 .
\end{aligned} \tag{43}$$

Therefore, since $\mathrm{tr}\left((\boldsymbol{L}^d)^2\right) = \sum_{ij}(L^d_{ij})^2 \geq 0$, it follows that

$$\left(2\bar{\mu}\boldsymbol{L} + \bar{\lambda}\nabla\cdot\boldsymbol{u}\boldsymbol{I}\right) : \boldsymbol{L} \geq 0 \tag{44}$$

for any $\bar{\mu}$ and $\bar{\lambda}$ such that,

$$\frac{2}{3}\bar{\mu} + \bar{\lambda} \geq 0 \qquad \text{and} \qquad \bar{\mu} \geq 0. \tag{45}$$

Note that our choice in Eq. (42) leads to a classical model of Newtonian fluids if we assume that $\widehat{\Psi}$ depends neither on $\nabla\rho$ nor on c.

To complete the theory, we need to define the nonlinear function Ψ. Within the constitutive class given by Eq. (10), we consider the expression

$$\widehat{\Psi}(\rho, \nabla\rho, c) = \mathcal{W}(\rho) + \frac{\lambda(c)}{2}|\nabla\rho|^2 + \mathcal{U}(c), \tag{46}$$

where λ is a function of c that takes positive values and $\mathcal{U}(c)$ is the free energy associated to the surfactant. The second term represents the free energy that leads to the capillary forces at the gas–liquid interfaces. $\mathcal{W}(\rho)$ is the Helmholtz free energy of a van der Waals fluid [61,85], which is given by

$$\mathcal{W}(\rho) = R\theta\rho\log\left(\frac{\rho}{b-\rho}\right) - a\rho^2. \tag{47}$$

In the above expression, a and b are positive constants, R is the specific gas constant and θ represents the temperature of the system. Eq. (47) may be thought of as a higher-order modification of the perfect gas Helmholtz free energy that allows for spontaneous phase changes. The ability of Eq. (47) to predict phase transformations stems from the fact that $\mathcal{W}$ may be a non-convex function of ρ for low temperatures. Using Eq. (46) and isolating the stress tensor in (42), we obtain the following expression for $\boldsymbol{T}$

$$\begin{aligned}\boldsymbol{T} = &\left[\mathcal{W}(\rho) + \frac{\lambda(c)}{2}|\nabla\rho|^2 + \mathcal{U}(c) - \rho\mathcal{W}'(\rho) + \rho\lambda'(c)\nabla c\cdot\nabla\rho + \lambda(c)\rho\Delta\rho - c\frac{\lambda'(c)}{2}|\nabla\rho|^2 - c\ \mathcal{U}'(c)\right]\boldsymbol{I}\\ &- \lambda(c)\nabla\rho\otimes\nabla\rho + 2\bar{\mu}\boldsymbol{L} + \bar{\lambda}\nabla\cdot\boldsymbol{u}\boldsymbol{I}.\end{aligned} \tag{48}$$

Finally, identifying $\rho\mathcal{W}'(\rho) - \mathcal{W}(\rho)$ with the thermodynamic pressure p, the stress tensor $\boldsymbol{T}$ can be written as

$$\begin{aligned}\boldsymbol{T} = &-p\boldsymbol{I} + \left[\frac{1}{2}\left(\lambda(c) - c\lambda'(c)\right)|\nabla\rho|^2 + \mathcal{U}(c) - c\ \mathcal{U}'(c) + \rho\lambda'(c)\nabla c\cdot\nabla\rho + \lambda(c)\rho\Delta\rho\right]\boldsymbol{I}\\ &- \lambda(c)\nabla\rho\otimes\nabla\rho + 2\bar{\mu}\boldsymbol{L} + \bar{\lambda}\nabla\cdot\boldsymbol{u}\boldsymbol{I}.\end{aligned} \tag{49}$$

For the surfactant energy $\mathcal{U}(c)$, there are several possible choices. One of the simplest options is to consider $\mathcal{U}(c) = c^2\alpha/2$ where α is a positive constant. This is the free energy associated to classical diffusion processes. With this expression in mind, the stress tensor becomes

$$\boldsymbol{T} = -p\boldsymbol{I} + \left[\frac{1}{2}\left(\lambda(c) - c\lambda'(c)\right)|\nabla\rho|^2 - \frac{\alpha}{2}c^2 + \rho\lambda'(c)\nabla c\cdot\nabla\rho + \lambda(c)\rho\Delta\rho\right]\boldsymbol{I} - \lambda(c)\nabla\rho\otimes\nabla\rho + 2\bar{\mu}\boldsymbol{L} + \bar{\lambda}\nabla\cdot\boldsymbol{u}\boldsymbol{I}. \tag{50}$$

Note also that the stress tensor is symmetric, ensuring that the angular momentum equation (14) is satisfied. This completes the derivation of the theory.

4. Numerical algorithm

4.1. Governing equations

We start by recasting the governing equations in a convenient form for our numerical algorithms. Using the definition of the material time derivative, and the fundamental equations defined in (12), (13) and (15), it is straightforward to obtain the Navier–Stokes–Korteweg equations with surfactant in the Eulerian description as follows

$$\frac{\partial\rho}{\partial t} + \nabla\cdot(\rho\boldsymbol{u}) = 0, \tag{51}$$

$$\frac{\partial(\rho\boldsymbol{u})}{\partial t} + \nabla\cdot(\rho\boldsymbol{u}\otimes\boldsymbol{u}) - \nabla\cdot\boldsymbol{T} - \rho\boldsymbol{f} = 0, \tag{52}$$

$$\frac{\partial c}{\partial t} + \nabla\cdot(c\boldsymbol{u}) + \nabla\cdot\boldsymbol{j} = 0. \tag{53}$$

Notice that the rest of the elements that completely define the theory, that is, a constitutive equation for the stress tensor and the surfactant mass flux as well as a thermodynamic potential from which we can derive the state variables, have already been defined in Section 3.2. Nevertheless, these elements will be analyzed in more detail in the following sections.

4.1.1. Stress tensor

The constitutive equation for the stress tensor $\boldsymbol{T}$ was defined in (50). However, in order to simplify the notation we will adopt the following splitting

$$\boldsymbol{T} = \boldsymbol{\tau} - p\boldsymbol{I} + \boldsymbol{\varsigma} + \boldsymbol{\varsigma}_s, \tag{54}$$

where

$$\boldsymbol{\tau} = \bar{\mu}\left(\nabla\boldsymbol{u} + \nabla\boldsymbol{u}^T\right) + \bar{\lambda}\nabla\cdot\boldsymbol{u}\boldsymbol{I}, \tag{55}$$

$$\boldsymbol{\varsigma} = \lambda(c)\left(\rho\Delta\rho + \frac{1}{2}|\nabla\rho|^2\right)\boldsymbol{I} - \lambda(c)\nabla\rho\otimes\nabla\rho, \tag{56}$$

$$\boldsymbol{\varsigma}_s = \left(-\frac{\alpha}{2}c^2 - c\frac{\lambda'(c)}{2}|\nabla\rho|^2 + \rho\lambda'(c)\nabla c\cdot\nabla\rho\right)\boldsymbol{I}. \tag{57}$$

In the above expressions, $\boldsymbol{\varsigma}$ is the so-called Korteweg tensor, $\boldsymbol{\varsigma}_s$ is the part of the stress tensor associated to the surfactant and $\boldsymbol{\tau}$ corresponds to the viscous stress tensor of a Newtonian fluid (see, for example, [86]). Throughout this paper, we will assume that the Stokes hypothesis is satisfied, that is, $\bar{\lambda} = -2\bar{\mu}/3$. Finally, λ is a function that takes positive values and that modulates the strength of capillary forces. Later, we will show that λ is related with the surface tension at liquid–vapor interfaces. In particular, surface tension scales approximately linearly with $\sqrt{\lambda}$. Our goal is to model the capability of surfactants to lower surface tension. For this reason, λ must be a decreasing function of the surfactant concentration c. There are several possible choices for $\lambda(c)$. Among them, we adopt the following expression

$$\lambda(c) = \lambda_{min}g(c), \tag{58}$$

where λ_{min} is a positive constant that represents the minimum value allowed for the capillarity coefficient. Later, we will adopt a value for λ_{min} that depends on the mesh size as proposed in [45]. The function g is defined as $g(c) = 1 + \beta e^{-c^2}$ where β is a positive constant that controls the strength with which the surface tension decreases with the surfactant concentration. Throughout this paper, we will use the value $\beta = 4$. Larger values of β would produce greater variations of the surface tension, and thus, a more significant impact of the surfactant on the dynamics. Lower values of β would reduce the influence of the surfactant distribution and would produce dynamics which are closer to those of a classical Navier–Stokes–Korteweg fluid. The detailed dependency of the solution on β and on the functional form of λ is an interesting topic that warrants further research.

Remarks.

1. We wish to highlight the difference between λ and $\bar{\lambda}$. The former is a function that represents the strength of capillary forces while the latter is one of the viscosity coefficients.
2. Note that since $\boldsymbol{\varsigma}$ depends upon $\Delta\rho$, the linear momentum balance equation includes third-order partial differential operators.

4.1.2. Surfactant mass flux

The constitutive form of the mass flux $\boldsymbol{j}$ has already been defined in Eq. (32). Using the expression adopted for Ψ [Eq. (46)] and considering the particular case in which $\mathcal{U}(c) = c^2\alpha/2$, $\boldsymbol{j}$ may be expressed as

$$\boldsymbol{j} = -\kappa\nabla\left(\alpha c + \frac{\lambda'(c)}{2}|\nabla\rho|^2\right) = -\kappa\alpha\nabla c - \frac{\kappa}{2}\left(\lambda''(c)\nabla c|\nabla\rho|^2 + 2\lambda'(c)\nabla\nabla\rho^T\nabla\rho\right). \tag{59}$$

Notice that the parameters κ and α govern the relative strength of convection and diffusion processes in the surfactant equation. They will also allow to control the intensity with which the surfactant is drawn by liquid–vapor interfaces. Note also that since $\boldsymbol{j}$ depends upon $\nabla\nabla\rho^T$, the convection–diffusion equation (53) includes third-order partial differential operators.

4.1.3. State variables

In Section 3.2 we have seen that the thermodynamic pressure p can be identified as $\rho\mathcal{W}'(\rho) - \mathcal{W}(\rho)$. Using van der Waals–Helmholtz free energy (47), it is straightforward to obtain

$$p = Rb\left(\frac{\rho\theta}{b-\rho}\right) - a\rho^2. \tag{60}$$

The above equation is known as van der Waals equation and gives the pressure in terms of density and temperature, which for the isothermal model is assumed to be constant. Considering θ as a parameter, we can represent a non-dimensional plot of the pressure as a function of density for different values of θ (see Fig. 2). In this figure, we can observe different behaviors

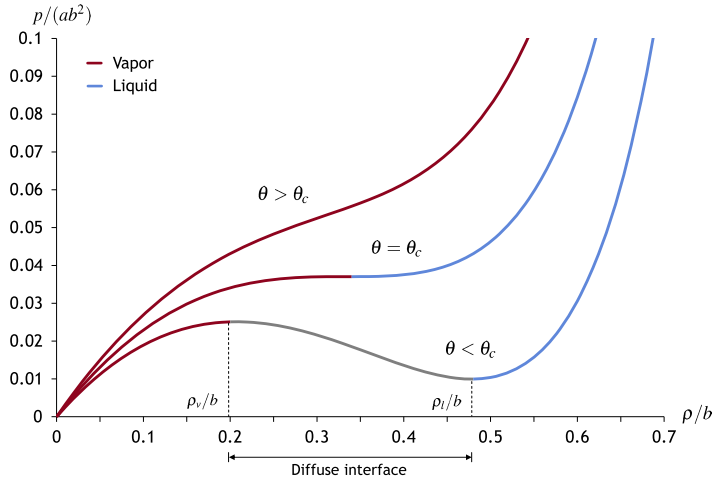

Fig. 2. Non-dimensional plot of van der Waals pressure as a function of density for $\theta > \theta_c$, $\theta = \theta_c$ and $\theta < \theta_c$. Note that for values of temperature below the critical temperature ($\theta < \theta_c$), the pressure is a non-monotone function of density, which allows for spontaneous phase transformations.

of the function p for temperatures below and above a critical temperature $\theta_c = 8ab/(27R)$. For $\theta > \theta_c$, p is a monotonically increasing function of ρ, and the only phase that is stable is the vapor phase. However, for values of the temperature below the critical temperature, that is, $\theta < \theta_c$, the pressure function is no longer monotone, and we can differentiate three regions. The density interval $\rho \in (0, \rho_v)$ corresponds to the vapor phase and the interval $\rho \in (\rho_l, b)$ corresponds to the liquid phase. Additionally, there exists a region $\rho \in (\rho_v, \rho_l)$ where the pressure function decreases with respect to density (gray line in Fig. 2). This allows for the fluid to evaporate and condensate naturally due to pressure and/or temperature variations without introducing additional fields and without precursors. The region where $\rho \in (\rho_v, \rho_l)$ has no physical meaning, however, mathematically it is just a smooth interface between the vapor and liquid phases which spans over a length scale $\sqrt{\lambda/a}$. Note also that in the inviscid, non-conducting limit, the equations are ill-posed for $\lambda = 0$, and capillary forces are necessary to restore well-posedness. The reader is referred to [45,61,85] for further details on the NSK equations without surfactants.

4.2. Boundary conditions

To define a well-posed boundary value problem we need to specify suitable boundary conditions. For some of the numerical examples that we will present in Section 5 we have adopted periodic boundary conditions. However, in order to analyze more practical situations we will consider other possibilities. In particular, we will focus on solid wall boundary conditions. In classical isothermal compressible gas dynamics, solid wall boundary conditions may be imposed, for example, by setting velocity to given values, that is, $\boldsymbol{u} = \boldsymbol{u}_D$ on the solid wall boundary. However, in the NSK system, the third-order spatial derivative on the density included in the linear momentum equation [see Eq. (56)] urges to impose an extra boundary condition to attain well-posedness. One possibility is to set the following boundary condition,

$$\nabla\rho \cdot \boldsymbol{n} = |\nabla\rho| \cos(\varphi), \tag{61}$$

where $\boldsymbol{n}$ denotes the unit outward normal to the boundary, and φ is the static contact angle between the liquid–vapor interface and the solid, measured in the liquid phase. To define suitable boundary conditions for the surfactant equation, we must take into account that surfactants are naturally trapped by liquid–vapor interfaces. Thus, the boundary conditions for the surfactant equation must be compatible with this phenomenon. For the majority of cases of practical relevance, we will also need the boundary conditions to be mass-preserving. With this idea in mind, we propose the following boundary condition,

$$\nabla c \cdot \boldsymbol{n} = |\nabla c| \cos(\varphi_s) \tag{62}$$

where φ_s represents the angle between the surfactant gradient and the outward normal to the boundary. We will relate φ_s with the contact angle φ in order to ensure that the surfactant is able to follow the liquid–vapor interface without any incompatibility caused by the presence of the boundary. To do so, we define the following relation,

$$\cos(\varphi_s) = \cos(\varphi) h(\rho) \tag{63}$$

with

$$h(\rho) = \tanh\left(\left(\frac{\rho_l^M + \rho_v^M}{2} - \rho\right) s\right) \tag{64}$$

In the above expression, s is a parameter that controls the slope of the hyperbolic tangent function and that we set to $s = 4/(\rho_l^M - \rho_v^M)$; the constants ρ_l^M and ρ_v^M denote the Maxwell states[1] for the liquid and the vapor phases, respectively. To define the function $h(\rho)$ in Eq. (64), let us first note that a typical equilibrium solution to our model produces a density profile which is composed by patches of constant density in which $\rho = \rho_l^M$ or $\rho = \rho_v^M$. These patches are linked by smooth transitions which span over a length scale $\sqrt{\lambda/a}$. Therefore, the function $h(\rho)$ produces a smooth and sufficiently fast transition between $+1$ and -1 when ρ varies in the interval $\rho \in (\rho_v^M, \rho_l^M)$. As a consequence, Eq. (64) enforces $\varphi_s \simeq \varphi$ for values of the density close to ρ_v^M and $\varphi_s \simeq \pi - \varphi$ for $\rho \simeq \rho_l^M$. The boundary condition (62)–(64) is also mass preserving. This is due to the fact that the surfactant gets quickly trapped on the liquid–vapor interface and $|\nabla c|$ is expected to be small everywhere else. Within the interface, there may be mass flow through the boundary, but the net contribution will be approximately zero because $h(\rho)$ is an odd function with respect to the contact line, which is assumed to be located at $\rho = (\rho_l^M + \rho_v^M)/2$.

4.3. Continuous problem in the weak form

Our derivation is based on a weak form of the governing equation. The usual practice to derive a weak form of a third-order partial differential equation is to introduce additional fields to lower the order of the derivatives in the variational form and use standard $\mathcal{C}^0$-continuous finite elements. Due to the use of IGA, we can generate globally $\mathcal{C}^1$-continuous basis functions and avoid the introduction of additional degrees of freedom. However, in order to facilitate the imposition of the boundary condition (61), we will introduce the new variable $\Upsilon = \Delta\rho$. The consequence of this choice is that our weak form will naturally enforce the boundary condition (61), which otherwise would have to be built strongly in the finite element space. As we will see later, our formulation still requires the use of $\mathcal{C}^1$-continuous basis functions and IGA due to the higher-order term in the surfactant equation.

We will consider that Eqs. (51)–(53) hold in $\Omega \subset \mathbb{R}^3$. The boundary of Ω is denoted Γ. To derive our weak form, let us introduce the trial solution space $\mathcal{X} = \mathcal{X}(\Omega)$. Let $\boldsymbol{U} = \{\rho, \boldsymbol{u}, \Upsilon, c\}$ be a typical member of $\mathcal{X}$. We assume that for all $\boldsymbol{U} \in \mathcal{X}$ the velocity field satisfies the solid–wall Dirichlet boundary condition on Γ. For the remaining fields in $\boldsymbol{U}$, namely ρ, Υ, and c, Dirichlet boundary conditions are not very relevant in practical applications, so we do not consider that case. The weighting function space $\mathcal{Y} = \mathcal{Y}(\Omega)$ is identical to $\mathcal{X}$, but all restrictions on the Dirichlet boundary are homogeneous. The variational formulation is stated as follows: Find $\boldsymbol{U} = \{\rho, \boldsymbol{u}, \Upsilon, c\} \in \mathcal{X}$ such that $\forall \boldsymbol{W} = \{w^1, \boldsymbol{w}^2, w^3, w^4\} \in \mathcal{Y}$,

$$B(\boldsymbol{W}, \boldsymbol{U}) = 0, \tag{65}$$

where

$$\begin{aligned}
B(\boldsymbol{W}, \boldsymbol{U}) = & \int_\Omega w^1 \frac{\partial \rho}{\partial t} \mathrm{d}\Omega - \int_\Omega \nabla w^1 \cdot \boldsymbol{u} \rho \mathrm{d}\Omega + \int_\Omega \boldsymbol{w}^2 \cdot \left(\rho \frac{\partial \boldsymbol{u}}{\partial t} + \boldsymbol{u} \frac{\partial \rho}{\partial t} - \rho \boldsymbol{f} \right) \mathrm{d}\Omega - \int_\Omega \nabla \boldsymbol{w}^2 : \boldsymbol{u} \otimes \boldsymbol{u} \rho \mathrm{d}\Omega \\
& + \int_\Omega \nabla \boldsymbol{w}^2 : (\boldsymbol{\tau} - p\boldsymbol{I}) \, \mathrm{d}\Omega \\
& + \int_\Omega \nabla \cdot \boldsymbol{w}^2 \lambda(c) \left(\rho \Upsilon + \frac{1}{2} |\nabla \rho|^2 \right) \mathrm{d}\Omega - \int_\Omega \nabla \boldsymbol{w}^2 : \lambda(c) \nabla \rho \otimes \nabla \rho \mathrm{d}\Omega \\
& - \int_\Omega \nabla \cdot \boldsymbol{w}^2 \left(\frac{\alpha c^2}{2} + \frac{c \lambda'(c)}{2} |\nabla \rho|^2 \right) \mathrm{d}\Omega \\
& + \int_\Omega \nabla \cdot \boldsymbol{w}^2 \lambda'(c) \, \rho \nabla c \cdot \nabla \rho \mathrm{d}\Omega + \int_\Omega w^3 \Upsilon \mathrm{d}\Omega + \int_\Omega \nabla w^3 \cdot \nabla \rho \mathrm{d}\Omega - \int_\Gamma w^3 |\nabla \rho| \cos(\varphi) \mathrm{d}\Gamma + \int_\Omega w^4 \frac{\partial c}{\partial t} \mathrm{d}\Omega \\
& - \int_\Omega \nabla w^4 \cdot \boldsymbol{u} c \mathrm{d}\Omega + \int_\Omega \alpha \kappa \nabla w^4 \cdot \nabla c \mathrm{d}\Omega - \int_\Gamma w^4 \kappa \alpha \, |\nabla c| \cos(\varphi_s) \mathrm{d}\Gamma + \int_\Omega \frac{\kappa}{2} \nabla w^4 \cdot \nabla \left(\lambda'(c) \, |\nabla \rho|^2 \right) \mathrm{d}\Omega \\
& - \int_\Gamma w^4 \frac{\kappa}{2} \lambda''(c) \, |\nabla \rho|^2 \, |\nabla c| \cos(\varphi_s) \mathrm{d}\Gamma - \int_\Gamma w^4 \kappa \lambda'(c) \nabla \nabla^T \rho \nabla \rho \cdot \boldsymbol{n} \mathrm{d}\Gamma
\end{aligned} \tag{66}$$

Note that the variational formulation (65)–(66) weakly imposes the fluid dynamics and the surfactant equations as well as the boundary conditions (61) and (62). Note also that if we do not set Dirichlet boundary conditions for velocity on the entire boundary, then the variational formulation weakly imposes the conjugate stress-free condition.

[1] The Maxwell states represent values of the density for which there is chemical and mechanical equilibrium. For a given temperature, they are simply the equilibrium values of the liquid and vapor densities.

4.4. Semidiscrete formulation

For the spatial discretization of Eq. (66) we make use of the Galerkin method. We define finite-dimensional approximations of the functional spaces, namely, $\mathcal{X}_h$ and $\mathcal{Y}_h$, such that $\mathcal{X}_h \subset \mathcal{X} \subset \mathcal{H}^2$ and $\mathcal{Y}_h \subset \mathcal{Y} \subset \mathcal{H}^2$. Here, $\mathcal{H}^2$ denotes the Sobolev space of square integrable functions with square integrable first and second derivatives. We approximate (66) by the following variational problem over the finite element spaces: Find $\boldsymbol{U}_h = \{\rho_h, \boldsymbol{u}_h, \Upsilon_h, c_h\} \in \mathcal{X}_h$, such that $\forall \boldsymbol{W}_h = \{w_h^1, \boldsymbol{w}_h^2, w_h^3, w_h^4\} \in \mathcal{Y}_h$,

$$B(\boldsymbol{W}_h, \boldsymbol{U}_h) = 0, \tag{67}$$

where

$$\rho_h(\boldsymbol{x}, t) = \sum_{A \in I} \rho_A(t) N_A(\boldsymbol{x}), \qquad w_h^1(\boldsymbol{x}, t) = \sum_{A \in I} w_A^1 N_A(\boldsymbol{x}), \tag{68}$$

$$\boldsymbol{u}_h(\boldsymbol{x}, t) = \sum_{A \in I} \boldsymbol{u}_A(t) N_A(\boldsymbol{x}), \qquad \boldsymbol{w}_h^2(\boldsymbol{x}, t) = \sum_{A \in I} \boldsymbol{w}_A^2 N_A(\boldsymbol{x}), \tag{69}$$

$$\Upsilon_h(\boldsymbol{x}, t) = \sum_{A \in I} \Upsilon_A(t) N_A(\boldsymbol{x}), \qquad w_h^3(\boldsymbol{x}, t) = \sum_{A \in I} w_A^3 N_A(\boldsymbol{x}), \tag{70}$$

$$c_h(\boldsymbol{x}, t) = \sum_{A \in I} c_A(t) N_A(\boldsymbol{x}), \qquad w_h^4(\boldsymbol{x}, t) = \sum_{A \in I} w_A^4 N_A(\boldsymbol{x}), \tag{71}$$

In Eqs. (68)–(71), the N_A's are a set of basis functions defined on Ω and I is their global-index set. By taking the N_A's as globally $\mathcal{C}^1$-continuous functions, we can define conforming discrete spaces that make the variational formulation well defined.

4.5. Time discretization and numerical implementation

In this section, we present the time integration algorithm for the semi-discrete Eq. (67). We employ the generalized-α method, which was originally proposed by Chung and Hulbert [79] for the equations of structural dynamics, and subsequently extended to the equations of fluid mechanics by Jansen et al. [87]. This method has also been successfully applied in other fields as fluid–structure interaction [88–90] and phase-field modeling [29,45,50].

4.5.1. Time stepping scheme

Let $\boldsymbol{V}$ denote the vector of control variable degrees of freedom and let $\dot{\boldsymbol{V}}$ be its time derivative. We define the residual vectors

$$\boldsymbol{R}^{cont} = \{R_A^{cont}\}, \tag{72}$$

$$\boldsymbol{R}^{mom} = \{R_{A,i}^{mom}\}, \tag{73}$$

$$\boldsymbol{R}^{aux} = \{R_A^{aux}\}, \tag{74}$$

$$\boldsymbol{R}^{surf} = \{R_A^{surf}\}, \tag{75}$$

where A is a control-variable index and i is an index associated to the spatial dimensions. The residual components are defined as

$$R_A^{cont} = B(\{N_A, 0, 0, 0\}, \{\rho_h, \boldsymbol{u}_h, \Upsilon_h, c_h\}), \tag{76}$$

$$R_{A,i}^{mom} = B(\{0, N_A \boldsymbol{e}_i, 0, 0\}, \{\rho_h, \boldsymbol{u}_h, \Upsilon_h, c_h\}), \tag{77}$$

$$R_A^{aux} = B(\{0, 0, N_A, 0\}, \{\rho_h, \boldsymbol{u}_h, \Upsilon_h, c_h\}), \tag{78}$$

$$R_A^{surf} = B(\{0, 0, 0, N_A\}, \{\rho_h, \boldsymbol{u}_h, \Upsilon_h, c_h\}), \tag{79}$$

where $\boldsymbol{e}_i$ is the ith cartesian basis vector. The time stepping scheme can be stated as follows: Given the discrete approximation to the global vectors of control variables at time t_n, namely, $\boldsymbol{V}_n$, $\dot{\boldsymbol{V}}_n$ and the current time step $\Delta t = t_{n+1} - t_n$ find $\boldsymbol{V}_{n+1}$ and $\dot{\boldsymbol{V}}_{n+1}$ such that

$$\boldsymbol{R}^{cont}(\boldsymbol{V}_{n+\alpha_f}, \dot{\boldsymbol{V}}_{n+\alpha_m}) = 0, \tag{80}$$

$$\boldsymbol{R}^{mom}(\boldsymbol{V}_{n+\alpha_f}, \dot{\boldsymbol{V}}_{n+\alpha_m}) = 0, \tag{81}$$

$$\boldsymbol{R}^{aux}(\boldsymbol{V}_{n+\alpha_f}, \dot{\boldsymbol{V}}_{n+\alpha_m}) = 0, \tag{82}$$

$$\boldsymbol{R}^{surf}(\boldsymbol{V}_{n+\alpha_f}, \dot{\boldsymbol{V}}_{n+\alpha_m}) = 0, \tag{83}$$

$$\boldsymbol{V}_{n+1} = \boldsymbol{V}_n + \Delta t((1-\gamma)\dot{\boldsymbol{V}}_n + \gamma\dot{\boldsymbol{V}}_{n+1}), \tag{84}$$

where

$$\boldsymbol{V}_{n+\alpha_f} = \boldsymbol{V}_n + \alpha_f\left(\boldsymbol{V}_{n+1} - \boldsymbol{V}_n\right), \tag{85}$$

$$\dot{\boldsymbol{V}}_{n+\alpha_m} = \dot{\boldsymbol{V}}_n + \alpha_m\left(\dot{\boldsymbol{V}}_{n+1} - \dot{\boldsymbol{V}}_n\right). \tag{86}$$

The parameters α_f, α_m and γ are chosen as in [45] to ensure second-order accuracy and unconditional stability of the time-integration algorithm. The non-linear system of equations (80)–(83) may be approximated by using a Newton–Raphson method, which leads to the following two-stage predictor–multicorrector algorithm.

Predictor stage: We adopt a constant-velocity predictor, that is,

$$\boldsymbol{V}^{(0)}_{n+1} = \boldsymbol{V}_n, \tag{87}$$

$$\dot{\boldsymbol{V}}^{(0)}_{n+1} = \frac{\gamma-1}{\gamma}\dot{\boldsymbol{V}}_n, \tag{88}$$

where the superscript with parentheses denotes the nonlinear iteration index.

Multicorrector stage: Repeat the following steps for $i = 1, 2, \ldots, i_{max}$ or until convergence

1. Evaluate solution iterates at the α-levels

$$\boldsymbol{V}^{(i)}_{n+\alpha_f} = \boldsymbol{V}_n + \alpha_f\left(\boldsymbol{V}^{(i-1)}_{n+1} - \boldsymbol{V}_n\right), \tag{89}$$

$$\dot{\boldsymbol{V}}^{(i)}_{n+\alpha_m} = \dot{\boldsymbol{V}}_n + \alpha_m\left(\dot{\boldsymbol{V}}^{(i-1)}_{n+1} - \dot{\boldsymbol{V}}_n\right). \tag{90}$$

2. Use the solutions at the α-levels to assemble the residual and the tangent matrix of the linear system

$$\frac{\partial \boldsymbol{R}^{cont}_{(i)}}{\partial \dot{\boldsymbol{V}}_{n+1}}\Delta\dot{\boldsymbol{V}}^{(i)}_{n+1} = -\boldsymbol{R}^{cont}_{(i)}, \tag{91}$$

$$\frac{\partial \boldsymbol{R}^{mom}_{(i)}}{\partial \dot{\boldsymbol{V}}_{n+1}}\Delta\dot{\boldsymbol{V}}^{(i)}_{n+1} = -\boldsymbol{R}^{mom}_{(i)}, \tag{92}$$

$$\frac{\partial \boldsymbol{R}^{aux}_{(i)}}{\partial \dot{\boldsymbol{V}}_{n+1}}\Delta\dot{\boldsymbol{V}}^{(i)}_{n+1} = -\boldsymbol{R}^{aux}_{(i)}, \tag{93}$$

$$\frac{\partial \boldsymbol{R}^{surf}_{(i)}}{\partial \dot{\boldsymbol{V}}_{n+1}}\Delta\dot{\boldsymbol{V}}^{(i)}_{n+1} = -\boldsymbol{R}^{surf}_{(i)}. \tag{94}$$

   The resulting linear system is solved using a preconditioned GMRES algorithm [91]. In particular, as preconditioner we have used an incomplete LU factorization. For the numerical examples presented here, solving the linear system with a tolerance of 10^{-5} requires normally 30 to 40 GMRES iterations.

3. Use $\Delta\dot{\boldsymbol{V}}^{(i)}_{n+1}$ to update the iterates as

$$\dot{\boldsymbol{V}}^{(i)}_{n+1} = \dot{\boldsymbol{V}}^{(i-1)}_{n+1} + \Delta\dot{\boldsymbol{V}}^{(i)}_{n+1}, \tag{95}$$

$$\boldsymbol{V}^{(i)}_{n+1} = \boldsymbol{V}^{(i-1)}_{n+1} + \gamma\Delta t\Delta\dot{\boldsymbol{V}}^{(i)}_{n+1}, \tag{96}$$

This completes one nonlinear iteration. The nonlinear iterative algorithm should be repeated until the norm of each of the residual vectors defined in (72)–(75) has been reduced to a given tolerance ϵ_r of its value using the predictions defined in (87)–(88). In this work, we use $\epsilon_r = 10^{-4}$. For the examples presented herein, this typically requires two to four nonlinear iterations.

5. Numerical examples

In this section we present a series of numerical examples that illustrate the predictive ability of our model and the effectiveness of our computational method. The first group of numerical examples shows how surface tension relates with the parameters of the problem and how our model succeeds in reproducing the way in which surfactants lower surface tension. The second simulation demonstrates that surfactants are naturally trapped at liquid–vapor interfaces in accordance with the physical behavior of surface active agents. For this example, we also plot the evolution of the free energy with respect to time, showing that it decreases monotonically as it was imposed in the derivation of the theory. Subsequently, we present a numerical simulation in which a drop of water is being attached to a solid boundary. The aim is to point out that

our theory easily allows to model how the contact angle between the liquid–vapor interface and the boundary is modified due to the presence of the surfactant. The last example involves the three-dimensional coalescence of two vapor bubbles. For all the examples, we neglect body forces taking $\boldsymbol{f} = 0$ in Eq. (13). In order to test our code for NSK with surfactants, we have also run several numerical computations (not included in the manuscript) taking the surfactant concentration to zero in the residual. Then, we have verified that these results agree with overkill numerical solutions to the NSK equations. We have also repeated these computations adding the surfactant equation to the residual, but taking very small values for β. In all cases, we achieved the expected results.

All the parameters and the results presented in Section 5 are given in non-dimensional form. We have rescaled the units of measurement of length, mass, time and temperature by L_0, bL_0^3, $L_0/\sqrt{ab}$ and θ_c, respectively, where $L_0 = 1$ denotes a length scale of the computational domain size. Using this non-dimensionalization, it may be shown that the dynamics of the governing equations are controlled by four dimensionless numbers,

$$Re = \frac{L_0 b\sqrt{ab}}{\bar{\mu}}, \quad Ca = \frac{\sqrt{\lambda_{min}/a}}{L_0}, \quad Ba = \frac{\alpha}{ab^2}, \quad Pe = \frac{L_0\sqrt{ab}}{\kappa\alpha}, \tag{97}$$

where Re is the Reynolds number, Ca denotes the capillary number, Ba is the non-dimensional form of α and Pe is the Peclet number. The capillary number Ca and the Reynolds number Re were chosen according to the methodology proposed in [45], which relates these parameters to the computational mesh. The objective of this upscaling method is to obtain the largest Reynolds number and the lowest capillary number that can be resolved by a particular mesh. To this end, in [45] the authors propose to scale Ca and Re as

$$Ca = h/L_0 \quad \text{and} \quad Re = \phi L_0/h, \tag{98}$$

where h is a characteristic length scale of the spatial mesh and ϕ is an $O(1)$ constant. We have adopted $\phi = 2$ for all the computations. The reader is referred to [45] for further details about this method.

Remarks.

1. Note that Eqs. (97) and (98) imply that λ_{min} is related to the mesh size h by the expression $\lambda_{min} = ah^2$.
2. Note also that the interface thickness $\sqrt{\lambda/a}$ depends on the surfactant concentration through the relation $\sqrt{\lambda/a} = \sqrt{\lambda_{min} g(c)/a} = h\sqrt{g(c)}$.

5.1. Surface tension in the proposed model

It is already known the way surface tension and the NSK parameters are related (see, for example, [61]). In particular, the effect of surface tension σ_{LV} is implicitly included in the NSK model by the relation

$$\sigma_{LV} \simeq K_0\sqrt{\lambda}, \tag{99}$$

where K_0 is a nonlinear function of θ. Eq. (99) is accurate for values of the temperature close to the critical temperature θ_c. Our goal is to show that (99), or equivalently, the non-dimensional form

$$\gamma_{LV} \simeq k_0 Ca\sqrt{g(c)} \tag{100}$$

stands approximately for the NSK model with surfactants, where γ_{LV} is the non-dimensional surface tension, k_0 is a constant for a given temperature and $g(c)$ has been defined right after Eq. (58). With this purpose, we have carried out a number of numerical simulations (each point in Fig. 3 represents a computation) for different initial conditions of the surfactant. In all cases, the initial configuration for the density was the same, namely, it consisted in two vapor bubbles of radius $R_1 = 0.17$ and $R_2 = 0.1$ centered at $C_1 = (0.35, 0.5)$ and $C_2 = (0.75, 0.5)$, respectively. The initial values of the density for the liquid and the vapor phases were those corresponding to the Maxwell states.[2] As expected, the two bubbles merge into one circular vapor area, whose radius is given by the temperature (see, e.g., [45]). The initial density condition does not have an impact on the scaling that we want to analyze, so the study could be repeated with different density initial conditions and the results would not be altered. For the surfactant, we have employed in all cases a flat initial condition representing a constant surfactant concentration. Different simulations employed different values of the constant so as to vary the right-hand side of Eq. (100). In each simulation we have waited for the steady state and then we have measured the radius r of the resulting bubble and the pressure difference

[2] The Maxwell States for the liquid (ρ_l^M) and the vapor phases (ρ_v^M) employed in the numerical examples of Sect. 5.1 are those listed below:

θ	ρ_v^M	ρ_l^M
0.85	0.10	0.60
0.7	0.04	0.71

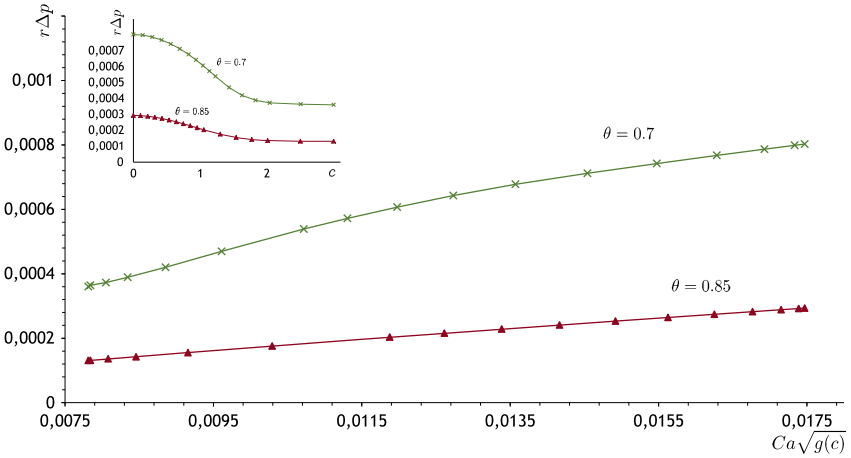

Fig. 3. Non-dimensional plot of our estimate of surface tension $r\Delta p$ as a function of capillarity for two different temperatures. For the steady state, surface tension scales almost linearly with the values of the capillarity function at the interface. In the inset we also plot surface tension as a function of the surfactant concentration at the interface. Note that surface tension decreases with surfactant concentration.

Δp between the liquid and the vapor phases. Then, we have used the two dimensional form of Young–Laplace equation

$$\Delta p = \frac{\gamma_{LV}}{r}, \tag{101}$$

to define an estimate of surface tension at the liquid–vapor interface, that is, $\gamma_{LV} = r\Delta p$. Finally, we have plotted (see Fig. 3) our estimate of surface tension with respect to $Ca\sqrt{g(c)}$. This procedure was carried out for two different temperatures, $\theta = 0.7$ and $\theta = 0.85$.

The computational domain, $\Omega = (0, 1)^2$, was comprised of 128 $\mathcal{C}^1$-quadratic elements in each direction. We adopted periodic boundary conditions. The other parameters employed in these computations are $Re = 256$, $Ca = 0.0078125$, $Ba = 0.1$ and $Pe = 500$. The time step used was constant and equal to $\Delta t = 0.01$.

As it can be seen in Fig. 3, the surface tension follows approximately a linear relation with the values of the capillarity function at the interface. This proves that the parameter k_0 remains constant in our model for given temperatures close to the critical temperature θ_c. Thus, the expression (100) is valid for the theory presented herein. We have also plotted our estimate of surface tension with respect to the surfactant concentration at the interface (see inset in Fig. 3), which makes evident that surface tension decreases with surfactant concentration. This is in agreement with the behavior of most of the surfactants employed in the chemical industry.

5.2. Trapping of surfactant at the liquid–vapor interface

This numerical example shows how our model naturally predicts the trapping of the surfactant at the liquid–vapor interface. As shown in the previous example, the surfactant can also change the properties of the interface, which, in turn may alter the dynamics of the system, for example, inhibiting partially or completely the coalescence of vapor bubbles. This example illustrates both phenomena. Finally, we also use this computation to show that the free-energy defined in Eq. (9) decreases along solutions to the governing equations. We have carried out a numerical simulation predicting the dynamics of three vapor bubbles (see left column in Fig. 4) using the traditional NSK model without surfactants (see [45] for further details). Then, we repeated exactly the same simulation with the theory presented herein (middle and right columns in Fig. 4).

Three bubbles of radius $R_1 = 0.11$, $R_2 = 0.18$ and $R_3 = 0.08$ were initially centered at $C_1 = (0.25, 0.45)$, $C_2 = (0.65, 0.45)$ and $C_3 = (0.51, 0.70)$. The initial condition for the density variable [see Figs. 4(a) and 4(b)] inside and outside of the bubbles was that corresponding to the Maxwell states of the vapor (red color) and the liquid water (blue color), respectively, for a temperature $\theta = 0.85$, that is, $\rho_v^M = 0.10$ and $\rho_l^M = 0.60$. We have used a uniform mesh comprised of 512 $\mathcal{C}^1$-quadratic elements in each direction and we have imposed periodic boundary conditions. In both simulations we have employed $Re = 1024$ and $Ca = 0.001953125$. For the NSK theory with surfactant we have adopted $Ba = 0.005$ and $Pe = 10000$. Initially, the surfactant [see Fig. 4(c)] was evenly distributed on the whole domain so that the initial surfactant concentration was the constant $c_0 = 0.8$. In both cases, we used a constant time step equal to $\Delta t = 0.00125$.

In Fig. 4 we plot the evolution of the density for the NSK theory (left column) and the evolution of the density and surfactant concentration for the NSK theory with surfactant (middle and right columns) for different time steps until a steady state is reached. As it can be seen, in the simulation without surfactants, the bubbles that are closer are able to coalesce [Fig. 4(d)]. However, the presence of the surfactant can inhibit the coalescence of these two bubbles [Fig. 4(e)], altering the behavior of the system. The surfactant is attracted by the regions with a higher density gradient, that is, the

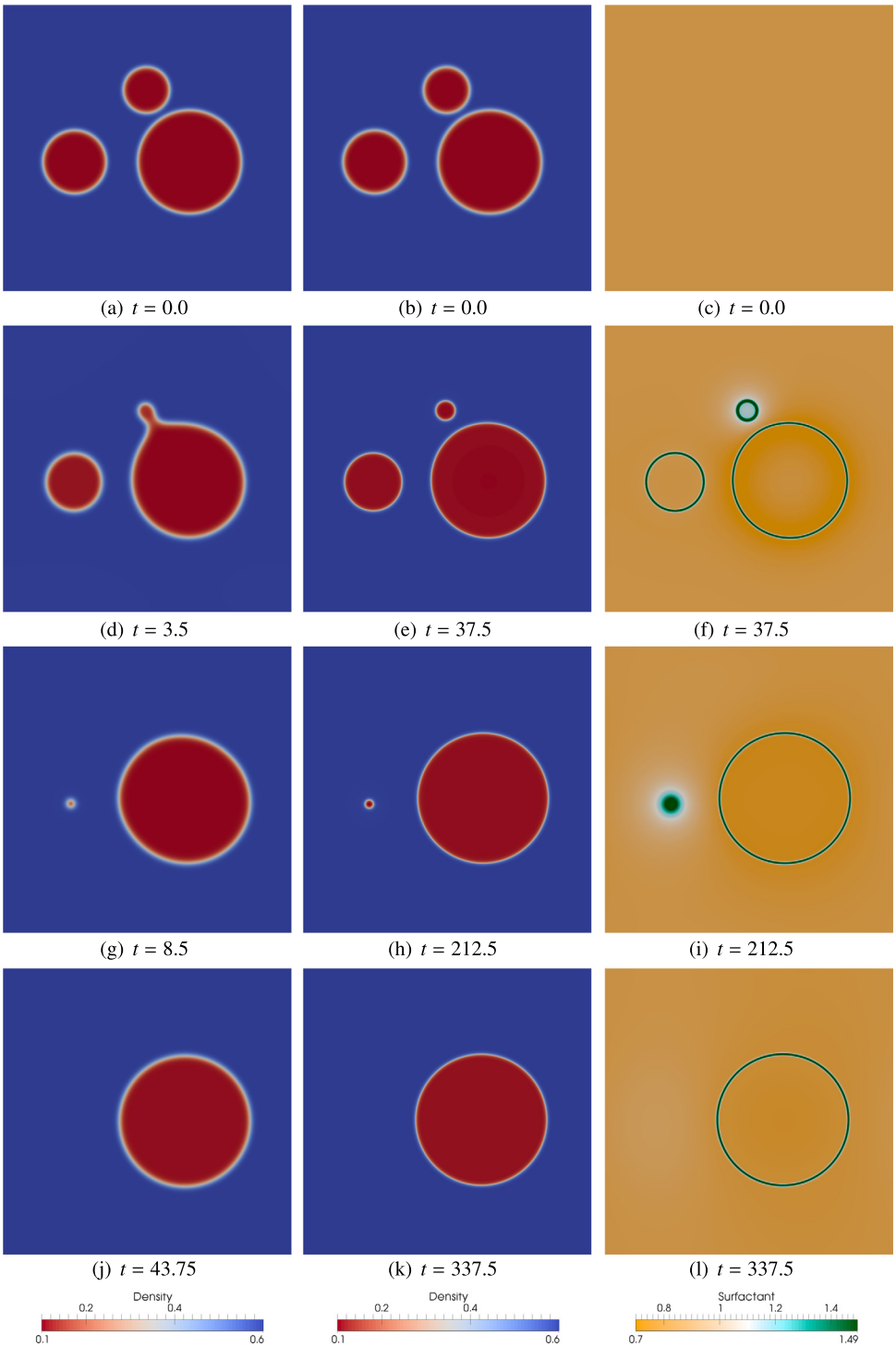

Fig. 4. Simulation of three vapor bubbles using the NSK theory without surfactant (left column) and with surfactant (middle and right columns). In both cases, we use a square-shaped domain $\Omega = (0, 1)^2$ composed of 512^2 elements. The initial configuration consists in three vapor bubbles [red color in the density plots (a) and (b)] deposited on a liquid matrix (blue color). For the NSK theory with surfactant we also adopt as initial condition an homogeneous distribution of the surfactant concentration, namely, $c_0 = 0.8$. Comparing the density plots of both theories (left and middle columns) we can see that the NSK model with surfactant inhibits the coalescence of the small and big bubbles. Since the surfactant is attracted by the areas with higher density gradients, the surfactant concentration increases at the interfaces (green color in the surfactant plots). The parameters used in these simulations are $Re = 1024$, $Ca = 0.001953125$, $Ba = 0.005$ and $Pe = 10000$. (For interpretation of the references to color in this figure legend, the reader is referred to the web version of this article.)

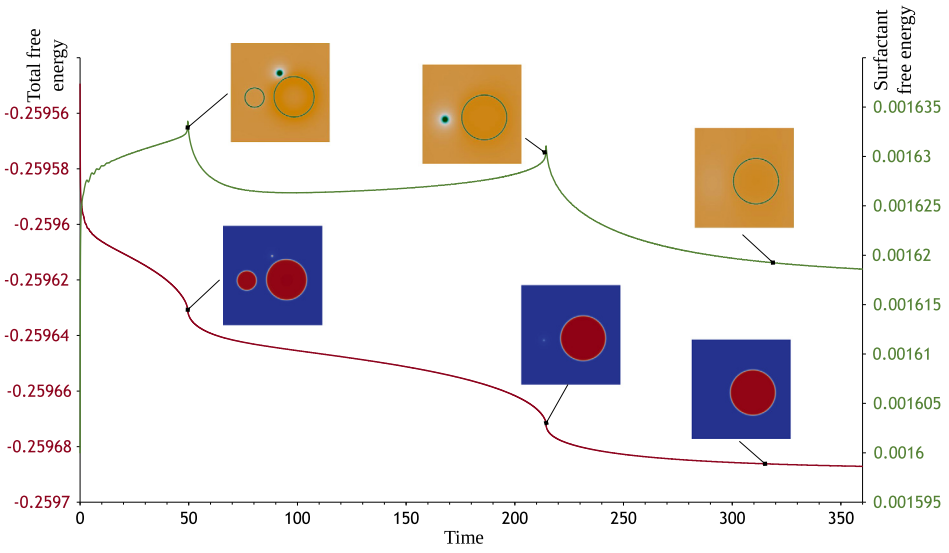

Fig. 5. Plot of the total free energy of the system (red color) and the surfactant free energy $\mathcal{U}$ (green color) with respect to time. The total energy is a monotonically decreasing function in agreement with the conditions imposed during the derivation of our model. The surfactant energy reaches two peaks in the moments previous to the collapse of the smaller bubbles. Initially, the surfactant concentration is uniform. We have used the parameters $Re = 1024$, $Ca = 0.001953125$, $Ba = 0.005$ and $Pe = 10000$. (For interpretation of the references to color in this figure legend, the reader is referred to the web version of this article.)

interfaces between the vapor and the liquid phases (see the right column of Fig. 4). This is in agreement with the physical behavior of surface active agents.

Fig. 5 (red line) shows the time evolution of the free-energy of the system [see Eq. (9)], which is monotonically decreasing as predicted by the theory. For further insight into the model, we also plot the evolution of the free energy corresponding to the surfactant (green line), that is, $\mathcal{U}$ in Eq. (46). There is no reason why we should expect $\mathcal{U}$ to be a decreasing function of time, and, in fact, it is not. One can observe two sharp increases in the surfactant free energy at times $t \simeq 50$ and $t \simeq 215$, which coincide with the previous instants to the disappearance of each of the bubbles [see Figs. 4(h) and 4(i)]. When bubbles collapse, the surfactant gets trapped in smaller areas and therefore, achieves higher concentrations. The oscillatory behavior of the surfactant free energy at early stages ($t < 20$) is caused by the initial conditions.[3] The initial condition for the surfactant is a flat function representing a constant value. The surfactant gets quickly trapped at the interfaces and produces strong dynamics at early times, which manifests itself with small-amplitude oscillations in the surfactant free energy.

5.3. Attachment of a drop of water to a wall

In all the previous simulations we have imposed periodic boundary conditions. However, in this case we will try to emulate how the presence of the surfactant may modify the contact angle φ between a drop of water and a solid substrate. For ideal solid surfaces, where the solid is flat and rigid, the equilibrium contact angle φ_E between the liquid–vapor interface and the boundary is given by Young equation, that is,

$$\gamma_{SL} + \gamma_{LV}\cos(\varphi_E) = \gamma_{SV} \tag{102}$$

where γ_{SV} and γ_{SL} are the surface tension at the solid–vapor interface and at the solid–liquid interface, respectively. Young's relation (102) and expression (100) allow us to approximate the contact angle φ as

$$\cos(\varphi) \simeq \frac{\gamma_{SV} - \gamma_{SL}}{\gamma_{LV}} \simeq \frac{\varepsilon}{Ca\sqrt{g(c)}} \tag{103}$$

where we consider $\varepsilon = \dfrac{\gamma_{SV} - \gamma_{SL}}{k_0}$ as a positive constant. Therefore, the boundary condition (61) becomes

$$\nabla\rho \cdot \boldsymbol{n} = |\nabla\rho| \frac{\varepsilon}{Ca\sqrt{g(c)}} \tag{104}$$

[3] We have repeated the computation with a time step four times smaller to make sure that the oscillatory behavior was not a consequence of the discretization errors.

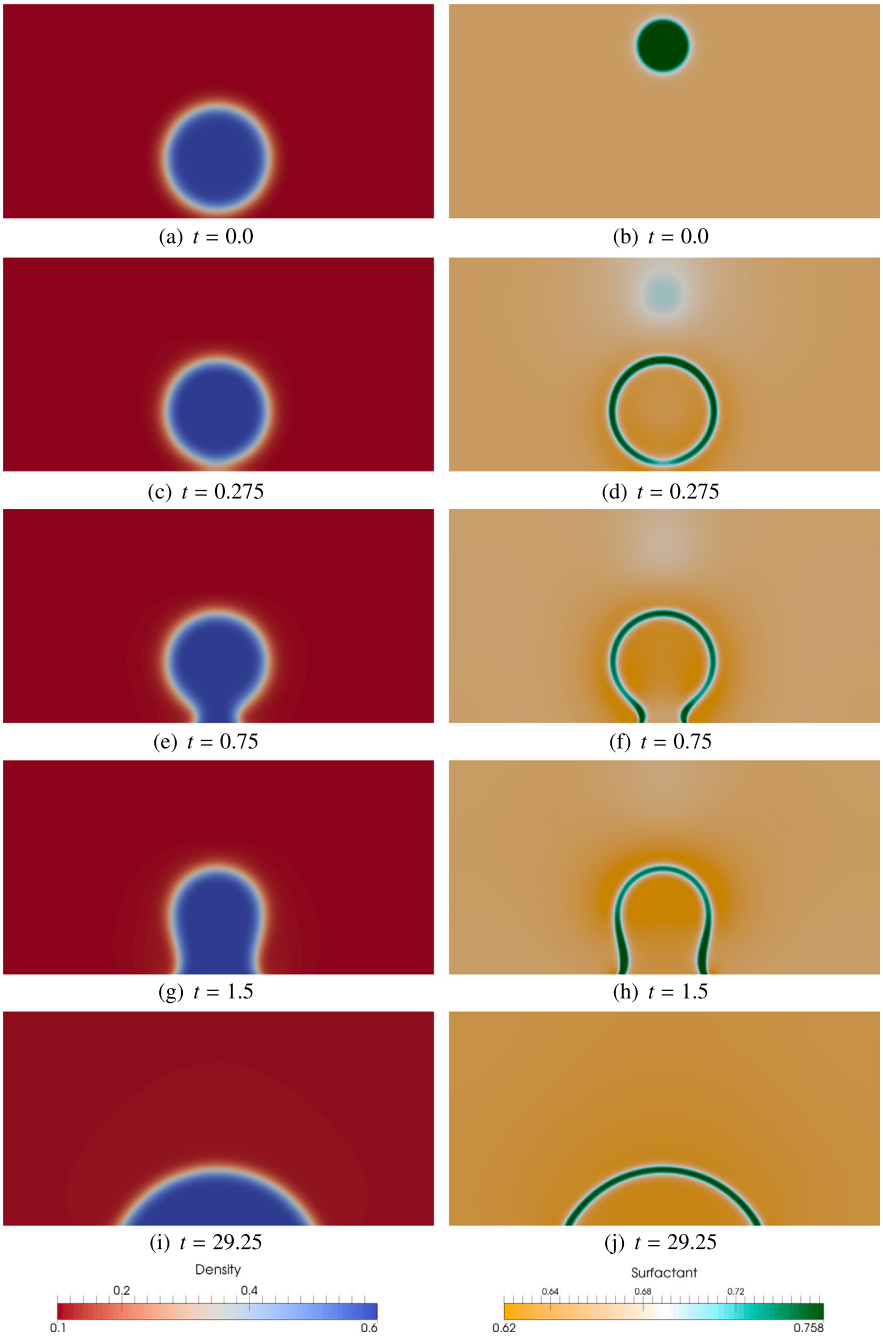

Fig. 6. Evolution of density (left) and surfactant concentration (right) for the attachment of a drop of water to a wall. The computational domain is the rectangle $\Omega = (0, 1.0) \times (0, 0.5)$ and the computational mesh is uniform and composed of 256×128 $\mathcal{C}^1$-quadratic elements. Initially, a drop of liquid water (blue color in the density plot) is located close to the lower boundary where we are controlling the contact angle as a function of surfactant concentration. In the horizontal direction we adopt periodic boundary conditions. The surfactant is initially concentrated close to the upper boundary (Fig. 6(b)) though it is rapidly attracted by the liquid–vapor interface (green color in the surfactant plot). The water droplet is attracted by the lower boundary due to the capillary forces (see Fig. 6(e)). Note that we are neglecting gravity forces. We have adopted $Re = 512$, $Ca = 0.00390625$, $Ba = 0.04$, $Pe = 125$ and $\varepsilon = 0.003845215$. (For interpretation of the references to color in this figure legend, the reader is referred to the web version of this article.)

Analogously, (62) takes on the form

$$\nabla c \cdot \boldsymbol{n} = |\nabla c| \frac{\varepsilon}{Ca\sqrt{g(c)}} h(\rho) \tag{105}$$

where $h(\rho)$ is given by (64).

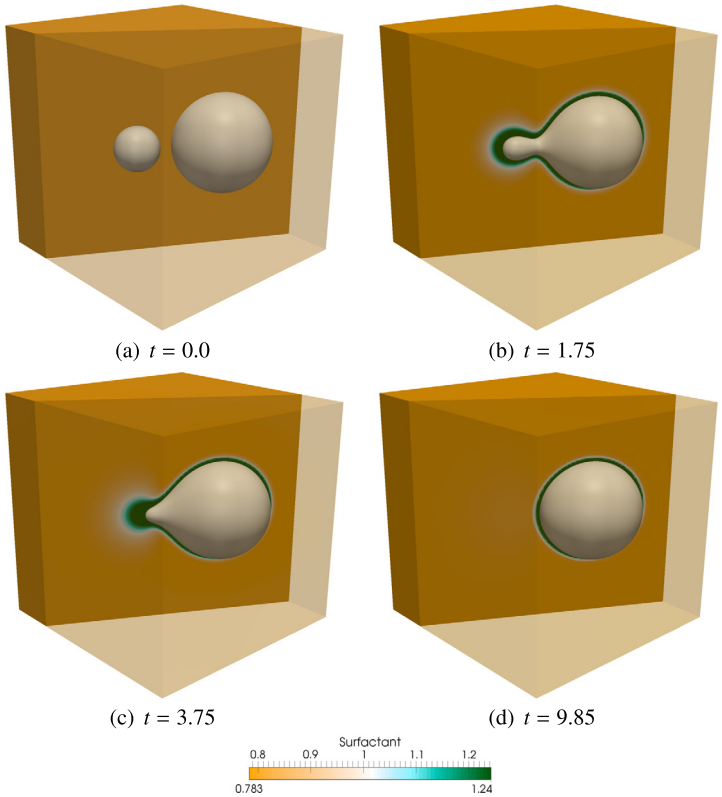

Fig. 7. Evolution of surfactant concentration for the three dimensional coalescence of two vapor bubbles. The computational domain is the cube $\Omega = (0, 1)^3$, which is composed of 128^3 $\mathcal{C}^1$-quadratic elements. We impose periodic boundary conditions in all directions. Initially, an homogeneous distribution of the surfactant concentration is adopted (Fig. 7(a)), namely, $c_0 = 0.8$. We have made a clip of the geometry to facilitate the visualization of the results. We are plotting an isocontour surface of the density (gray color) which represents the liquid–vapor interface. The surfactant is trapped by the regions with higher density gradients, that is, the liquid–vapor interfaces. We have used the parameters $Re = 256$, $Ca = 0.0078125$, $Ba = 0.01$ and $Pe = 1000$.

In order to illustrate the effectiveness of our model we have carried out the following numerical simulation (see Fig. 6). A drop of liquid water [blue color in Fig. 6(a)] is initially located close to a solid boundary where we are imposing (104) and (105). In the horizontal direction we adopt periodic boundary conditions. The computational domain is a rectangle $\Omega = (0, 1.0) \times (0, 0.5)$ and the computational mesh is uniform and composed of 256×128 $\mathcal{C}^1$-quadratic elements. Initially, the water droplet has a radius $R = 0.12$ and is centered at $C = (0.5, 0.15)$. For the initial values of the density in the liquid and the vapor phase we use the Maxwell States at $\theta = 0.85$, that is, $\rho_l^M = 0.60$ and $\rho_v^M = 0.10$. The initial distribution for the surfactant is the one indicated in Fig. 6(b) and it consists of a drop of surfactant of radius $R_s = 0.05$ (green color) located near to the upper boundary, more specifically, centered at $C_s = (0.5, 0.4)$. Note that the water droplet is attracted by the lower boundary due to the capillary forces [see Fig. 6(e)], as we have neglected gravity forces. The parameters used in this numerical example are $Re = 512$, $Ca = 0.00390625$, $Ba = 0.04$, $Pe = 125$ and $\varepsilon = 0.003845215$. The time step was constant and equal to $\Delta t = 0.0001$. From Eq. (104), it is obvious that different initial conditions for the surfactant would lead to different static contact angles. This phenomena is very important to control wettability with surfactants in practical applications.

5.4. Coalescence of vapor bubbles in three dimensions

This example shows the details of two coalescing bubbles with surfactants in three dimensions (see Fig. 7). The computational domain is the cube $\Omega = (0, 1)^3$ which is discretized with 128 $\mathcal{C}^1$-quadratic elements in each direction. The two vapor bubbles have a radius $R_1 = 0.12$ and $R_2 = 0.25$ and they are initially centered at $C_1 = (0.35, 0.57, 0.5)$ and $C_2 = (0.70, 0.40, 0.50)$. The initial values of the density for the liquid and the vapor phases are those corresponding to the Maxwell states at $\theta = 0.85$, that is, $\rho_l^M = 0.60$ and $\rho_v^M = 0.10$. For the surfactant [see Fig. 7(a)], we have adopted a constant initial condition, namely, $c_0 = 0.8$. The rest of the parameters are $Re = 256$, $Ca = 0.0078125$, $Ba = 0.01$, $Pe = 1000$ and $\Delta t = 0.005$. We impose periodic boundary conditions in all directions.

In order to facilitate the visualization of the results in the surfactant plot (see Fig. 7), we have made a clip of the cubic domain. Moreover, we are plotting an isocontour surface of the density (gray color) which represents the liquid–vapor interface so that we can know where the bubbles are located. As in the previous examples, the surfactant (green color in Fig. 7) is trapped by the regions with a higher density gradient, that is, the liquid–vapor interfaces (gray color).

6. Conclusions

We propose a model for single-component, two-phase flow with surfactants. The fluid naturally undergoes phase-transformations between vapor and liquid states. The model is derived from a free-energy functional using the thermodynamics framework and successfully predicts important features of two-phase flow with surfactants. For example, the model predicts that the surfactant reduces the liquid–vapor surface tension and is naturally trapped at the interface, as observed in experiments.

The discretization of the model poses significant challenges for classical numerical algorithms due to the presence of higher-order derivatives, stiffness in space and time an the existence of moving interfaces. We propose a computational method based on Isogeometric Analysis that leads to an efficient and accurate numerical solution.

Finally, we show the viability of our theoretical framework and numerical algorithm by showcasing several examples of vapor bubble dynamics in two and three dimensions. We believe our model has significant potential to study the influence of surfactants on phase transformations. In the future, we plan to extend it to the non-isothermal case.

Acknowledgements

HG was partially supported by the European Research Council through the FP7 Ideas Starting Grant Program (Contract #307201). HG and JB were partially supported by Xunta de Galicia, co-financed with FEDER funds. The authors are also grateful to Prof. Uwe Thiele for valuable discussions.

References

[1] A. Singh, J.V. Hamme, O. Ward, Surfactants in microbiology and biotechnology: Part 2. Application aspects, Biotechnology Advances 25 (2007) 99–121.
[2] J. Van Hamme, A. Singh, O. Ward, Surfactants in microbiology and biotechnology: Part 1. Physiological aspects, Biotechnology Advances 24 (2006) 604–620.
[3] M. Rosen, Surfactants in Emerging Technology, Surfactant Science, Taylor & Francis, 1987.
[4] Q. Tang, Y. Chan, N. Wong, R. Cheung, Surfactant-assisted processing of polyimide/multiwall carbon nanotube nanocomposites for microelectronics applications, Polymer International 59 (2010) 1240–1245.
[5] A. Florence, J. Gillan, Biological implications of the use of surfactants in medicines: and the biphasic effects of surfactants in biological systems, Pestic. Sci. 6 (1975) 429–439.
[6] L. Rodrigues, I. Banat, J. Teixeira, R. Oliveira, Biosurfactants: potential applications in medicine, J. Antimicrob. Chemother. 57 (2006) 609–618.
[7] R. King, Pulmonary surfactant, J. Appl. Physiol. 53 (1982) 1–8.
[8] H. Halliday, Surfactants: past, present and future, J. Perinatol. 28 (2008) S47–S56.
[9] S. Anna, H. Mayer, Microscale tipstreaming in a microfluidic flow focusing device, Phys. Fluids 18 (2006).
[10] L. Leal, Flow induced coalescence of drops in a viscous fluid, Phys. Fluids 16 (2004) 1833–1851.
[11] A. Pereira, P.M.J. Trevelyan, U. Thiele, S. Kalliadasis, Dynamics of a horizontal thin liquid film in the presence of reactive surfactants, Phys. Fluids 19 (2007).
[12] H. Stone, L. Leal, The effects of surfactants on drop deformation and breakup, J. Fluid Mech. 220 (1990) 161–186.
[13] U. Thiele, A.J. Archer, M. Plapp, Thermodynamically consistent description of the hydrodynamics of free surfaces covered by insoluble surfactants of high concentration, Phys. Fluids 24 (2012) 102–107.
[14] R. Farn, Chemistry and Technology of Surfactants, Wiley, 2008.
[15] D. Myers, An Overview of Surfactant Science and Technology, John Wiley & Sons, Inc., 2005, pp. 1–28.
[16] M. Rosen, Characteristic Features of Surfactants, John Wiley & Sons, Inc., 2004, pp. 1–33.
[17] S. Aland, A. Voigt, Simulation of common features and differences of surfactant-based and solid-stabilized emulsions, Colloids Surf. A, Physicochem. Eng. Asp. 413 (2012) 298–302.
[18] H. Garcke, K. Lam, B. Stinner, Diffuse interface modelling of soluble surfactants in two-phase flow, Commun. Math. Sci. 12 (2014) 1475–1522.
[19] M. Muradoglu, G. Tryggvason, A front-tracking method for computation of interfacial flows with soluble surfactants, J. Comput. Phys. 227 (2008) 2238–2262.
[20] C. Teng, I. Chern, M. Lai, Simulating binary fluid-surfactant dynamics by a phase field model, Discrete Contin. Dyn. Syst., Ser. B 17 (2012) 1289–1307.
[21] R. van der Sman, S. van der Graaf, Diffuse interface model of surfactant adsorption onto flat and droplet interfaces, Rheol. Acta 46 (2006) 3–11.
[22] H. Ceniceros, The effects of surfactants on the formation and evolution of capillary waves, Phys. Fluids 15 (2003) 245–256.
[23] M.A. Drumright-Clarke, Y. Renardy, The effect of insoluble surfactant at dilute concentration on drop breakup under shear with inertia, Phys. Fluids 16 (2004) 14–21.
[24] A. James, J. Lowengrub, A surfactant-conserving volume-of-fluid method for interfacial flows with insoluble surfactant, J. Comput. Phys. 201 (2004) 685–722.
[25] S. Engblom, M. Do-Quang, G. Amberg, A. Tornberg, On diffuse interface modeling and simulation of surfactants in two-phase fluid flow, Commun. Comput. Phys. 14 (2013) 879–915.
[26] S. Khatri, A.-K. Tornberg, An embedded boundary method for soluble surfactants with interface tracking for two-phase flows, J. Comput. Phys. 256 (2014) 768–790.
[27] H. Liu, Y. Zhang, Phase-field modeling droplet dynamics with soluble surfactants, J. Comput. Phys. 229 (2010) 9166–9187.
[28] J. Crank, Free and Moving Boundary Problems, Oxford Science Publications, Clarendon Press, 1987.
[29] H. Gomez, V. Calo, Y. Bazilevs, T. Hughes, Isogeometric Analysis of the Cahn–Hilliard phase-field model, Comput. Methods Appl. Mech. Eng. 197 (2008) 4333–4352.
[30] H. Gomez, T. Hughes, Provably unconditionally stable, second-order time-accurate, mixed variational methods for phase-field models, J. Comput. Phys. 230 (2011) 5310–5327.
[31] H. Gomez, A. Reali, G. Sangalli, Accurate, efficient, and (iso) geometrically flexible collocation methods for phase-field models, J. Comput. Phys. 262 (2014) 153–171.
[32] J. Liu, H. Gomez, J. Evans, T. Hughes, C. Landis, Functional entropy variables: a new methodology for deriving thermodynamically consistent algorithms for complex fluids, with particular reference to the isothermal Navier–Stokes–Korteweg equations, J. Comput. Phys. 248 (2013) 47–86.
[33] G. Caginalp, Stefan and Hele–Shaw type models as asymptotic limits of the phase-field equations, Phys. Rev. A 39 (1989) 5887–5896.

[34] R. Kobayashi, A numerical approach to three-dimensional dendritic solidification, Exp. Math. 3 (1994) 59–81.
[35] O. Penrose, P. Fife, Thermodynamically consistent models of phase-field type for the kinetic of phase transitions, Physica D 43 (1990) 44–62.
[36] I. Fonseca, M. Morini, V. Slastikov, Surfactants in foam stability: a phase-field model, Arch. Ration. Mech. Anal. 183 (2007) 411–456.
[37] M. Borden, C. Verhoosel, M. Scott, T. Hughes, C. Landis, A phase-field description of dynamic brittle fracture, Comput. Methods Appl. Mech. Eng. 217–220 (2012) 77–95.
[38] J. Jeong, N. Goldenfeld, J. Dantzig, Phase field model for three-dimensional dendritic growth with fluid flow, Phys. Rev. E 64 (2001) 041602.
[39] Y. Kim, N. Provatas, N. Goldenfeld, J. Dantzig, Universal dynamics of phase-field models for dendritic growth, Phys. Rev. E 59 (1999) 2546.
[40] T. Biben, K. Kassner, C. Misbah, Phase-field approach to three-dimensional vesicle dynamics, Phys. Rev. E 72 (2005) 041921.
[41] E. Fried, M. Gurtin, Dynamic solid-solid transitions with phase characterized by an order parameter, Physica D 72 (1994) 287–308.
[42] S. Tremaine, On the origin of irregular structure in Saturn's rings, Astron. J. 125 (2003) 894.
[43] L. Cueto-Felgueroso, R. Juanes, Nonlocal interface dynamics and pattern formation in gravity-driven unsaturated flow through porous media, Phys. Rev. Lett. 101 (2008) 244504.
[44] H. Gomez, L. Cueto-Felgueroso, R. Juanes, Three-dimensional simulation of unstable gravity-driven infiltration of water into a porous medium, J. Comput. Phys. 238 (2013) 217–239.
[45] H. Gomez, T. Hughes, X. Nogueira, V. Calo, Isogeometric Analysis of the isothermal Navier–Stokes–Korteweg equations, Comput. Methods Appl. Mech. Eng. 199 (2010) 1828–1840.
[46] H.B. Frieboes, J.S. Lowengrub, S. Wise, X. Zheng, P. Macklin, E.L. Bearer, V. Cristini, Computer simulation of glioma growth and morphology, NeuroImage 37 (2007) 59–70.
[47] G. Vilanova, I. Colominas, H. Gomez, Capillary networks in tumor angiogenesis: from discrete endothelial cells to phase-field averaged descriptions via isogeometric analysis, Int. J. Numer. Methods Biomed. Eng. 29 (2013) 1015–1037.
[48] J. Xu, G. Vilanova, H. Gomez, A mathematical model coupling tumor growth and angiogenesis, PLoS One 11 (2) (2016) e0149422.
[49] E. van Brummelen, H.S. Roudbari, G. van Zwieten, Elasto-capillarity simulations based on the Navier–Stokes–Cahn–Hilliard equations, arXiv: 1510.02441v1, 2015, pp. 1–8.
[50] J. Bueno, C. Bona-Casas, Y. Bazilevs, H. Gomez, Interaction of complex fluids and solids: theory, algorithms and application to phase-change-driven implosion, Comput. Mech. 55 (2015) 1105–1118.
[51] D.M. Anderson, G.B. McFadden, A.A. Wheeler, Diffuse-interface methods in fluid mechanics, Annu. Rev. Fluid Mech. 30 (1998) 139–165.
[52] A. Bray, Theory of phase ordering kinetics, Physica A 194 (1993) 41–52.
[53] L. Chen, Phase-field models for microstructure evolution, Annu. Rev. Mater. Res. 32 (2002) 113–140.
[54] H. Gomez, K. van der Zee, Encyclopedia of Computational Mechanics. Computational Phase-Field Modeling, John Wiley & Sons, Ltd, 2016.
[55] I. Steinbach, Phase-field models in materials science, Model. Simul. Mater. Sci. Eng. 17 (2009) 073001.
[56] J. Gibbs, On the Equilibrium of Heterogeneous Substances, 1874.
[57] D. Korteweg, Sur la forme que prennent les équations du mouvement des fluides si l'on tient compte des forces capillaires causées par des variations de densité considérables mais continues et sur la théorie de la capillarité dans l'hypothèse d'une variation continue de la densité, Arch. Néerl. (2) 6 (1901) 1–24.
[58] J. van der Waals, The thermodynamic theory of capillarity under the hypothesis of a continuous variation of density, J. Stat. Phys. 20 (1979) 200–244.
[59] J. Dunn, J. Serrin, On the thermomechanics of interstitial working, Arch. Ration. Mech. Anal. 88 (1985) 95–133.
[60] L. Tian, Y. Xu, J. Kuerten, J. van der Vegt, A local discontinuous Galerkin method for the (non)-isothermal Navier–Stokes–Korteweg equations, J. Comput. Phys. 295 (2015) 685–714.
[61] D. Diehl, Higher order schemes for simulation of compressible liquid–vapor flows with phase change, Ph.D. thesis, Albert-Ludwigs-Universitat, 2007.
[62] J. Giesselmann, C. Makridakis, T. Pryer, Energy consistent discontinuous Galerkin methods for the Navier–Stokes–Korteweg system, Math. Comput. 83 (2014) 2071–2099.
[63] J. Liu, C.M. Landis, H. Gomez, T.J. Hughes, Liquid–vapor phase transition: thermomechanical theory, entropy stable numerical formulation, and boiling simulations, Comput. Methods Appl. Mech. Eng. 297 (2015) 476–553.
[64] T. Hughes, J. Cottrell, Y. Bazilevs, Isogeometric Analysis: CAD, Finite Elements, NURBS, exact geometry and mesh refinement, Comput. Methods Appl. Mech. Eng. 194 (2005) 4135–4195.
[65] Y. Bazilevs, L. Beirão Da Veiga, J. Cottrell, T. Hughes, G. Sangalli, Isogeometric Analysis: approximation, stability and error estimates for h-refined meshes, Math. Models Methods Appl. Sci. 16 (2006) 1031–1090.
[66] Y. Bazilevs, V. Calo, J. Cottrell, J. Evans, T. Hughes, S. Lipton, M. Scott, T. Sederberg, Isogeometric Analysis using T-splines, Comput. Methods Appl. Mech. Eng. 199 (2010) 229–263.
[67] Y. Bazilevs, V. Calo, Y. Zhang, T. Hughes, Isogeometric Fluid–Structure Interaction analysis with applications to arterial blood flow, Comput. Mech. 38 (2006) 310–322.
[68] J. Cottrell, T. Hughes, A. Reali, Studies of refinement and continuity in isogeometric structural analysis, Comput. Methods Appl. Mech. Eng. 196 (2007) 4160–4183.
[69] J. Cottrell, A. Reali, Y. Bazilevs, T. Hughes, Isogeometric Analysis of structural vibrations, Comput. Methods Appl. Mech. Eng. 195 (2006) 5257–5296.
[70] H. Casquero, L. Lei, J. Zhang, A. Reali, H. Gomez, Isogeometric collocation using analysis-suitable T-splines of arbitrary degree, Comput. Methods Appl. Mech. Eng. 301 (2016) 164–186.
[71] H. Casquero, L. Lei, Y. Zhang, A. Reali, J. Kiendl, H. Gomez, Arbitrary-degree T-splines for isogeometric analysis of fully nonlinear Kirchhoff–Love shells, 2016, submitted for publication.
[72] J. Warren, H. Weimer, Subdivision Methods for Geometric Design: A Constructive Approach, 1st ed., Morgan Kaufmann Publishers, Inc., San Francisco, CA, USA, 2001.
[73] M. Borden, T. Hughes, C. Landis, C. Verhoosel, A higher-order phase-field model for brittle fracture: formulation and analysis within the isogeometric analysis framework, Comput. Methods Appl. Mech. Eng. 273 (2014) 100–118.
[74] J. Bueno, I. Starodumov, H. Gomez, P. Galenko, D. Alexandrov, Three dimensional structures predicted by the modified phase field crystal equation, Comput. Mater. Sci. 111 (2016) 310–312.
[75] L. Dedè, M. Borden, T. Hughes, Isogeometric analysis for topology optimization with a phase field model, Arch. Comput. Methods Eng. 19 (2012) 427–465.
[76] R. Dhote, H. Gomez, R. Melnik, J. Zu, Isogeometric analysis of coupled thermo-mechanical phase-field models for shape memory alloys using distributed computing, in: 2013 International Conference on Computational Science, Proc. Comput. Sci. 18 (2013) 1068–1076.
[77] H. Gomez, L. De Lorenzis, The variational collocation method, Comput. Methods Appl. Mech. Eng. (2016), http://dx.doi.org/10.1016/j.cma.2016.06.003.
[78] M. Gurtin, E. Fried, L. Anand, Thermodynamics and constitutive restrictions: the Coleman–Noll procedure, in: The Mechanics and Thermodynamics of Continua, in: Cambridge Books Online, Cambridge University Press, 2010, pp. 232–233.
[79] J. Chung, G. Hulbert, A time integration algorithm for structural dynamics with improved numerical dissipation: the generalized-α method, J. Appl. Mech. 60 (1993) 371–375.
[80] J. Cottrell, T. Hughes, Y. Bazilevs, Isogeometric Analysis: Toward Integration of CAD and FEA, Wiley, 2009.

[81] C. de Boor, On calculating with B-splines, J. Approx. Theory 6 (1972) 50–62.
[82] M.G. Cox, The numerical evaluation of B-splines, IMA J. Appl. Math. 10 (1972) 134–149.
[83] J.E. Marsden, T. Hughes, Mathematical Foundations of Elasticity, Dover Publications, Inc, 1994.
[84] J. Cahn, J. Hilliard, Free Energy of a Nonuniform System. I. Interfacial Free Energy, John Wiley & Sons, Inc., 2013, pp. 29–38.
[85] J. Liu, Thermodynamically consistent modeling and simulation of multiphase flows, Ph.D. thesis, The University of Texas at Austin, 2014.
[86] F. White, Fluid Mechanics, McGraw–Hill International Editions, McGraw–Hill, 2003.
[87] K. Jansen, C. Whiting, G. Hulbert, A generalized-α method for integrating the filtered Navier–Stokes equations with a stabilized Finite Element Method, Comput. Methods Appl. Mech. Eng. 190 (2000) 305–319.
[88] Y. Bazilevs, V. Calo, T. Hughes, Y. Zhang, Isogeometric fluid–structure interaction: theory, algorithms, and computations, Comput. Mech. 43 (2008) 3–37.
[89] H. Casquero, C. Bona-Casas, H. Gomez, A NURBS-based immersed methodology for fluid–structure interaction, Comput. Methods Appl. Mech. Eng. 284 (2015) 943–970.
[90] H. Casquero, L. Lei, C. Bona-Casas, J. Zhang, H. Gomez, A hybrid variational-collocation immersed method for fluid–structure interaction using unstructured T-splines, Int. J. Numer. Methods Eng. (2016), http://dx.doi.org/10.1002/nme.5004, Accepted for publication.
[91] Y. Saad, M. Schultz, GMRES: a generalized minimal residual algorithm for solving nonsymmetric linear systems, SIAM J. Sci. Stat. Comput. 7 (1986) 856–869.

B Paper #2: "Interaction of complex fluids and solids: theory, algorithms and application to phase-change-driven implosion"

Comput Mech
DOI 10.1007/s00466-014-1098-x

ORIGINAL PAPER

Interaction of complex fluids and solids: theory, algorithms and application to phase-change-driven implosion

Jesus Bueno · Carles Bona-Casas · Yuri Bazilevs · Hector Gomez

Received: 13 October 2014 / Accepted: 1 November 2014

Abstract There is a large body of literature dealing with the interaction of solids and classical fluids, but the mechanical coupling of solids and complex fluids remains practically unexplored, at least from the computational point of view. Yet, complex fluids produce much richer physics than classical fluids when they interact with solids, especially at small scales. Here, we couple a nonlinear hyperelastic solid with a single-component two-phase flow, where the fluid can condensate and evaporate naturally due to temperature and/or pressure changes. We propose a fully-coupled fluid–structure interaction algorithm to solve the problem. We illustrate the viability of the theoretical framework and the effectiveness of our algorithms by solving several problems of phase-change-driven implosion, a physical process in which a thin structure collapses due to the condensation of a fluid.

Keywords Complex fluids · Fluid–structure interaction (FSI) · Navier–Stokes–Korteweg (NSK) equations · Implosion · Isogeometric analysis (IGA) · Arbitrary Lagrangian–Eulerian (ALE) description

J. Bueno ( )
Department of Mathematical Methods, University of A Coruña, Campus de Elviña, 15192 A Coruña, Spain
e-mail: jesus.bueno@udc.es

C. Bona-Casas ( ) · H. Gomez
Department of Mathematical Methods, University of A Coruña, Campus de Elviña, 15192 A Coruña, Spain
e-mail: carlesbona@gmail.com

Y. Bazilevs
Department of Structural Engineering, University of California, San Diego, 9500 Gilman Drive, La Jolla, CA 92093, USA

Published online: 28 November 2014

1 Introduction

1.1 Interaction of complex fluids and solids

Traditional fluid–structure interaction (FSI) methods have mainly focused on the interaction of solids with classical fluids governed by the Navier–Stokes equations of incompressible or compressible flows [8,13,46–48,56,60,62,64,66,67,71,73]. Yet, there are a number of open FSI problems that cannot be modeled using this paradigm because they fundamentally depend on physical mechanisms not captured by the Navier–Stokes equations. Prime examples are fluid–solid systems that involve multi-phase and/or multi-component flows, liquid crystals or micropolar fluids. These are just some examples of a broad class of fluids typically referred to as *complex fluids* [29]. One of the areas that could potentially benefit from accurate and efficient computational methods for the interaction of complex fluids and solids is that of mechanobiology. Just as an example, phenomena as important as cellular migration [52] or even cellular division [51] seem to be controlled to a significant extent by mechanics, and it seems plausible that at cellular scale capillary forces and spontaneous polarizations need to be considered.

Here, we present our initial steps toward a computational method for the interaction of complex fluids and solids. To illustrate our ideas, we focus on a particular engineering application, namely, the implosion of solids that enclose a compressible fluid. Structures containing a compressible fluid at a pressure below the external pressure have the potential to collapse inwards. For example, an air-filled structure may suffer an implosive collapse when it is immersed underwater, due to the increase of the external pressure. This is just an example of implosion which has been addressed before in the literature [26,27,38,42,50,81], and that may be modeled

using classical fluid theories. However, the aforementioned mechanism is not the only one that can cause the implosive collapse of a structure. For example, in the case of vapor-filled structures, thermal variations can make vapor transform into liquid, reducing the internal pressure. We will refer to this phenomenon as *phase-change-driven implosion*, and this will be the subject of the current paper. It is clear that to model phase-change-driven implosion the way we have defined it, we will need a complex-fluid theory in which the fluid can undergo phase transformations.

1.2 Fluid dynamics with phase changes

Our approach to phase transformation is based on the *diffuse-interface* of *phase-field* method. The diffuse-interface approach can be defined as an alternative to the classical *sharp-interface* description. In the sharp-interface theory, several partial-differential equations must be solved on the different phases and they are coupled through boundary conditions that hold on a moving, and a priori unknown, interface. Thus, this technique may result in mathematical models that require complex numerical treatment. The key idea of the diffuse interface method is to use a field, namely the phase field, which is defined on the entire computational domain, and is a marker of the location of the different phases. The phase field varies smoothly on the computational domain, and naturally produces thin layers which represent interfaces between phases. This conceptualization notably simplifies the numerics because the problem reduces to solving a partial-differential equation on a fixed and known domain. From the computational point of view, the main disadvantage of the phase-field approach is that it typically leads to higher-order partial-differential equations that are stiff in space and time, and produce thin layers which evolve dynamically over the computational domain. However, most of these computational challenges are being addressed [31,32,35,45], and computational phase-field modeling is becoming a mature topic. Phase-field models have been widely used in the condensed matter physics [19,28,49,80] and material science [14,55] and are rapidly getting established in the engineering field [12,34,83]. In this paper, we employ a phase-field approach based on the Navier–Stokes–Korteweg (NSK) equations to describe the behavior of the fluid in the implosion problem. The NSK equations constitute the most widely accepted mathematical model for single-component, two-phase (liquid and gas) flows [33]. Thus, the NSK theory may be used to model fluid flows in which the fluid can evaporate and condensate naturally due to pressure and/or temperature variations. The NSK system is the result of several works. The contribution of Gibbs [30], Korteweg, van der Waals [82] and Dunn and Serrin [24] should be highlighted. The current form of the system has been known for several years, though very few numerical solutions can be found in the literature. Notable exceptions include [21,33,45].

1.3 Computational challenges

From the computational point of view, there are at least two significant challenges in the phase-change-driven implosion problem as compared to other FSI simulations. First, phase-change-driven implosions lead to a violent and rapid collapse of the structure with strong compressions and large deformations [41]. Strong implosions may also involve contact, plastic deformation, and fracture, although this is out of the scope of this paper. Second, the NSK theory is more difficult to treat numerically than classical Navier–Stokes equations due to the presence of thin interfaces that must be resolved by the computational mesh. We try to address these challenges by using isogeometric analysis (IGA) for the spatial discretization of the problem. IGA is a generalization of the finite element method that was introduced in [37] and further developed in [1,2,6,16–18,25,59,84]. The main idea of IGA is to use functions from computational geometry to represent both the solution and the domain of a boundary-value problem. The most frequently utilized functions are non-uniform rational B-splines (NURBSs) which are widely used in computational geometry and design, and will also be used in this work for our simulations.

We feel that IGA successfully addresses the two computational challenges that we mentioned before. In particular, IGA has been shown to perform well under large structural deformations [11,43]. Additionally, IGA has been successfully used in computational phase-field modeling. In fact, it was shown that the higher-order global continuity of NURBS leads to a more accurate and stable solution of the thin layers that naturally arise in the solution of phase-field theories [32]. Finally, IGA has been previously used to solve FSI problems with remarkable success [2,4,5,7].

2 Governing equations

2.1 Kinematics

Let us introduce a reference domain $\Omega_{\widehat{x}}$ which is fixed in time, and whose points are parameterized by coordinates $\widehat{\boldsymbol{x}}$. The reference domain is arbitrary and may take on different interpretations. Let us define a mapping $\widehat{\boldsymbol{\phi}} : \Omega_{\widehat{x}} \times]0, T[\rightarrow \Omega_t$, where $]0, T[$ is the time interval of interest. For each time $t \in]0, T[$, the function $\widehat{\boldsymbol{\phi}}$ maps the reference domain $\Omega_{\widehat{x}}$ into its spatial configuration at time t, namely Ω_t. Let us call $\boldsymbol{x}$ the coordinates in the spatial configuration, such that $\Omega_t \ni \boldsymbol{x} = \widehat{\boldsymbol{\phi}}(\widehat{\boldsymbol{x}}, t)$. In the following, we will also use the notation $\widehat{\boldsymbol{\phi}}_t(\widehat{\boldsymbol{x}}) = \widehat{\boldsymbol{\phi}}(\widehat{\boldsymbol{x}}, t)$. Using the mapping $\widehat{\boldsymbol{\phi}}$, we can define the displacement of a point in the referential domain

$$\widehat{\boldsymbol{u}}(\widehat{\boldsymbol{x}},\, t) = \widehat{\boldsymbol{\phi}}(\widehat{\boldsymbol{x}},\, t) - \widehat{\boldsymbol{x}}, \tag{1}$$

and its velocity

$$\widehat{\boldsymbol{v}} = \frac{\partial \widehat{\boldsymbol{u}}}{\partial t}. \tag{2}$$

Let us also define the mapping $\boldsymbol{\phi} : \Omega_X \times]0,\, T[\rightarrow \Omega_t$. For each time $t \in]0,\, T[$, this mapping transforms each material particle $\boldsymbol{X}$ into its spatial coordinate at time t, that is, $\boldsymbol{x} = \boldsymbol{\phi}(\boldsymbol{X},\, t)$. Note that due to the arbitrariness of the referential domain, the mapping $\boldsymbol{\phi}$ can be simply thought of as a particular case of $\widehat{\boldsymbol{\phi}}$, but each mapping will be employed for a different purpose in this work, so we will use different notations. From the mapping $\boldsymbol{\phi}$, we can define the deformation gradient $\boldsymbol{F} = \frac{\partial \boldsymbol{\phi}}{\partial \boldsymbol{X}}$, the particle displacement

$$\boldsymbol{u}(\boldsymbol{X},\, t) = \boldsymbol{\phi}(\boldsymbol{X},\, t) - \boldsymbol{X}, \tag{3}$$

and the particle velocity

$$\boldsymbol{v} = \frac{\partial \boldsymbol{\phi}}{\partial t} = \frac{\partial \boldsymbol{u}}{\partial t}. \tag{4}$$

In what follows, we will also make use of the Eulerian counterpart of the particle velocity $\boldsymbol{v}$, namely, $\boldsymbol{v} \circ \boldsymbol{\phi}^{-1}$. From now on, in most instances, we will only use one symbol to denote a physical quantity (velocity, in this case) even if the functions $\boldsymbol{v}$ and $\boldsymbol{v} \circ \boldsymbol{\phi}^{-1}$ are clearly different. To avoid ambiguity in our notation we will use subscripts to clarify how derivatives are to be understood. For example, we will use the notation $\frac{\partial \boldsymbol{u}}{\partial t}|_X$ (respectively, $\frac{\partial \boldsymbol{u}}{\partial t}|_{\widehat{x}}$) to indicate that the time derivative is taken by holding $\boldsymbol{X}$ (respectively, $\widehat{\boldsymbol{x}}$) fixed. When neither $|_X$ nor $|_{\widehat{x}}$ are used in the time derivative, it is assumed to be taken by holding $\boldsymbol{x}$ fixed. We use a similar convention for spatial derivatives. For example, we denote by ∇ the gradient with respect to the spatial coordinates $\boldsymbol{x}$. If coordinates other than $\boldsymbol{x}$ are used, the gradient operator will be assigned the appropriate subscript.

2.2 Governing equations of solid mechanics

The equations governing the structural dynamics will be presented in Lagrangian description, therefore all quantities are derived from the mapping $\boldsymbol{\phi}$. The deformation gradient takes on the form $\boldsymbol{F} = \boldsymbol{I} + \nabla_X \boldsymbol{u}$, where $\boldsymbol{I}$ denotes the identity tensor. We will also make use of the Cauchy–Green deformation tensor $\boldsymbol{C} = \boldsymbol{F}^T \boldsymbol{F}$, and the Green–Lagrange strain tensor $\boldsymbol{E} = (\boldsymbol{C} - \boldsymbol{I})/2$. The momentum balance in Lagrangian form can be written as

$$\rho_0^s \left.\frac{\partial^2 \boldsymbol{u}}{\partial t^2}\right|_X = \nabla_X \cdot \boldsymbol{P} + \rho_0^s \boldsymbol{f}^s, \tag{5}$$

where ρ_0^s is the mass density in the initial configuration, $\boldsymbol{f}^s$ represents body forces per unit mass, and $\boldsymbol{P}$ is the first Piola–Kirchhoff stress tensor. To define $\boldsymbol{P}$, we need to introduce a constitutive theory. We will use a hyperelastic model, therefore, the material behavior is described by a stored elastic energy density per unit volume of the undeformed configuration W. In particular, we will use the generalized neo-Hookean model with dilatational penalty proposed in [53], which is defined by

$$W = \frac{\mu}{2}\left(J^{-2/d}\mathrm{tr}(\boldsymbol{C}) - d\right) + \frac{\kappa}{2}\left(\frac{1}{2}\left(J^2 - 1\right) - \ln J\right), \tag{6}$$

where d is the number of spatial dimensions, κ and μ are the material bulk and shear moduli, $\mathrm{tr}(\cdot)$ denotes the trace operator and $J = \det(\boldsymbol{F})$. Note that in Eq. (6), the $\ln J$ term stabilizes the equation for the regime of strong compression, while the $J^2 - 1$ term penalizes the deviation of the Jacobian from unity. The second Piola–Kirchhoff stress tensor can be computed from W as

$$\boldsymbol{S} = \frac{\partial W}{\partial \boldsymbol{E}} = \mu J^{-2/d}\left(\boldsymbol{I} - \frac{1}{d}\mathrm{tr}(\boldsymbol{C})\boldsymbol{C}^{-1}\right) + \frac{\kappa}{2}\left(J^2 - 1\right)\boldsymbol{C}^{-1}. \tag{7}$$

The first Piola–Kirchhoff stress tensor is simply defined as $\boldsymbol{P} = \boldsymbol{F}\boldsymbol{S}$. For future reference, we define the solid Cauchy stress tensor as

$$\boldsymbol{\sigma}^s = J^{-1}\boldsymbol{F}\boldsymbol{S}\boldsymbol{F}^T = J^{-1}\boldsymbol{P}\boldsymbol{F}^T. \tag{8}$$

2.3 Governing equations of fluid mechanics

In our model, the fluid dynamics is governed by the NSK equations, which account for mass, momentum and energy conservation. The NSK equations allow for liquid–gas and gas–liquid phase transformations, which can happen spontaneously without precursors. In the Eulerian frame, the NSK equations are given by

$$\frac{\partial \rho}{\partial t} + \nabla \cdot (\rho \boldsymbol{v}) = 0, \tag{9a}$$

$$\frac{\partial (\rho \boldsymbol{v})}{\partial t} + \nabla \cdot (\rho \boldsymbol{v} \otimes \boldsymbol{v}) - \nabla \cdot \boldsymbol{\sigma}^f - \rho \boldsymbol{f} = 0, \tag{9b}$$

$$\frac{\partial (\rho s)}{\partial t} + \nabla \cdot (\rho s \boldsymbol{v}) + \nabla \cdot \left(\frac{\boldsymbol{q}}{\theta}\right) = \mathscr{P}, \tag{9c}$$

where s is the entropy density and the entropy production $\mathscr{P}$ depends on the fluid constitutive theory described later in the paper. The rest of the notation is as follows: ρ is the density, $\boldsymbol{v}$ is the velocity vector, and $\otimes$ denotes the usual vector outer product, $\boldsymbol{\sigma}^f$ is the fluid stress tensor and $\boldsymbol{f}$ represents body forces per unit mass, s is the entropy density, θ the temperature, and $\boldsymbol{q}$ the heat flux. Notice that to completely define

the NSK equations, we need constitutive equations for the stress tensor and the heat flux, as well as a thermodynamic potential from which we can derive the state variables.

2.3.1 Stress tensor

The fluid Cauchy stress tensor $\boldsymbol{\sigma}^f$ is given by

$$\boldsymbol{\sigma}^f = \boldsymbol{\tau} - p\boldsymbol{I} + \boldsymbol{\varsigma}, \tag{10}$$

where p is the pressure, $\boldsymbol{\tau}$ is the viscous stress tensor, and $\boldsymbol{\varsigma}$ denotes the so-called Korteweg tensor. We consider Newtonian fluids, therefore, the viscous stress tensor is defined as

$$\boldsymbol{\tau} = \bar{\mu}\left(\nabla \boldsymbol{v} + \nabla^T \boldsymbol{v}\right) + \bar{\lambda}\nabla \cdot \boldsymbol{v}\boldsymbol{I}, \tag{11}$$

where $\bar{\mu}$ and $\bar{\lambda}$ are the viscosity coefficients. Throughout this paper, we will assume that the Stokes hypothesis is satisfied, that is, $\bar{\lambda} = -2\bar{\mu}/3$. The Korteweg tensor is defined by the expression

$$\boldsymbol{\varsigma} = \lambda\left(\rho\Delta\rho + \frac{1}{2}|\nabla\rho|^2\right)\boldsymbol{I} - \lambda\nabla\rho \otimes \nabla\rho, \tag{12}$$

where $\lambda > 0$ is the capillarity coefficient, and $|\cdot|$ denotes the Euclidean norm of a vector. The Korteweg tensor gives rise to capillary forces which are withstood by gas–liquid interfaces. Note also that since $\boldsymbol{\varsigma}$ depends upon $\Delta\rho$, the linear momentum balance equation includes third-order partial differential operators.

2.3.2 Heat conduction

We use the isotropic Fourier law, that is, $\boldsymbol{q} = -k\nabla\theta$, where k is the thermal conductivity.

2.3.3 Entropy production

With the above-presented constitutive theory, the entropy production $\mathscr{P}$ takes on the form

$$\mathscr{P} = k\frac{1}{\theta^2}|\nabla\theta|^2 + \frac{1}{\theta}\boldsymbol{\tau} : \nabla\boldsymbol{v} + \frac{\rho r}{\theta} + \frac{\rho\boldsymbol{f}\cdot\boldsymbol{v}}{\theta}, \tag{13}$$

where r is the heat supply per unit mass.

2.3.4 State variables

The NSK theory fits into classical thermodynamics, and as a consequence, state variables can be derived from a Helmholtz free-energy potential. To allow for phase transformations in the fluid, we do not use the classical Helmholtz free-energy of a perfect gas, but that of a so-called van der Waals fluid [21, 44]. The peculiarity of the van der Waals–Helmholtz free-energy is that it may be non-convex for low temperatures, allowing for spontaneous phase changes. Using the van der Waals–Helmholtz free-energy and standard thermodynamics [44], we obtain the pressure as

$$p = Rb\left(\frac{\rho\theta}{b-\rho}\right) - a\rho^2, \tag{14}$$

which is known as van der Waals equation. In Eq. (14), R is the specific gas constant, while a and b are positive constants. Also from the Helmholtz free-energy, we can obtain the entropy density as

$$s = -R\log\left(\frac{\rho}{b-\rho}\right) + c_{\boldsymbol{v}}\log\left(\frac{\theta}{\theta_c}\right), \tag{15}$$

where $c_{\boldsymbol{v}}$ is the specific heat capacity and θ_c is a reference temperature to be defined later. In the NSK theory, phase transformations are naturally accommodated without introducing additional fields, and without precursors. The density itself is a marker of the vapor and liquid phases (see [33]). To give a precise definition of the phases, let us consider θ a parameter in Eq. (14). Figure 1 shows a non-dimensional plot of the pressure as a function of density for different values of θ. We observe qualitatively different behaviors for $\theta > \theta_c$, and $\theta < \theta_c$, where

$$\theta_c = \frac{8}{27}\frac{ab}{R}, \tag{16}$$

is the so-called critical temperature. For $\theta > \theta_c$, p is a monotonic function of ρ, the gaseous phase is stable and the liquid phase is unstable (not proven here). For $\theta < \theta_c$, there

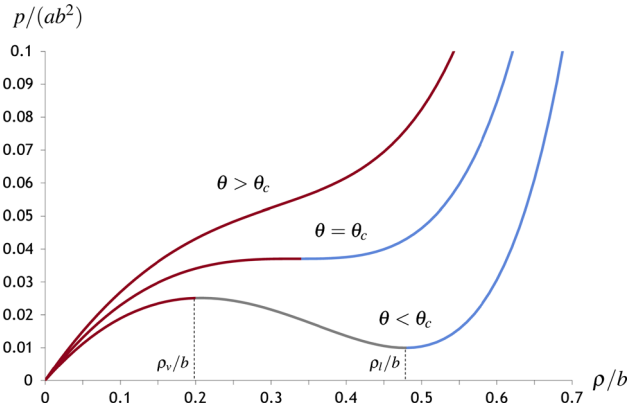

Fig. 1 Non-dimensional plot of van der Waals pressure as a function of density. The pressure is a non-monotone function of density for $\theta < \theta_c$. For comparison purposes, we note that for a given temperature, the pressure–density law of a perfect gas, would be a *straight line* tangent to the van der Waals curve at $\rho = 0$

is a density interval, namely $(\rho_v,\ \rho_l)$, in which $\partial p/\partial\rho < 0$, and as a consequence, there may be stable co-existence of gas and liquid. In this temperature range, the gaseous phase is defined by $\rho \in (0,\ \rho_v)$, while the liquid phase is defined by $\rho \in (\rho_l,\ b)$. The region $\rho \in (\rho_v,\ \rho_l)$ has no physical meaning, but in the NSK theory, may be interpreted as a smooth interface between the vapor and liquid phases which spans over a length scale $\sqrt{\lambda/a}$. Note also that in the inviscid, non-conducting limit, the NSK equations are ill-posed for $\lambda = 0$, and capillary forces are necessary to restore well-posedness. For further details on the NSK equations, the reader is referred to [33,44].

Remark Note that our model neglects the thermal physics in the solid. Although it would be straightforward to consider a thermo-elastic theory, we believe that it is not a key ingredient for the objectives of this paper.

3 Numerical formulation

In this section we propose FSI algorithms to solve the implosion problem. Our methods extend those presented in [4] to the realm of complex fluids.

3.1 Computational framework

In our model, the structure is treated as a nonlinear hyperelastic solid in Lagrangian description. The fluid is a complex, viscous and compressible fluid, governed by the NSK theory. The NSK equations hold on a moving domain, and heretofore, have been presented in Eulerian description. From a computational viewpoint, we aim at using a semidiscrete algorithm in which space discretization is performed using IGA, and time discretization is carried out by a finite-difference-type method. Eulerian descriptions are not well-suited for semidiscretized methods on moving domains, so we will use the arbitrary Lagrangian–Eulerian (ALE) formulation [22,23,36]. In ALE methods the partial time and space derivatives employed in the balance equations are taken with respect to different domains, namely, the reference and the current domain. This particularity allows for a straightforward use of semi-discrete methods, even when the equations are posed on a moving domain [4].

Using the techniques presented in [9,23], the NSK system in the ALE description may be written as:

$$\left.\frac{\partial\rho}{\partial t}\right|_{\widehat{x}} + (\boldsymbol{v}-\widehat{\boldsymbol{v}})\cdot\nabla\rho + \rho\nabla\cdot\boldsymbol{v} = 0, \tag{17a}$$

$$\rho\left.\frac{\partial\boldsymbol{v}}{\partial t}\right|_{\widehat{x}} + \rho(\boldsymbol{v}-\widehat{\boldsymbol{v}})\cdot\nabla\boldsymbol{v} - \nabla\cdot\boldsymbol{\sigma}^f - \rho\boldsymbol{f} = 0, \tag{17b}$$

$$\left.\frac{\partial(\rho s)}{\partial t}\right|_{\widehat{x}} + (\boldsymbol{v}-\widehat{\boldsymbol{v}})\cdot\nabla(\rho s) + \rho s\nabla\cdot\boldsymbol{v} + \nabla\cdot\left(\frac{\boldsymbol{q}}{\theta}\right) = \mathscr{P}, \tag{17c}$$

where $\widehat{\boldsymbol{v}}$ is the fluid domain velocity [4], which is associated to the mapping $\widehat{\boldsymbol{\phi}}$ that transforms the referential domain into the spatial configuration. The details of the mapping $\widehat{\boldsymbol{\phi}}$ will be will be provided later in the paper.

Remark For moving domain applications, the Eulerian form of the NSK equations may be discretized using a space–time technique, an alternative to the ALE approach. See [9,10,57,58,60,61,63,65,68–70,72] for recent advances in space–time methods for fluid mechanics and FSI.

3.2 Definition of the computational domain

Let Ω_0 denote the initial configuration of the entire domain of the problem, that is, the fluid and solid domains combined. Ω_0 will be adopted as the reference configuration and also as material configuration. We may decompose Ω_0 as

$$\Omega_0 = \overline{\Omega_0^f \cup \Omega_0^s}, \quad \text{with} \quad \Omega_0^f \cap \Omega_0^s = \emptyset, \tag{18}$$

where superscripts s and f refer to the solid and the fluid domain, respectively. We may also decompose the spatial configuration of Ω_0 at time t, namely Ω_t, as

$$\Omega_t = \overline{\Omega_t^f \cup \Omega_t^s}, \quad \text{with} \quad \Omega_t^f \cap \Omega_t^s = \emptyset. \tag{19}$$

Let Γ_0 and Γ_t be the fluid–solid interface where the subscripts 0 and t denote the initial and the current configuration, respectively. We will denote by Γ_0^s and Γ_t^s the boundary of the solid subdomain without the part of the fluid–structure interface. Likewise, Γ_0^f and Γ_t^f denote the boundary of the fluid subdomain without the fluid–structure interface. See Fig. 2 for an illustration.

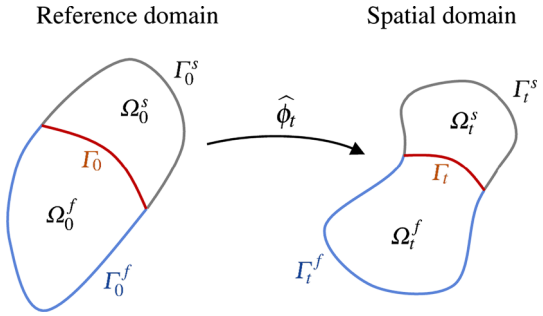

Fig. 2 Fluid and solid subdomains in the reference and spatial configuration

3.3 Continuous problem in the weak form

3.3.1 Solid mechanics problem

To define the weak form of the solid problem we need to consider suitable boundary conditions. Let us assume that the solid boundary Γ_0^s can be decomposed into Neumann and Dirichlet parts denoted by $(\Gamma_0^s)_N$ and $(\Gamma_0^s)_D$, respectively. Note that this splitting may be different for each spatial direction, although this is not explicitly indicated in our notation. Let us define a trial solution functional space $\mathscr{X}^s = \mathscr{X}^s(\Omega_0^s)$ whose members verify the Dirichlet boundary conditions of the problem, and a weighting function space $\mathscr{Y}^s = \mathscr{Y}^s(\Omega_0^s)$ which is identical to $\mathscr{X}^s$, but verifies homogeneous conditions on $(\Gamma_0^s)_D$. The variational formulation can be stated as follows: find $\boldsymbol{u} \in \mathscr{X}^s$ such that $\forall \boldsymbol{w}^s \in \mathscr{Y}^s$,

$$B^s\left(\boldsymbol{w}^s,\, \boldsymbol{u}\right) = F^s\left(\boldsymbol{w}^s\right), \tag{20}$$

where

$$B^s\left(\boldsymbol{w}^s,\, \boldsymbol{u}\right) = \int_{\Omega_0^s} \left(\boldsymbol{w}^s \cdot \rho_0^s \left.\frac{\partial^2 \boldsymbol{u}}{\partial t^2}\right|_X + \nabla_X \boldsymbol{w}^s : \boldsymbol{P} \right) \mathrm{d}\Omega_0^s, \tag{21}$$

and

$$F^s\left(\boldsymbol{w}^s\right) = \int_{\Omega_0^s} \boldsymbol{w}^s \cdot \rho_0^s \boldsymbol{f}^s \mathrm{d}\Omega_0^s + \int_{(\Gamma_0^s)_N} \boldsymbol{w}^s \cdot \widehat{\boldsymbol{h}} \mathrm{d}\left(\Gamma_0^s\right)_N. \tag{22}$$

Note that this variational formulation weakly enforces Eq. (5), and the Neumman boundary condition $\boldsymbol{P}\widehat{\boldsymbol{n}}^s = \widehat{\boldsymbol{h}}$ on $(\Gamma_0^s)_N$. Here, $\widehat{\boldsymbol{h}}$ is a given traction and $\widehat{\boldsymbol{n}}^s$ is the unit outward normal to the solid boundary in the referential domain. For future reference, we note that the boundary condition corresponding to a follower load p in the direction of the inner normal to the solid boundary may be imposed by taking $\widehat{\boldsymbol{h}} = -\mathsf{p} J \boldsymbol{F}^{-T} \widehat{\boldsymbol{n}}^s$.

3.3.2 Fluid mechanics problem

To derive our weak form we need to specify suitable boundary conditions. For the time being, we will focus on solid-wall boundary conditions. In classical compressible gas dynamics, solid-wall boundary conditions may be imposed, for example, by setting velocity and temperature to given values. This is not sufficient to get a well-posed boundary value problem for the NSK equations, due to the third-order spatial derivative of the density in the linear momentum balance. To attain well-posedness, the boundary condition

$$\nabla\rho \cdot \boldsymbol{n}^f = -|\nabla\rho| \cos(\varphi), \tag{23}$$

may be imposed. Here, $\boldsymbol{n}^f$ denotes the unit outward normal to the fluid boundary, and φ is the contact angle between the liquid–vapor interface and the solid, measured in the vapor phase. Let us also mention that to derive our weak form, we will split the momentum balance equation (17b) into two lower-order equations by introducing a new variable defined as $\Upsilon = \Delta\rho$. Notice that this step is not necessary with IGA since IGA allows to use the globally $\mathscr{C}^0$-continuous basis functions that are required to approximate the NSK equations in primal form (see [33]). However, to allow for the use of classical $\mathscr{C}^1$ finite elements, and to simplify the imposition of the boundary condition (23), we chose to use the split form. Let us introduce the trial solution space $\mathscr{X}^f = \mathscr{X}^f(\Omega_t^f)$ whose members satisfy all Dirichlet boundary conditions. The weighting functions space $\mathscr{Y}^f = \mathscr{Y}^f(\Omega_t^f)$ is identical to $\mathscr{X}^f$, but all restrictions on the Dirichlet boundary are homogeneous. The variational formulation is stated as follows: find $\boldsymbol{U} = \{\rho,\, \boldsymbol{v},\, \Upsilon,\, \theta\} \in \mathscr{X}^f$ such that $\forall \boldsymbol{W} = \{w^1,\, \boldsymbol{w}^2,\, w^3,\, w^4\} \in \mathscr{Y}^f$,

$$B^f(\boldsymbol{W},\, \boldsymbol{U};\, \widehat{\boldsymbol{v}}) = 0, \tag{24}$$

where

$$\begin{aligned}
B^f(\boldsymbol{W},\, \boldsymbol{U};\, \widehat{\boldsymbol{v}}) = &\int_{\Omega_t^f} w^1 \left(\left.\frac{\partial\rho}{\partial t}\right|_{\widehat{x}} + (\boldsymbol{v}-\widehat{\boldsymbol{v}}) \cdot \nabla\rho + \rho \nabla \cdot \boldsymbol{v} \right) \mathrm{d}\Omega_t^f \\
&+ \int_{\Omega_t^f} \boldsymbol{w}^2 \cdot \left(\rho \left.\frac{\partial \boldsymbol{v}}{\partial t}\right|_{\widehat{x}} + \rho(\boldsymbol{v}-\widehat{\boldsymbol{v}}) \cdot \nabla\boldsymbol{v} - \rho\boldsymbol{f} \right) \mathrm{d}\Omega_t^f \\
&+ \int_{\Omega_t^f} \nabla\boldsymbol{w}^2 : (\boldsymbol{\tau} - p\boldsymbol{I}) \mathrm{d}\Omega_t^f \\
&+ \int_{\Omega_t^f} \nabla \cdot \boldsymbol{w}^2 \lambda \left(\rho\Upsilon + \frac{1}{2}|\nabla\rho|^2 \right) \mathrm{d}\Omega_t^f \\
&- \int_{\Omega_t^f} \nabla\boldsymbol{w}^2 : \lambda \nabla\rho \otimes \nabla\rho \mathrm{d}\Omega_t^f \\
&+ \int_{\Omega_t^f} w^3 \Upsilon \mathrm{d}\Omega_t^f + \int_{\Omega_t^f} \nabla w^3 \cdot \nabla\rho \mathrm{d}\Omega_t^f \\
&+ \int_{\Gamma_t^f \cup \Gamma_t} w^3 |\nabla\rho| \cos(\varphi) \mathrm{d}\left(\Gamma_t^f \cup \Gamma_t\right) \\
&+ \int_{\Omega_t^f} w^4 \left(\left.\frac{\partial(\rho s)}{\partial t}\right|_{\widehat{x}} + (\boldsymbol{v}-\widehat{\boldsymbol{v}}) \cdot \nabla(\rho s) \right) \mathrm{d}\Omega_t^f \\
&+ \int_{\Omega_t^f} w^4 \left(\rho s \nabla \cdot \boldsymbol{v} - \frac{1}{\theta}\boldsymbol{\tau} : \nabla\boldsymbol{v} \right. \\
&\left. - k\frac{1}{\theta^2}|\nabla\theta|^2 \right) \mathrm{d}\Omega_t^f \\
&- \int_{\Omega_t^f} w^4 \left(\frac{\rho r}{\theta} + \frac{\rho \boldsymbol{f} \cdot \boldsymbol{v}}{\theta} \right) \mathrm{d}\Omega_t^f \\
&- \int_{\Omega_t^f} \nabla w^4 \cdot \frac{\boldsymbol{q}}{\theta} \mathrm{d}\Omega_t^f .
\end{aligned} \tag{25}$$

Note that the variational formulation (24)–(25) weakly imposes the NSK equations and the boundary condition (23). If Dirichlet boundary conditions are not set on the entire

boundary for velocity or temperature, then the variational formulation weakly imposes the conjugate stress-free condition or vanishing heat flux at the wall.

3.3.3 Fluid domain motion

The goal of this motion is to produce a smooth evolution of the fluid domain given the displacement data on the fluid–solid interface. This motion will be associated to the mapping $\widehat{\boldsymbol{\phi}}$, and will be understood as a succession of fictitious linear elastic boundary-value problems [4,40,54,74–77]. Let us use the notation $\widehat{\boldsymbol{\phi}}_t(\widehat{\boldsymbol{x}}) = \widehat{\boldsymbol{\phi}}(\widehat{\boldsymbol{x}}, t)$. We may define the displacement of the reference domain at time t as

$$\widehat{\boldsymbol{u}}_t(\widehat{\boldsymbol{x}}) = \widehat{\boldsymbol{u}}(\widehat{\boldsymbol{x}}, t) = \widehat{\boldsymbol{\phi}}(\widehat{\boldsymbol{x}}, t) - \widehat{\boldsymbol{x}}. \tag{26}$$

The function $\widehat{\boldsymbol{\phi}}_{\tilde{t}}$ is the analogue of $\widehat{\boldsymbol{\phi}}_t$ at time $\tilde{t}$, and $\widehat{\boldsymbol{u}}_t \circ \widehat{\boldsymbol{\phi}}_{\tilde{t}}^{-1}$ is simply the displacement of the reference domain at time t with respect to the configuration of the reference domain at time $\tilde{t}$. Here, we understand $\tilde{t} < t$ as a time instant close to t, which in a time-discrete context is usually the final configuration of the previous time step. To determine $\widehat{\boldsymbol{\phi}}_t$, and thus, the motion of the fluid subdomain, we use the identity

$$\widehat{\boldsymbol{\phi}}_t(\widehat{\boldsymbol{x}}) = \widehat{\boldsymbol{\phi}}_{\tilde{t}}(\widehat{\boldsymbol{x}}) + \left(\widehat{\boldsymbol{u}}_t \circ \widehat{\boldsymbol{\phi}}_{\tilde{t}}^{-1}\right)\left(\widehat{\boldsymbol{\phi}}_{\tilde{t}}(\widehat{\boldsymbol{x}})\right), \tag{27}$$

where $\widehat{\boldsymbol{u}}_t \circ \widehat{\boldsymbol{\phi}}_{\tilde{t}}^{-1}$ is obtained from a linear elastic boundary-value problem. Let us call $\boldsymbol{u}^m$ our "approximation" of $\widehat{\boldsymbol{u}}_t \circ \widehat{\boldsymbol{\phi}}_{\tilde{t}}^{-1}$ obtained by solving a fictitious linear-elastic boundary value problem. The unknown $\boldsymbol{u}^m$ is subject to Dirichlet boundary conditions $\boldsymbol{u}^m = \boldsymbol{u}_t \circ \widehat{\boldsymbol{\phi}}_{\tilde{t}}^{-1}$ on $\Gamma_{\tilde{t}}$, where $\boldsymbol{u}_t$ is the particle displacement at time t. These Dirichlet boundary conditions are strongly built into the trial solution space $\mathscr{V}^m = \mathscr{V}^m(\Omega_{\tilde{t}}^f)$. The corresponding weighting function space, satisfying homogeneous conditions on the boundary, is denoted by $\mathscr{W}^m = \mathscr{W}^m(\Omega_{\tilde{t}}^f)$. The variational formulation can be stated as follows: find $\boldsymbol{u}^m \in \mathscr{V}^m$ such that $\forall \boldsymbol{w}^m \in \mathscr{W}^m$,

$$B^m\left(\boldsymbol{w}^m, \boldsymbol{u}^m\right) = 0, \tag{28}$$

where

$$B^m\left(\boldsymbol{w}^m, \boldsymbol{u}^m\right) = \int_{\Omega_{\tilde{t}}^f} \nabla_{\tilde{x}}^{sym} \boldsymbol{w}^m : 2\mu^m \nabla_{\tilde{x}}^{sym} \boldsymbol{u}^m \mathrm{d}\Omega_{\tilde{t}}^f + \int_{\Omega_{\tilde{t}}^f} \nabla_{\tilde{x}} \cdot \boldsymbol{w}^m \lambda^m \nabla_{\tilde{x}} \cdot \boldsymbol{u}^m \mathrm{d}\Omega_{\tilde{t}}^f, \tag{29}$$

while μ^m and λ^m are the Lamé parameters of the fictitious elastic model characterizing the motion of the fluid domain; $\nabla_{\tilde{x}}$ is the gradient operator on $\Omega_{\tilde{t}}$ and $\nabla_{\tilde{x}}^{sym}$ is its symmetric part. Once $\boldsymbol{u}^m$ has been determined, the ALE mapping in the fluid subdomain can be obtained from Eq. (27) by replacing $\widehat{\boldsymbol{u}}_t \circ \widehat{\boldsymbol{\phi}}_{\tilde{t}}^{-1}$ with $\boldsymbol{u}^m$.

3.3.4 Coupled FSI problem

Here, we present the coupled FSI problem. The variational formulation of the problem is stated as follows: find $\boldsymbol{U} = \{\rho, \boldsymbol{v}, \Upsilon, \theta\} \in \mathscr{X}^f$, $\boldsymbol{u} \in \mathscr{X}^s$ and $\boldsymbol{u}^m \in \mathscr{V}^m$ such that $\forall \boldsymbol{W} = \{w^1, \boldsymbol{w}^2, w^3, w^4\} \in \mathscr{Y}^f$, $\forall \boldsymbol{w}^s \in \mathscr{Y}^s$ and $\forall \boldsymbol{w}^m \in \mathscr{W}^m$,

$$B^f(\boldsymbol{W}, \boldsymbol{U}; \widehat{\boldsymbol{v}}) + B^s\left(\boldsymbol{w}^s, \boldsymbol{u}\right) + B^m\left(\boldsymbol{w}^m, \boldsymbol{u}^m\right) = F^s\left(\boldsymbol{w}^s\right), \tag{30}$$

with the following fluid–solid interface conditions:

$$\boldsymbol{v} = \frac{\partial \boldsymbol{u}}{\partial t} \circ \widehat{\boldsymbol{\phi}}^{-1} \quad \text{on} \quad \Gamma_t, \tag{31}$$

$$\boldsymbol{w}^2 = \boldsymbol{w}^s \circ \widehat{\boldsymbol{\phi}}^{-1} \quad \text{on} \quad \Gamma_t. \tag{32}$$

In (30), $\widehat{\boldsymbol{v}}$ is obtained from $\widehat{\boldsymbol{\phi}}$ which is determined as explained in Sect. 3.3.3. Note also that Eq. (31) ensures strong kinematical compatibility at the fluid–structure interface. Equation (32) leads to a weak enforcement of traction compatibility at the interface, which in the spatial configuration may be expressed as $\boldsymbol{\sigma}^f \boldsymbol{n}^f + \boldsymbol{\sigma}^s \boldsymbol{n}^s = 0$ on Γ_t, where $\boldsymbol{n}^s$ is the unit outward normal to the solid in the spatial configuration.

3.4 Semidiscrete formulation

For the spatial discretization of the coupled problem we make use of NURBS-based IGA. We define finite-dimensional approximations of the functional spaces, namely, $\mathscr{X}_h^f$, $\mathscr{X}_h^s$ and $\mathscr{V}_h^m$ such that $\mathscr{X}_h^f \subset \mathscr{X}^f$, $\mathscr{X}_h^s \subset \mathscr{X}^s$, and $\mathscr{V}_h^m \subset \mathscr{V}^m$. Analogously, we introduce $\mathscr{Y}_h^f \subset \mathscr{Y}^f$, $\mathscr{Y}_h^s \subset \mathscr{Y}^s$, and $\mathscr{W}_h^m \subset \mathscr{W}^m$. We approximate (30) by the following variational problem over the finite element spaces: find $\boldsymbol{U}_h = \{\rho_h, \boldsymbol{v}_h, \Upsilon_h, \theta_h\} \in \mathscr{X}_h^f$, $\boldsymbol{u}_h \in \mathscr{X}_h^s$ and $\boldsymbol{u}_h^m \in \mathscr{V}_h^m$ such that $\forall \boldsymbol{W}_h = \{w_h^1, \boldsymbol{w}_h^2, w_h^3, w_h^4\} \in \mathscr{Y}_h^f$, $\forall \boldsymbol{w}_h^s \in \mathscr{Y}_h^s$ and $\forall \boldsymbol{w}_h^m \in \mathscr{W}_h^m$,

$$B^f(\boldsymbol{W}_h, \boldsymbol{U}_h; \widehat{\boldsymbol{v}}_h) + B^s\left(\boldsymbol{w}_h^s, \boldsymbol{u}_h\right) + B^m\left(\boldsymbol{w}_h^m, \boldsymbol{u}_h^m\right) = F^s\left(\boldsymbol{w}_h^s\right), \tag{33}$$

where

$$\rho_h(\boldsymbol{x}, t) = \sum_{A \in I_f} \rho_A(t) N_A(\boldsymbol{x}, t), \qquad w_h^1(\boldsymbol{x}, t) = \sum_{A \in I_f} w_A^1 N_A(\boldsymbol{x}, t), \tag{34a}$$

$$\boldsymbol{u}_h(\boldsymbol{X}, t) = \sum_{A \in I_s} \boldsymbol{u}_A(t) \widehat{N}_A(\boldsymbol{X}), \qquad \boldsymbol{w}_h^s(\boldsymbol{X}) = \sum_{A \in I_s} \boldsymbol{w}_A^s \widehat{N}_A(\boldsymbol{X}), \tag{34b}$$

$$\boldsymbol{u}_h^m(\tilde{\boldsymbol{x}},\,\tilde{t}) = \sum_{A\in I_f} \widehat{\boldsymbol{u}}_A(\tilde{t})\tilde{N}_A(\tilde{\boldsymbol{x}},\,\tilde{t}),$$
$$\boldsymbol{w}_h^m(\tilde{\boldsymbol{x}},\,\tilde{t}) = \sum_{A\in I_f} \boldsymbol{w}_A^m\tilde{N}_A(\tilde{\boldsymbol{x}},\,\tilde{t}), \tag{34c}$$

while the discrete fluid mesh velocity in the spatial configuration is given by

$$\widehat{\boldsymbol{v}}_h(\boldsymbol{x},\,t) = \sum_{A\in I_f} \frac{\partial\widehat{\boldsymbol{u}}_A}{\partial t}(t)N_A(\boldsymbol{x},\,t). \tag{35}$$

The variables $\boldsymbol{v}_h$, Υ_h and θ_h are defined analogously to ρ_h, while $\boldsymbol{w}_h^2$, w_h^3 and w_h^4 are defined similarly to w_h^1. In Eqs. (34), the $\widehat{N}_A$'s are a set of basis functions defined on Ω_0 and I_s is their global-index set. The $\widehat{N}_A$'s are fixed in time and have square integrable first spatial derivatives. Their continuity can be arbitrarily high inside the solid and fluid subdomains, but they are exactly $\mathscr{C}^0$ on Γ_0 (in the normal direction). N_A is the push forward of $\widehat{N}_A$ to the spatial domain Ω_t, that is, $N_A(\boldsymbol{x},\,t) = \widehat{N}_A\circ\widehat{\boldsymbol{\phi}^h}^{-1}(\boldsymbol{x},\,t)$, where $\widehat{\boldsymbol{\phi}^h}^{-1}$ is the discrete counterpart of $\widehat{\boldsymbol{\phi}}^{-1}$. Likewise, $\tilde{N}_A$ is the push forward of $\widehat{N}_A$ to the spatial domain at time $\tilde{t}$ (see Sect. 3.3.3), i.e., $\tilde{N}_A(\tilde{\boldsymbol{x}},\,\tilde{t}) = \widehat{N}_A\circ\widehat{\boldsymbol{\phi}^h}^{-1}(\tilde{\boldsymbol{x}},\,\tilde{t})$. I_f is the global-index set of the N_A's.

In order to ensure a correct coupling between the fluid and solid, we must enforce the compatibility of kinematics and tractions at the fluid–structure interface Γ_t. To do so, we use a unique set of trial functions for the velocity degrees-of-freedom, and the corresponding test functions for the linear momentum equations at the fluid–structure interface. This leads to a typical monolithic FSI formulation with a matching interface discretization, and gives strong (pointwise) satisfaction of the kinematics, and weak satisfaction of the traction compatibility conditions.

3.5 Time discretization and numerical implementation

We integrate the FSI equations in time using the generalized-α method. This method was originally proposed by Chung and Hulbert [15] for the equations of structural dynamics, and successfully applied in the context of turbulence simulation [3,39] and phase-field modeling [32,33].

3.5.1 Time stepping scheme

Let $\boldsymbol{U}$, $\dot{\boldsymbol{U}}$, $\ddot{\boldsymbol{U}}$ denote the vectors of control variable degrees of freedom of the fluid–structure system, and its first and second time derivatives, respectively. Let $\boldsymbol{V}$, $\dot{\boldsymbol{V}}$, $\ddot{\boldsymbol{V}}$ denote the vectors of control variable degrees of freedom of mesh displacements, velocities and accelerations. We define the residual vectors

$$\boldsymbol{R}^{cont} = \left\{R_A^{cont}\right\}, \tag{36a}$$
$$\boldsymbol{R}^{mom} = \left\{R_{A,i}^{mom}\right\}, \tag{36b}$$
$$\boldsymbol{R}^{aux} = \left\{R_A^{aux}\right\}, \tag{36c}$$
$$\boldsymbol{R}^{ener} = \left\{R_A^{ener}\right\}, \tag{36d}$$
$$\boldsymbol{R}^{mesh} = \left\{R_{A,i}^{mesh}\right\}, \tag{36e}$$

where A is a control-variable index and i is an index associated to the spatial dimensions. The residual components are defined as

$$R_A^{cont} = B^f\left(\{N_A,\,0,\,0,\,0\},\,\{\rho_h,\,\boldsymbol{v}_h,\,\Upsilon_h,\,\theta_h\};\,\widehat{\boldsymbol{v}}_h\right), \tag{37a}$$
$$R_{A,i}^{mom} = B^f\left(\{0,\,N_A\boldsymbol{e}_i,\,0,\,0\},\,\{\rho_h,\,\boldsymbol{v}_h,\,\Upsilon_h,\,\theta_h\};\,\widehat{\boldsymbol{v}}_h\right) + B^s\left(\widehat{N}_A\boldsymbol{e}_i,\,\boldsymbol{u}_h\right) - F^s\left(\widehat{N}_A\boldsymbol{e}_i\right), \tag{37b}$$
$$R_A^{aux} = B^f\left(\{0,\,0,\,N_A,\,0\},\,\{\rho_h,\,\boldsymbol{v}_h,\,\Upsilon_h,\,\theta_h\};\,\widehat{\boldsymbol{v}}_h\right), \tag{37c}$$
$$R_A^{ener} = B^f\left(\{0,\,0,\,0,\,N_A\},\,\{\rho_h,\,\boldsymbol{v}_h,\,\Upsilon_h,\,\theta_h\};\,\widehat{\boldsymbol{v}}_h\right), \tag{37d}$$
$$R_{A,i}^{mesh} = B^m\left(\tilde{N}_A\boldsymbol{e}_i,\,\boldsymbol{u}_h^m\right), \tag{37e}$$

where $\boldsymbol{e}_i$ is the ith cartesian basis vector. Our time stepping scheme can be defined as follows: given the discrete approximation to the global vectors of control variables at time t_n, namely, $\boldsymbol{U}_n$, $\dot{\boldsymbol{U}}_n$, $\ddot{\boldsymbol{U}}_n$, $\boldsymbol{V}_n$, $\dot{\boldsymbol{V}}_n$, $\ddot{\boldsymbol{V}}_n$ and the current time step $\Delta t = t_{n+1} - t_n$ find $\boldsymbol{U}_{n+1}$, $\dot{\boldsymbol{U}}_{n+1}$, $\ddot{\boldsymbol{U}}_{n+1}$, $\boldsymbol{V}_{n+1}$, $\dot{\boldsymbol{V}}_{n+1}$, $\ddot{\boldsymbol{V}}_{n+1}$ such that

$$\begin{aligned}
&\boldsymbol{R}^{cont}\left(\boldsymbol{U}_{n+\alpha_f},\,\dot{\boldsymbol{U}}_{n+\alpha_f},\,\ddot{\boldsymbol{U}}_{n+\alpha_m},\,\boldsymbol{V}_{n+\alpha_f},\,\dot{\boldsymbol{V}}_{n+\alpha_f},\,\ddot{\boldsymbol{V}}_{n+\alpha_m}\right) = 0,\\
&\boldsymbol{R}^{mom}\left(\boldsymbol{U}_{n+\alpha_f},\,\dot{\boldsymbol{U}}_{n+\alpha_f},\,\ddot{\boldsymbol{U}}_{n+\alpha_m},\,\boldsymbol{V}_{n+\alpha_f},\,\dot{\boldsymbol{V}}_{n+\alpha_f},\,\ddot{\boldsymbol{V}}_{n+\alpha_m}\right) = 0,\\
&\boldsymbol{R}^{aux}\left(\boldsymbol{U}_{n+\alpha_f},\,\dot{\boldsymbol{U}}_{n+\alpha_f},\,\ddot{\boldsymbol{U}}_{n+\alpha_m},\,\boldsymbol{V}_{n+\alpha_f},\,\dot{\boldsymbol{V}}_{n+\alpha_f},\,\ddot{\boldsymbol{V}}_{n+\alpha_m}\right) = 0,\\
&\boldsymbol{R}^{ener}\left(\boldsymbol{U}_{n+\alpha_f},\,\dot{\boldsymbol{U}}_{n+\alpha_f},\,\ddot{\boldsymbol{U}}_{n+\alpha_m},\,\boldsymbol{V}_{n+\alpha_f},\,\dot{\boldsymbol{V}}_{n+\alpha_f},\,\ddot{\boldsymbol{V}}_{n+\alpha_m}\right) = 0,\\
&\boldsymbol{R}^{mesh}\left(\boldsymbol{U}_{n+\alpha_f},\,\dot{\boldsymbol{U}}_{n+\alpha_f},\,\ddot{\boldsymbol{U}}_{n+\alpha_m},\,\boldsymbol{V}_{n+\alpha_f},\,\dot{\boldsymbol{V}}_{n+\alpha_f},\,\ddot{\boldsymbol{V}}_{n+\alpha_m}\right) = 0,\\
&\dot{\boldsymbol{U}}_{n+1} = \dot{\boldsymbol{U}}_n + \Delta t\left((1-\gamma)\ddot{\boldsymbol{U}}_n + \gamma\ddot{\boldsymbol{U}}_{n+1}\right),\\
&\boldsymbol{U}_{n+1} = \boldsymbol{U}_n + \Delta t\dot{\boldsymbol{U}}_n + \frac{\Delta t^2}{2}\left((1-2\beta)\ddot{\boldsymbol{U}}_n + 2\beta\ddot{\boldsymbol{U}}_{n+1}\right),\\
&\dot{\boldsymbol{V}}_{n+1} = \dot{\boldsymbol{V}}_n + \Delta t\left((1-\gamma)\ddot{\boldsymbol{V}}_n + \gamma\ddot{\boldsymbol{V}}_{n+1}\right),\\
&\boldsymbol{V}_{n+1} = \boldsymbol{V}_n + \Delta t\dot{\boldsymbol{V}}_n + \frac{\Delta t^2}{2}\left((1-2\beta)\ddot{\boldsymbol{V}}_n + 2\beta\ddot{\boldsymbol{V}}_{n+1}\right),
\end{aligned} \tag{38}$$

(39)

where

$$\square_{n+\alpha_f} = \square_n + \alpha_f\,(\square_{n+1} - \square_n)\,, \tag{40a}$$
$$\square_{n+\alpha_m} = \square_n + \alpha_m\,(\square_{n+1} - \square_n)\,, \tag{40b}$$

and $\square$ denotes a generic control variable vector. Note that although $\boldsymbol{U}_{n+1}$, $\dot{\boldsymbol{U}}_{n+1}$, $\ddot{\boldsymbol{U}}_{n+1}$ are treated separately in the algorithm, they are not independent because they need to satisfy Eqns. (39). The same argument applies to $\boldsymbol{V}_{n+1}$, $\dot{\boldsymbol{V}}_{n+1}$ and $\ddot{\boldsymbol{V}}_{n+1}$. The parameters α_f, α_m, γ and β are chosen as in [4] to ensure second-order accuracy and unconditional stability of the time-integration algorithm.

The non-linear system of Eqs. (38) may be solved using a Newton–Raphson iteration procedure, which leads to the following two-stage predictor–multicorrector algorithm.

Predictor stage there are different options for the predictor phase. Here, a constant-velocity predictor is adopted. Thus, we take

$$\begin{aligned}
\dot{\boldsymbol{U}}^{(0)}_{n+1} &= \dot{\boldsymbol{U}}_n,\\
\ddot{\boldsymbol{U}}^{(0)}_{n+1} &= \frac{\gamma-1}{\gamma}\ddot{\boldsymbol{U}}_n,\\
\boldsymbol{U}^{(0)}_{n+1} &= \boldsymbol{U}_n + \Delta t\dot{\boldsymbol{U}}_n + \frac{\Delta t^2}{2}\left((1-2\beta)\ddot{\boldsymbol{U}}_n + 2\beta\ddot{\boldsymbol{U}}^{(0)}_{n+1}\right),\\
\dot{\boldsymbol{V}}^{(0)}_{n+1} &= \dot{\boldsymbol{V}}_n,\\
\ddot{\boldsymbol{V}}^{(0)}_{n+1} &= \frac{\gamma-1}{\gamma}\ddot{\boldsymbol{V}}_n,\\
\boldsymbol{V}^{(0)}_{n+1} &= \boldsymbol{V}_n + \Delta t\dot{\boldsymbol{V}}_n + \frac{\Delta t^2}{2}\left((1-2\beta)\ddot{\boldsymbol{V}}_n + 2\beta\ddot{\boldsymbol{V}}^{(0)}_{n+1}\right),
\end{aligned} \tag{41}$$

where in the above equations, and in what follows, an index with parentheses is the nonlinear iteration index.

Multicorrector stage repeat the following steps for $i = 1, 2, \ldots, i_{max}$ or until convergence

(1) Evaluate solution iterates at the α-levels

$$\boldsymbol{U}^{(i)}_{n+\alpha_f} = \boldsymbol{U}_n + \alpha_f\left(\boldsymbol{U}^{(i-1)}_{n+1} - \boldsymbol{U}_n\right), \tag{42a}$$
$$\dot{\boldsymbol{U}}^{(i)}_{n+\alpha_f} = \dot{\boldsymbol{U}}_n + \alpha_f\left(\dot{\boldsymbol{U}}^{(i-1)}_{n+1} - \dot{\boldsymbol{U}}_n\right), \tag{42b}$$
$$\ddot{\boldsymbol{U}}^{(i)}_{n+\alpha_m} = \ddot{\boldsymbol{U}}_n + \alpha_m\left(\ddot{\boldsymbol{U}}^{(i-1)}_{n+1} - \ddot{\boldsymbol{U}}_n\right), \tag{42c}$$
$$\boldsymbol{V}^{(i)}_{n+\alpha_f} = \boldsymbol{V}_n + \alpha_f\left(\boldsymbol{V}^{(i-1)}_{n+1} - \boldsymbol{V}_n\right), \tag{42d}$$
$$\dot{\boldsymbol{V}}^{(i)}_{n+\alpha_f} = \dot{\boldsymbol{V}}_n + \alpha_f\left(\dot{\boldsymbol{V}}^{(i-1)}_{n+1} - \dot{\boldsymbol{V}}_n\right), \tag{42e}$$
$$\ddot{\boldsymbol{V}}^{(i)}_{n+\alpha_m} = \ddot{\boldsymbol{V}}_n + \alpha_m\left(\ddot{\boldsymbol{V}}^{(i-1)}_{n+1} - \ddot{\boldsymbol{V}}_n\right). \tag{42f}$$

(2) Use the solutions at the α-levels to assemble the residual and the tangent matrix of the linear system

$$\frac{\partial \boldsymbol{R}^{cont}_{(i)}}{\partial \ddot{\boldsymbol{U}}_{n+1}}\Delta\ddot{\boldsymbol{U}}^{(i)}_{n+1} + \frac{\partial \boldsymbol{R}^{cont}_{(i)}}{\partial \ddot{\boldsymbol{V}}_{n+1}}\Delta\ddot{\boldsymbol{V}}^{(i)}_{n+1} = -\boldsymbol{R}^{cont}_{(i)}, \tag{43a}$$
$$\frac{\partial \boldsymbol{R}^{mom}_{(i)}}{\partial \ddot{\boldsymbol{U}}_{n+1}}\Delta\ddot{\boldsymbol{U}}^{(i)}_{n+1} + \frac{\partial \boldsymbol{R}^{mom}_{(i)}}{\partial \ddot{\boldsymbol{V}}_{n+1}}\Delta\ddot{\boldsymbol{V}}^{(i)}_{n+1} = -\boldsymbol{R}^{mom}_{(i)}, \tag{43b}$$
$$\frac{\partial \boldsymbol{R}^{aux}_{(i)}}{\partial \ddot{\boldsymbol{U}}_{n+1}}\Delta\ddot{\boldsymbol{U}}^{(i)}_{n+1} + \frac{\partial \boldsymbol{R}^{aux}_{(i)}}{\partial \ddot{\boldsymbol{V}}_{n+1}}\Delta\ddot{\boldsymbol{V}}^{(i)}_{n+1} = -\boldsymbol{R}^{aux}_{(i)}, \tag{43c}$$
$$\frac{\partial \boldsymbol{R}^{ener}_{(i)}}{\partial \ddot{\boldsymbol{U}}_{n+1}}\Delta\ddot{\boldsymbol{U}}^{(i)}_{n+1} + \frac{\partial \boldsymbol{R}^{ener}_{(i)}}{\partial \ddot{\boldsymbol{V}}_{n+1}}\Delta\ddot{\boldsymbol{V}}^{(i)}_{n+1} = -\boldsymbol{R}^{ener}_{(i)}, \tag{43d}$$
$$\frac{\partial \boldsymbol{R}^{mesh}_{(i)}}{\partial \ddot{\boldsymbol{U}}_{n+1}}\Delta\ddot{\boldsymbol{U}}^{(i)}_{n+1} + \frac{\partial \boldsymbol{R}^{mesh}_{(i)}}{\partial \ddot{\boldsymbol{V}}_{n+1}}\Delta\ddot{\boldsymbol{V}}^{(i)}_{n+1} = -\boldsymbol{R}^{mesh}_{(i)}. \tag{43e}$$

The resulting linear system is solved using a preconditioned GMRES algorithm.

(3) Use $\Delta\ddot{\boldsymbol{U}}^{(i)}_{n+1}$ and $\Delta\ddot{\boldsymbol{V}}^{(i)}_{n+1}$ to update the iterates as

$$\ddot{\boldsymbol{U}}^{(i)}_{n+1} = \ddot{\boldsymbol{U}}^{(i-1)}_{n+1} + \Delta\ddot{\boldsymbol{U}}^{(i)}_{n+1}, \tag{44a}$$
$$\dot{\boldsymbol{U}}^{(i)}_{n+1} = \dot{\boldsymbol{U}}^{(i-1)}_{n+1} + \gamma\Delta t\Delta\ddot{\boldsymbol{U}}^{(i)}_{n+1}, \tag{44b}$$
$$\boldsymbol{U}^{(i)}_{n+1} = \boldsymbol{U}^{(i-1)}_{n+1} + \beta\Delta t^2\Delta\ddot{\boldsymbol{U}}^{(i)}_{n+1}, \tag{44c}$$
$$\ddot{\boldsymbol{V}}^{(i)}_{n+1} = \ddot{\boldsymbol{V}}^{(i-1)}_{n+1} + \Delta\ddot{\boldsymbol{V}}^{(i)}_{n+1}, \tag{44d}$$
$$\dot{\boldsymbol{V}}^{(i)}_{n+1} = \dot{\boldsymbol{V}}^{(i-1)}_{n+1} + \gamma\Delta t\Delta\ddot{\boldsymbol{V}}^{(i)}_{n+1}, \tag{44e}$$
$$\boldsymbol{V}^{(i)}_{n+1} = \boldsymbol{V}^{(i-1)}_{n+1} + \beta\Delta t^2\Delta\ddot{\boldsymbol{V}}^{(i)}_{n+1}. \tag{44f}$$

This completes one nonlinear iteration. The nonlinear iterative algorithm should be repeated until the norm of each of the residual vectors defined in (36) has been reduced to a given tolerance ϵ of its value using the predictions defined in (41). In this work, we use $\epsilon = 10^{-4}$.

Remark To solve the FSI equations, we adopt a quasi-direct solution strategy (see [75,78,79] for the definition of terminology and methods), where the fluid and solid equations are solved in a coupled fashion, while the mesh motion equations are solved separately, using the data from the fluid–solid solve as input. As a result, the so-called shape derivatives, that is, the derivatives of the continuity, momentum and energy residuals with respect to the mesh motion variables, are omitted. It was shown in [4,20] that omitting shape derivatives has little effect on the convergence of Newton–Raphson iterations, and leads to non-negligible computational savings. In the implementation of the quasi-direct solution strategy, Eqns. (43) in the above predictor–multicorrector algorithm are simplified to

$$\frac{\partial \boldsymbol{R}^{cont}_{(i)}}{\partial \ddot{\boldsymbol{U}}_{n+1}}\Delta\ddot{\boldsymbol{U}}^{(i)}_{n+1} = -\boldsymbol{R}^{cont}_{(i)}, \tag{45a}$$

$$\frac{\partial \boldsymbol{R}^{mom}_{(i)}}{\partial \ddot{\boldsymbol{U}}_{n+1}} \Delta \ddot{\boldsymbol{U}}^{(i)}_{n+1} = -\boldsymbol{R}^{mom}_{(i)}, \tag{45b}$$

$$\frac{\partial \boldsymbol{R}^{aux}_{(i)}}{\partial \ddot{\boldsymbol{U}}_{n+1}} \Delta \ddot{\boldsymbol{U}}^{(i)}_{n+1} = -\boldsymbol{R}^{aux}_{(i)}, \tag{45c}$$

$$\frac{\partial \boldsymbol{R}^{ener}_{(i)}}{\partial \ddot{\boldsymbol{U}}_{n+1}} \Delta \ddot{\boldsymbol{U}}^{(i)}_{n+1} = -\boldsymbol{R}^{ener}_{(i)}, \tag{45d}$$

$$\frac{\partial \boldsymbol{R}^{mesh}_{(i)}}{\partial \ddot{\boldsymbol{V}}_{n+1}} \Delta \ddot{\boldsymbol{V}}^{(i)}_{n+1} = -\boldsymbol{R}^{mesh}_{(i)}, \tag{45e}$$

where the last equation, which governs the deformation of the fluid mechanics mesh, is solved using the solution of the first four equations as input.

4 Numerical examples

We present two numerical examples of phase-change-driven implosion of relatively thin structures initially filled with water vapor. The first one corresponds to a cylinder of infinite length, which is modeled as a two-dimensional system. The second one studies the implosive collapse of a three-dimensional box. All the parameters and the results presented in Sect. 4 are given in non-dimensional form. To do so, we have rescaled the units of measurement of length, mass, time and temperature by L_0, bL_0^3, $L_0/\sqrt{ab}$ and θ_c, respectively, where $L_0 = 1$ denotes a length scale of the computational domain size. Using this non-dimensionalization, it may be shown that the fluid mechanics problem has four dimensionless numbers,

$$Re = \frac{L_0 b\sqrt{ab}}{\bar{\mu}}, \quad Ca = \frac{\sqrt{\lambda/a}}{L_0}, \tag{46}$$

$$Pr = \frac{L_0 ab^2\sqrt{ab}/\theta_c}{k}, \quad c = \frac{8}{27}\frac{c_v}{R}, \tag{47}$$

where Re is the Reynolds number, Ca denotes the capillary number, Pr is the Prandtl number, and c is the dimensionless heat capacity. The solid mechanics problem has two dimensionless numbers,

$$\widehat{\mu} = \frac{\mu}{\rho_0^s ab}, \quad \widehat{\kappa} = \frac{\kappa}{\rho_0^s ab}. \tag{48}$$

The capillary number Ca and the Reynolds number Re were chosen according to the methodology proposed in [33], which is an upscaling method to desensitize the solution to mesh refinement. In particular, we take

$$Ca = h/L_0 \quad \text{and} \quad Re = \alpha L_0/h, \tag{49}$$

where h is a characteristic length scale of the spatial mesh (see [33]) and α is an $O(1)$ constant. Following [33], we have adopted $\alpha = 2$ for all the computations.

Remark We note that solving very strong implosions at full scale is extremely difficult from the modeling and computational point of view. First, from the computational point of view, the fluid subdomain volume would be reduced quite dramatically and remeshing would be necessary. Second, very strong implosions are associated to strong temperature reductions in the structure, and the van der Waals equation is significantly less accurate for low temperatures than for high temperatures. For these reasons, we focus on moderately strong implosions.

4.1 2D example

Here, we simulate the collapse of a solid ring which is initially filled with water vapor in equilibrium. The external radius of the ring is $L_0 = 1$, and the thickness of the solid is $L_0/40$. We suppose that there is a follower load acting on the solid external surface, which is identical to the water vapor pressure inside the ring, so the system is initially in thermal and mechanical equilibrium. We trigger the implosion by suddenly reducing the temperature at the fluid–solid interface using the temperature boundary condition. The temperature reduction makes the vapor condensate, reducing the internal pressure and increasing the density. Our problem setup is completely symmetric, so we perform the computation on one quarter of the physical domain (see Fig. 3, where we specify the geometry and the boundary conditions of the problem).

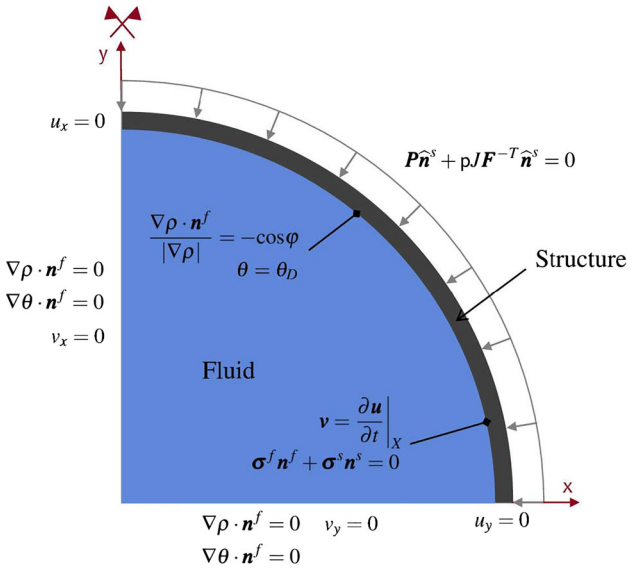

Fig. 3 Computational domain of the 2D example. The symmetry conditions for the fluid velocity $\boldsymbol{v}$, density ρ and temperature θ, and for the solid displacements $\boldsymbol{u}$ are indicated on the *left* and *bottom* boundaries (in the plot, $\square_x$ and $\square_y$ denote the first and second components of the vector $\square$, respectively). The external pressure p (follower load) acting on the structure and the temperature θ_D applied at the fluid–structure interface are also depicted. Finally, a certain angle φ is imposed between the solid wall and the liquid–vapor interface

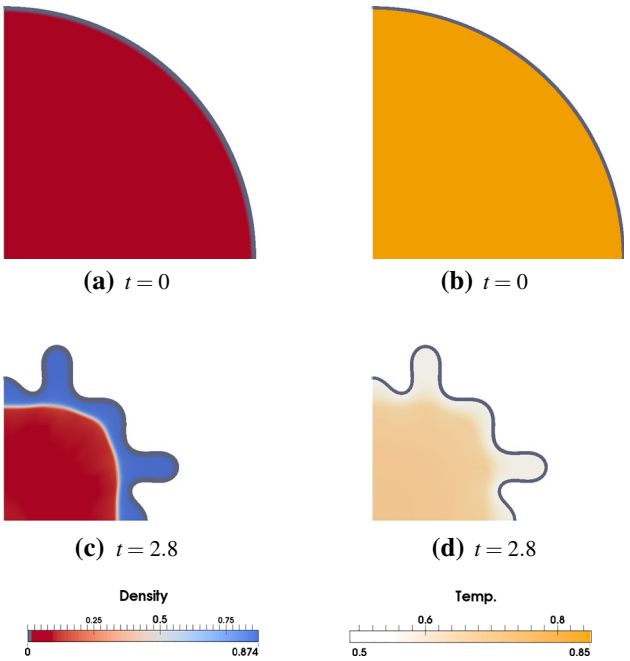

Fig. 4 Evolution of density (*left*) and temperature (*right*) in a 2D phase-change-driven implosion problem. Initially, water-vapor (*red color* in the density plot) is filling up a hollow structure (**a**) and a low temperature $\theta_D = 0.5$ is applied at the fluid–structure interface (b). The vapor close to the boundaries increases its density and turns into liquid (*blue* in the density plot, **c**). The pressure inside is reduced and the structure deforms due to the external load (c, d). We have used the parameters $Re = 256$, $Ca = 0.0078125$, $Pr = 0.013$, $c = 0.73$, $\widehat{\mu} = 1.0$, $\widehat{\kappa} = 1.0$. (Color figure online)

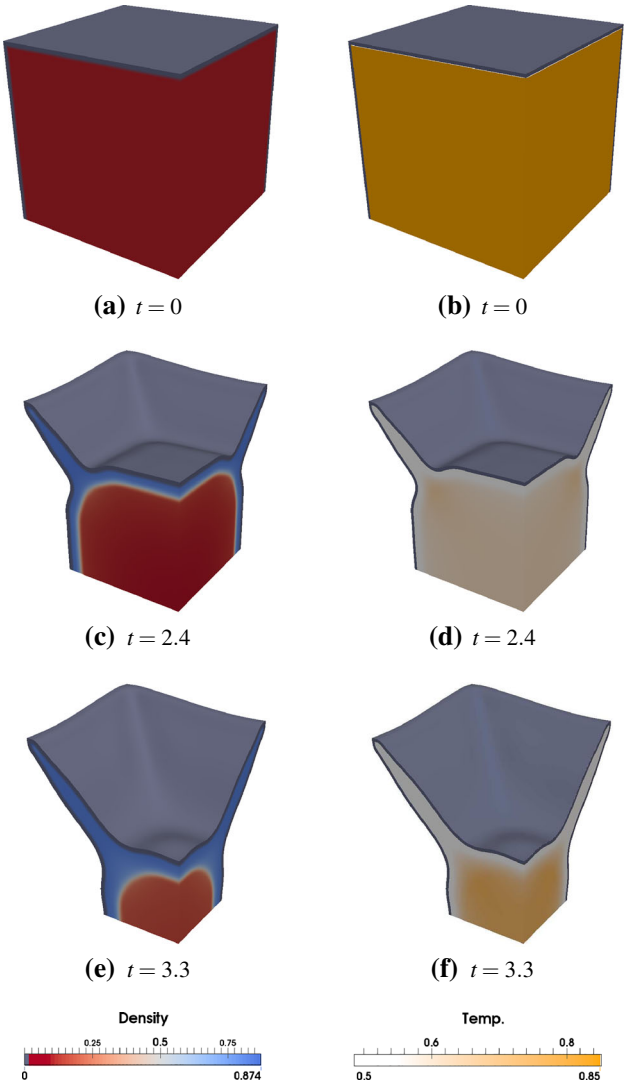

Fig. 5 Evolution of density (*left*) and temperature (*right*) in a 3D phase-change-driven implosion problem. Initially, water-vapor (*red color* in the density plot) is filling up a hollow structure (**a**) and a low temperature $\theta_D = 0.5$ is applied at the fluid–structure interface (b). The vapor close to the boundaries reduces its temperature (*white color* in d, f), increases its density and turns into liquid (*blue color* in the density plot, **c**, **e**). The pressure inside is reduced and the structure deforms due to the external load. We have used the parameters $Re = 256$, $Ca = 0.0078125$, $Pr = 0.013$, $c = 0.73$, $\widehat{\mu} = 1.0$, $\widehat{\kappa} = 1.0$. (Color figure online)

Figure 4 shows the time evolution of the density (left) and temperature (right) in the fluid subdomain. The solid is analyzed only by plotting its deformed configuration (we have also made use of the symmetry for visualization purposes, and we only represent one quarter of the domain). In the NSK theory, the density is a marker of the phases, and in our density color scale, red represents vapor and blue represents liquid. It may be observed that at the initial time, all the fluid subdomain is in gaseous state (Fig. 4a). The thin grey subdomain that encloses the fluid represents the structure. The problem is initialized by taking as initial density, velocity and temperature the values $\rho_0 = 0.1$, $\boldsymbol{v}_0 = 0$ and $\theta_0 = 0.85$, respectively. On the fluid–structure interface we apply a temperature boundary condition given by $\theta_D = 0.5 < \theta_0$ which triggers the implosion. In particular, the temperature of the gas close to the structure is reduced and the gas turns into liquid (blue) (Fig. 4c). The pressure decreases inside and the structure is deformed due to the external pressure (Fig. 4c). The process continues so that all the gas is transformed into liquid and the structure is completely collapsed (data not shown). The parameters employed in this example are $c = 0.73$, $Pr = 0.013$, $Re = 256$, $Ca = 0.0078125$ for the fluid and $\widehat{\mu} = 1.0$ and $\widehat{\kappa} = 1.0$ for the solid. The contact angle was assumed $\varphi = \pi/2$. We used a computational mesh composed of 128^2 NURBS quadratic elements. The basis functions have a $\mathscr{C}^0$ line on the fluid–structure interface, but otherwise are globally $\mathscr{C}^1$-continuous.

4.2 3D example

The setup of this example is identical to that of the two-dimensional problem, but here we focus on the collapse of a three-dimensional box of side $2L_0$. Due to the symmetry our computational domain is a box of side L_0, representing one eight of the physical domain. The box is hollow and its thickness is $L_0/40$ (see Fig. 5a). All the parameters and

initial conditions are also the same as in Sect. 4.1, but the collapse is stronger because the structure is geometrically softer. Figure 5 shows the evolution of the density (left) and temperature (right). It is observed that the temperature boundary condition triggers the transformation of vapor into liquid creating a blue area in the density plot which represents liquid water. We used a computational mesh composed of 128^3 NURBS quadratic elements. The basis functions have $\mathscr{C}^0$ lines on the fluid–structure interface, but otherwise are globally $\mathscr{C}^1$-continuous. The time step was selected adaptively using the algorithm proposed in [32].

5 Conclusions

We reported on our initial efforts to study computationally the interaction of complex fluids and solids. From a methodological point of view, our theoretical framework and algorithms may be thought of as an extension of well-established FSI methods to the realm of complex fluids. We showed the viability of the approach by way of two numerical examples. Although our examples focus only on phase-change-driven implosion, we believe that our theories and algorithms may be used to solve other, largely unexplored problems that involve the interaction of complex fluids and solids.

Acknowledgments HG was partially supported by the European Research Council through the FP7 Ideas Starting Grant Program (Contract #307201), Xunta de Galicia, co-financed with FEDER funds, and Ministerio de Economia y Competitividad (Contract # DPI2013-44406-R). YB was partially supported by the NSF CAREER Award OCI-1055091.

References

1. Bazilevs Y, Beiro Da Veiga L, Cottrell JA, Hughes TJR, Sangalli G (2006a) Isogeometric Analysis: approximation, stability and error estimates for h-refined meshes. Math Models Methods Appl Sci 16(07):1031–1090
2. Bazilevs Y, Calo VM, Zhang Y, Hughes TJR (2006b) Isogeometric Fluid–Structure Interaction analysis with applications to arterial blood flow. Comput Mech 38(4–5):310–322
3. Bazilevs Y, Calo VM, Cottrell JA, Hughes TJR, Reali A, Scovazzi G (2007) Variational multiscale residual-based turbulence modeling for large eddy simulation of incompressible flows. Comput Methods Appl Mech Eng 197(14):173–201
4. Bazilevs Y, Calo VM, Hughes TJR, Zhang Y (2008) Isogeometric Fluid–Structure Interaction: theory, algorithms, and computations. Comput Mech 43(1):3–37
5. Bazilevs Y, Gohean JR, Hughes TJR, Moser RD, Zhang Y (2009) Patient-specific isogeometric fluid–structure interaction analysis of thoracic aortic blood flow due to implantation of the jarvik 2000 left ventricular assist device. Comput. Methods Appl Mech Eng 198(45):3534–3550
6. Bazilevs Y, Calo VM, Cottrell JA, Evans JA, Hughes TJR, Lipton S, Scott MA, Sederberg TW (2010) Isogeometric Analysis using T-splines. Comput. Methods Appl Mech Eng 199(58):229–263
7. Bazilevs Y, Hsu M-C, Kiendl J, Wüchner R, Bletzinger K-U (2011) 3D simulation of wind turbine rotors at full scale. Part II: fluid–structure interaction modeling with composite blades. Int J Numer Methods Fluids 65(1–3):236–253
8. Bazilevs Y, Takizawa K, Tezduyar TE (2013a) Challenges and directions in computational fluid–structure interaction. Math Models Methods Appl Sci 23:215–221
9. Bazilevs Y, Takizawa K, Tezduyar TE (2013b) Computational fluid–structure interaction. Methods and applications. Wiley, Chichester
10. Bazilevs Y, Takizawa K, Tezduyar TE, Hsu M-C, Kostov N, McIntyre S (2014) Aerodynamic and FSI analysis of wind turbines with the ALE-VMS and ST-VMS methods. Arch Comput Methods Eng, published online. doi:10.1007/s11831-014-9119-7
11. Benson DJ, Bazilevs Y, Hsu MC, Hughes TJR (2010) Isogeometric shell analysis: the Reissner–Mindlin shell. Comput Methods Appl Mech Eng 199(5):276–289
12. Borden MJ, Verhoosel CV, Scott MA, Hughes TJR, Landis CM (2012) A phase-field description of dynamic brittle fracture. Comput Methods Appl Mech Eng 217–220:77–95
13. Casquero H, Bona-Casas C, Gomez H (2014) A NURBS-based immersed methodology for fluid–structure interaction. Comput Methods Appl Mech Eng. doi:10.1016/j.cma.2014.10.055
14. Chen L-Q (2002) Phase-field models for microstructure evolution. Annu Rev Mater Res 32(1):113–140
15. Chung J, Hulbert GM (1993) A time integration algorithm for structural dynamics with improved numerical dissipation: the generalized-α method. J Appl Mech 60:371–375
16. Cottrell JA, Reali A, Bazilevs Y, Hughes TJR (2006) Isogeometric Analysis of structural vibrations. Comput Methods Appl Mech Eng 195(4143):5257–5296
17. Cottrell JA, Hughes TJR, Reali A (2007) Studies of refinement and continuity in Isogeometric structural analysis. Comput Methods Appl Mech Eng 196(4144):4160–4183
18. Cottrell JA, Hughes TJR, Bazilevs Y (2009) Isogeometric analysis: toward integration of CAD and FEA. Wiley, Chichester
19. Cueto-Felgueroso L, Juanes R (2008) Nonlocal interface dynamics and pattern formation in gravity-driven unsaturated flow through porous media. Phys Rev Lett 101:244504
20. Dettmer WG, Peric D (2008) On the coupling between fluid flow and mesh motion in the modelling of fluid–structure interaction. Comput Mech 43:81–90
21. Diehl D (2007) Higher order schemes for simulation of compressible liquid–vapor flows with phase change. PhD Thesis, Albert-Ludwigs-Universitat
22. Donea J, Huerta A (2003) Finite element methods for flow problems. Wiley, Chichester
23. Donea J, Huerta A, Ponthot J-Ph, Rodrguez-Ferran A (2004) Encyclopedia of computational mechanics. Arbitrary Lagrangian–Eulerian methods, vol 1, Chapter 14. Wiley, New York
24. Dunn JE, Serrin J (1985) On the thermomechanics of interstitial working. Arch Rational Mech Anal 88(2):95–133
25. Elguedj T, Bazilevs Y, Calo VM, Hughes TJR (2008) $\bar{B}$ and $\bar{F}$ projection methods for nearly incompressible linear and non-linear elasticity and plasticity using higher-order NURBS elements. Comput Methods Appl Mech Eng 197(3340):2732–2762
26. Farhat C, Rallu A, Shankaran S (2008) A higher-order generalized Ghost Fluid Method for the Poor for the three-dimensional two-phase flow computation of underwater implosions. J Comput Phys 227(16):7674–7700
27. Farhat C, Rallu A, Wang K, Belytschko T (2010) Robust and provably second-order explicit–explicit and implicit–explicit staggered time-integrators for highly non-linear compressible Fluid–Structure Interaction problems. Int J Numer Methods Eng 84(1):73–107

28. Galenko PK, Gomez H, Kropotin NV, Elder KR (2013) Unconditionally stable method and numerical solution of the hyperbolic phase-field crystal equation. Phys Rev E 88(1):013310
29. Gelbart WM, Ben-Shaul A (1996) The new science of complex fluids. J Phys Chem 100(31):13169–13189
30. Gibbs JW (1876) On the equilibrium of heterogeneous substances. Trans Conn Acad 3:108–248
31. Gomez H, Hughes TJR (2011) Provably unconditionally stable, second-order time-accurate, mixed variational methods for phase-field models. J Comput Phys 230(13):5310–5327
32. Gomez H, Calo VM, Bazilevs Y, Hughes TJR (2008) Isogeometric Analysis of the Cahn–Hilliard phase-field model. Comput Methods Appl Mech Eng 197:4333–4352
33. Gomez H, Hughes TJR, Nogueira X, Calo VM (2010) Isogeometric Analysis of the isothermal Navier–Stokes–Korteweg equations. Comput Methods Appl Mech Eng 199(25–28):1828–1840
34. Gomez H, Cueto-Felgueroso L, Juanes R (2013) Three-dimensional simulation of unstable gravity-driven infiltration of water into a porous medium. J Comput Phys 238:217–239
35. Gomez H, Reali A, Sangalli G (2014) Accurate, efficient, and (iso) geometrically flexible collocation methods for phase-field models. J Comput Phys 262:153–171
36. Hughes TJR, Liu WK, Zimmermann TK (1981) Lagrangian–Eulerian Finite Element formulation for incompressible viscous flows. Comput Methods Appl Mech Eng 29(3):329–349
37. Hughes TJR, Cottrell JA, Bazilevs Y (2005) Isogeometric Analysis: CAD, Finite Elements, NURBS, exact geometry and mesh refinement. Comput. Methods Appl Mech Eng 194(3941):4135–4195
38. Ikeda CM (2012) Fluid–Structure Interactions. Implosions of shell structures and wave impact on a flat plate. PhD Thesis, University of Maryland
39. Jansen KE, Whiting CH, Hulbert GM (2000) A generalized-α method for integrating the filtered Navier–Stokes equations with a stabilized Finite Element Method. Comput Methods Appl Mech Eng 190(34):305–319
40. Johnson AA, Tezduyar TE (1994) Mesh update strategies in parallel finite element computations of flow problems with moving boundaries and interfaces. Comput Methods Appl Mech Eng 119:73–94
41. Kamran K, Rossi R, Oñate E, Idelshon SR (2013a) A compressible Lagrangian framework for modeling the fluid–structure interaction in the underwater implosion of an aluminum cylinder. Math Models Methods Appl Sci 23(02):339–367
42. Kamran K, Rossi R, Oñate E, Idelsohn SR (2013b) A compressible Lagrangian framework for the simulation of the underwater implosion of large air bubbles. Comput Methods Appl Mech Eng 255:210–225
43. Lipton S, Evans JA, Bazilevs Y, Elguedj T, Hughes TJR (2010) Robustness of isogeometric structural discretizations under severe mesh distortion. Comput Methods Appl Mech Eng 199(5):357–373
44. Liu J (2014) Thermodynamically consistent modeling and simulation of multiphase flows. PhD Thesis, The University of Texas at Austin
45. Liu J, Gomez H, Evans JA, Hughes TJR, Landis CM (2013) Functional entropy variables: a new methodology for deriving thermodynamically consistent algorithms for complex fluids, with particular reference to the isothermal Navier–Stokes–Korteweg equations. J Comput Phys 248:47–86
46. Long CC, Marsden AL, Bazilevs Y (2013) Fluid–structure interaction simulation of pulsatile ventricular assist devices. Comput Mech 52:971–981
47. Long CC, Esmaily-Moghadam M, Marsden AL, Bazilevs Y (2014a) Computation of residence time in the simulation of pulsatile ventricular assist devices. Comput Mech 54:911–919
48. Long CC, Marsden AL, Bazilevs Y (2014b) Shape optimization of pulsatile ventricular assist devices using FSI to minimize thrombotic risk. Comput Mech 54:921–932
49. Penrose O, Fife PC (1990) Thermodynamically consistent models of phase-field type for the kinetic of phase transitions. Physica D 43(1):44–62
50. Rallu ASD (2009) A multiphase fluid–structure computational framework for underwater implosion problems. PhD Thesis, Stanford University
51. Sedzinski J, Biro M, Oswald A, Tinevez J-Y, Salbreux G, Paluch E (2011) Polar actomyosin contractility destabilizes the position of the cytokinetic furrow. Nature 476(7361):462–466
52. Shao D, Levine H, Rappel W-J (2012) Coupling actin flow, adhesion, and morphology in a computational cell motility model. Proc Natl Acad Sci USA 109(18):6851–6856
53. Simo JC, Hughes TJR (1998) Computational inelasticity. Springer, New York
54. Stein K, Tezduyar T, Benney R (2003) Mesh moving techniques for fluid–structure interactions with large displacements. J Appl Mech 70:58–63
55. Steinbach I (2009) Phase-field models in materials science. Model Simul Mater Sci Eng 17(7):073001
56. Suito H, Takizawa K, Huynh VQH, Sze D, Ueda T (2014) FSI analysis of the blood flow and geometrical characteristics in the thoracic aorta. Comput Mech 54:1035–1045
57. Takizawa K (2014) Computational engineering analysis with the new-generation space–time methods. Comput Mech 54:193–211
58. Takizawa K, Tezduyar TE (2014) Space–time computation techniques with continuous representation in time (ST-C). Comput Mech 53(1):91–99
59. Takizawa K, Bazilevs Y, Tezduyar TE (2012) Space–Time and ALE-VMS techniques for patient-specific cardiovascular Fluid–Structure Interaction modeling. Arch Comput Methods Eng 19(2):171–225
60. Takizawa K, Montes D, Fritze M, McIntyre S, Boben J, Tezduyar TE (2013a) Methods for FSI modeling of spacecraft parachute dynamics and cover separation. Math Models Methods Appl Sci 23:307–338
61. Takizawa K, Montes D, McIntyre S, Tezduyar TE (2013b) Space–time VMS methods for modeling of incompressible flows at high Reynolds numbers. Math Models Methods Appl Sci 23: 223–248
62. Takizawa K, Tezduyar TE, Boben J, Kostov N, Boswell C, Buscher A (2013c) Fluid–structure interaction modeling of clusters of spacecraft parachutes with modified geometric porosity. Comput Mech 52(6):1351–1364
63. Takizawa K, Schjodt K, Puntel A, Kostov N, Tezduyar TE (2013d) Patient-specific computational analysis of the influence of a stent on the unsteady flow in cerebral aneurysms. Comput Mech 51:1061–1073
64. Takizawa K, Takagi H, Tezduyar TE, Torii R (2014a) Estimation of element-based zero-stress state for arterial FSI computations. Comput Mech 54:895–910
65. Takizawa K, Bazilevs Y, Tezduyar TE, Long CC, Marsden AL, Schjodt K (2014b) ST and ALE-VMS methods for patient-specific cardiovascular fluid mechanics modeling. Math Models Methods Appl Sci 24:2437–2486
66. Takizawa K, Bazilevs Y, Tezduyar TE, Hsu M-C, Oiseth O, Mathisen KM, Kostov N, McIntyre S (2014c) Engineering analysis and design with ALE-VMS and space–time methods. Arch Comput Methods Eng, published online. doi:10.1007/s11831-014-9113-0
67. Takizawa K, Tezduyar TE, Kolesar R, Boswell C, Kanai T, Montel K (2014d) Multiscale methods for gore curvature calculations from FSI modeling of spacecraft parachutes. Comput Mech, published online. doi:10.1007/s00466-014-1069-2
68. Takizawa K, Tezduyar TE, Boswell C, Kolesar R, Montel K (2014e) FSI modeling of the reefed stages and disreefing of the Orion spacecraft parachutes. Comput Mech 54(5):1203–1220

69. Takizawa K, Tezduyar TE, Buscher A, Asada S (2014f) Space–time fluid mechanics computation of heart valve models. Comput Mech 54:973–986
70. Takizawa K, Tezduyar TE, Buscher A, Asada S (2014g) Space–time interface-tracking with topology change (ST-TC). Comput Mech 54(4):955–971
71. Takizawa K, Tezduyar TE, Kostov N (2014h) Sequentially-coupled space–time FSI analysis of bio-inspired flapping-wing aerodynamics of an MAV. Comput Mech 54:213–233
72. Takizawa K, Tezduyar TE, McIntyre S, Kostov N, Kolesar R, Habluetzel C (2014i) Space–time VMS computation of wind-turbine rotor and tower aerodynamics. Comput Mech 53(1):1–15
73. Takizawa K, Torii R, Takagi H, Tezduyar TE, Xu XY (2014j) Coronary arterial dynamics computation with medical-image-based time-dependent anatomical models and element-based zero-stress state estimates. Comput Mech 54:1047–1053
74. Tezduyar TE (2001) Finite element methods for flow problems with moving boundaries and interfaces. Arch Comput Methods Eng 8:83–130
75. Tezduyar TE, Sathe S (2007) Modeling of fluid–structure interactions with the space–time finite elements: solution techniques. Int J Numer Methods Fluids 54:855–900
76. Tezduyar TE, Behr M, Mittal S, Johnson AA (1992) Computation of unsteady incompressible flows with the finite element methods-space–time formulations, iterative strategies and massively parallel implementations. In: New methods in transient analysis, PVP-Vol. 246/AMD-Vol. 143. ASME, New York, pp 7–24
77. Tezduyar TE, Aliabadi S, Behr M, Johnson A, Mittal S (1993) Parallel finite-element computation of 3D flows. Computer 26(10): 27–36
78. Tezduyar TE, Sathe S, Keedy R, Stein K (2006a) Space–time finite element techniques for computation of fluid–structure interactions. Comput Methods Appl Mech Eng 195(17–18):2002–2027
79. Tezduyar TE, Sathe S, Stein K (2006b) Solution techniques for the fully-discretized equations in computation of fluid–structure interactions with the space–time formulations. Comput Methods Appl Mech Eng 195:5743–5753
80. Thiele U, Archer AJ, Robbins MJ, Gomez H, Knobloch E (2013) Localized states in the conserved Swift–Hohenberg equation with cubic nonlinearity. Phys Rev E 87(4):042915
81. Turner SE (2007) Underwater implosion of glass spheres. J Acoust Soc Am 121(2):844–852
82. van der Waals JD (1979) The thermodynamic theory of capillarity under the hypothesis of a continuous variation of density. J Stat Phys 20(2):200–244
83. Vilanova G, Colominas I, Gomez H (2013) Capillary networks in tumor angiogenesis: from discrete endothelial cells to phase-field averaged descriptions via isogeometric analysis. Int J Numer Methods Biomed Eng 29(10):1015–1037
84. Zhang Y, Bazilevs Y, Goswami S, Bajaj CL, Hughes TJR (2007) Patient-specific vascular NURBS modeling for Isogeometric Analysis of blood flow. Comput Methods Appl Mech Eng 196(2930):2943–2959

C Paper #3: "Droplet motion driven by tensotaxis"

Extreme Mechanics Letters 13 (2017) 10–16

Contents lists available at ScienceDirect

Extreme Mechanics Letters

journal homepage: www.elsevier.com/locate/eml

Droplet motion driven by tensotaxis

Jesus Bueno [a,*], Yuri Bazilevs [b], Ruben Juanes [c], Hector Gomez [d]

[a] Departamento de Métodos Matemáticos e de Representación, Universidade da Coruña. Campus de Elviña, 15192, A Coruña, Spain
[b] Department of Structural Engineering, University of California, San Diego. 9500 Gilman Drive, La Jolla, CA 92093, USA
[c] Department of Civil and Environmental Engineering, Massachusetts Institute of Technology. 77 Massachusetts Avenue, Cambridge, MA 02139, USA
[d] School of Mechanical Engineering, Purdue University, 585 Purdue Mall, West Lafayette, IN 47907, USA

ARTICLE INFO

Article history:
Received 26 November 2016
Received in revised form
10 January 2017
Accepted 10 January 2017
Available online 12 January 2017

Keywords:
Tensotaxis
Soft materials
Fluid–structure interaction (FSI)
Complex fluids
Navier–Stokes–Korteweg equations (NSK)
Isogeometric analysis (IGA)

ABSTRACT

It is well documented that cells can migrate in response to gradients in stiffness (durotaxis) and gradients in strain (tensotaxis) in the underlying substrate. Understanding the potential physical mechanisms at play during this motion has motivated recent efforts to unravel the role of surface tension in the interaction between droplets and soft solids. Here, we present a multiphysics phase-field model of fluid–solid interaction, which allows us to isolate the effects of strain gradients—something difficult to achieve in experiments. Our high-fidelity numerical simulations in two and three dimensions elucidate the physics of tensotaxis, and show how localized forces in a soft substrate can be used to move and merge droplets deposited on it.

1. Introduction

Understanding wetting – the affinity of a solid to a fluid – is essential in many natural and engineered processes spanning a wide range of length and time scales, including microfabrication [1,2], microfluidics [3–5], and porous media flow applications like oil recovery [6,7] and geologic carbon sequestration [8]. While wetting and spreading of fluids on rigid substrates has been studied extensively (e.g., [9,10]), the interaction of a partially-wetting fluid with a deformable solid substrate has started to receive attention more recently [11–17]. In particular, detailed measurements using confocal microscopy have revealed the universal character of the deformation of soft substrates near the contact line [13], and theory and experimental observation have elucidated important aspects of the interaction between droplets and soft substrates. For example, it was recently shown that liquid drops on deformable substrates attract or repel by the so-called inverted Cheerios effect [18], and that droplets move spontaneously on substrates with stiffness variations [19]. The latter phenomenon is reminiscent of durotaxis—cell motion along stiffness gradients [20,21]. However, while cells tend to move toward stiffer substrates, droplets have been reported to migrate toward softer regions. This observation has rekindled the debate about the role of mechanics in cell durotaxis.

It has also been observed that cells undergo tensotaxis, that is, motion along strain gradients. Tensotaxis has been consistently observed for fibroblasts which migrate toward areas of higher compressive strains [20]. While several mechanistic models have been proposed [22,23], the understanding of tensotaxis is still very limited. Controlled experimental studies of tensotaxis are particularly challenging because prestraining the substrate is often accompanied by an increase in the substrate stiffness as a result of nonlinear material response [24], thus producing a combination of tensotaxis and durotaxis. A theoretical model that allows isolating the effects of tensotaxis would contribute to a better understanding of the process.

Here, we show that liquid droplets on soft substrates undergo tensotaxis. Droplets move toward areas of higher compressive strains, the same behavior observed in cell migration. Our methodology is based on a theoretical model that describes the coupled interaction of a solid and a fluid with liquid and gaseous phases. We solve the governing equations by means of high-fidelity numerical simulations, and show that tensotaxis enables the motion and merging of droplets. The migration patterns depend on the solid deformation globally, thus pointing to the usefulness of a computational approach to help elucidate the physics of tensotaxis.

* Corresponding author.
E-mail address: jesus.bueno@udc.es (J. Bueno).

http://dx.doi.org/10.1016/j.eml.2017.01.004
2352-4316/

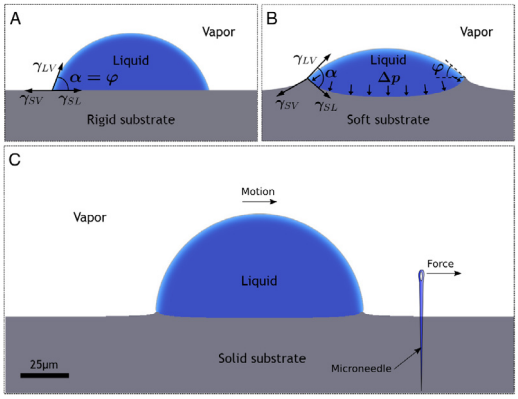

Fig. 1. Droplet motion driven by tensotaxis. (A) Liquid droplet (blue) deposited on a rigid substrate (gray). The surface tensions at the contact line γ_{LV}, γ_{SV} and γ_{SL} are represented with arrows. (B) Liquid droplet on a soft substrate. The solid is deformed under the combined action of the surface tensions and the internal Laplace pressure Δp. The plot shows that the static contact angle α and the apparent contact angle φ are different when the solid is deformable. (C) Tensotaxis can be triggered by inserting a microneedle in the substrate and moving it toward the droplet or away from the droplet. The deformation produced by the droplet has been computed using the model presented in Section 2.1. The computational domain $\Omega = [0, 1.0] \times [0, 0.5]$ is discretized with a uniform mesh of 512×256 $\mathcal{C}^1$-quadratic elements. We have adopted the parameters $\nu = 0.45$, $\widehat{\mu} = 1/1024$, $\widehat{\gamma} = 1/512$, $\widehat{E} = 0.1$, and $\widehat{\theta} = 0.39$. Neither gravity nor other external forces were considered in this simulation, i.e., $|\widehat{\boldsymbol{f}}^s| = 0.0$. (For interpretation of the references to color in this figure legend, the reader is referred to the web version of this article.)

2. Model of droplet tensotaxis

The static configuration that droplets adopt on rigid, flat substrates is governed by the Young–Dupré equation, $\gamma_{SL} + \gamma_{LV}\cos\alpha = \gamma_{SV}$, where α is the static contact angle, and γ_{LV}, γ_{SV} and γ_{SL} denote the interfacial tension at the liquid–vapor, solid–vapor and solid–liquid interfaces, respectively [25] [Fig. 1(A)]. When the substrate is soft, elastocapillary forces create a dimple below the droplet and a ridge at the contact line. This produces a rotation of the liquid–vapor interface [13], which after deformation is oriented at an apparent contact angle $\varphi < \alpha$ with respect to the horizontal [Fig. 1(B)]. Elastocapillary forces are relevant when the elastocapillary length $l_{ec} = \gamma_{LV}/E^s$ (E^s is the Young modulus of the solid) is comparable to the droplet radius. For values of l_{ec} much smaller than the droplet radius, the deformation of the solid is negligible. Most theoretical efforts to understand the interaction of droplets and deformable substrates are based on thin film descriptions of the fluid problem and linear elastic solids [12,18]. The approaches are variational and allow computing a minimum-energy configuration. Here, we study the interaction between droplets and a soft solid by developing a three-dimensional model that couples the nonlinear dynamics of a solid with a fluid composed of a liquid and a gaseous phase. We obtain numerical solutions to the proposed equations with a computational method based on isogeometric analysis [26]. Using this computational approach, we show that droplet tensotaxis emerges in a system that mimics the one employed in cell locomotion experiments [20]. A microneedle is inserted into the substrate and exerts a force either toward the droplet or away from the droplet [Fig. 1(C)]. The droplet moves in the direction of the force applied by the needle.

2.1. Methods

We develop a fluid–structure interaction model that couples a Saint Venant–Kirchhoff solid with a complex fluid. Our choice of a Saint Venant–Kirchhoff model for the solid allows us to consider geometric nonlinearities with a linear material response. As a consequence, the strains introduced in the substrate to trigger tensotaxis do not alter the stiffness of the solid, avoiding a situation with simultaneous tensotaxis and durotaxis. The fluid is governed by the Navier–Stokes–Korteweg (NSK) equations, a phase-field theory that allows for the stable coexistence of a liquid and a gaseous phase.

Solid mechanics equations

The solid dynamics is described by the Lagrangian form of the momentum balance equation

$$\rho_0^s \left.\frac{\partial^2 \boldsymbol{u}}{\partial t^2}\right|_{\boldsymbol{X}} = \nabla_{\boldsymbol{X}} \cdot \boldsymbol{P} + \rho_0^s \boldsymbol{f}^s, \tag{1}$$

where $\nabla_{\boldsymbol{X}}$ is the gradient with respect to the material coordinates $\boldsymbol{X}$ and $|_{\boldsymbol{X}}$ indicates that the time derivative is taken by holding $\boldsymbol{X}$ fixed; $\boldsymbol{u}$ is the solid displacement and ρ_0^s is the mass density in the initial configuration; $\boldsymbol{f}^s$ represents body forces per unit mass, and $\boldsymbol{P}$ is the first Piola–Kirchhoff stress tensor. The Saint Venant–Kirchhoff model is described by the stored elastic energy density [27,28]

$$W = \frac{\lambda^s}{2}(\mathrm{tr}(\boldsymbol{E}))^2 + \mu^s \,\mathrm{tr}(\boldsymbol{E}^2). \tag{2}$$

Here, $\mathrm{tr}(\cdot)$ denotes the trace operator whereas λ^s and μ^s are the first and second Lamé parameters, which can be written as a function of the Young modulus E^s and the Poisson ratio ν: $\lambda^s = \nu E^s/((1+\nu)(1-2\nu))$ and $\mu^s = E^s/(2(1+\nu))$. The Green–Lagrange strain tensor is defined by $\boldsymbol{E} = (\boldsymbol{C}-\boldsymbol{I})/2$, where $\boldsymbol{I}$ denotes the identity tensor and $\boldsymbol{C} = \boldsymbol{F}^T\boldsymbol{F}$ is the Cauchy–Green deformation tensor. Here, $\boldsymbol{F}$ denotes the deformation gradient, i.e., $\boldsymbol{F} = \boldsymbol{I} + \nabla_X \boldsymbol{u}$. The second Piola–Kirchhoff stress tensor can be computed from W as $\boldsymbol{S} = \partial W/\partial \boldsymbol{E}$ while the first Piola–Kirchhoff stress tensor is obtained by $\boldsymbol{P} = \boldsymbol{F}\boldsymbol{S}$. The Cauchy stress tensor in the solid is given by $\boldsymbol{\sigma}^s = J^{-1}\boldsymbol{F}\boldsymbol{S}\boldsymbol{F}^T = J^{-1}\boldsymbol{P}\boldsymbol{F}^T$, where $J = \det(\boldsymbol{F})$.

Fluid mechanics equations

We use the isothermal Navier–Stokes–Korteweg (NSK) equations to describe the fluid dynamics. The NSK equations account for mass and momentum conservation. They describe single-component two-phase flow and naturally allow for phase transformations, which can happen spontaneously due to pressure and/or temperature variations. The multiphase nature of the flow is treated using the phase-field method. Phase-field models, also known as diffuse-interface models, represent an alternative to sharp-interface models, in which interfaces are replaced by thin transition regions. The underlying idea is to define an order parameter, or phase-field, that varies smoothly over the entire computational domain and acts as a marker for the location of the different phases [29]. In the NSK theory, the fluid density itself is the phase-field that identifies the liquid and vapor phases. Phase-field models have been successfully used in many fields (e.g., [30–35]), including the description of partial wetting [36,37]. The phase-field modeling permits, in our case, a unified and efficient computational treatment of the coupled multiphysics problem.

In the Eulerian description, the isothermal NSK equations are given by

$$\frac{\partial \rho}{\partial t} + \nabla \cdot (\rho \boldsymbol{v}) = 0, \tag{3a}$$

$$\frac{\partial (\rho \boldsymbol{v})}{\partial t} + \nabla \cdot (\rho \boldsymbol{v} \otimes \boldsymbol{v}) - \nabla \cdot \boldsymbol{\sigma}^f = 0, \tag{3b}$$

where ρ is the density, $\boldsymbol{v}$ is the velocity vector, $\boldsymbol{\sigma}^f$ is the fluid stress tensor and $\otimes$ denotes the outer vector product. The Cauchy stress tensor for the fluid is defined as $\boldsymbol{\sigma}^f = \boldsymbol{\tau} - p\boldsymbol{I} + \varsigma$, where $\boldsymbol{\tau}$ is the viscous stress tensor, p denotes the pressure, and ς is the so-called

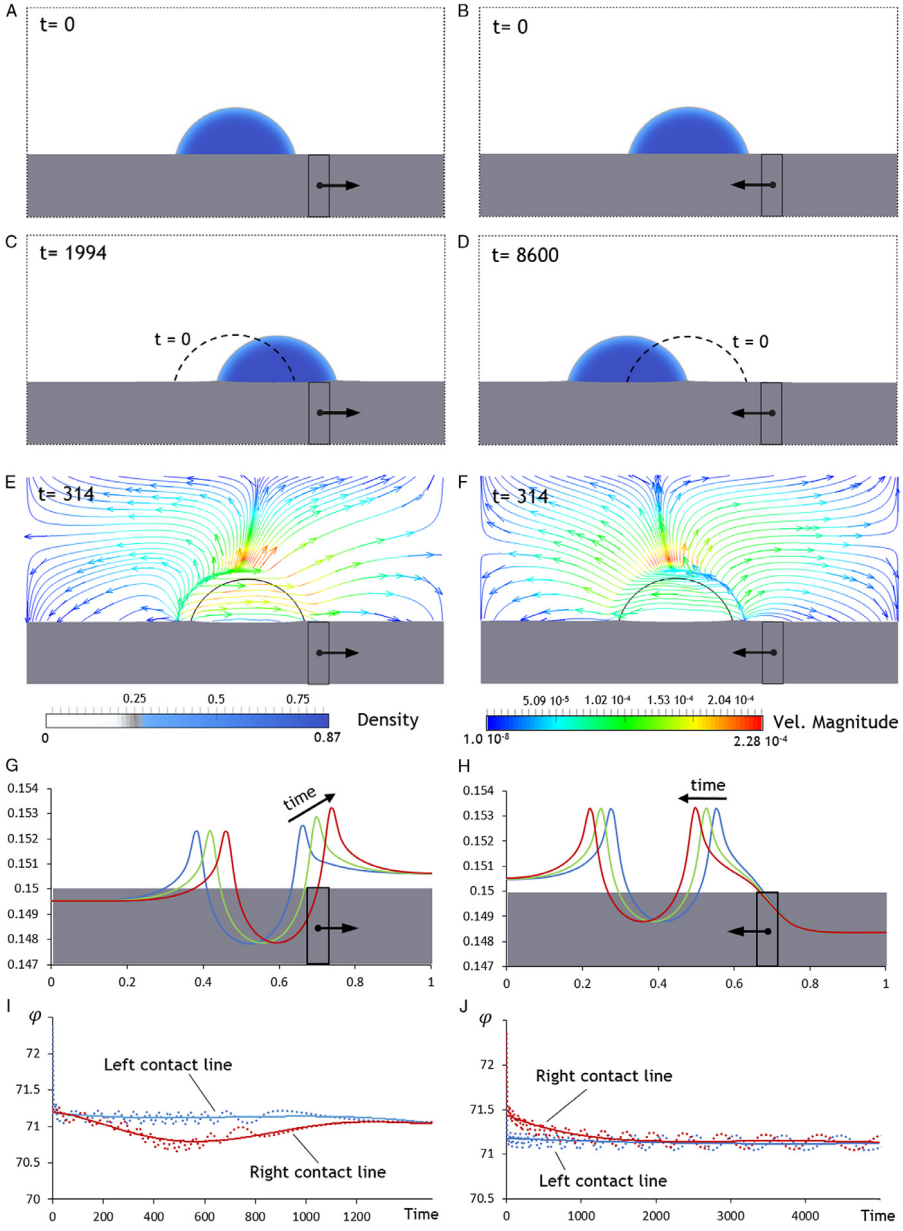

Fig. 2. Mechanism of tensotaxis. Left panels refer to the case in which the applied force pulls the droplet. Right panels refer to case in which the applied force pushes the droplet. (A) and (B) Initial configuration of a droplet on a deformable substrate. We apply a force per unit mass that points away from the droplet (A) and toward the droplet (B) in the marked rectangular region. (C) and (D) The droplet moves in the direction of the applied force. The dashed black line represents the position of the droplet at the initial time. (E) and (F) Streamlines of the fluid velocity colored with the velocity magnitude. The droplet is represented by a black, solid line. (G) Vertical displacements at the fluid–solid interface at three different dimensionless times, $t = 235$, $t = 471$ and $t = 1884$. (H) Vertical displacements at the fluid–solid interface at time $t = 1962$, $t = 3924$ and $t = 7848$. (I) and (J) Time evolution of the apparent contact angles at the left (blue dashed line) and right (red dashed line) contact lines of the droplet. Trend lines are plotted using a blue and red solid lines, respectively. The difference in apparent contact angles between the two contact lines is responsible for the motion of the droplet. The computational domain is the rectangle $\Omega = [0, 1.0] \times [0, 0.5]$, which is discretized with a uniform mesh of 128×64 $\mathcal{C}^1$-quadratic elements. On the left, right and lower boundaries of the computational domain, we impose zero velocity in normal direction. On the upper boundary, zero velocity is imposed in both directions. The static contact angle is $\alpha = 75°$. We have used the parameters $\nu = 0.45$, $\widehat{\mu} = 1/256$, $\widehat{\gamma} = 1/64$, $\widehat{E} = 0.7554$, and $\widehat{\theta} = 0.39$. The magnitude of the force applied on the substrate is $\left|\widehat{\boldsymbol{f}}^s\right| = 0.16215$. (For interpretation of the references to color in this figure legend, the reader is referred to the web version of this article.)

Korteweg tensor. As we consider Newtonian fluids, the viscous stress tensor is given by

$$\boldsymbol{\tau} = \bar{\mu}\left(\nabla \boldsymbol{v} + \nabla^T \boldsymbol{v}\right) + \bar{\lambda}\nabla \cdot \boldsymbol{v}\boldsymbol{I}, \tag{4}$$

where $\bar{\mu}$ and $\bar{\lambda}$ are the viscosity coefficients, which are assumed to be related through the Stokes hypothesis, that is, $\bar{\lambda} = -2\bar{\mu}/3$. The Korteweg tensor [38,39] is defined by

$$\boldsymbol{\varsigma} = \lambda\left(\rho\Delta\rho + \frac{1}{2}|\nabla\rho|^2\right)\boldsymbol{I} - \lambda\nabla\rho \otimes \nabla\rho, \tag{5}$$

where $|\cdot|$ denotes the Euclidean norm of a vector, and $\lambda > 0$ is the capillarity coefficient. The Korteweg tensor results in the capillary forces that are withstood by the liquid–vapor interfaces.

We use the Helmholtz free-energy of a van der Waals fluid [40, 41] to allow for stable coexistence of liquid and gas phases. Using the Helmholtz free-energy and standard thermodynamics [41], we obtain the van der Waals equation, which gives the pressure p in terms of density and temperature θ, i.e.,

$$p = Rb\left(\frac{\rho\theta}{b - \rho}\right) - a\rho^2. \tag{6}$$

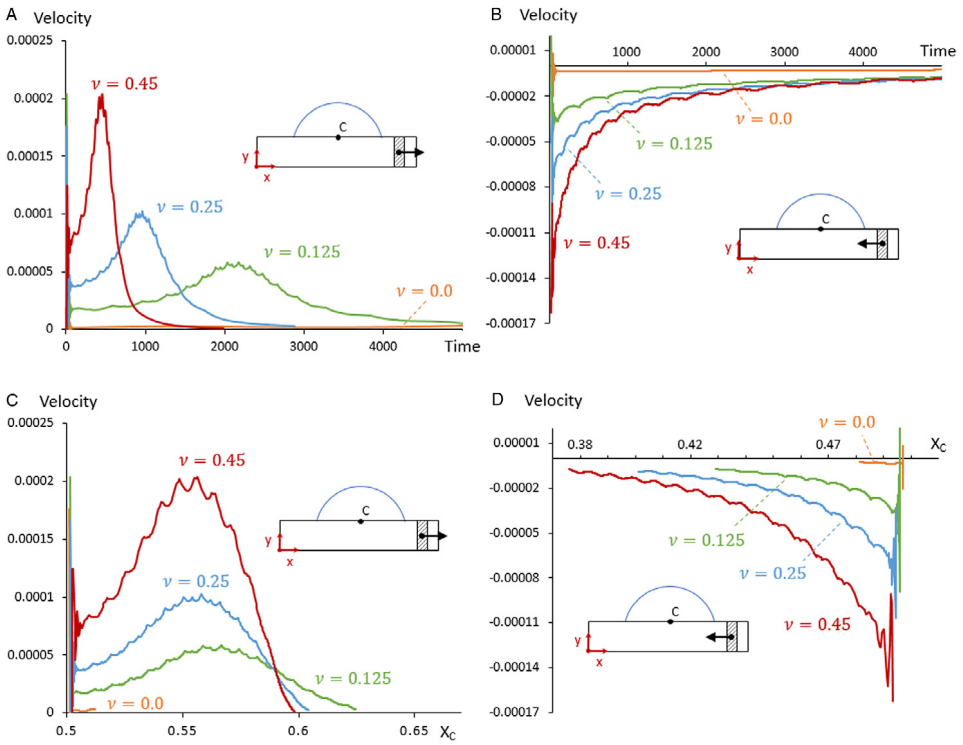

Fig. 3. Pulling and pushing the droplet. Left panels refer to the case in which the applied force pulls the droplet. Right panels refer to case in which the applied force pushes the droplet. (A) and (B) Droplet velocity with respect to time for different Poisson's ratios ν. The velocity of the droplet is computed as the average of the contact line velocities. When pulling, the droplet initially accelerates and then decelerates as it passes through the localized applied force, and is eventually trapped (A). When pushing, the magnitude of the velocity is monotonically decreasing as the influence of the applied force decreases as the droplet moves away from the force (B). (C) and (D) Droplet velocity with respect to the position of the droplet center X_c, which is assumed to be at the midpoint between the contact line positions at each time step. In all cases the velocity is reduced as the Poisson ratio drops, and for $\nu = 0$ the applied force induces no droplet motion.

Here, a and b are positive constants and R is the specific gas constant.

Since the NSK system includes a third-order spatial derivative of the fluid density in the linear momentum balance equation, the classical solid-wall boundary conditions are insufficient to render a well-posed boundary value problem. Therefore, we additionally impose the boundary condition $\nabla\rho \cdot \boldsymbol{n}^f = |\nabla\rho| \cos\alpha$, where $\boldsymbol{n}^f$ denotes the unit outward normal to the fluid boundary, and α is the contact angle between the liquid–vapor interface and the solid surface, measured in the liquid phase (see Fig. 1). This boundary condition prescribes the contact angle α at the fluid–structure interface, while the apparent contact angle φ is determined as part of the solution to the coupled equations as a result of the substrate deformation.

Coupled problem

The differential equations governing the solid and fluid motions must be satisfied simultaneously. These equations are coupled at the fluid–solid interface through compatibility conditions. We impose kinematic compatibility ($\boldsymbol{v} = \partial\boldsymbol{u}/\partial t$) and traction balance ($\boldsymbol{\sigma}^f\boldsymbol{n}^f - \boldsymbol{\sigma}^s\boldsymbol{n}^f = 0$).

Computational method

Our computational approach is similar to those presented in [42,43]. We solve the coupled system composed by Eqs. (1) and (3) subject to the kinematic compatibility and traction balance constraints. Eq. (1) is solved in the reference (undeformed) configuration of the solid domain. Eq. (3) is solved in the spatial domain occupied by the fluid, which changes over time. This requires the use of geometrically flexible algorithms, such as the finite element method. Here, we use isogeometric analysis, which is a spline-based finite-element-like method that combines geometric flexibility with smooth basis functions [44,26]. The use of smooth basis functions allows for a direct discretization of higher-order partial differential equations such as the NSK equation. To enable the use of classical finite-difference-type methods for time integration, we recast the NSK equations in an arbitrary Lagrangian Eulerian (ALE) formulation:

$$\left.\frac{\partial\rho}{\partial t}\right|_{\widehat{\boldsymbol{x}}} + (\boldsymbol{v} - \widehat{\boldsymbol{v}}) \cdot \nabla\rho + \rho\nabla \cdot \boldsymbol{v} = 0, \tag{7a}$$

$$\rho\left.\frac{\partial\boldsymbol{v}}{\partial t}\right|_{\widehat{\boldsymbol{x}}} + \rho\,(\boldsymbol{v} - \widehat{\boldsymbol{v}}) \cdot \nabla\boldsymbol{v} - \nabla \cdot \boldsymbol{\sigma}^f = 0. \tag{7b}$$

Here, $\widehat{\boldsymbol{v}}$ is the fluid domain velocity and $\widehat{\boldsymbol{x}}$ is a coordinate in a reference domain that is used for computational purposes. Eqs. (1) and (7) can then be written in variational form and discretized in space using isogeometric analysis. We use the generalized-α method [45] as a time integration scheme. The nonlinear system of equations is solved using a Newton–Raphson iteration procedure, which leads to a two-stage predictor–multicorrector algorithm. The resulting linear system is solved using a preconditioned GMRES method.

We express the problem in non-dimensional form by rescaling length, time, mass and temperature by L_0, $L_0/\sqrt{ab}$, bL_0^3 and θ_c, respectively, where $L_0 = 1$ is a length scale of the computational domain and $\theta_c = 8ab/(27R)$ is the so-called critical temperature. Using this non-dimensionalization, the problem is characterized by the following dimensionless numbers,

$$\widehat{\gamma} = \frac{\sqrt{\lambda/a}}{L_0} \quad \text{(dimensionless surface tension)}, \tag{8}$$

$$\widehat{\mu} = \frac{\bar{\mu}}{L_0 b\sqrt{ab}} \quad \text{(dimensionless viscosity)}, \tag{9}$$

$$\widehat{\theta} = \frac{\theta}{\theta_c} \quad \text{(dimensionless temperature)}, \tag{10}$$

$$\nu \quad \text{(Poisson ratio)}, \tag{11}$$

$$\widehat{E} = \frac{E^s}{\rho_0^s ab} \quad \text{(dimensionless Young modulus)}, \tag{12}$$

$$\widehat{\boldsymbol{f}}^s = \frac{\boldsymbol{f}^s}{ab/L_0} \quad \text{(dimensionless body force)}. \tag{13}$$

In all our computations, the values adopted for the dimensionless surface tension and viscosity were chosen according to the upscaling method proposed in [46], which relates these parameters to the computational mesh.

3. Results

We begin by performing numerical simulations of droplet motion that mimic the experiments conducted for cells [Fig. 1(C)]. In our computations, the effect of the needle is modeled as a horizontal force per unit mass applied on a localized area [Fig. 2(A)–(B)]. Our simulations show that the droplet moves in the direction of the force [Fig. 2(C)–(D)]. The coupling between solid and fluid elicits flow of the gas phase surrounding the droplet [Fig. 2(E)–(F)]. The applied load produces vertical displacements in the solid, as it would be expected in a material with a nonzero Poisson ratio [Fig. 2(G)–(H)]. These vertical displacements are opposite in sign at each side of the load. The droplet's excess pressure produces a depression of the substrate, while the localized force at the contact line pulls up the solid. Away from the droplet the substrate acquires a flat shape, but the vertical displacement is different at both sides of the droplet and is controlled by the external force applied to the substrate: positive where the load induces compressive stresses, and negative on the side where the load induces tensile stresses. The difference in vertical displacements at either side of the droplet produces a rotation of the droplet that drives motion. This can be understood with a force balance in the deformed contact line, which is rotated due to the solid compliance [13]. The solid deformation produces different apparent contact angles at the two contact lines, leading to an unbalanced horizontal force similar to that present when the wettability of the substrate is different at either contact line [Fig. 2(I)–(J)]. The tensotaxis mechanism is independent of gravity, which is negligible at this scale.

Further insight into the mechanics of tensotaxis is gained by plotting the droplet velocity with respect to time and space (Fig. 3). It is apparent from these simulations that the behavior is remarkably different depending on the direction of the applied force. Pulling induces increasing velocities of the droplet as the contact line approaches the region of the applied force, but ultimately trap the droplet in the loaded area [Fig. 3(A) and (C)]. In contrast, pushing repels the droplet monotonically, albeit with a time-decreasing velocity [Fig. 3(B) and (D)]. In all cases, the droplet velocity is smaller as the Poisson ratio decreases—indeed, the droplet remains immobile if the Poisson ratio is zero. All these observations are consistent with the proposed mechanism of droplet tensotaxis.

To more faithfully represent the physical reality we also carried out 3D simulations of tensotaxis. The 3D analogue of the needle experiment in Fig. 1(C) is shown in Fig. 4. A horizontal force applied at the center of the substrate drives droplet motion in the direction of the force [Fig. 4(B)]. A cross section of the system through the (diagonal) axis of symmetry shows that the substrate deformation is consistent with the picture that emerges from the 2D simulations [Fig. 4(C)].

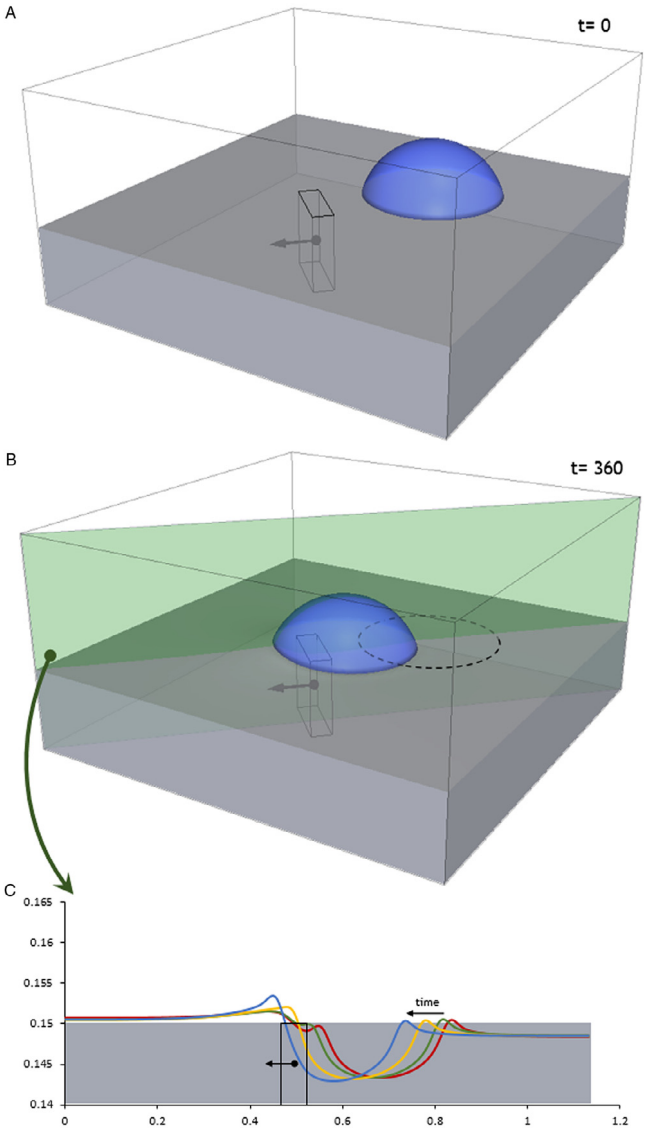

Fig. 4. Three-dimensional droplet motion triggered by tensotaxis. (A) Initial configuration of the numerical experiment. A liquid droplet is deposited on a deformable substrate. A horizontal force is applied at the center of the substrate. (B) The droplet moves in the direction of the applied force. The black, dashed line on the surface of the substrate indicates the initial position of the droplet. (C) Vertical displacement of the solid–liquid interface at the diagonal plane [green color in panel (B)] at different times, $t = 63$ (red), $t = 125$ (green), $t = 188$ (yellow), and $t = 251$ (blue). The computational domain $\Omega = [0, 0.8] \times [0, 0.8] \times [0, 0.4]$ is discretized with $80 \times 80 \times 40$ $\mathcal{C}^1$-quadratic elements. On the upper boundary, we prescribe zero velocity in the horizontal and vertical directions. On the lateral and lower boundaries, zero velocity is imposed in normal direction. We have adopted $\nu = 0.45$, $\widehat{\mu} = 1/200$, $\widehat{\gamma} = 1/50$, $\widehat{E} = 0.7554$, and $\widehat{\theta} = 0.39$. The load that triggers droplet motion is a body force per unit mass of value $|\widehat{\boldsymbol{f}}^s| = 1.376$. The static contact angle is $\alpha = 75°$. (For interpretation of the references to color in this figure legend, the reader is referred to the web version of this article.)

The investigation of tensotaxis behavior in the presence of multiple droplets is revealing. The presence of multiple droplets increases the complexity of the problem, as we must consider their mechanical interactions through the deformable substrate, as well as through the fluid domain. We simulate this interaction in a system with two droplets of different size, each "pushed" toward the other by the action of a localized force [Fig. 5(A)]. As the droplets approach each other, they eventually coalesce [Fig. 5(B)] and quickly readjust into a single droplet, trapped by the two applied forces of opposite sign [Fig. 5(C)]. These predictions illustrate the ability of the phase-field methodology to simulate complex

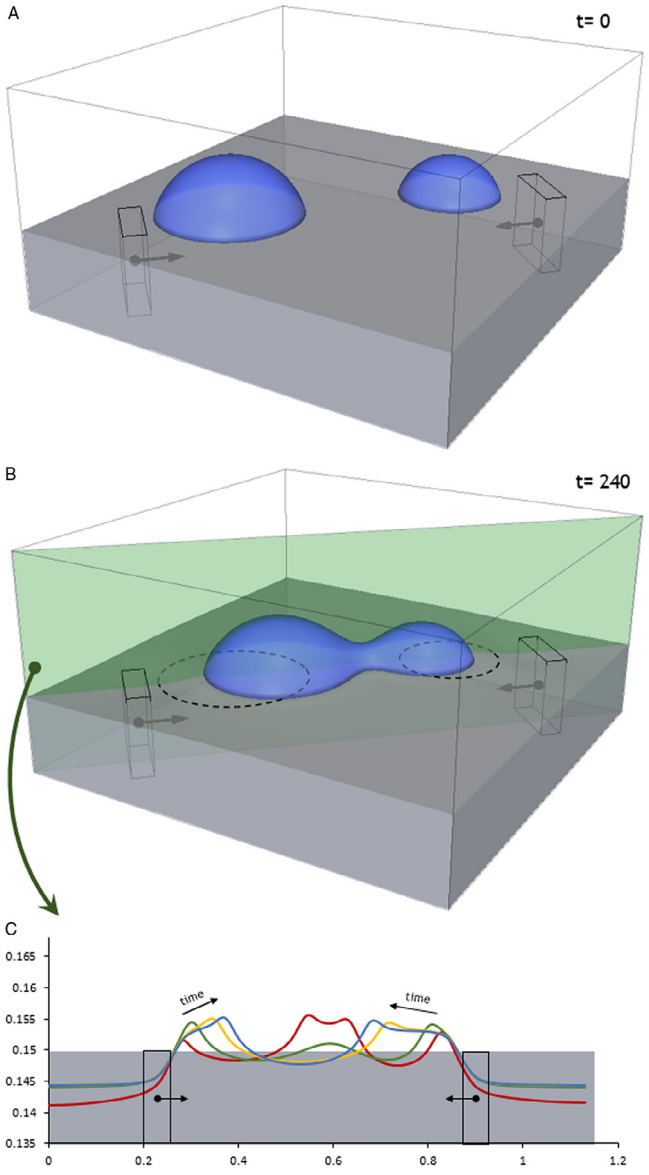

Fig. 5. Droplet coalescence induced by tensotaxis. (A) Setup of the numerical experiment. Two forces of the same magnitude are applied on the substrate, pushing the droplets toward the center of the domain. (B) When the droplets are sufficiently close, capillary forces promote coalescence of the two droplets. The black, dashed line on the surface of the substrate represents the initial position of the droplets. (C) Vertical displacement at the solid–fluid interface at different times, $t = 66$ (red), $t = 240$ (green), $t = 267$ (yellow), and $t = 314$ (blue). The computational domain is the box $\Omega = [0, 0.8] \times [0, 0.8] \times [0, 0.4]$, which is comprised of $80 \times 80 \times 40$ $\mathcal{C}^1$-quadratic elements. On the lateral and lower boundaries, we impose zero velocity in normal direction. On the upper boundary, zero velocity is prescribed in the horizontal and vertical directions. We have adopted $\nu = 0.45$, $\widehat{\mu} = 1/200$, $\widehat{\gamma} = 1/50$, $\widehat{E} = 0.7554$, and $\widehat{\theta} = 0.39$. The load that triggers droplet motion is a body force per unit mass of value $\left|\widehat{\boldsymbol{f}}^s\right| = 2.7519$. The static contact angle is $\alpha = 75°$. (For interpretation of the references to color in this figure legend, the reader is referred to the web version of this article.)

scenarios of tensotaxis in 3D, in which the coupling between surface tension forces and substrate deformation lead to droplet motion, coalescence and trapping.

4. Conclusions

Tensotaxis, or motion driven by strain gradients, has been reproducibly observed for several cell types, but the mechanisms that control the process remain unknown. Here, we have shown that simple liquid droplets on soft substrates also undergo tensotaxis. We have used a nonlinear coupled model of fluid–structure interaction to elucidate the physics of droplet tensotaxis. Our results indicate that droplet tensotaxis is controlled by the global deformation of the solid, making the migration pattern sensitive to boundary conditions and additional external loads. Although the droplet always moves in the direction of the force – as observed in cell locomotion experiments – our results reveal the symmetry-breaking depending on the nature of the applied force. Upon the action of pulling forces, a droplet first accelerates but is then trapped as it traverses the localized force. The action of pushing forces, in contrast, leads to monotonic motion of the droplet with decaying velocity. The computational model suggests that droplet tensotaxis occurs for arbitrary values of the applied force, while cell tensotaxis has been only observed for loads that are larger than a threshold value. This might be a consequence of active contractile forces exerted by the cell on the substrate, which are not considered in droplet tensotaxis. Our computational model also reveals the key role of Poisson's ratio in tensotaxis, and the ability of localized forces to induce droplet coalescence. These observations from computational modeling allow us to gain insight into the mechanisms that govern tensotaxis, and may suggest new experimental studies for cell migration.

Acknowledgments

HG was partially supported by the European Research Council through the FP7 Ideas Starting Grant Program (Contract #307201). HG and JB were partially supported by Xunta de Galicia, co-financed with FEDER funds. JB is grateful to the Ph.D. student grant UDC-Inditex for the financial support during his visit at the University of California, San Diego, where part of this work was accomplished. RJ acknowledges support from the US Department of Energy through a DOE Mathematical Multifaceted Integrated Capability Center Award (Grant No. DE-SC0009286).

References

[1] M. Srinivasarao, D. Collings, A. Philips, S. Patel, Three-dimensionally ordered array of air bubbles in a polymer film, Science 292 (5514) (2001) 79–83.
[2] D.B. Weibel, W.R. DiLuzio, G.M. Whitesides, Microfabrication meets microbiology, Nat. Rev. Microbiol. 5 (2007) 209–218.
[3] P. Tabeling, S. Chen, Introduction to Microfluidics, Oxford University Press, 2005.
[4] T.M. Squires, S.R. Quake, Microfluidics: Fluid physics at the nanoliter scale, Rev. Modern Phys. 77 (3) (2005) 977–1026.
[5] B. Zhao, C.W. MacMinn, R. Juanes, Wettability control on multiphase flow in patterned microfluidics, Proc. Natl. Acad. Sci. 113 (37) (2016) 10251–10256.
[6] D.C. Standnes, T. Austad, Wettability alteration in carbonates: Interaction between cationic surfactant and carboxylates as a key factor in wettability alteration from oil-wet to water-wet conditions, Colloids Surf. A 216 (2003) 243–259.
[7] M. Trojer, M.L. Szulczewski, R. Juanes, Stabilizing fluid-fluid displacements in porous media through wettability alteration, Phys. Rev. Appl. 3 (2015) 054008.
[8] P. Chiquet, D. Broseta, S. Thibeau, Wettability alteration of caprock minerals by carbon dioxide, Geofluids 7 (2) (2007) 112–122.
[9] P.G. de Gennes, Wetting: statics and dynamics, Rev. Modern Phys. 57 (1985) 827–863.
[10] D. Bonn, J. Eggers, J. Indekeu, J. Meunier, E. Rolley, Wetting and spreading, Rev. Mod. Phys. 81 (2009) 739–805.
[11] C. Duprat, S. Protiere, A.Y. Beebe, H.A. Stone, Wetting of flexible fibre arrays, Nature 482 (7386) (2012) 510–513.
[12] R.W. Style, E.R. Dufresne, Static wetting on deformable substrates, from liquids to soft solids, Soft Matter 8 (27) (2012) 7177–7184.
[13] R.W. Style, R. Boltyanskiy, Y. Che, J.S. Wettlaufer, L.A. Wilen, E.R. Dufresne, Universal deformation of soft substrates near a contact line and the direct measurement of solid surface stresses, Phys. Rev. Lett. 110 (2013) 066103.
[14] T. Kajiya, A. Daerr, T. Narita, L. Royon, F. Lequeux, L. Limat, Advancing liquid contact line on visco-elastic gel substrates: stick–slip vs. continuous motions, Soft Matter 9 (2013) 454–461.
[15] J.B. Bostwick, M. Shearer, K.E. Daniels, Elastocapillary deformations on partially-wetting substrates: rival contact-line models, Soft Matter 10 (2014) 7361–7369.

[16] S. Karpitschka, S. Das, M. Van Gorcum, H. Perrin, B. Andreotti, J. Snoeijer, Droplets move over viscoelastic substrates by surfing a ridge, Nature Commun. 6 (2015) 7891.
[17] B. Andreotti, O. Bäumchen, F. Boulogne, K.E. Daniels, E.R. Dufresne, H. Perrin, T. Salez, J.H. Snoeijer, R.W. Style, Solid capillarity: when and how does surface tension deform soft solids? Soft Matter 12 (12) (2016) 2993–2996.
[18] S. Karpitschka, A. Pandey, L.A. Lubbers, J.H. Weijs, L. Botto, S. Das, B. Andreotti, J.H. Snoeijer, Liquid drops attract or repel by the inverted cheerios effect, Proc. Natl. Acad. Sci. 113 (27) (2016) 7403–7407.
[19] R.W. Style, Y. Che, S.J. Park, B.M. Weon, J.H. Je, C. Hyland, G.K. German, M.P. Power, L.A. Wilen, J.S. Wettlaufer, et al., Patterning droplets with durotaxis, Proc. Natl. Acad. Sci. 110 (31) (2013) 12541–12544.
[20] C.-M. Lo, H.-B. Wang, M. Dembo, Y.-l. Wang, Cell movement is guided by the rigidity of the substrate, Biophys. J. 79 (1) (2000) 144–152.
[21] R. Sunyer, V. Conte, J. Escribano, A. Elosegui-Artola, A. Labernadie, L. Valon, D. Navajas, J.M. García-Aznar, J.J. Muñoz, P. Roca-Cusachs, X. Trepat, Collective cell durotaxis emerges from long-range intercellular force transmission, Science 353 (6304) (2016) 1157–1161.
[22] I.B. Bischofs, U.S. Schwarz, Cell organization in soft media due to active mechanosensing, Proc. Natl. Acad. Sci. 100 (16) (2003) 9274–9279.
[23] P. Moreo, J.M. García-Aznar, M. Doblaré, Modeling mechanosensing and its effect on the migration and proliferation of adherent cells, Acta Biomater. 4 (3) (2008) 613–621.
[24] S.-L. Lin, J.-C. Yang, K.-N. Ho, C.-H. Wang, C.-W. Yeh, H.-M. Huang, Effects of compressive residual stress on the morphologic changes of fibroblasts, Med. Biol. Eng. Comput. 47 (12) (2009) 1273–1279.
[25] P.-G. De Gennes, F. Brochard-Wyart, D. Quéré, Capillarity and Wetting Phenomena: Drops, Bubbles, Pearls, Waves, Springer Science & Business Media, 2004.
[26] J. Cottrell, T. Hughes, Y. Bazilevs, Isogeometric Analysis: Toward Integration of CAD and FEA, Wiley, 2009.
[27] J.E. Marsden, T.J.R. Hughes, Mathematical Foundations of Elasticity, Prentice-Hall, Englewood Cliffs, NJ, 1983, reprinted with corrections, Dover, New York, 1994.
[28] Y. Bazilevs, K. Takizawa, T. Tezduyar, Computational Fluid-Structure Interaction. Methods and Applications, Wiley, 2013.
[29] H. Gomez, K. van der Zee, Encyclopedia of Computational Mechanics. Phase Field Models and Methods, John Wiley & Sons, Ltd., 2016.
[30] G. Caginalp, Stefan and hele-shaw type models as asymptotic limits of the phase-field equations, Phys. Rev. A 39 (1989) 5887–5896.
[31] D.M. Anderson, G.B. McFadden, A.A. Wheeler, Diffuse-interface methods in fluid mechanics, Annu. Rev. Fluid Mech. 30 (1998) 139–165.
[32] J. Jeong, N. Goldenfeld, J. Dantzig, Phase field model for three-dimensional dendritic growth with fluid flow, Phys. Rev. E 64 (2001) 041602.
[33] W.J. Boettinger, J.A. Warren, C. Beckermann, A. Karma, Phase-field simulation of solidification, Annu. Rev. Mater. Res. 32 (2002) 163–194.
[34] T. Biben, K. Kassner, C. Misbah, Phase-field approach to three-dimensional vesicle dynamics, Phys. Rev. E 72 (2005) 041921.
[35] H. Gomez, L. Cueto-Felgueroso, R. Juanes, Three-dimensional simulation of unstable gravity-driven infiltration of water into a porous medium, J. Comput. Phys. 238 (2013) 217–239.
[36] L. Cueto-Felgueroso, R. Juanes, Macroscopic phase-field modeling of partial wetting: bubbles in a capillary tube, Phys. Rev. Lett. 108 (2012) 144502.
[37] A. Alizadeh Pahlavan, L. Cueto-Felgueroso, R. Juanes, Thin films in partial wetting: internal selection of contact-line dynamics, Phys. Rev. Lett. 115 (2015) 034502.
[38] D.J. Korteweg, Sur la forme que prennent les équations du mouvement des fluides si lon tient compte des forces capillaires causées par des variations de densité considérables mais continues et sur la théorie de la capillarité dans lhypothese dune variation continue de la densité, Arch. Néerl. Sci. Exactes Nat. 6 (1) (1901) 6.
[39] J. Dunn, J. Serrin, On the thermomechanics of interstitial working, Arch. Ration. Mech. Anal. 88 (2) (1985) 95–133.
[40] D. Diehl, Higher order schemes for simulation of compressible liquid-vapor flows with phase change (Ph.D. thesis), Albert-Ludwigs-Universitat, 2007.
[41] J. Liu, C.M. Landis, H. Gomez, T.J. Hughes, Liquid-vapor phase transition: Thermomechanical theory, entropy stable numerical formulation, and boiling simulations, Comput. Methods Appl. Mech. Engrg. 297 (2015) 476–553.
[42] J. Bueno, C. Bona-Casas, Y. Bazilevs, H. Gomez, Interaction of complex fluids and solids: Theory, algorithms and application to phase-change-driven implosion, Comput. Mech. 55 (6) (2015) 1105–1118.
[43] Y. Bazilevs, V. Calo, T. Hughes, Y. Zhang, Isogeometric fluid-structure interaction: Theory, algorithms, and computations, Comput. Mech. 43 (1) (2008) 3–37.
[44] T. Hughes, J. Cottrell, Y. Bazilevs, Isogeometric analysis: CAD, finite elements, NURBS, exact geometry and mesh refinement, Comput. Methods Appl. Mech. Engrg. 194 (39–41) (2005) 4135–4195.
[45] J. Chung, G. Hulbert, A time integration algorithm for structural dynamics with improved numerical dissipation: The generalized-α method, J. Appl. Mech. 60 (1993) 371–375.
[46] H. Gomez, T. Hughes, X. Nogueira, V. Calo, Isogeometric Analysis of the isothermal Navier-Stokes-Korteweg equations, Comput. Methods Appl. Mech. Engrg. 199 (25–28) (2010) 1828–1840.

D Paper #4: "Three–dimensional dynamic simulation of elastocapillarity"

Meccanica manuscript No.
(will be inserted by the editor)

Three–dimensional dynamic simulation of elastocapillarity

Jesus Bueno · Hugo Casquero · Yuri Bazilevs · Hector Gomez

Received: date / Accepted: date

Abstract At small scales, the interaction of multicomponent fluids and solids can be dominated by capillary forces giving rise to elastocapillarity. Surface tension may deform or even collapse slender structures and thus, cause important damage in microelectromechanical systems. However, under control, elastocapillarity could be used as a fabrication technique for the design of new materials and structures. Here, we propose a computational model for elastocapillarity that couples nonlinear hyperelastic solids with two–component immiscible fluids described by the Navier–Stokes–Cahn–Hilliard equations. As fluid–structure interaction computational technique, we employ a boundary–fitted approach. For the spatial discretization of the problem we adopt a NURBS–based isogeometric analysis methodology. A strongly–coupled algorithm is proposed for the solution of the problem. The potential of this model is illustrated by solving several numerical examples, including, capillary origami, the static wetting of soft substrates, the deformation of micropillars and the three dimensional wrapping of a liquid droplet.

Keywords Elastocapillarity · Fluid–Structure Interaction (FSI) · Navier–Stokes–Cahn–Hilliard (NSCH) equations · Isogeometric Analysis (IGA) · Arbitrary Lagrangian–Eulerian (ALE) description

J. Bueno (*Corresponding Author*) - H. Casquero
Departamento de Métodos Matemáticos e de Representación,
Universidade da Coruña
Campus de Elviña, 15192, A Coruña, Spain
Tel.: +34-981-167000 Ext.: 5470
E-mail: jesus.bueno@udc.es

Y. Bazilevs
Department of Structural Engineering,
University of California, San Diego
9500 Gilman Drive, La Jolla, CA 92093, USA

H. Gomez
School of Mechanical Engineering,
Purdue University
585 Purdue Mall, West Lafayette, IN 47907, USA

1 Introduction

Multiphase and multicomponent flows have been widely studied [11,48] due to their importance in, e.g., mechanical, environmental and biomedical engineering. However, their mechanical interaction with solids has not received much attention until recently [36,49]. Understanding how these flows interact with solids is crucial to study, for example, cavitation–induced structural damage, phase–change–driven implosion and elastocapillarity. The phenomenon of elastocapillarity, whereby capillary forces at fluid–fluid interfaces deform solids, is particularly intriguing. Elastocapillarity [51,58], can be observed, for example, when water interacts with hair and other flexible fibers, which tend to assemble into bundles [9,29,28]. Another example can be found in our organism, where capillary forces may cause atelectasis [44], that is, the complete or partial collapse of the pulmonary alveoli. However, it is in micro and nanotechnologies, where the effect of elastocapillary forces is sparking greatest interest. Understanding elastocapillarity is essential for the design of new materials and devices at small scales. Capillary forces can damage microelectromechanical structures [50,63] and carbon nanotube carpets [21], but, under control, they can be used as a fabrication technique to deform straight pillars and build complex and robust 3D geometries at the micrometer and nanometer scales [25,65]. A numerical method capable of capturing the physics behind elastocapillary phenomena could become a useful tool for a better design of microfabricated products.

In the last decades, numerous efforts have been devoted to develop numerical methods for Fluid–Structure Interaction (FSI) problems. FSI methods may be classified into two

main groups, namely, boundary-fitted [6,53] and immersed approaches [15,19,42,75]. These methods have been applied to a large variety of problems such as, wind turbines [5, 35], heart valves [43,62], parachutes [55,60], and cell-scale blood flow [16,70] to name a few. However, most of the applications addressed up to now involve classical fluids. The interaction of complex fluids and solids has remained practically unexplored, although there has been recent works involving two–phase fluids [13,12]. In this paper, we propose a model for the interaction of two–component immiscible flows and hyperelastic structures. We use the model to study several elastocapillary problems, including, capillary origami [49], deformation of elastic micropillars [64] and static wetting of soft substrates [57].

Our computational method uses a boundary–fitted approach with a sharp fluid–solid interface. However, our approach to two–component immiscible flows is based on the Navier–Stokes–Cahn–Hilliard (NSCH) equations, which treat the fluid–fluid interface using a phase–field method. Phase–field approaches can be thought of as an alternative to sharp–interface methods in which interfaces are represented by thin transition regions. The key idea is to define an order parameter, or phase–field, that varies smoothly on the entire computational domain and acts as a marker for the location of the different phases. This notably simplifies the numerics compared to sharp–interface methods, although it implies the resolution of an additional equation for the evolution of the order parameter. This equation usually includes higher–order partial–differential operators that are stiff in space and time, and produce thin layers that evolve dynamically over the computational domain. Different strategies have been developed to deal with these computational challenges [31–33] allowing to use phase–field models for a wide range of applications such as, liquid-vapor transformations [14, 45], cancer growth [46,74], tumor angiogenesis [69,71], cell motility [52,47], and dendritic growth [40]. For a thorough discussion on phase-field models, see [34]. The NSCH equations can also be thought of as an extension of the incompressible Navier–Stokes equations to a multicomponent fluid with regularized surface tension. As a consequence, the NSCH model inherits the saddle point nature of the incompressible Navier-Stokes equations. This produces difficulties in the numerics that can be tackled using inf-sup stable discretizations, stabilized formulations or divergence-conforming bases.

In this work, we tackle the computational challenges associated with phase–field models by adopting Isogeometric Analysis (IGA) for the spatial discretization of the problem. IGA is a generalization of the finite element method that was proposed in [37]; see also [23]. IGA started using Non–Uniform Rational B–Splines (NURBS) as basis functions and, subsequently, was generalized to T–Splines (see, for example, [2,4,8,17,18]) and subdivision surfaces [73,72]. In the numerical examples presented here, we have used isogeometric analysis based on NURBS, but our algorithms could be used in conjunction with other types of basis functions. To be able to use equal-order spaces for pressure and velocity in the fluid dynamics equations, we adopt a stabilized formulation for the NSCH equations based on the variational multiscale method (VMS). Regarding the time discretization, we use the generalized–α method [3,22,39].

2 Governing equations

2.1 Kinematics

Let us denote by $\widehat{\boldsymbol{x}}$ the coordinates of a reference domain $\Omega_{\widehat{\boldsymbol{x}}}$, which is fixed in time. We define a function $\widehat{\boldsymbol{\phi}}$ that maps the reference domain $\Omega_{\widehat{\boldsymbol{x}}}$ into its spatial configuration at time t, Ω_t, that is, $\widehat{\boldsymbol{\phi}} : \Omega_{\widehat{\boldsymbol{x}}} \times]0,T[\rightarrow \Omega_t$, where $]0,T[$ is the time interval of interest. We denote by $\boldsymbol{x}$ the coordinates in the spatial configuration, i.e., $\Omega_t \ni \boldsymbol{x} = \widehat{\boldsymbol{\phi}}(\widehat{\boldsymbol{x}},t)$. Using the mapping $\widehat{\boldsymbol{\phi}}$, we can define the displacement of a point in the referential domain $\widehat{\boldsymbol{u}}(\widehat{\boldsymbol{x}},t) = \widehat{\boldsymbol{\phi}}(\widehat{\boldsymbol{x}},t) - \widehat{\boldsymbol{x}}$, and its velocity $\widehat{\boldsymbol{v}} = \partial\widehat{\boldsymbol{\phi}}/\partial t$. Let us also define a material domain $\Omega_{\boldsymbol{X}}$ and the function $\boldsymbol{\phi} : \Omega_{\boldsymbol{X}} \times]0,T[\rightarrow \Omega_t$, which maps each material particle $\boldsymbol{X}$ into its spatial coordinate at time t, that is, $\boldsymbol{x} = \boldsymbol{\phi}(\boldsymbol{X},t)$. From the function $\boldsymbol{\phi}$, we can define the particle displacement $\boldsymbol{u}(\boldsymbol{X},t) = \boldsymbol{\phi}(\boldsymbol{X},t) - \boldsymbol{X}$, its velocity $\boldsymbol{v} = \partial\boldsymbol{\phi}/\partial t = \partial\boldsymbol{u}/\partial t$, and the deformation gradient $\boldsymbol{F} = \partial\boldsymbol{\phi}/\partial\boldsymbol{X}$.

In what follows, we will make use of the Eulerian counterpart of the particle velocity $\boldsymbol{v}$, namely, $\boldsymbol{v} \circ \boldsymbol{\phi}^{-1}$. However, in most cases, we will only use one symbol to denote a physical quantity. Furthermore, to avoid ambiguity in our notation we will use subscripts to clarify how derivatives should be understood. We will adopt the subscript $\boldsymbol{X}$ (respectively, $\widehat{\boldsymbol{x}}$) to indicate that the derivative is taken by holding $\boldsymbol{X}$ (respectively, $\widehat{\boldsymbol{x}}$) fixed. When no subscript is specified, the derivative is assumed to be taken by holding $\boldsymbol{x}$ fixed. For example, $\left.\dfrac{\partial \boldsymbol{v}}{\partial t}\right|_X$ denotes the time derivative of the velocity holding $\boldsymbol{X}$ fixed.

2.2 Governing equations of fluid mechanics

In our model, the dynamics of the two–component fluid system is described by the Navier–Stokes–Cahn–Hilliard equations. The model describes the motion of two immiscible and incompressible fluids with matched density and viscosity. In the Eulerian frame, the equations can be written as

$$\nabla \cdot \boldsymbol{v} = 0, \tag{1a}$$

$$\rho\left(\frac{\partial \boldsymbol{v}}{\partial t} + \boldsymbol{v}\cdot\nabla\boldsymbol{v}\right) - \nabla\cdot\boldsymbol{\sigma}^f - \rho\boldsymbol{f} = 0, \tag{1b}$$

$$\frac{\partial \varphi}{\partial t} + \nabla\cdot(\varphi\boldsymbol{v}) - \nabla\cdot\left(M_\varphi\gamma_f\nabla\left(\frac{1}{\varepsilon}W'_\varphi - \varepsilon\Delta\varphi\right)\right) = 0, \tag{1c}$$

where ρ is the fluid density that we consider to be constant, $\boldsymbol{f}$ represents body forces per unit mass and $\varphi \in [-1,1]$ is the phase–field variable. W_φ is a double–well potential, which we define as $W_\varphi = \left(\varphi^2-1\right)^2/4$. The constant γ_f denotes the surface tension and ε is the interface thickness. M_φ represents the mobility, which is assumed to be constant for the examples presented herein. The fluid Cauchy stress tensor $\boldsymbol{\sigma}^f$ is given by $\boldsymbol{\sigma}^f = \boldsymbol{\tau} - p\boldsymbol{I} - \gamma_f\varepsilon\nabla\varphi\otimes\nabla\varphi$, where $\otimes$ denotes the usual vector outer product, p represents the pressure and $\boldsymbol{\tau}$ is the viscous stress tensor. For incompressible Newtonian fluids, $\boldsymbol{\tau}$ is defined as $\boldsymbol{\tau} = \bar{\mu}\left(\nabla\boldsymbol{v} + \nabla^T\boldsymbol{v}\right)$, where $\bar{\mu}$ is the viscosity coefficient, which is assumed to be constant. A complete derivation of Eqs. (1) from the sharp–interface theory may be found in [34].

2.3 Governing equations of solid mechanics

The behavior of the structure will be described by the momentum balance equation, which can be written in Lagrangian form as

$$\rho_0^s \left.\frac{\partial^2 \boldsymbol{u}}{\partial t^2}\right|_X = \nabla_X\cdot\boldsymbol{P} + \rho_0^s\boldsymbol{f}^s. \tag{2}$$

Here, ρ_0^s is the mass density in the initial configuration, $\boldsymbol{P}$ denotes the first Piola–Kirchhoff stress tensor and $\boldsymbol{f}^s$ represents body forces per unit mass. To completely define the system, we adopt a nonlinear hyperelastic material as constitutive theory. In particular, we use the generalized neo–Hookean model with dilatational penalty proposed in [54]. In this model, the second Piola–Kirchhoff stress tensor is defined as

$$\boldsymbol{S} = \mu J^{-2/d}\left(\boldsymbol{I} - \frac{1}{d}\mathrm{tr}(\boldsymbol{C})\boldsymbol{C}^{-1}\right) + \frac{\kappa}{2}\left(J^2-1\right)\boldsymbol{C}^{-1}, \tag{3}$$

where κ and μ are the material bulk and shear moduli, which can be obtained from the Young modulus E and the Poisson ratio ν^s using the relations $\kappa = E/(3(1-2\nu^s))$ and $\mu = E/(2(1+\nu^s))$; $\boldsymbol{I}$ represents the identity tensor and d is the number of spatial dimensions; $\mathrm{tr}(\cdot)$ denotes the trace operator and J is the determinant of the deformation gradient, that is, $J = \det(\boldsymbol{F})$, where $\boldsymbol{F} = \boldsymbol{I} + \nabla_X\boldsymbol{u}$. Finally, $\boldsymbol{C}$ stands for the Cauchy–Green deformation tensor, i.e., $\boldsymbol{C} = \boldsymbol{F}^T\boldsymbol{F}$. From $\boldsymbol{S}$, the first Piola–Kirchhoff stress tensor can be computed by taking $\boldsymbol{P} = \boldsymbol{F}\boldsymbol{S}$. Let us also define the solid Cauchy stress tensor $\boldsymbol{\sigma}^s = J^{-1}\boldsymbol{F}\boldsymbol{S}\boldsymbol{F}^T = J^{-1}\boldsymbol{P}\boldsymbol{F}^T$.

3 Numerical formulation

3.1 Computational framework

We adopt a boundary–fitted technique with matching discretization at the fluid–structure interface. This choice permits to strongly impose kinematic boundary conditions at the fluid-solid interface and results in more accurate solutions at the fluid–solid interface as long as the mesh does not undergo large distortions. We use the Lagrangian description to derive the semi–discrete form of the solid equations and the Arbitrary Lagrangian–Eulerian (ALE) description [26,27,38] for the fluid domain. This means that the fluid mesh needs to be updated to accommodate the motion of the structure. For this purpose, we solve an additional linear elasticity problem subject to displacement boundary conditions coming from the motion of the solid. In ALE approaches, the partial time derivatives in the governing equations are taken by holding $\widehat{\boldsymbol{x}}$ fixed while the space derivatives are taken with respect to $\boldsymbol{x}$. This particularity enables to use semi–discrete methods, even when the equations are posed on a moving domain [3]. The ALE form of the NSCH equations can be derived using the techniques presented in [6, 27]. This leads to the system

$$\nabla\cdot\boldsymbol{v} = 0, \tag{4a}$$

$$\rho\left(\left.\frac{\partial \boldsymbol{v}}{\partial t}\right|_{\widehat{x}} + (\boldsymbol{v}-\widehat{\boldsymbol{v}})\cdot\nabla\boldsymbol{v}\right) - \nabla\cdot\boldsymbol{\sigma}^f - \rho\boldsymbol{f} = 0, \tag{4b}$$

$$\left.\frac{\partial \varphi}{\partial t}\right|_{\widehat{x}} + (\boldsymbol{v}-\widehat{\boldsymbol{v}})\cdot\nabla\varphi - \nabla\cdot\left(M_\varphi\gamma_f\nabla\left(\frac{1}{\varepsilon}W'_\varphi - \varepsilon\Delta\varphi\right)\right) = 0, \tag{4c}$$

where $\widehat{\boldsymbol{v}}$ is the velocity of the fluid domain [3].

Remark Another boundary–fitted approach that could be adopted as alternative to ALE methods is the space–time technique. This would allow to discretize directly the Eulerian form of the NSCH equations; see [6,7,59,61] for recent advances in space–time methods.

3.2 Computational domain

We will denote by Ω_0 the initial configuration of the fluid and solid domains combined, that is, $\Omega_0 = \overline{\Omega_0^f \cup \Omega_0^s}$, with $\Omega_0^f \cap \Omega_0^s = \emptyset$, where superscripts s and f refer to the solid and the fluid domain, respectively. Ω_0 is adopted as the material and reference configuration. The spatial configuration of Ω_0 at time t is designated as Ω_t, and can also be decomposed as $\Omega_t = \overline{\Omega_t^f \cup \Omega_t^s}$, with $\Omega_t^f \cap \Omega_t^s = \emptyset$. Let us also denote by Γ_0 and Γ_t the fluid–solid interface at the initial and the current configuration, respectively. Γ_0^s and Γ_t^s (Γ_0^f and Γ_t^f) will refer to the boundary of the solid (fluid) domain without the part of the fluid–structure interface.

3.3 Continuous problem in the weak form

3.3.1 Fluid mechanics

In the fluid mechanics problem we focus on solid–wall boundary conditions, by setting the velocity to a given value. Additionally, and with the purpose of attaining well–posedness in the NSCH system, we enforce the following boundary conditions on the phase–field variable,

$$\nabla\varphi\cdot\boldsymbol{n}^f = |\nabla\varphi|\cos(\theta_c) \quad \text{on} \quad \Gamma_t, \tag{5a}$$

$$\nabla\varphi\cdot\boldsymbol{n}^f = 0 \quad \text{on} \quad \Gamma_t^f, \tag{5b}$$

and

$$M_\varphi\gamma_f\nabla\left(\frac{1}{\varepsilon}W'_\varphi - \varepsilon\Delta\varphi\right)\cdot\boldsymbol{n}^f = 0 \quad \text{on} \quad \Gamma_t^f\cup\Gamma_t, \tag{6}$$

where $\boldsymbol{n}^f$ is the unit outward normal to the fluid boundary and θ_c denotes the contact angle between the fluid–fluid interface and the solid, measured in the phase of value $\varphi = 1$. The imposition of boundary condition (5) can be notably simplified by introducing in our problem a new variable $\Upsilon = \Delta\varphi$. This implies that the phase–field equation (4c) is split into two lower–order equations, allowing to use the classical finite element method for the spatial discretization of the problem. Note that this increases the number of degrees of freedom in our problem, resulting in 5 for 2D and 6 for 3D problems

In preparation for the spatial discretization of the fluid dynamics problem, we derive a weak form of Eqs. (4). Let $L^2(\Omega_t^f)$ be the space of scalar–valued functions that are square–integrable on Ω_t^f. We define the trial function space for the pressure variable as

$$\mathscr{X}^p = \left\{ p \mid p\in L^2\left(\Omega_t^f\right), \int_{\Omega_t^f} p\,\mathrm{d}\Omega_t^f = 0 \right\}. \tag{7}$$

The weighting function space for the pressure variable $\mathscr{Y}^p$ will be indentical to $\mathscr{X}^p$. The trial solution spaces for Υ and φ are denoted by $\mathscr{X}^\Upsilon$ and $\mathscr{X}^\varphi$, respectively. We take $\mathscr{X}^\Upsilon = \mathscr{X}^\varphi = H^1(\Omega_t^f)$, where $H^1(\Omega_t^f)$ is the Sobolev space of square–integrable functions with square–integrable first derivatives. The weighting function spaces for Υ and φ are identical to their corresponding trial solution spaces. The trial solution space $\mathscr{X}^v$ for $\boldsymbol{v}$ is also a subset of $H^1(\Omega_t^f)$ whose members satisfy all Dirichlet boundary conditions. The weighting function space $\mathscr{Y}^v$ is identical to $\mathscr{X}^v$, but all restrictions on the Dirichlet boundary are homogeneous. With the above considerations, the variational formulation of the fluid mechanics problem may be stated as follows: Find $p\in\mathscr{X}^p$, $\boldsymbol{v}\in\mathscr{X}^v$, $\varphi\in\mathscr{X}^\varphi$ and $\Upsilon\in\mathscr{X}^\Upsilon$ such that $\forall w^1\in\mathscr{Y}^p$, $\boldsymbol{w}^2\in\mathscr{Y}^v$, $w^3\in\mathscr{Y}^\varphi$ and $w^4\in\mathscr{Y}^\Upsilon$,

$$B^f(w^1,\boldsymbol{w}^2,w^3,w^4,p,\boldsymbol{v},\varphi,\Upsilon;\widehat{\boldsymbol{v}}) = F^f(\boldsymbol{w}^2). \tag{8}$$

where

$$\begin{aligned}
&B^f(w^1,\boldsymbol{w}^2,w^3,w^4,p,\boldsymbol{v},\varphi,\Upsilon;\widehat{\boldsymbol{v}}) = \\
&\int_{\Omega_t^f} w^1\nabla\cdot\boldsymbol{v}\,\mathrm{d}\Omega_t^f + \int_{\Omega_t^f}\boldsymbol{w}^2\cdot\rho\left(\left.\frac{\partial\boldsymbol{v}}{\partial t}\right|_{\widehat{x}} + (\boldsymbol{v}-\widehat{\boldsymbol{v}})\cdot\nabla\boldsymbol{v}\right)\mathrm{d}\Omega_t^f \\
&+\int_{\Omega_t^f}\nabla\boldsymbol{w}^2:\boldsymbol{\sigma}^f\,\mathrm{d}\Omega_t^f + \int_{\Omega_t^f} w^3\left(\left.\frac{\partial\varphi}{\partial t}\right|_{\widehat{x}} + (\boldsymbol{v}-\widehat{\boldsymbol{v}})\cdot\nabla\varphi\right)\mathrm{d}\Omega_t^f \\
&+\int_{\Omega_t^f}\nabla w^3\cdot M_\varphi\gamma_f\nabla\left(\frac{1}{\varepsilon}W'_\varphi - \varepsilon\Upsilon\right)\mathrm{d}\Omega_t^f \\
&+\int_{\Omega_t^f} w^4\Upsilon\,\mathrm{d}\Omega_t^f + \int_{\Omega_t^f}\nabla w^4\cdot\nabla\varphi\,\mathrm{d}\Omega_t^f \\
&-\int_{\Gamma_t} w^4|\nabla\varphi|\cos(\theta_c)\,\mathrm{d}\Gamma_t,
\end{aligned} \tag{9}$$

and

$$F^f(\boldsymbol{w}^2) = \int_{\Omega_t^f}\boldsymbol{w}^2\cdot\rho\,\boldsymbol{f}\,\mathrm{d}\Omega_t^f. \tag{10}$$

Note that the variational formulation (8)–(10) weakly imposes the NSCH equations and the boundary conditions (5) and (6). If Dirichlet boundary conditions are not set on the entire boundary for velocity, then the variational formulation weakly imposes the conjugate stress–free condition on that part of the boundary.

In order to stabilize the NSCH equations, we make use of the VMS method and split the weighting and the trial solution spaces corresponding to pressure and velocity into a coarse and a fine scale subspaces, that is, $\mathscr{X}^p = \mathscr{X}_g^p\oplus\mathscr{X}_q^p$, $\mathscr{X}^v = \mathscr{X}_g^v\oplus\mathscr{X}_q^v$, $\mathscr{Y}^p = \mathscr{Y}_g^p\oplus\mathscr{Y}_q^p$ and $\mathscr{Y}^v = \mathscr{Y}_g^p\oplus\mathscr{Y}_q^v$. Here, the subscripts g and q denote the coarse and the fine scales, respectively. This implies that p, $\boldsymbol{v}$, w^1 and $\boldsymbol{w}^2$ may be written as

$$p = p_g + p_q, \tag{11a}$$

$$w^1 = w_g^1 + w_q^1, \tag{11b}$$

$$\boldsymbol{v} = \boldsymbol{v}_g + \boldsymbol{v}_q, \tag{11c}$$

$$\boldsymbol{w}^2 = \boldsymbol{w}_g^2 + \boldsymbol{w}_q^2. \tag{11d}$$

3.3.2 Solid mechanics

In order to define suitable boundary conditions for the solid mechanics problem, we assume that the solid boundary Γ_0^s can be decomposed into Dirichlet and Neumann parts, which will be designated as $(\Gamma_0^s)_D$ and $(\Gamma_0^s)_N$, respectively. We denote by $\mathscr{X}^s = \mathscr{X}^s(\Omega_0^s)$ a trial function space whose members satisfy all Dirichlet boundary conditions. $\mathscr{Y}^s = \mathscr{Y}^s(\Omega_0^s)$ is a weighting function space identical to $\mathscr{X}^s$, which verifies homogeneous conditions on $(\Gamma_0^s)_D$. The trial and weighting function spaces are subsets of $H^1\left(\Omega_0^s\right)$. The variational formulation of the solid mechanics problem may be stated as follows: Find $\boldsymbol{u}\in\mathscr{X}^s$ such that $\forall\boldsymbol{w}^s\in\mathscr{Y}^s$,

$$B^s(\boldsymbol{w}^s,\boldsymbol{u}) = F^s(\boldsymbol{w}^s), \tag{12}$$

where

$$B^s(\boldsymbol{w}^s,\boldsymbol{u}) = \int_{\Omega_0^s} \left(\boldsymbol{w}^s \cdot \rho_0^s \left. \frac{\partial^2 \boldsymbol{u}}{\partial t^2} \right|_X + \nabla_X \boldsymbol{w}^s : \boldsymbol{P} \right) \mathrm{d}\Omega_0^s \tag{13}$$

and

$$F^s(\boldsymbol{w}^s) = \int_{\Omega_0^s} \boldsymbol{w}^s \cdot \rho_0^s \boldsymbol{f}^s \mathrm{d}\Omega_0^s + \int_{(\Gamma_0^s)_N} \boldsymbol{w}^s \cdot \widehat{\boldsymbol{h}} \, \mathrm{d}(\Gamma_0^s)_N. \tag{14}$$

The previous variational formulation weakly enforces the Neumman boundary condition $\boldsymbol{P}\widehat{\boldsymbol{n}}^s = \widehat{\boldsymbol{h}}$ on $(\Gamma_0^s)_N$, where $\widehat{\boldsymbol{n}}^s$ represents the unit outward normal to the solid boundary in the material domain and $\widehat{\boldsymbol{h}}$ is a given traction.

3.3.3 Mesh motion

As the solid deforms, the fluid domain needs to be updated to accommodate to the fluid–structure interface motion. With this purpose, we solve a succession of fictitious linear elastic boundary–value problems [3,41,56,66–68], using as boundary conditions the displacement data on the fluid–solid interface. The fluid domain motion will be associated to the mapping $\widehat{\boldsymbol{\phi}}$. Let us define the displacement of the reference domain at time t as

$$\widehat{\boldsymbol{u}}_t(\widehat{\boldsymbol{x}}) = \widehat{\boldsymbol{u}}(\widehat{\boldsymbol{x}},t) = \widehat{\boldsymbol{\phi}}_t(\widehat{\boldsymbol{x}}) - \widehat{\boldsymbol{x}}. \tag{15}$$

where $\widehat{\boldsymbol{\phi}}_t(\widehat{\boldsymbol{x}}) = \widehat{\boldsymbol{\phi}}(\widehat{\boldsymbol{x}},t)$. To determine $\widehat{\boldsymbol{\phi}}_t$, and thus, the motion of the fluid domain, we use the identity

$$\widehat{\boldsymbol{\phi}}_t(\widehat{\boldsymbol{x}}) = \widehat{\boldsymbol{\phi}}_{\tilde{t}}(\widehat{\boldsymbol{x}}) + (\widehat{\boldsymbol{u}}_t - \widehat{\boldsymbol{u}}_{\tilde{t}})(\widehat{\boldsymbol{x}}), \tag{16}$$

where $\widehat{\boldsymbol{u}}_t - \widehat{\boldsymbol{u}}_{\tilde{t}}$ is obtained from a linear elastic boundary–value problem. Here, $\tilde{t} < t$ is a time instant close to t. In general, in our problems $\tilde{t}$ is the final configuration of the previous time step.

Let us define $\boldsymbol{u}^m$ as $\boldsymbol{u}^m = \widehat{\boldsymbol{u}}_t - \widehat{\boldsymbol{u}}_{\tilde{t}}$. $\boldsymbol{u}^m$ is obtained by solving fictitious linear–elastic boundary value problems, subject to the Dirichlet boundary conditions $\boldsymbol{u}^m = \boldsymbol{u}_t \circ \boldsymbol{\phi}_t^{-1} - \boldsymbol{u}_{\tilde{t}} \circ \boldsymbol{\phi}_{\tilde{t}}^{-1}$ on $\Gamma_{\tilde{t}}$, where $\boldsymbol{u}_t$ and $\boldsymbol{u}_{\tilde{t}}$ are the particle displacement at times t and $\tilde{t}$, respectively. These Dirichlet boundary conditions are strongly built into the trial solution space $\mathscr{V}^m = \mathscr{V}^m(\Omega_{\tilde{t}}^f)$, which is a subset of $H^1(\Omega_{\tilde{t}}^f)$. $\mathscr{W}^m = \mathscr{W}^m(\Omega_{\tilde{t}}^f)$ is a weighting function space identical to $\mathscr{V}^m$ except that it satisfies homogeneous conditions on the boundary. The variational formulation of the fluid domain motion can be stated as follows: Find $\boldsymbol{u}^m \in \mathscr{V}^m$ such that $\forall \boldsymbol{w}^m \in \mathscr{W}^m$,

$$B^m(\boldsymbol{w}^m,\boldsymbol{u}^m) = 0, \tag{17}$$

where

$$B^m(\boldsymbol{w}^m,\boldsymbol{u}^m) = \int_{\Omega_{\tilde{t}}^f} \nabla_{\tilde{x}}^{sym} \boldsymbol{w}^m : 2\mu^m \nabla_{\tilde{x}}^{sym} \boldsymbol{u}^m \mathrm{d}\Omega_{\tilde{t}}^f + \int_{\Omega_{\tilde{t}}^f} \nabla_{\tilde{x}} \cdot \boldsymbol{w}^m \lambda^m \nabla_{\tilde{x}} \cdot \boldsymbol{u}^m \mathrm{d}\Omega_{\tilde{t}}^f, \tag{18}$$

Here, $\nabla_{\tilde{x}}$ is the gradient operator on $\Omega_{\tilde{t}}$ and $\nabla_{\tilde{x}}^{sym}$ is its symmetric counterpart; μ^m and λ^m are the Lamé parameters of the fictitious elastic problem.

3.3.4 Coupled FSI problem

The variational formulation of the coupled fluid–structure interaction problem is stated as follows: Find $p_g \in \mathscr{X}_g^p$, $p_q \in \mathscr{X}_q^p$, $\boldsymbol{v}_g \in \mathscr{X}_g^v$, $\boldsymbol{v}_q \in \mathscr{X}_q^v$, $\varphi \in \mathscr{X}^\varphi$, $\Upsilon \in \mathscr{X}^\Upsilon$, $\boldsymbol{u} \in \mathscr{X}^s$ and $\boldsymbol{u}^m \in \mathscr{V}^m$ such that $\forall w_g^1 \in \mathscr{Y}_g^p$, $\boldsymbol{w}_g^2 \in \mathscr{Y}_g^v$, $w^3 \in \mathscr{Y}^\varphi$, $w^4 \in \mathscr{Y}^\Upsilon$, $\boldsymbol{w}^s \in \mathscr{Y}^s$ and $\boldsymbol{w}^m \in \mathscr{W}^m$,

$$B^f(w_g^1,\boldsymbol{w}_g^2,w^3,w^4,p_g+p_q,\boldsymbol{v}_g+\boldsymbol{v}_q,\varphi,\Upsilon;\widehat{\boldsymbol{v}}) + B^s(\boldsymbol{w}^s,\boldsymbol{u}) + B^m(\boldsymbol{w}^m,\boldsymbol{u}^m) = F^f(\boldsymbol{w}^2) + F^s(\boldsymbol{w}^s), \tag{19}$$

with the following compatibility conditions at the fluid–structure interface:

$$\boldsymbol{v}_g = \frac{\partial \boldsymbol{u}}{\partial t} \circ \boldsymbol{\phi}^{-1} \quad \text{on} \quad \Gamma_t, \tag{20a}$$

$$\boldsymbol{w}_g^2 = \boldsymbol{w}^s \circ \boldsymbol{\phi}^{-1} \quad \text{on} \quad \Gamma_t. \tag{20b}$$

Note that Eq. (20a) imposes strongly the kinematical compatibility at the fluid–structure interface while Eq. (20b) leads to a weak enforcement of traction compatibility, i.e., $\boldsymbol{\sigma}^f \boldsymbol{n}^f + \boldsymbol{\sigma}^s \boldsymbol{n}^s = 0$ on Γ_t, where $\boldsymbol{n}^s$ is the unit outward normal to the solid boundary in the spatial configuration.

3.4 Semidiscrete formulation

We use NURBS–based isogeometric analysis for the spatial discretization of the coupled problem. Let us define finite–dimensional approximations of the funtional spaces, namely, $\mathscr{X}_h^p \subset \mathscr{X}_g^p$, $\mathscr{X}_h^v \subset \mathscr{X}_g^v$, $\mathscr{X}_h^\varphi \subset \mathscr{X}^\varphi$, $\mathscr{X}_h^\Upsilon \subset \mathscr{X}^\Upsilon$, $\mathscr{X}_h^s \subset \mathscr{X}^s$, and $\mathscr{V}_h^m \subset \mathscr{V}^m$. Analogously, we introduce $\mathscr{Y}_h^p \subset \mathscr{Y}_g^p$, $\mathscr{Y}_h^v \subset \mathscr{Y}_g^v$, $\mathscr{Y}_h^\varphi \subset \mathscr{Y}^\varphi$, $\mathscr{Y}_h^\Upsilon \subset \mathscr{Y}^\Upsilon$, $\mathscr{Y}_h^s \subset \mathscr{Y}^s$, and $\mathscr{W}_h^m \subset \mathscr{W}^m$.

Let us now use $\varphi_h \in \mathscr{X}_h^\varphi$ and the coarse–scale velocity $\boldsymbol{v}_h \in \mathscr{X}_h^v$ and pressure fields $p_h \in \mathscr{X}_h^p$ to approximate the fine scales of the velocity and pressure fields as

$$\boldsymbol{v}_q = -\frac{\tau_{SUPS}}{\rho} \boldsymbol{r}_M, \tag{21a}$$

$$p_q = -\rho \nu_{LSIC} r_C. \tag{21b}$$

Here, $\boldsymbol{r}_M$ and r_C are given by

$$\boldsymbol{r}_M = \rho \left(\left. \frac{\partial \boldsymbol{v}_h}{\partial t} \right|_{\widehat{x}} + (\boldsymbol{v}_h - \widehat{\boldsymbol{v}}_h) \cdot \nabla \boldsymbol{v}_h \right) - \nabla \cdot \boldsymbol{\sigma}_h^f - \rho \boldsymbol{f}, \tag{22a}$$

$$r_C = \nabla \cdot \boldsymbol{v}_h, \tag{22b}$$

where $\boldsymbol{\sigma}_h^f = \bar{\mu} \left(\nabla \boldsymbol{v}_h + \nabla^T \boldsymbol{v}_h \right) - p_h \boldsymbol{I} - \gamma_f \varepsilon \nabla \varphi_h \otimes \nabla \varphi_h$. For the stabilization parameters τ_{SUPS} and ν_{LSIC} we use the expressions

$$\tau_{SUPS} = \left(\frac{4}{\Delta t^2} + (\boldsymbol{v}_h - \widehat{\boldsymbol{v}}_h) \cdot \boldsymbol{G} (\boldsymbol{v}_h - \widehat{\boldsymbol{v}}_h) + C_I \nu^2 \boldsymbol{G} : \boldsymbol{G} \right)^{-1/2}, \tag{23a}$$

$$\nu_{LSIC} = \left(\mathrm{tr}(\boldsymbol{G})\, \tau_{SUPS} \right)^{-1}, \tag{23b}$$

where Δt is, in a time-discrete context, the time step; $C_I = 1/12$ is a positive constant; ν is the kinematic viscosity; and $\boldsymbol{G}$ denotes the element metric tensor [6]. The stabilized formulation of the fluid problem over the finite element spaces can be stated as: Find $p_h \in \mathscr{X}_h^p$, $\boldsymbol{v}_h \in \mathscr{X}_h^v$, $\varphi_h \in \mathscr{X}_h^\varphi$ and $\Upsilon_h \in \mathscr{X}_h^\Upsilon$ such that $\forall w_h^1 \in \mathscr{Y}_h^p$, $\boldsymbol{w}_h^2 \in \mathscr{Y}_h^v$, $w_h^3 \in \mathscr{Y}_h^\varphi$ and $w_h^4 \in \mathscr{Y}_h^\Upsilon$,

$$B_{MS}^f(w_h^1, \boldsymbol{w}_h^2, w_h^3, w_h^4, p_h, \boldsymbol{v}_h, \varphi_h, \Upsilon_h; \widehat{\boldsymbol{v}}_h) = F^f(\boldsymbol{w}_h^2), \tag{24}$$

where

$$\begin{aligned}
B_{MS}^f(w_h^1, \boldsymbol{w}_h^2, w_h^3, w_h^4, p_h, \boldsymbol{v}_h, \varphi_h, \Upsilon_h; \widehat{\boldsymbol{v}}_h) &= \int_{\Omega_t^f} w_h^1 \nabla \cdot \boldsymbol{v}_h \mathrm{d}\Omega_t^f \\
&+ \int_{\Omega_t^f} \boldsymbol{w}_h^2 \cdot \rho \left(\left. \frac{\partial \boldsymbol{v}_h}{\partial t} \right|_{\widehat{x}} + (\boldsymbol{v}_h - \widehat{\boldsymbol{v}}_h) \cdot \nabla \boldsymbol{v}_h \right) \mathrm{d}\Omega_t^f \\
&+ \int_{\Omega_t^f} \nabla \boldsymbol{w}_h^2 : \boldsymbol{\sigma}_h^f \mathrm{d}\Omega_t^f + \int_{\Omega_t^f} w_h^3 \left(\left. \frac{\partial \varphi_h}{\partial t} \right|_{\widehat{x}} + (\boldsymbol{v}_h - \widehat{\boldsymbol{v}}_h) \cdot \nabla \varphi_h \right) \mathrm{d}\Omega_t^f \\
&+ \int_{\Omega_t^f} \nabla w_h^3 \cdot M_\varphi \gamma_f \nabla \left(\frac{1}{\varepsilon} W_\varphi' - \varepsilon \Upsilon_h \right) \mathrm{d}\Omega_t^f \\
&+ \int_{\Omega_t^f} w_h^4 \Upsilon_h \mathrm{d}\Omega_t^f + \int_{\Omega_t^f} \nabla w_h^4 \cdot \nabla \varphi_h \mathrm{d}\Omega_t^f \\
&- \int_{\Gamma_t} w_h^4 |\nabla \varphi_h| \cos(\theta_c) \mathrm{d}\Gamma_t \\
&+ \sum_{e=1}^{n_{el}} \int_{\Omega_t^{f,e}} \tau_{SUPS} \left((\boldsymbol{v}_h - \widehat{\boldsymbol{v}}_h) \cdot \nabla \boldsymbol{w}_h^2 + \frac{\nabla w_h^1}{\rho} \right) \cdot \boldsymbol{r}_M \mathrm{d}\Omega_t^f \\
&+ \sum_{e=1}^{n_{el}} \int_{\Omega_t^{f,e}} \nu_{LSIC} \rho \nabla \cdot \boldsymbol{w}_h^2 r_C \mathrm{d}\Omega_t^f \\
&- \sum_{e=1}^{n_{el}} \int_{\Omega_t^{f,e}} \tau_{SUPS} \boldsymbol{w}_h^2 \cdot (\boldsymbol{r}_M \cdot \nabla \boldsymbol{v}_h) \, \mathrm{d}\Omega_t^f \\
&- \sum_{e=1}^{n_{el}} \int_{\Omega_t^{f,e}} \frac{\nabla \boldsymbol{w}_h^2}{\rho} : (\tau_{SUPS} \boldsymbol{r}_M \otimes \tau_{SUPS} \boldsymbol{r}_M) \, \mathrm{d}\Omega_t^f \\
&- \sum_{e=1}^{n_{el}} \int_{\Omega_t^{f,e}} \frac{\tau_{SUPS}}{\rho} w_h^3 \boldsymbol{r}_M \cdot \nabla \varphi_h \mathrm{d}\Omega_t^f
\end{aligned} \tag{25}$$

Here, n_{el} is the total number of elements on the fluid mesh and $\Omega_t^{f,e}$ the region of the physical space occupied by element e at time t.

We can now approximate the coupled FSI problem (19) by the following variational formulation over the finite element spaces: Find $p_h \in \mathscr{X}_h^p$, $\boldsymbol{v}_h \in \mathscr{X}_h^v$, $\varphi_h \in \mathscr{X}_h^\varphi$, $\Upsilon_h \in \mathscr{X}_h^\Upsilon$, $\boldsymbol{u}_h \in \mathscr{X}_h^s$ and $\boldsymbol{u}_h^m \in \mathscr{V}_h^m$ such that $\forall w_h^1 \in \mathscr{Y}_h^p$, $\boldsymbol{w}_h^2 \in \mathscr{Y}_h^v$, $w_h^3 \in \mathscr{Y}_h^\varphi$, $w_h^4 \in \mathscr{Y}_h^\Upsilon$, $\boldsymbol{w}_h^s \in \mathscr{Y}^s{}_h$ and $\boldsymbol{w}_h^m \in \mathscr{W}_h^m$,

$$\begin{aligned}
&B_{MS}^f(w_h^1, \boldsymbol{w}_h^2, w_h^3, w_h^4, p_h, \boldsymbol{v}_h, \varphi_h, \Upsilon_h; \widehat{\boldsymbol{v}}_h) + B^s(\boldsymbol{w}_h^s, \boldsymbol{u}_h) \\
&+ B^m(\boldsymbol{w}_h^m, \boldsymbol{u}_h^m) = F^f(\boldsymbol{w}_h^2) + F^s(\boldsymbol{w}_h^s),
\end{aligned} \tag{26}$$

where

$$p_h(\boldsymbol{x}, t) = \sum_{A \in I_f} p_A(t) N_A(\boldsymbol{x}, t), \tag{27a}$$

$$w_h^1(\boldsymbol{x}, t) = \sum_{A \in I_f} w_A^1 N_A(\boldsymbol{x}, t), \tag{27b}$$

$$\boldsymbol{u}_h(\boldsymbol{X}, t) = \sum_{A \in I_s} \boldsymbol{u}_A(t) \widehat{N}_A(\boldsymbol{X}), \tag{27c}$$

$$\boldsymbol{w}_h^s(\boldsymbol{X}) = \sum_{A \in I_s} \boldsymbol{w}_A^s \widehat{N}_A(\boldsymbol{X}), \tag{27d}$$

$$\boldsymbol{u}_h^m(\tilde{\boldsymbol{x}}, \tilde{t}) = \sum_{A \in I_f} \widehat{\boldsymbol{u}}_A(\tilde{t}) \tilde{N}_A(\tilde{\boldsymbol{x}}, \tilde{t}), \tag{27e}$$

$$\boldsymbol{w}_h^m(\tilde{\boldsymbol{x}}, \tilde{t}) = \sum_{A \in I_f} \boldsymbol{w}_A^m \tilde{N}_A(\tilde{\boldsymbol{x}}, \tilde{t}), \tag{27f}$$

$$\widehat{\boldsymbol{v}}_h(\boldsymbol{x}, t) = \sum_{A \in I_f} \frac{\partial \widehat{\boldsymbol{u}}_A}{\partial t}(t) N_A(\boldsymbol{x}, t). \tag{27g}$$

The rest of the variables ($\boldsymbol{v}_h$, φ_h and Υ_h) and the weighting functions ($\boldsymbol{w}_h^2$, w_h^3 and w_h^4) are defined analogously to p_h and w_h^1, respectively. In Eqs. (27), the $\widehat{N}_A$'s are a set of basis functions defined on Ω_0 that are fixed in time. In the context of IGA, these functions are splines with controllable continuity. In the interior of the fluid and solid domains, their continuity can be arbitrarily high but on Γ_0 (in the normal direction) is exactly $\mathscr{C}^0$. I_s denotes the global–index set of the $\widehat{N}_A$'s that correspond to the solid domain. N_A is the push forward of $\widehat{N}_A$ to the spatial domain Ω_t, i.e., $N_A(\boldsymbol{x}, t) = \widehat{N}_A \circ \widehat{\boldsymbol{\phi}^h}^{-1}(\boldsymbol{x}, t)$, where $\widehat{\boldsymbol{\phi}^h}^{-1}$ is the discrete counterpart of $\widehat{\boldsymbol{\phi}}^{-1}$. Likewise, $\tilde{N}_A$ is the push forward of $\widehat{N}_A$ to the spatial domain at time $\tilde{t}$, i.e., $\tilde{N}_A(\tilde{\boldsymbol{x}}, \tilde{t}) = \widehat{N}_A \circ \widehat{\boldsymbol{\phi}^h}^{-1}(\tilde{\boldsymbol{x}}, \tilde{t})$. I_f is the global–index set of the N_A's that correspond to the fluid domain.

In order to enforce the compatibility conditions at the fluid-structure interface and taking into account that we work with matching discretizations, we define a unique set of both trial an test functions for the velocity at the fluid–structure interface. This leads to strong (pointwise) satisfaction of the kinematics condition and weak satisfaction of the traction compatibility condition.

3.5 Time discretization and numerical implementation

In this section, we present the time integration algorithm for our FSI problem. We use the generalized-α method, which was originally proposed by Chung and Hulbert [22] for the equations of structural dynamics. Subsequently, this technique was extended to the equations of fluid mechanics [39] and successfully applied to fluid-structure interaction problems (see, for instance, [3, 13, 15]).

3.5.1 Time stepping scheme

Let us call $\boldsymbol{U}, \dot{\boldsymbol{U}}, \ddot{\boldsymbol{U}}$ the vectors of control variable degrees of freedom of the fluid–structure system, and its first and second time derivatives, respectively. Analogously, let us call $\boldsymbol{V}$, $\dot{\boldsymbol{V}}$, $\ddot{\boldsymbol{V}}$ the vectors of control variable degrees of freedom of mesh displacements, velocities and accelerations. We define the residual vectors

$$\boldsymbol{R}^{cont} = \{R_A^{cont}\}, \tag{28a}$$
$$\boldsymbol{R}^{mom} = \{R_{A,i}^{mom}\}, \tag{28b}$$
$$\boldsymbol{R}^{\varphi} = \{R_A^{\varphi}\}, \tag{28c}$$
$$\boldsymbol{R}^{aux} = \{R_A^{aux}\}, \tag{28d}$$
$$\boldsymbol{R}^{mesh} = \{R_{A,i}^{mesh}\}, \tag{28e}$$

where A is a control–variable index and i is an index associated to the spatial dimensions. The residual components are defined as

$$R_A^{cont} = B_{MS}^f(\{N_A,0,0,0\},\{p_h,\boldsymbol{v}_h,\varphi_h,\Upsilon_h\};\widehat{\boldsymbol{v}}_h), \tag{29a}$$
$$R_{A,i}^{mom} = B_{MS}^f(\{0,N_A\boldsymbol{e}_i,0,0\},\{p_h,\boldsymbol{v}_h,\varphi_h,\Upsilon_h\};\widehat{\boldsymbol{v}}_h) + B^s(\widehat{N}_A\boldsymbol{e}_i,\boldsymbol{u}_h) - F^s(\widehat{N}_A\boldsymbol{e}_i) - F^f(\widehat{N}_A\boldsymbol{e}_i), \tag{29b}$$
$$R_A^{\varphi} = B_{MS}^f(\{0,0,N_A,0\},\{p_h,\boldsymbol{v}_h,\varphi_h,\Upsilon_h\};\widehat{\boldsymbol{v}}_h), \tag{29c}$$
$$R_A^{aux} = B_{MS}^f(\{0,0,0,N_A\},\{p_h,\boldsymbol{v}_h,\varphi_h,\Upsilon_h\};\widehat{\boldsymbol{v}}_h), \tag{29d}$$
$$R_{A,i}^{mesh} = B^m(\tilde{N}_A\boldsymbol{e}_i,\boldsymbol{u}_h^m), \tag{29e}$$

where $\boldsymbol{e}_i$ is the ith cartesian basis vector. Our time stepping scheme can be defined as follows: Given the discrete approximation to the global vectors of control variables at time t_n, namely, $\boldsymbol{U}_n, \dot{\boldsymbol{U}}_n, \ddot{\boldsymbol{U}}_n, \boldsymbol{V}_n, \dot{\boldsymbol{V}}_n, \ddot{\boldsymbol{V}}_n$ and the current time step size $\Delta t = t_{n+1} - t_n$, find $\boldsymbol{U}_{n+1}$, $\dot{\boldsymbol{U}}_{n+1}$, $\ddot{\boldsymbol{U}}_{n+1}$, $\boldsymbol{V}_{n+1}$, $\dot{\boldsymbol{V}}_{n+1}$, $\ddot{\boldsymbol{V}}_{n+1}$ such that

$$\boldsymbol{R}^{cont}(\boldsymbol{U}_{n+\alpha_f},\dot{\boldsymbol{U}}_{n+\alpha_f},\ddot{\boldsymbol{U}}_{n+\alpha_m},\boldsymbol{V}_{n+\alpha_f},\dot{\boldsymbol{V}}_{n+\alpha_f},\ddot{\boldsymbol{V}}_{n+\alpha_m}) = 0, \tag{30a}$$
$$\boldsymbol{R}^{mom}(\boldsymbol{U}_{n+\alpha_f},\dot{\boldsymbol{U}}_{n+\alpha_f},\ddot{\boldsymbol{U}}_{n+\alpha_m},\boldsymbol{V}_{n+\alpha_f},\dot{\boldsymbol{V}}_{n+\alpha_f},\ddot{\boldsymbol{V}}_{n+\alpha_m}) = 0, \tag{30b}$$
$$\boldsymbol{R}^{\varphi}(\boldsymbol{U}_{n+\alpha_f},\dot{\boldsymbol{U}}_{n+\alpha_f},\ddot{\boldsymbol{U}}_{n+\alpha_m},\boldsymbol{V}_{n+\alpha_f},\dot{\boldsymbol{V}}_{n+\alpha_f},\ddot{\boldsymbol{V}}_{n+\alpha_m}) = 0, \tag{30c}$$
$$\boldsymbol{R}^{aux}(\boldsymbol{U}_{n+\alpha_f},\dot{\boldsymbol{U}}_{n+\alpha_f},\ddot{\boldsymbol{U}}_{n+\alpha_m},\boldsymbol{V}_{n+\alpha_f},\dot{\boldsymbol{V}}_{n+\alpha_f},\ddot{\boldsymbol{V}}_{n+\alpha_m}) = 0, \tag{30d}$$
$$\boldsymbol{R}^{mesh}(\boldsymbol{U}_{n+\alpha_f},\dot{\boldsymbol{U}}_{n+\alpha_f},\ddot{\boldsymbol{U}}_{n+\alpha_m},\boldsymbol{V}_{n+\alpha_f},\dot{\boldsymbol{V}}_{n+\alpha_f},\ddot{\boldsymbol{V}}_{n+\alpha_m}) = 0, \tag{30e}$$

where

$$\dot{\boldsymbol{U}}_{n+1} = \dot{\boldsymbol{U}}_n + \Delta t((1-\gamma)\ddot{\boldsymbol{U}}_n + \gamma\ddot{\boldsymbol{U}}_{n+1}), \tag{31a}$$
$$\boldsymbol{U}_{n+1} = \boldsymbol{U}_n + \Delta t\dot{\boldsymbol{U}}_n + \frac{\Delta t^2}{2}\left((1-2\beta)\ddot{\boldsymbol{U}}_n + 2\beta\ddot{\boldsymbol{U}}_{n+1}\right), \tag{31b}$$
$$\dot{\boldsymbol{V}}_{n+1} = \dot{\boldsymbol{V}}_n + \Delta t((1-\gamma)\ddot{\boldsymbol{V}}_n + \gamma\ddot{\boldsymbol{V}}_{n+1}), \tag{31c}$$
$$\boldsymbol{V}_{n+1} = \boldsymbol{V}_n + \Delta t\dot{\boldsymbol{V}}_n + \frac{\Delta t^2}{2}\left((1-2\beta)\ddot{\boldsymbol{V}}_n + 2\beta\ddot{\boldsymbol{V}}_{n+1}\right). \tag{31d}$$

The α–levels are defined as

$$\boldsymbol{U}_{n+\alpha_f} = \boldsymbol{U}_n + \alpha_f(\boldsymbol{U}_{n+1} - \boldsymbol{U}_n), \tag{32a}$$
$$\boldsymbol{U}_{n+\alpha_m} = \boldsymbol{U}_n + \alpha_m(\boldsymbol{U}_{n+1} - \boldsymbol{U}_n). \tag{32b}$$

The parameters α_f, α_m, γ and β are chosen as in [3] leading to second–order time accuracy, unconditional stability of the time–integration algorithm for linear ordinary differential equation systems with constant coefficients, and an optimally damped fluid subproblem. In particular, we have adopted the following expressions,

$$\alpha_f = \frac{1}{1+\rho_\infty}, \tag{33a}$$
$$\alpha_m = \frac{1}{2}\left(\frac{3-\rho_\infty}{1+\rho_\infty}\right), \tag{33b}$$
$$\gamma = \frac{1}{2} + \alpha_m - \alpha_f, \tag{33c}$$
$$\beta = \frac{1}{4}(1-\alpha_f+\alpha_m)^2, \tag{33d}$$

where ρ_∞ denotes the spectral radius. We have adopted $\rho_\infty = 0.5$ for all the examples presented in this paper. The nonlinear system of equations (30) is solved using a Newton–Raphson iteration procedure.

4 Numerical examples

In this section, we present a series of numerical examples that illustrate the predictive ability of our model and the effectiveness of our computational method. The first numerical example uses the NSCH equations without solid to reproduce the coalescence of two droplets. We aim to show that the radius of the meniscus formed during the coalescence process follows the scaling law observed in experimental and theoretical results. The second example demonstrates that our model can be used to simulate the deformation caused by a droplet on an underlying substrate. Our results are compared with experimental data taken from the literature. Subsequently, we present a numerical simulation of capillary origami. A droplet of glycerol is deposited on a solid membrane and the capillary forces at the interface fold the structure until the droplet is partially wrapped by the membrane. Our next example reproduces the deformation

caused by capillary forces in elastic micropillars. Finally, we present a three dimensional simulation of a slender structure deformed by a wetting droplet. Note that gravity forces are negligible at small scales and, as a consequence, they are not considered in the numerical examples presented in this paper.

4.1 Coalescence of droplets

When two droplets come into contact, they form a bridge and coalesce due to surface tension. The NSCH model given in Eqs. (1) can be used to study droplet coalescence for incompressible, two-component, immiscible fluids with matched density and viscosity. To solve the NSCH equations, we use the algorithm described in Section 3, annihilating all the terms corresponding to the solid mechanics and the mesh–motion subproblems. Fig. 1 shows a sequence of isocontour plots of the interface along the coalescence process of two water droplets. For simplicity, we considered a two-dimensional domain. Note that the time $t = 0.0$ does not refer to the initial time of the simulation, but to the instant when the interfaces of both droplets come into contact. Initially, the dynamics is driven by a large Laplace pressure originating from the high curvature at the contact region, where a meniscus is formed. Early in the process, the droplets retain their circular shape to some extent ($t < 0.15\,ms$). By time $t \sim 4\,ms$ the two initial droplets can be barely discerned. At this point, the dynamics starts to operate on larger time scales. The shape of the droplet evolves toward a circle that minimizes the interfacial length. However, the gradual accumulation of kinetic energy along the process produces a "rebound" effect in the shape of the droplet; see the evolution between $t \sim 8\,ms$ and $t \sim 400\,ms$. We consider that the solution at time $t = 400\,ms$ is a good approximation of the steady state.

The initial dynamics of the merger process is amenable to simplified theoretical models that provide the time evolution of the meniscus radius $r(t)$; see the bottom-right inset of Fig. 2 for a pictorial description of $r(t)$. The theoretical model [30] predicts the scaling $r(t) \sim \sqrt{t}$ for $r \gtrsim 0.03R$, where R is the droplet radius. This result is also backed up by experimental observations [1]. Fig. 2 shows the time evolution of r obtained from the simulation (red squares) and the function $g(t) = \chi\sqrt{t}$ (blue solid line), where χ is a fitting constant parameter. The diagram shows a good agreement between both datasets, demonstrating that our model reproduces correctly the initial dynamics of merging droplets.

4.2 Static wetting on soft substrates

The static equilibrium shape of a liquid droplet on a flat and rigid substrate is well understood. The droplet's shape

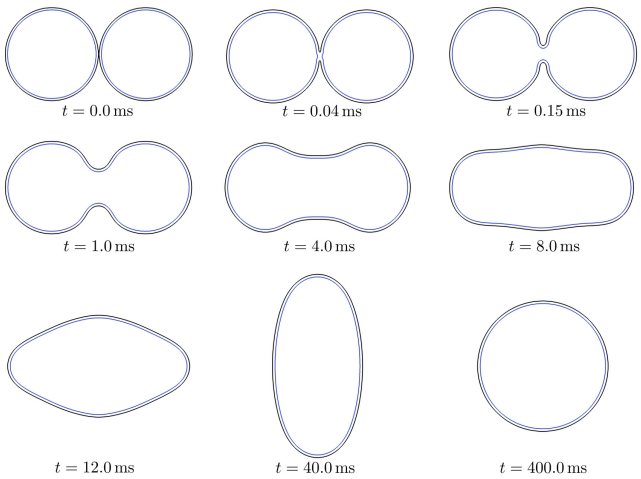

Fig. 1 Time evolution of the interface shown by isocontour lines of φ. We plot $\varphi = 0.7$ (blue) and $\varphi = -0.7$ (black). The computational domain (not shown) is $\Omega = (0, 1.5L) \times (0, L)$, where $L = 1.0\,\mathrm{cm}$. The mesh is composed of 256×384 $\mathscr{C}^1$-quadratic elements. We imposed periodic boundary conditions in both directions. The initial configuration consisted of two water droplets of radius $R = 0.2\,\mathrm{cm}$ centered at $(0.543L, 0.5L)$ and $(0.957L, 0.5L)$, respectively. The physical parameters correspond to water at 20°C, i.e., $\gamma_f = 72.86\,m\mathrm{N/m}$, $\mu = 1.0\,m\mathrm{Pa\,s}$ and $\rho = 1.0\,\mathrm{g/cm^3}$. The thickness of the interface and the mobility were set to $\varepsilon = 3.9\,10^{-3}\,\mathrm{cm}$, and $M_\varphi = 10^{-3}\,\mathrm{cm^3 s/g}$, respectively. The time step is $\Delta t = 10^{-6}\,\mathrm{s}$ and the computational time was 12 h using 128 cores.

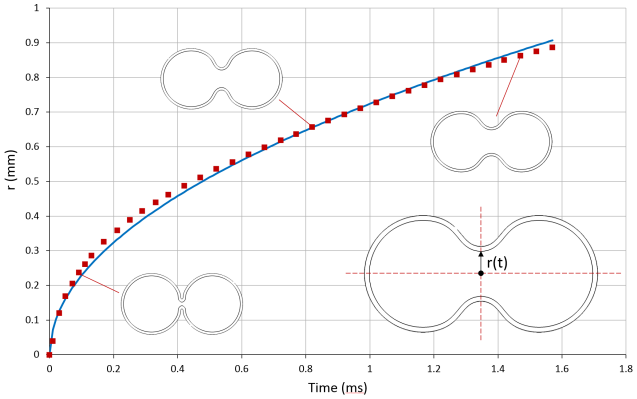

Fig. 2 Time evolution of the meniscus radius r obtained from the computation (red points) and trend line given by $g(t) = \chi\sqrt{t}$ with $\chi = 22.9$ (blue line). The initial time on the horizontal axis refers to the instant when the interfaces of both droplets come into contact.

is a spherical cap which contacts the solid with an equilibrium contact angle $\theta_E = \arccos[(\gamma_{SG} - \gamma_{SL})/\gamma_f]$ given by the Young-Dupré equation [24]. In the contact angle equation, γ_{SG} and γ_{SL} are the surface tension at the solid-gas and at the solid-liquid interface, respectively. When the solid is sufficiently compliant or the droplet sufficiently small for the elastocapillary length scale $l_{ec} = \gamma_f/E$ to be comparable to the droplet radius, Young–Dupré's equation breaks down. The excess Laplace pressure in the interior of the droplet creates a dimple in the wet area and capillary forces pro-

duce a ridge at the contact line. To show that our FSI model can successfully predict this phenomenon, we reproduce one of the experiments reported in [57]. In particular, a glycerol droplet of radius $R = 225.5\,\mu$m is deposited on a soft substrate with Young's modulus $E = 3.0\,k$Pa. The droplet deforms the substrate as shown on the left–hand side of Fig. 3(a). The contact angle θ_c in the boundary condition (5) is given by $\theta_E = \arccos[(\gamma_{SG} - \gamma_{SL})/\gamma_f]$, but the solid deformation produces an apparent contact angle (measured with respect to a horizontal line) that is smaller than θ_E. In simple words, the droplet "sinks" in the substrate and looks "more wetting" that it would do on a rigid surface. The right–hand side of Fig. 3(a) portraits a detailed view of the contact line neighborhood and also shows the mesh in the current configuration. It may be observed that the fictitious linear elasticity problem used to move the fluid domain produces a smooth transition of the element shape using the solid displacement at the fluid–solid interface as boundary condition. Figs. 3(b) and 3(c) show, respectively, the substrate's displacements in the horizontal and vertical directions, when equilibrium is reached.

To perform a more quantitative analysis, we measured the displacement of the fluid–solid interface close to the contact line and we compared our results with the experimental data reported in [57]; see Fig. 4. The experimental results are available only for the stationary configuration (blue dots). Our computational method enables us to understand the dynamics of the process. We report the solution at times $t = 0.25\,m$s (yellow), $t = 0.75\,m$s (purple) and $t = 21.0\,m$s (red), when we considered the solution to be stationary. Note that our model neglects the disjoining pressure. At the length scales considered in this paper, the disjoining pressure is expected to have an impact only close to the contact line. Based on the results presented in Fig. 4, the impact of the disjoining pressure on the global deformation seems to be small, which justifies our assumption.

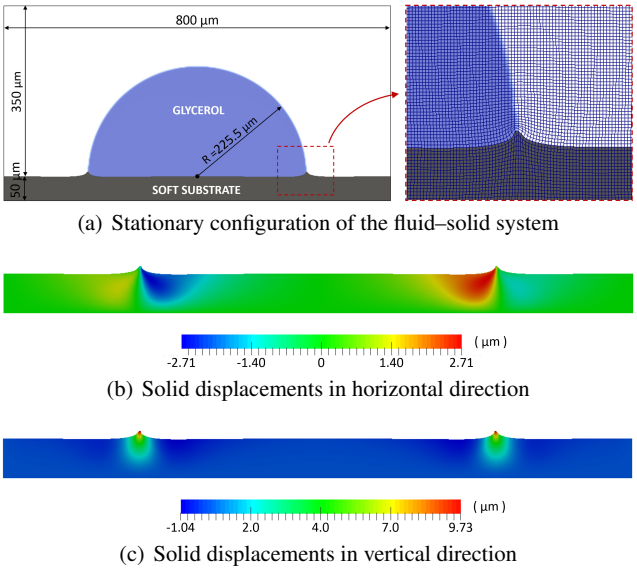

(a) Stationary configuration of the fluid–solid system

(b) Solid displacements in horizontal direction

(c) Solid displacements in vertical direction

Fig. 3 Glycerol droplet deposited on a soft substrate. (a) Stationary configuration (left) and detail of the contact line region after deformation (right). (b), (c) solid displacements in the horizontal and vertical directions, respectively. We use a uniform mesh of 400×200 quadratic elements. On the left, right and lower boundaries of the computational domain, we impose zero velocity in the normal direction. On the upper boundary, zero velocity is imposed in both directions. We adopted the values of surface tension reported in [57], i.e., $\gamma_f = 46.0\,m$N/m, $\gamma_{SA} = 31\,m$N/m and $\gamma_{SL} = 36\,m$N/m. For the viscosity and density parameters, we use values for glycerol: $\mu = 1412.0\,m$Pa s and $\rho = 1.26\,pg/\mu$m^3. We took $\varepsilon = 2.0\,\mu$m and $M_\varphi = 0.1\,\mu$m$^3\mu$s$/pg$. The parameters for the solid correspond to a silicone gel with $E = 3.0\,k$Pa, $\nu^s = 0.499$ and $\rho^s = 12.6\,pg/\mu$m^3. Finally, the time step is $\Delta t = 10^{-6}$ s and the computational time was 47 h using 128 cores.

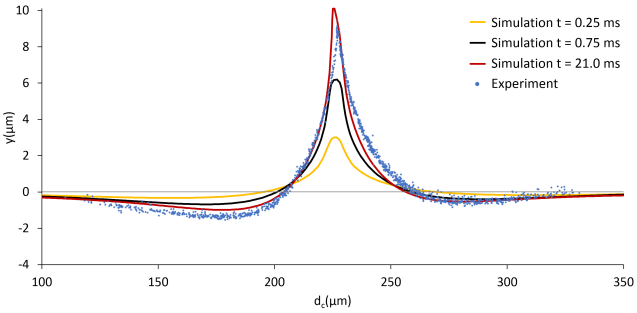

Fig. 4 Vertical displacements of the fluid–solid interface. d_c in the horizontal axis represents the distance to the center of the droplet. The blue circles are the experimental measurements reported in [57], which represent a stationary configuration. The computational results are reported at $t = 0.25\,m$s (yellow), $t = 0.75\,m$s (purple) and $t = 21.0\,m$s (red), when the solution is considered to be stationary. The horizontal line $y = 0$ corresponds to the fluid–solid interface before deformation. The experimental data in this figure has been reprinted with permission from [57]. Copyright 2013 American Physical Society.

4.3 Capillary origami

A droplet deposited on an elastic membrane will pull the solid through surface tension. If the membrane is sufficiently compliant, the drop will fold it, giving rise to a capillary origami [49]. This process has triggered significant interest because it can be used for self-assembly of micro- and nanostructures. We use our theory to simulate the spontaneous wrapping of glycerol droplets with elastic membranes. The experiments in [49] were performed by placing the membrane on a rigid surface. Modeling this system in its entirety would require the use of contact algorithms. It is also very likely that we would need to remesh the fluid domain due to changes in its topology. To avoid this, we simply placed the membrane in the fluid omitting the underlying rigid surface; see Fig 5(a). Since we are neglecting gravity forces,

we expect this simplified system to behave similarly to the capillary origamis formed on top of a rigid surface. Another difference with the experiments in [49] is that we do not consider the evaporation of the droplet. As shown in [49], a capillary origami can be produced without evaporation, but the complete encapsulation of the droplet is harder to achieve without reducing the droplet's volume.

We place a semicircular droplet of radius $R = 146.0\,\mu$m on an elastic membrane [see Fig. 5(a) for the setup of the problem] and we impose different contact angles θ_c along the fluid–structure interface. The membrane is modeled as a 3D solid. Figs. 5(b)–5(d) show how the membrane folds wrapping a droplet with contact angle $\theta_c = 90°$. After the droplet is deposited, the membrane bends downwards due to the internal Laplace pressure. Later, the ends of the membrane move upwards until the droplet gets almost fully encapsulated. Fig. 5(e) provides a detail of the computational mesh in the area that undergoes more distortion (the dashed line rectangle in Fig. 5(d) indicates the region of interest). Note that the fluid elements contiguous to the solid undergo lower distortion since we are adopting higher values for the Lamé parameters in these elements. The idea is to preserve the quality of the mesh for as long as possible. Fig. 6 shows the solid mesh in the current configuration and the streamlines at time $t = 0.045\,$s. The fluid–fluid interface is drawn as a black solid line. The flow inside the droplet is predominantly vertical. Outside the droplet, the membrane's motion produces well-defined vortices. In order to check if the conservation of volume is satisfied, we compare the area of the liquid droplet at time $t = 0\,$s and $t = 0.138\,$s and we observe that there is an increase in the droplet area of 3.4%.

Fig. 7 shows the influence of the contact angle on the dynamics of the process. The initial conditions are the same as before. The results suggest that droplet encapsulation occurs faster for more wetting fluids. This observation can be used to have better control in the process of self-assembly of micro- and nano-structures. Figs. 7(b) and 7(d) represent a detail of the mesh distortion in the regions indicated in Figs. 7(a) and 7(c), respectively.

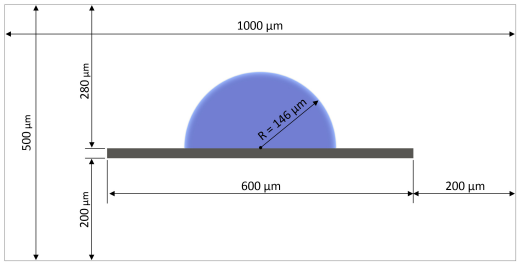

(a) $\theta_c = 90°, t = 0.0\,$s

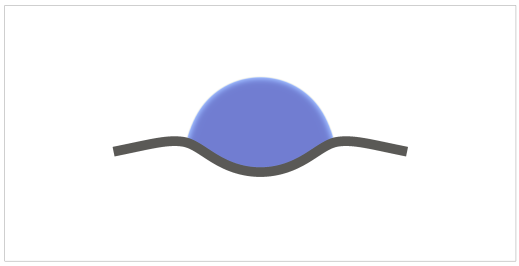

(b) $\theta_c = 90°, t = 0.014\,$s

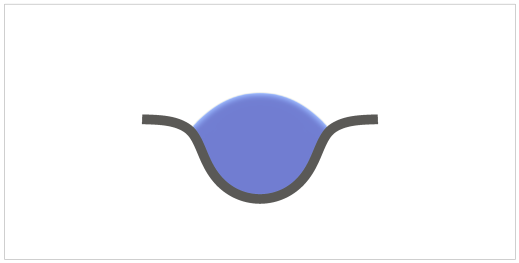

(c) $\theta_c = 90°, t = 0.075\,$s

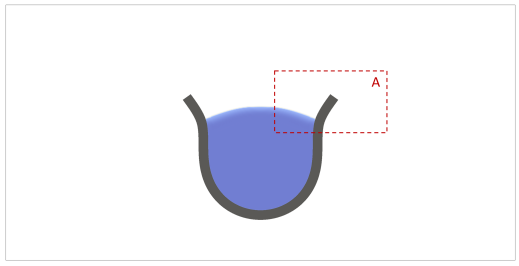

(d) $\theta_c = 90°, t = 0.138\,$s

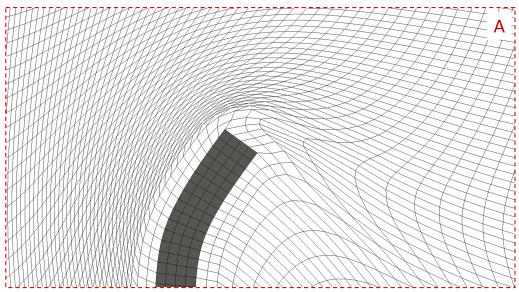

(e) $\theta_c = 90°, t = 0.138\,$s

Fig. 5 Capillary origami. (a) Initial condition. A semicircular droplet (blue) is deposited on an elastic membrane (grey). (b), (c) and (d) Current configuration at $t = 0.014\,$s, $t = 0.075\,$s and $t = 0.138\,$s, respectively. (e) Detail of the fluid and solid mesh at $t = 0.138\,$s in the dashed line rectangle represented in (d), that is, the area where the mesh undergoes higher distortion. We use a uniform mesh of 200×100 quadratic elements. We impose zero velocity in normal direction on all boundaries. The parameters employed in this computation for the fluid correspond to a glycerol droplet, in particular, $\mu = 1412.0m$Pa s, $\gamma_f = 46.0m$N/m, and $\rho = 1.26\,pg/\mu$m^3. We take $\varepsilon = 5.0\,\mu$m and $M_\varphi = 0.1\,\mu$m$^3\mu$s$/pg$. For the elastic membrane we adopt $E = 30.0k$Pa, $\nu^s = 0.45$, and $\rho^s = 12.6\,pg/\mu$m^3. Finally, $\Delta t = 10^{-5}\,$s and the computational time was approximately 30 h using 32 cores.

4.4 Wetting of elastic micropillars

Wetting of fibrous media has been widely studied due to its importance in natural and engineered systems. However, most of the research focuses on rigid fibers. At small scales, capillary forces outweigh bulk forces and deform fibers significantly, which produces a coupled problem combining elasticity and wetting [29]. Here, we use our FSI model to study quantitatively the deformation of micropillars produced by a fluid–fluid interface. Fig. 8(a) shows the setup of our problem. We place a small amount of liquid (blue) between the two micropillars (grey) and let capillary forces deform the

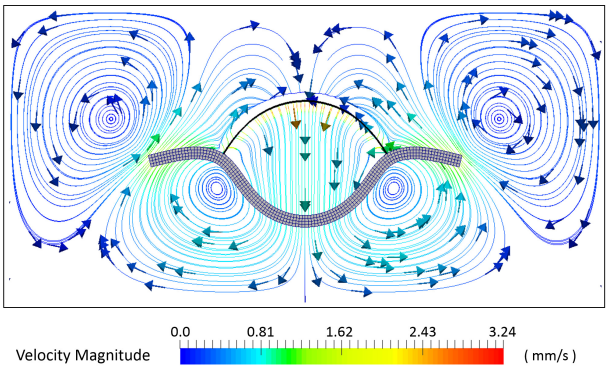

Fig. 6 Solid mesh and streamlines of the fluid velocity at time $t = 0.045\,\mathrm{s}$ for the capillary origami of Fig. 5. The arrows show the direction of the velocity field. The streamlines and the arrows are colored with the velocity magnitude. The interface of the droplet is represented by a black, solid line.

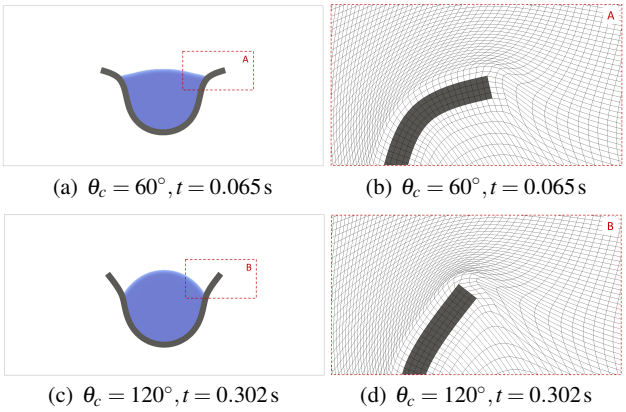

(a) $\theta_c = 60^\circ, t = 0.065\,\mathrm{s}$ (b) $\theta_c = 60^\circ, t = 0.065\,\mathrm{s}$

(c) $\theta_c = 120^\circ, t = 0.302\,\mathrm{s}$ (d) $\theta_c = 120^\circ, t = 0.302\,\mathrm{s}$

Fig. 7 Capillary origami for two different contact angles. [Upper row] Wetting droplet at time $t = 0.065\,\mathrm{s}$. [Bottom row] Non–wetting droplet at time $t = 0.302\,\mathrm{s}$. [Right column] Mesh distortion in the dashed line rectangles indicated in the left figures.

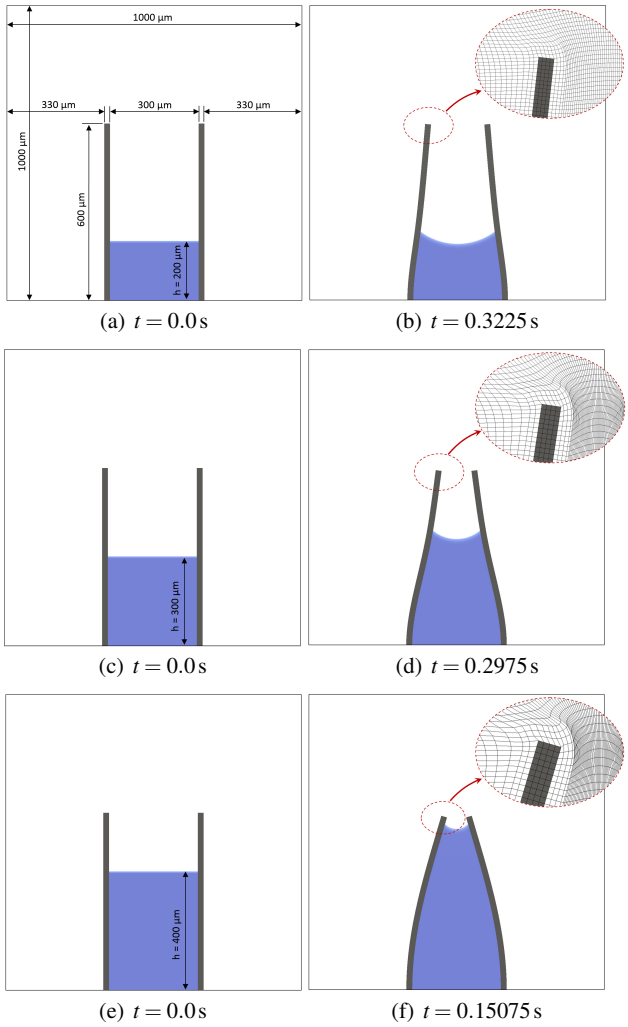

(a) $t = 0.0\,\mathrm{s}$ (b) $t = 0.3225\,\mathrm{s}$

(c) $t = 0.0\,\mathrm{s}$ (d) $t = 0.2975\,\mathrm{s}$

(e) $t = 0.0\,\mathrm{s}$ (f) $t = 0.15075\,\mathrm{s}$

Fig. 8 Wetting of elastic micropillars. The top, middle and bottom row correspond, respectively, to $h = 200.0\,\mu\mathrm{m}$, $h = 300.0\,\mu\mathrm{m}$ and $h = 400.0\,\mu\mathrm{m}$. The insets show the mesh distortion close to the tip of the micropillars. The computational domain is discretized with a uniform mesh of 200^2 quadratic elements. We impose zero velocity in normal direction on all the boundaries, except on the upper one, where we only enforce a stress–free condition. We use a wetting liquid with contact angle $\theta_c = 60^\circ$. The parameters are $\mu = 1412.0\,m\mathrm{Pa\,s}$, $\gamma_f = 46.0\,m\mathrm{N/m}$, $\varepsilon = 2.5\,\mu\mathrm{m}$, $\rho = 1.26\,pg/\mu\mathrm{m}^3$, $M_\varphi = 0.1\,\mu\mathrm{m}^3\mu\mathrm{s}/pg$, $E = 320.0\,k\mathrm{Pa}$, $\nu^s = 0.45$, $\rho^s = 12.6\,pg/\mu\mathrm{m}^3$ and $\Delta t = 2.5\,10^{-6}\,\mathrm{s}$. The computational time was approximately 62 h using 96 cores.

fibers. The micropillars are clamped at the bottom by preventing the displacements in horizontal and vertical directions. Fig. 8(b) shows how surface tension deforms the fibers bringing them close to each other, which, in turn, produces the rise of the liquid.

We observe that, in addition to the obvious parameters controlling the dynamics (the geometry and the mechanical properties of the fibers as well as the physical properties of the fluid) the volume of liquid placed between the micropillars plays a key role. We quantified the volume using the height of the liquid column as shown in Fig. 8; see the plots on the left-hand side. The top, middle and bottom rows correspond, respectively, to $h = 200.0\,\mu\mathrm{m}$, $h = 300.0\,\mu\mathrm{m}$ and $h = 400.0\,\mu\mathrm{m}$. It may be observed that for a given geometrical configuration of the fibers, larger volumes of liquid produce larger deformations. In addition, the dynamics of the process seems to be faster for larger volumes of liquid. This might be explained as follows: Capillary forces have a constant magnitude across all examples, but act at different points of the micropillars due to the different location of the interface. The torque applied to the micropillars is larger for larger volumes, producing stronger deformations. In addition, capillary forces are always oriented at an angle θ_c, owing to the boundary condition given by Eq. (5)(a). Since capillary forces act as follower loads, they have a larger vertical component as the micropillars deform.

4.5 Three dimensional wrapping of a liquid droplet

Here, we study the three dimensional wrapping of a liquid droplet with an elastic membrane. Fig. 9(a) shows the initial configuration of the problem, which consists of a droplet of radius $R = 146.0\,\mu$m (blue) deposited on a membrane of thickness $20.0\,\mu$m (grey) that covers an entire horizontal plane of the computational domain. The elastic membrame is clampled to the lateral boundaries, where we have prevented the displacements in normal and vertical directions. We carry out this simulation assuming that the droplet is a wetting liquid that forms a contact angle of $\theta_c = 60^\circ$ with the solid membrane. The left panels in Fig. 9 show an upper view of the problem. The right panels are vertically flipped, so that we can easily observe the membrane's deformation. The surface tension at the interface folds the solid, resulting in the partial wrapping of the droplet [see Fig. 9(b)]. The initial square shape of the elastic membrane leads to a non–axisymmetric deformation of the structure and triggers the formation of wrinkles [Fig. 9(c)]. Different values of surface tension and solid stiffness should result in different patterns of the wrinkling instability [20,36].

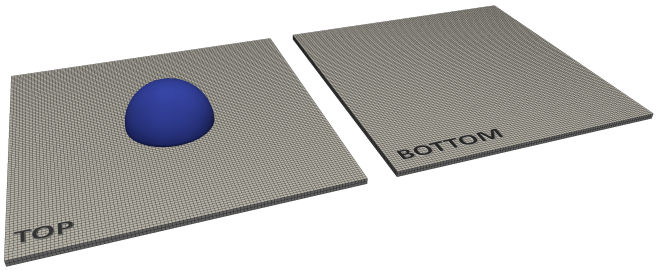

(a) $t = 0.0\,$s

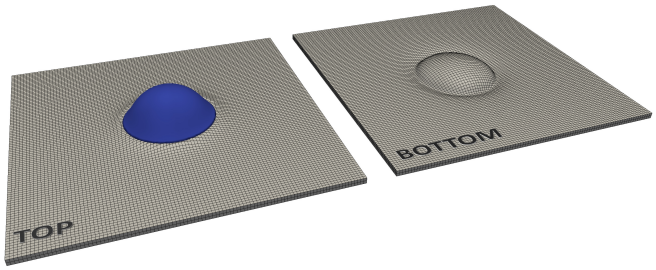

(b) $t = 0.00625\,$s

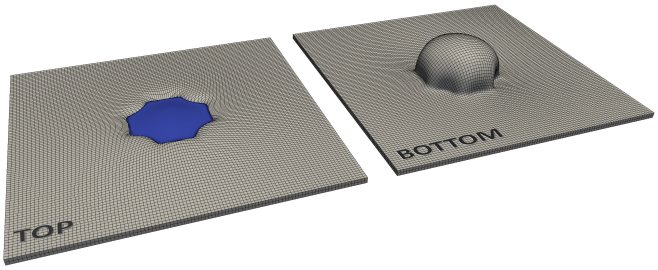

(c) $t = 0.125\,$s

Fig. 9 Top view (left panels) and bottom view (right panels) of the three dimensional wrapping of a liquid droplet. (a) A hemispherical droplet is deposited on a elastic membrane that is clamped to the lateral boundaries of the computational domain. (b) Capillary forces fold the membrane and lead to the partial wrapping of the liquid droplet. (c) A wrinkling instability is developed on the structure, triggered by the non–axisymmetric shape of the membrane. Note that we are only representing the solid domain and one of the fluid phases. The computational domain (not shown) is $\Omega = (0,L)\times(0,L)\times(0,0.5L)$, where $L = 1$ mm. We used a uniform mesh with $100\times100\times50$ quadratic elements. We impose zero velocity in normal direction on all the boundaries as well as zero vertical velocity on the lateral boundaries. The parameters correspond to a glycerol droplet: $\mu = 1412.0\,m$Pa s, $\gamma_f = 46.0\,m$N/m, $\rho = 1.26\,pg/\mu$m^3. We take $\varepsilon = 10.0\,\mu$m and $M_\varphi = 0.1\,\mu$m^3, μs$/pg$. For the membrane we employ $E = 0.6\,k$Pa, $\nu^s = 0.45$, and $\rho^s = 12.6\,pg/\mu$m^3. For the time step we have adopted $\Delta t = 2.5\,10^{-5}\,$s. The computational time was 194 h using 256 cores.

5 Conclusions

We have proposed a computational method for three–dimensional dynamic simulation of elastocapillarity. The solid dynamics is governed by the equations of nonlinear elastodynamics in the Lagrangian description. The fluid theory models the dynamics of two-component, immiscible fluids with surface tension. We adopt a fully–implicit fluid–structure interaction algorithm to solve the problem. We use a boundary–fitted method with the fluid equations written in Arbitrary Lagrangian–Eulerian coordinates. The motion of the mesh is described by the equations of elastostatics. We have shown the viability of our theoretical framework and numerical algorithm by solving several examples of elastocapillary phenomena in two and three dimensions. This work is expected to open new avenues in the study of elastocapillarity. For example, we believe that it would be interesting to study capillary origamis with a model that accounts for evaporation of the droplet. This can be accomplished by using a fluid theory that allows for liquid-vapor phase transformations, such as, the Navier–Stokes–Korteweg equations [13]. Our framework can also be extended to model capillary fracture [10]. This can be accomplished by coupling the current model with a fracture theory.

Acknowledgements The authors would like to thank Robert Style for the experimental data used in Fig. 4.

Compliance with Ethical Standards

Funding: HG and HC were partially supported by the European Research Council through the FP7 Ideas Starting Grant Program (Contract #307201). HG and JB were partially supported by Xunta de Galicia, co-financed with FEDER funds. YB was supported by AFOSR Grant No. FA9550-16-1-0131.

Conflict of interest: The authors declare that they have no conflict of interest.

References

1. D. G. A. L. Aarts, H. N. W. Lekkerkerker, H. Guo, G. H. Wegdam, and D. Bonn. Hydrodynamics of droplet coalescence. *Physical Review Letters*, 95:164503, 2005.
2. Y. Bazilevs, V.M. Calo, J.A. Cottrell, J.A. Evans, T.J.R. Hughes, S. Lipton, M.A. Scott, and T.W. Sederberg. Isogeometric Analysis using T-splines. *Computer Methods in Applied Mechanics and Engineering*, 199(58):229 – 263, 2010.
3. Y. Bazilevs, V.M. Calo, T.J.R. Hughes, and Y. Zhang. Isogeometric Fluid-Structure Interaction: Theory, algorithms, and computations. *Computational Mechanics*, 43(1):3–37, 2008.
4. Y. Bazilevs, M.-C. Hsu, and M.A. Scott. Isogeometric fluid-structure interaction analysis with emphasis on non-matching discretizations, and with application to wind turbines. *Computer Methods in Applied Mechanics and Engineering*, 249-252:28–41, 2012.
5. Y. Bazilevs, K. Takizawa, T. E. Tezduyar, M.-C. Hsu, N. Kostov, and S. McIntyre. Aerodynamic and fsi analysis of wind turbines with the ale-vms and st-vms methods. *Archives of Computational Methods in Engineering*, 21(4):359–398, 2014.
6. Y. Bazilevs, K. Takizawa, and T.E. Tezduyar. *Computational Fluid-Structure Interaction. Methods and Applications*. Wiley, 2013.
7. Y. Bazilevs, K. Takizawa, T.E. Tezduyar, M.-C. Hsu, N. Kostov, and S. McIntyre. Aerodynamic and FSI Analysis of Wind Turbines with the ALE-VMS and ST-VMS Methods. *Archives of Computational Methods in Engineering*, 21(4):359–398, 2014.
8. L. Beirao da Veiga, A. Buffa, G. Sangalli, and R. Vazquez. Analysis suitable T-splines of arbitrary degree: Definition, linear independence, and approximation properties. *Mathematical Models and Methods in Applied Sciences*, 23(11):1979–2003, 2013.
9. J. Bico, B. Roman, L. Moulin, and A. Boudaoud. Adhesion: elastocapillary coalescence in wet hair. *Nature*, 432(7018):690–690, 2004.
10. J. B. Bostwick and K. E. Daniels. Capillary fracture of soft gels. *Physical Review E*, 88(4):042410, 2013.
11. C. E. Brennen. *Fundamentals of multiphase flow*. Cambridge University Press, 2005.
12. J. Bueno, Y. Bazilevs, R. Juanes, and H. Gomez. Droplet motion driven by tensotaxis. *Extreme Mechanics Letters*, 13:10 – 16, 2017.
13. J. Bueno, C. Bona-Casas, Y. Bazilevs, and H. Gomez. Interaction of complex fluids and solids: Theory, algorithms and application to phase-change-driven implosion. *Computational Mechanics*, 55(6):1105–1118, 2015.
14. J. Bueno and H. Gomez. Liquid-vapor transformations with surfactants. phase-field model and isogeometric analysis. *Journal of Computational Physics*, 321:797 – 818, 2016.
15. H. Casquero, C. Bona-Casas, and H. Gomez. A NURBS-based immersed methodology for fluid-structure interaction. *Computer Methods in Applied Mechanics and Engineering*, 284:943–970, 2015.
16. H. Casquero, C. Bona-Casas, and H. Gomez. NURBS-based numerical proxies for red blood cells and circulating tumor cells in microscale blood flow. *Computer Methods in Applied Mechanics and Engineering*, 316:646 – 667, 2017. Special Issue on Isogeometric Analysis: Progress and Challenges.
17. H. Casquero, L. Lei, J. Zhang, A. Reali, and H. Gomez. Isogeometric collocation using analysis-suitable T-splines of arbitrary degree. *Computer Methods in Applied Mechanics and Engineering*, 301:164 – 186, 2016.
18. H. Casquero, L. Lei, Y. Zhang, A. Reali, J. Kiendl, and H. Gomez. Arbitrary-degree T-splines for isogeometric analysis of fully nonlinear Kirchhoff-Love shells. *Computer-Aided Design*, 82:140 – 153, 2017.
19. H. Casquero, L. Liu, C. Bona-Casas, Y. Zhang, and H. Gomez. A hybrid variational-collocation immersed method for fluid-structure interaction using unstructured T-splines. *International Journal for Numerical Methods in Engineering*, 105(11):855–880, 2016.
20. E. Cerda and L. Mahadevan. Geometry and physics of wrinkling. *Physical Review Letters*, 90(7):074302, 2003.
21. N. Chakrapani, B. Wei, A. Carrillo, P. M. Ajayan, and R. S. Kane. Capillarity-driven assembly of two-dimensional cellular carbon nanotube foams. *Proceedings of the National Academy of Sciences*, 101(12):4009–4012, 2004.
22. J. Chung and G.M. Hulbert. A time integration algorithm for structural dynamics with improved numerical dissipation: The generalized-α method. *Journal of Applied Mechanics*, 60:371–375, 1993.
23. J. Austin Cottrell, Thomas J. R. Hughes, and Yuri Bazilevs. *Isogeometric Analysis Toward Integration of CAD and FEA*. Wiley, 2009.
24. P. G. de Gennes. Wetting: statics and dynamics. *Reviews of Modern Physics*, 57:827–863, 1985.
25. M. DeVolder and A. J. Hart. Engineering hierarchical nanostructures by elastocapillary self-assembly. *Angewandte Chemie International Edition*, 52(9):2412–2425, 2013.
26. J. Donea and A. Huerta. *Finite Element Methods for Flow Problems*. Wiley, 2003.
27. J. Donea, A. Huerta, J.-Ph. Ponthot, and A. Rodrguez-Ferran. *Encyclopedia of Computational Mechanics. Arbitrary Lagrangian-Eulerian Methods.*, volume 1, chapter 14. John Wiley & Sons, Ltd, 2004.
28. C. Duprat, A. D. Bick, P. B. Warren, and H. A. Stone. Evaporation of drops on two parallel fibers: Influence of the liquid morphology and fiber elasticity. *Langmuir*, 29(25):7857–7863, 2013. PMID: 23705986.
29. C. Duprat, S. Protiere, A. Y. Beebe, and H. A. Stone. Wetting of flexible fibre arrays. *Nature*, 482(7386):510–513, 2012.
30. J. Eggers, J. R. Lister, and H. A. Stone. Coalescence of liquid drops. *Journal of Fluid Mechanics*, 401:293–310, 1999.
31. H. Gomez, V.M. Calo, Y. Bazilevs, and T.J.R. Hughes. Isogeometric Analysis of the Cahn-Hilliard phase-field model. *Computer Methods in Applied Mechanics and Engineering*, 197:43334352, 2008.
32. H. Gomez and T.J.R. Hughes. Provably unconditionally stable, second-order time-accurate, mixed variational methods for phase-field models. *Journal of Computational Physics*, 230(13):5310–5327, 2011.
33. H. Gomez, A. Reali, and G. Sangalli. Accurate, efficient, and (iso) geometrically flexible collocation methods for phase-field models. *Journal of Computational Physics*, 262:153–171, 2014.
34. H. Gomez and K. van der Zee. *Encyclopedia of Computational Mechanics. Computational phase-field modeling*. John Wiley & Sons, Ltd, 2016.
35. M.-C. Hsu, I. Akkerman, and Y. Bazilevs. Finite element simulation of wind turbine aerodynamics: validation study using nrel phase vi experiment. *Wind Energy*, 17(3):461–481, 2014.
36. J. Huang, M. Juszkiewicz, W. H. de Jeu, E. Cerda, T. Emrick, N. Menon, and T. P. Russell. Capillary wrinkling of floating thin polymer films. *Science*, 317(5838):650–653, 2007.
37. T.J.R. Hughes, J.A. Cottrell, and Y. Bazilevs. Isogeometric Analysis: CAD, Finite Elements, NURBS, exact geometry and mesh refinement. *Computer Methods in Applied Mechanics and Engineering*, 194(39-41):4135 – 4195, 2005.
38. T.J.R. Hughes, W.K. Liu, and T.K. Zimmermann. Lagrangian-Eulerian Finite Element formulation for incompressible viscous

flows. *Computer Methods in Applied Mechanics and Engineering*, 29(3):329 – 349, 1981.
39. K.E. Jansen, C.H. Whiting, and G.M. Hulbert. A generalized-α method for integrating the filtered Navier-Stokes equations with a stabilized Finite Element Method. *Computer Methods in Applied Mechanics and Engineering*, 190(34):305 – 319, 2000.
40. J.H. Jeong, N. Goldenfeld, and J.A. Dantzig. Phase field model for three-dimensional dendritic growth with fluid flow. *Physical Review E*, 64:041602, 2001.
41. A.A. Johnson and T.E. Tezduyar. Mesh update strategies in parallel finite element computations of flow problems with moving boundaries and interfaces. *Computer Methods in Applied Mechanics and Engineering*, 119:73–94, 1994.
42. D. Kamensky, M.-C. Hsu, Schillinger D., J. A. Evans, Aggarwal A., Bazilevs Y., M. S. Sacks, and T.J.R. Hughes. An immersogeometric variational framework for fluid-structure interaction: Application to bioprosthetic heart valves. *Computer Methods in Applied Mechanics and Engineering*, 284:1005–1053, 2015.
43. D. Kamensky, M.-C. Hsu, Y. Yu, J. A. Evans, M. S. Sacks, and T.J.R. Hughes. Immersogeometric cardiovascular fluid–structure interaction analysis with divergence-conforming b-splines. *Computer Methods in Applied Mechanics and Engineering*, 314:408–472, 2017.
44. R.J. King. Pulmonary surfactant. *Journal of Applied Physiology*, 53(1):1–8, 1982.
45. J. Liu, C. M. Landis, H. Gomez, and T.J.R. Hughes. Liquid–vapor phase transition: Thermomechanical theory, entropy stable numerical formulation, and boiling simulations. *Computer Methods in Applied Mechanics and Engineering*, 297:476–553, 2015.
46. G. Lorenzo, M. A. Scott, K. Tew, T.J.R. Hughes, Y. J. Zhang, L. Liu, G. Vilanova, and H. Gomez. Tissue-scale, personalized modeling and simulation of prostate cancer growth. *Proceedings of the National Academy of Sciences*, page 201615791, 2016.
47. A. Moure and H. Gomez. Computational model for amoeboid motion: Coupling membrane and cytosol dynamics. *Physical Review E*, 94(4):042423, 2016.
48. A. Prosperetti and G. Tryggvason. *Computational methods for multiphase flow*. Cambridge University Press, 2009.
49. C. Py, P. Reverdy, L. Doppler, J. Bico, B. Roman, and C. N. Baroud. Capillary origami: Spontaneous wrapping of a droplet with an elastic sheet. *Physical Review Letters*, 98:156103, Apr 2007.
50. O. Raccurt, F. Tardif, F. A. d'Avitaya, and T. Vareine. Influence of liquid surface tension on stiction of soi mems. *Journal of Micromechanics and Microengineering*, 14(7):1083, 2004.
51. B. Roman and J. Bico. Elasto-capillarity: deforming an elastic structure with a liquid droplet. *Journal of Physics: Condensed Matter*, 22(49):493101, 2010.
52. D. Shao, H. Levine, and W-J. Rappel. Coupling actin flow, adhesion, and morphology in a computational cell motility model. *Proceedings of the National Academy of Sciences*, 109(18):6851–6856, 2012.
53. J.-F. Sigrist. *Fluid-Structure Interaction*. John Wiley & Sons, Ltd, 2015.
54. J.C. Simo and T.J.R. Hughes. *Computational Inelasticity*. Springer-Verlag, New Yoirk, 1998.
55. K. Stein, R. Benney, V. Kalro, T. E. Tezduyar, J. Leonard, and M. Accorsi. Parachute fluid–structure interactions: 3-D computation. *Computer Methods in Applied Mechanics and Engineering*, 190(3):373–386, 2000.
56. K. Stein, T. Tezduyar, and R. Benney. Mesh moving techniques for fluid–structure interactions with large displacements. *Journal of Applied Mechanics*, 70:58–63, 2003.
57. R. W. Style, R. Boltyanskiy, Y. Che, J. S. Wettlaufer, L. A. Wilen, and E. R. Dufresne. Universal deformation of soft substrates near a contact line and the direct measurement of solid surface stresses. *Physical Review Letters*, 110:066103, Feb 2013.
58. R. W. Style, A. Jagota, C.-Y. Hui, and E. R. Dufresne. Elastocapillarity: Surface tension and the mechanics of soft solids. *arXiv preprint arXiv:1604.02052*, 2016.
59. K. Takizawa. Computational engineering analysis with the new-generation space–time methods. *Computational Mechanics*, 54:193–211, 2014.
60. K. Takizawa, Y. Bazilevs, and T.E. Tezduyar. Space-Time and ALE-VMS techniques for patient-specific cardiovascular Fluid-Structure Interaction modeling. *Archives of Computational Methods in Engineering*, 19(2):171–225, 2012.
61. K. Takizawa, Y. Bazilevs, T.E. Tezduyar, C.C. Long, A.L. Marsden, and K. Schjodt. ST and ALE-VMS methods for patient-specific cardiovascular fluid mechanics modeling. *Mathematical Models and Methods in Applied Sciences*, 24:2437–2486, 2014.
62. K. Takizawa, T. E. Tezduyar, T. Terahara, and T. Sasaki. Heart valve flow computation with the integrated space–time vms, slip interface, topology change and isogeometric discretization methods. *Computers & Fluids*, 2016.
63. T. Tanaka, M. Morigami, and N. Atoda. Mechanism of resist pattern collapse during development process. *Japanese journal of applied physics*, 32(12S):6059, 1993.
64. M. Taroni and D. Vella. Multiple equilibria in a simple elasto-capillary system. *Journal of Fluid Mechanics*, 712:273–294, 12 2012.
65. S. H. Tawfick, J. Bico, and S. Barcelo. Three-dimensional lithography by elasto-capillary engineering of filamentary materials. *MRS Bulletin*, 41(02):108–114, 2016.
66. T.E. Tezduyar. Finite element methods for flow problems with moving boundaries and interfaces. *Archives of Computational Methods in Engineering*, 8:83–130, 2001.
67. T.E. Tezduyar, S. Aliabadi, M. Behr, A. Johnson, and S. Mittal. Parallel finite-element computation of 3D flows. *Computer*, 26(10):27–36, 1993.
68. T.E. Tezduyar and S. Sathe. Modeling of fluid–structure interactions with the space–time finite elements: Solution techniques. *International Journal for Numerical Methods in Fluids*, 54:855–900, 2007.
69. R. D. M. Travasso, E. C. Poiré, M. Castro, J. C. Rodrguez-Manzaneque, and A. Hernández-Machado. Tumor angiogenesis and vascular patterning: a mathematical model. *PloS one*, 6(5):e19989, 2011.
70. K. Vahidkhah, P. Balogh, and P. Bagchi. Flow of red blood cells in stenosed microvessels. *Scientific Reports*, 6, 2016.
71. G. Vilanova, I. Colominas, and H. Gomez. A mathematical model of tumour angiogenesis: growth, regression and regrowth. *Journal of The Royal Society Interface*, 14(126), 2017.
72. X. Wei, Y. J. Zhang, T. J. R. Hughes, and M. A. Scott. Truncated hierarchical catmull–clark subdivision with local refinement. *Computer Methods in Applied Mechanics and Engineering*, 291:1–20, 2015.
73. X. Wei, Y. J. Zhang, T. J. R. Hughes, and M. A. Scott. Extended truncated hierarchical catmull–clark subdivision. *Computer Methods in Applied Mechanics and Engineering*, 299:316–336, 2016.
74. J. Xu, G. Vilanova, and H. Gomez. Full-scale, three-dimensional simulation of early-stage tumor growth: The onset of malignancy. *Computer Methods in Applied Mechanics and Engineering*, 314:126–146, 2017.
75. L. Zhang, A. Gerstenberger, X. Wang, and W. K. Liu. Immersed finite element method. *Computer Methods in Applied Mechanics and Engineering*, 193(21):2051–2067, 2004.